Raman Scattering, Magnetization and Magnetotransport Study of $SrFeO_{3-\delta}$, $Sr_3Fe_2O_{7-\delta}$ and $CaFeO_3$

Von der Fakultät Mathematik und Physik der Universität Stuttgart
zur Erlangung der Würde eines Doktors der Naturwissenschaften (Dr. rer. nat.)
genehmigte Abhandlung

vorgelegt von

Vladimir Damljanović
aus Belgrad (Serbien)

Hauptberichter: Prof. Dr. Bernhard Keimer
Mitberichter: Prof. Dr. Peter Michler

Tag der mündlichen Prüfung: 16. Dezember 2008

Max-Planck-Institut für Festkörperforschung

Stuttgart 2008

TABLE OF CONTENTS

ABSTRACT

In this thesis we have determined the Raman spectra as well as the magnetization, resistance and magnetoresistance of the compounds $SrFeO_{3-\delta}$, $Sr_3Fe_2O_{7-\delta}$ and $CaFeO_3$ as a function of temperature. These materials are interesting because they contain iron in the unusually high oxidation state +4, which has the same electronic configuration as the Mn^{3+} ion in $LaMnO_3$, a material that shows the giant magnetoresistance effect when doped with calcium or strontium. Materials that show this effect have a wide range of potential applications in electronics, for example in magnetic memory devices. A novel aspect of the work described in this thesis is that it was performed on single crystals with controlled oxygen stoichiometry. Prior research on this class of materials was almost exclusively performed on powder samples, where grain boundaries contribute significantly to the physical properties.

In the non-stoichiometric compound $SrFeO_{3-\delta}$, δ can vary continuously in the range 0 to 0.5. The material exhibits the following crystal structures due to oxygen vacancy ordering: cubic (δ=0), tetragonal (δ=0.125), orthorhombic (δ=0.25) or brownmillerite (δ=0.5). Since the material is a mixture of those phases for other values of δ, the determination of its physical properties is a challenging task.

The cubic phase has the ideal cubic perovskite structure down to the lowest temperature and up to the highest pressure investigated. This compound contains iron ions in the 4+ oxidation state only, and the material is metallic with itinerant e_g electrons at all temperatures. Jahn-Teller distortions of the FeO_6 octahedra are not observed, in contrast to $LaMnO_3$ which is insulating and shows a cooperative Jahn-Teller effect below 800 K. Below the Néel temperature of 134K, cubic $SrFeO_{3-\delta}$ is an antiferromagnet with a helical spin structure. The helix vector is oriented along the main diagonal of the cube. In this thesis we describe the preparation of nearly stoichiometric $SrFeO_{3-\delta}$ crystals with $\delta < 0.05$. The Raman spectrum of a sample annealed under 5kbar of pure oxygen showed no phonon modes above background at any temperature, as expected from a group-theoretical analysis of the ideal perovskite structure. The Raman data also confirm that the crystal structure does not change in the investigated temperature range (15 to 300 K). On the other hand the Möβbauer spectra on the sample annealed at 5kbar show that it contains 5.4% of the tetragonal phase. In another crystal annealed at oxygen pressure 40kbar, the Néel temperature was found to be 140K and Möβbauer spectra did not show any sign of additional phases, confirming that the sample is fully stoichiometric. In addition to the experiments we have performed lattice dynamics calculations for the ideal

composition $SrFeO_{3.00}$ in order to assign the phonon modes observed in infra-red experiments. A group-theoretical analysis for the $SrFeO_{3.00}$ structure shows that it has three triply degenerate infra-red active modes and one triply degenerate silent mode (apart from the one triply degenerate acoustical mode). The calculation accurately reproduces all three frequencies observed in infra-red experiments.

The tetragonal phase belongs to the space group I4/mmm and contains iron ions in the oxidation states 4+ as well as 3.5+. It orders antiferromagnetically below 70K. At the same temperature the material shows a metal to insulator transition which can be shifted by an external magnetic field. This gives rise to a large magnetoresistance effect. At the same temperature charge ordering occurs, in which the iron 3.5+ ions are converted to the 3+ and 4+ valence states. In order to test whether this ordering can be seen in Raman experiments we have measured the Raman spectra of the tetragonal phase in the temperature range 13K to 300K. While only three peaks can be resolved at room temperature, additional modes appear in the spectrum below the charge-ordering transition at 70K. This confirms that the crystal structure changes below this temperature. The self-energy of the peaks does not show any changes through the charge-ordering and magnetic transitions. The orthorhombic phase belongs to the space group Cmmm. It contains iron ions in the oxidation states 3+ and 4+. The magnetic moments of the former ions order antiferromagnetically below 230K, the latter remain disordered down to the lowest temperatures. We have performed measurements of Raman spectra of the orthorhombic phase in the temperature range 6K to 475K. The spectra do not show evidence of any structural phase transition, and the self-energies of observed modes are not affected by the magnetic ordering of the Fe^{3+} sub-lattice. This can be expected since the Fe^{3+} ions are located at the inversion centers and therefore are not involved in the Raman-active modes.

The compound $Sr_3Fe_2O_{7-\delta}$ is tetragonal and has a layered structure with double FeO_2 layers separated by SrO layers. The FeO_2 layers are isostructural to the CuO_2 layers in the cuprate high-temperature superconductors. The parameter δ in $Sr_3Fe_2O_{7-\delta}$ can vary continuously between 0 and 1. In contrast to $SrFeO_{3-\delta}$ where oxygen vacancies are ordered, in $Sr_3Fe_2O_{7-\delta}$ oxygen vacancies are randomly located at sites linking two FeO_6 octahedra in the c-direction (perpendicular to the FeO_2 planes). Above 343K the compound contains iron in the oxidation state 4+ only, while below this temperature charge disproportionation generates iron in the oxidation states 3+ and 5+. This transition is accompanied by a metal-insulator transition. Below the Néel temperature of 120K the material is an antiferromagnet. We have measured the temperature dependence of the magnetization for the magnetic field along high-symmetry axes of the crystal structure. The data indicate that the magnetic moments are aligned parallel to the c axis. We have also performed neutron diffraction measurements demonstrating that the magnetic moments are ordered in a helical structure with propagation vector parallel to the [100] direction. The resistivity and the magnetoresistance were measured in the range 10K to 300K. The resistivity shows a change in slope at the Néel temperature, but no magnetoresistance was observed beyond the experimental error at any temperature. Finally we have measured the Raman spectra of the same sample in the temperature range 15K to 440K. The low temperature spectra could be resolved into 8 modes, which could not be tracked any more above 320K probably due to the thermal smearing. The self-energy of the peaks remains unaffected by magnetic transition, and scattering from

free charge carriers was not observed. In order to assign the observed modes, we have performed lattice dynamics calculations based on the published crystal structure of $Sr_3Fe_2O_7$. While some modes could be successfully assigned, we observed more modes with A_{1g} symmetry than predicted by a group-theoretical analysis, indicating additional structural distortions due to oxygen vacancies.

The $CaFeO_3$ compound has an orthorhombic crystal structure above 290K, which changes to monoclinic below this temperature. The structural transition is accompanied by a metal-insulator transition. Prior work has shown that this transition is due to charge disproportionation of the iron oxidation state 4+ into 3+ and 5+. Here we describe the preparation of stoichiometric $CaFeO_3$ single crystals by high pressure oxygenation of as-grown $CaFeO_{2.5}$ samples, using $KClO_4$ as an oxygen source. Typical annealing conditions were 40kbar (pressure), 1000°C (temperature) and 2 hours (duration of annealing). The powder x-ray diffraction pattern after annealing corresponds closely to the one expected for the crystal structure of $CaFeO_3$ published in the literature, demonstrating that the oxygen enrichment was successful. Resistivity measurements confirmed the metal-insulator transition at 290 K. No magnetoresistance was observed within the experimental error up to magnetic fields of 9T. Magnetization measurements confirmed the transition to helical magnetic order at the Néel temperature of 115K known from previous work on $CaFeO_3$ powders. We have also measured the Raman spectra of this material in the temperature range 15K to 300K. The spectra only show two weak modes, probably because the crystal structure is close to the ideal cubic perovskite structure that does not allow Raman-active phonons. In contrast to tetragonal $SrFeO_{2.875}$ these spectra are unaffected by the charge-ordering transition at 290K within the experimental sensitivity, as expected because the structural distortions associated with this transition are very subtle, and because the iron ions are located at inversion centers and therefore do not contribute to the Raman-active modes.

ZUSAMMENFASSUNG

In dieser Doktorarbeit wurden die Ramanspektren, die Magnetisierung, die elektrische Widerstand und dessen Magnetfeldabhängigkeit der Verbindungen $SrFeO_{3-\delta}$, $Sr_3Fe_2O_{7-\delta}$ und $CaFeO_3$ als Funktion der Temperatur bestimmt. Das besondere Interesse an diesen Materialien liegt darin, dass das enthaltene Eisenatom in einem ungewöhnlich hohen Oxidationszustand 4+ vorliegt und damit in der gleichen elektronischen Konfiguration wie Mn^{3+} in $LaMnO_3$. In letzterem Material findet man den Riesenmagnetwiderstandseffekt, wenn man es mit Kalzium oder Strontium dotiert. Materialien mit dieser Eigenschaft haben viele mögliche elektronische Anwendungen wie zum Beispiel bei magnetischen Speichermedien. Das Neuartige an der hier vorgestellten Arbeit ist, dass Einkristalle mit einer genau eingestellten Sauerstoff-Stöchiometrie untersucht wurden. Vorherige Messungen an dieser Materialklasse beschränkten sich fast ausschlieβlich auf Pulverproben, in denen jedoch Korngrenzen wesentlich den physikalischen Eigenschaften beitrugen.

In der nicht-stöchiometrischen Verbindung $SrFeO_{3-\delta}$ kann δ kontinuierlich zwischen 0 und 0.5 verändert werden. Folgende Kristallstrukturen treten als Folge der einsetzenden Sauerstoffordnung auf: kubisch ($\delta = 0$), tetragonal ($\delta = 0.125$), orthorhombisch ($\delta = 0.25$) oder brownmillerite ($\delta = 0.5$). Auf Grund der Tatsache, dass die Verbindung für alle anderen δ ein Gemisch aus diesen Phasen ist, ist die Bestimmung von deren physikalischen Eigenschaften eine anspruchvolle Aufgabe.

Die kubische Phase zeigt eine ideale kubische Perowskitstruktur selbst bei den hier untersuchten tiefsten Temperaturen und den höchsten Drücken. Diese Verbindung enthält Eisenatome, welche gänzlich im 4+ Oxidationszustand vorliegen, und ist bei allen Temperaturen metallisch mit itineranten e_g Elektronen. Jahn-Teller-Verzerrungen der FeO_6 Oktaeder wurden nicht beobachtet, im Gegensatz zur $LaMnO_3$-Verbindung, die ein Isolator ist und unterhalb von 800K einen kooperativen Jahn-Teller Effekt aufweist. Unterhalb der Néel-Temperatur von 134K ist die kubische $SrFeO_{3-\delta}$ Verbindung ein Antiferromagnet mit einer spiralförmigen Spinstruktur. Der Helixvektor ist parallel zur Hauptdiagonale des Würfels. In dieser Doktorarbeit wird die Herstellung von fast stöchiometrischen $SrFeO_{3-\delta}$ Kristallen mit $\delta < 0.05$ beschrieben. Das Ramanspektrum einer Probe, welche in 5kbar reinem Sauerstoff annealt wurde, zeigte keine Phononenmoden oberhalb des Hintergrundlevels, was auch aus gruppentheoretischen Analysen der idealen Perowskitstruktur zu erwarten wäre. Die Ramanmessungen zeigen auch, dass keine Kristallstrukturänderung innerhalb des hier untersuchten

Temperaturbereiches auftritt (15K bis 300K). Im Gegensatz dazu zeigen Möβbauerspektren an einer Probe, welche bei 5kbar annealt wurde, dass diese 5.4% der tetragonalen Phase enthält. Ein weiterer Kristall, welcher bei einem Sauerstoffdruck von 40kbar annealt wurde, ergab eine Neel Temperatur von 140K und Möβbauerspektren, die keine Anzeichen von zusätzlichen Phasen zeigten, was belegt, dass die Probe gänzlich stöchiometrisch ist. Ergänzend zu den Experimenten wurden Kristallgitterdynamikberechnungen für die ideale $SrFeO_{3.00}$ Zusammensetzung durchgeführt, um die Phononmoden aus den Infrarotmessungen zu identifizieren. Eine gruppentheoretische Analyse der $SrFeO_{3.00}$ Struktur ergab, dass drei dreifach entartete infrarotaktive Moden und ein dreifach entarteter silent mode existiert (abgesehen von einer dreifach entarteten akustischen Mode). Die Berechnungen geben präzise alle drei Frequenzen der beobachteten Infrarotexperimente wieder.

In der tetragonalen Phase, die durch die Raumgruppe I4/mmm beschrieben wird, liegen die Eisen-Ionen in der Oxidationszuständen 4+ und 3.5+ vor. Bei 70K ordnet das Material antiferromagnetisch und zeigt einen Metall-Isolator Übergang. Da dieser durch ein äuβeres Magnetfeld verschoben werden kann, kommt es zu groβen Magnetwiderstandseffekten. Bei der gleichen Temperatur setzt Ladungsordnung ein, wobei die Oxidationszustände der Eisen-Ionen von ursprünglich 3.5+ in 3+ bzw. 4+ überführt werden. Um zu klären, ob diese Ladungsordnung in Raman-Experimenten nachzuweisen ist, haben wir Raman-Spektren in der tetragonalen Phase im Temperaturbereich von 13K bis 300K gemessen. Während nur drei Peaks bei Raumtemperatur beobachtbar sind, tauchen unterhalb der Ladungsordnungstemperatur von 70K weitere Moden auf. Dies bestätigt, dass die Kristallstruktur sich unterhalb dieser Temperatur ändert. Die Selbstenergie der Peaks ändert sich am Übergang nicht. In der orthorhombischen Phase, die zur Raumgruppe Cmmm gehört, haben die Eisen-Ionen die Oxidationzustände 3+ und 4+. Während die Fe^{3+}-Ionen antiferromagnetisch bei 230K ordnen, bleiben die Fe^{4+}-Ionen bis zu niedrigen Temperaturen ungeordnet. In der orthorhombischen Phase haben wir Raman-Spektren im Temperaturbereich von 6K bis 475K gemessen. Diese zeigen keinerlei Hinweise auf einen strukturellen Phasenübergang, und die Selbstenergie der Moden wird nicht durch die magnetische Ordnung des Fe^{3+} Untergitters beeinflusst. Dies ist auch zu erwarten, da die Fe^{3+}-Ionen in den Inversionszentren angeordnet sind und deshalb nicht zu den Raman-aktiven Moden beitragen.

Die Verbindung $Sr_3Fe_2O_{7-\delta}$ ist tetragonal und weist eine Schichtstruktur mit FeO_2 Doppellagen auf, die durch SrO Schichten voneinander getrennt werden. Die FeO_2 Schichten sind isostrukturell mit den CuO_2 Lagen in den Kupfer-Hochtemperatur-Supraleitern. Der Parameter δ in $Sr_3Fe_2O_{7-\delta}$ kann kontinuierlich zwischen 0 und 1 variiert werden. Im Gegensatz zu $SrFeO_{3-\delta}$, bei dem die Sauerstoff-Leerstellen geordnet sind, sind diese in $Sr_3Fe_2O_{7-\delta}$ zufällig auf Gitterplätze verteilt, die zwei FeO_6 Oktaeder (senkrecht zu den FeO_2 Ebenen) miteinander verbinden. Oberhalb von 343K enthält das Material nur Eisen-Ionen im Oxidationszustand 4+, während es unterhalb dieser Temperatur zu einer Ladungs-Disproportionierung kommt, die zu den Oxidationszuständen 3+ und 5+ führt. Bei der Temperatur von 343K erfolgt auch ein Metall-Isolator Übergang, und unterhalb der Néel-Temperatur von 120K wird die Verbindung antiferromagnetisch. Wir haben die Temperaturabhängigkeit der Magnetisierung für Magnetfelder entlang der Hauptsymmetrieachsen des Kristalls

gemessen. Diese Daten legen nahe, dass die magnetischen Momente entlang der c-Achse liegen. Zudem wurden Neutronenstreuexperimente durchgeführt, die auf eine spiralförmige Magnetstruktur mit einem Ausbreitungsvektor parallel zur (100) Richtung hinweisen. Auβerdem wurden Widerstands- und Magnetwiderstandsmessungen in einem Temperaturbereich von 10K bis 300K durchgeführt. Die Steigung des Widerstands ändert sich bei der Néel-Temperatur, allerdings wurden bei keiner Temperatur Magnetwiderstandseffekte auβerhalb des experimentellen Fehlers nachgewiesen. Schlieβlich haben wir das Ramanspektrum derselben Probe im Temperaturbereich von 15K bis 440K gemessen. Im Tieftemperaturspektrum konnten 8 Moden aufgelöst voneinander beobachtet werden, welche überhalb von 320K vermutlich aufgrund thermischer Bewegung nicht mehr ausfindig gemacht werden konnten. Die Selbstenergie der Peaks blieb vom magnetischen Phasenübergang unbeeinflusst, und Streuung durch freie Ladungsträger wurde nicht beobachtet. Um die beobachteten Moden zuzuordnen, haben wir Gitterdynamik-Berechnungen durchgeführt, welche auf der publizierten Kristallstruktur von $Sr_3Fe_2O_7$ basierten. Während einige Moden erfolgreich zugeordnet werden konnten, beobachteten wir mehr Moden mit A_{1g} Symmetrie als durch eine gruppentheoretische Analyse vorhergesagt wird. Dies weist auf zusätzliche strukturelle Unordnung aufgrund von Sauerstofffehlstellen hin.

Oberhalb von 290K hat $CaFeO_3$ eine orthorhombische Struktur, welche unterhalb dieser Temperatur monoklin wird. Dieser strukturelle Phasenübergang wird durch einen Metall-Isolator Übergang begleitet. Eine frühere Arbeit hat gezeigt, dass dieser Übergang aufgrund einer Ladungsdisproportionierung der Oxidationsstufe des Eisens von 4+ in 3+ und 5+ auftritt. Hier beschreiben wir die Herstellung von stochiometrischen $CaFeO_3$ Kristallen durch Hochdrucksauerstoffanreicherung von gewachsenen $CaFeO_{2.5}$ Proben mittels $KClO_4$ als Sauerstoffquelle. Typische Temperungsbedingungen waren 40kbar (Druck), 1000°C (Temperatur) und 2 Stunden (Temperungsdauer). Das Pulver-Röntgendiffraktionsbild nach dem Tempern entspricht genau der erwarteten Kristallstruktur von $CaFeO_3$, welche in der Literatur veröffentlicht ist. Dies zeigt, dass die Sauerstoffanreicherung erfolgreich war. Widerstandsmessungen bestätigen den Metall-Isolator Übergang bei 290K. Bis zu einer Magnetfeldstärke von 9T wurde kein Magnetwiderstand innerhalb des experimentellen Fehlerbalkens beobachtet. Magnetisierungsmessungen bestätigten den Übergang, welcher von früherer Arbeit an $CaFeO_3$ Pulver bekannt ist, zu helimagnetischer Ordnung bei der Néel-Temperatur von 115K. Wir haben ebenfalls das Raman Spektrum dieser Substanz in dem Temperaturbereich zwischen 15K und 300K gemessen. Das Spektrum zeigt lediglich zwei schwache Moden, vermutlich da die Struktur nahe der idealen kubischen Perovskitstruktur ist, welche keine Raman-aktiven Phononen erlaubt. Im Gegensatz zu tetragonalem $SrFeO_{2.875}$ sind diese Spektren unbeeinflusst durch den Ladungsordnungsübergang bei 290K innerhalb der experimentellen Messbarkeit. Dies wird nicht anders erwartet, da die strukturellen Verzerrungen, welche mit dem Übergang verbunden sind, sehr subtil sind, und weil die Eisen-Ionen an Inversionszentren lokalisiert sind und daher nicht zu den Ramanaktiven Moden beitragen.

1. INTRODUCTION

All compounds investigated in this work belong to the class of transition metal oxides. Oxides are compounds of chemical elements with oxygen while transition metals are chemical elements that belong to the 3rd to 12th group of the Mendeleyev system of elements. Those elements have similar chemical properties because they all (with very few exceptions) have a partially filled d electron sub-shell, all other sub-shells being either completely filled or completely empty. Some of the common characteristics are that they are shiny, conduct electricity and heat and appear in more than one different oxidation state. The latter characteristics give rise to the variety of interesting properties of transition metal compounds.

One of the methods of solving Schrödinger equation for a crystal in order to predict its properties is to neglect the interactions between electrons and consider only one electron in the periodic potential of the crystal. This so called one-electron Schrödinger equation could be solved in some cases by tight-binding (or linear combination of atomic orbitals (LCAO) or Bloch) method in which the wave function of one electron Schrödinger equation is found by a suitable linear combination of atomic wave functions centered at corresponding nuclei in the crystal. In such a way energy bands are formed, each band could be named according to which atomic orbital is involved in linear combination of corresponding wave function. Those bands are then filled with non-interacting electrons, and if all bands are either completely filled or completely empty then, within this model, the crystal is insulating. If there is a band of the crystal which is partially filled with electrons, it is expected that the crystal is a conductor. As an example let's take ZnO. Oxygen is in oxidation state O^{2-} which means that zinc is in oxidation state Zn^{2+}. Now this ion has the following configuration when it is alone

$$Zn^{2+}: [Ar]3d^{10}4s^{0}$$

where [Ar] means electronic configuration of the noble gas argon. We can see that it has a completely filled 3d sub-shell and completely empty 4s sub-shell which means that in ZnO the corresponding 3d-band would be completely filled and 4s-band completely empty. For that reason the system is predicted to be an insulator, which is actually the case.

In the year 1937 J. H. de Boer and E. J. W. Verwey pointed out that for some compound these considerations don't hold [BoeVer]. For example in MnO manganese

ions (with charge 2+) give rise to a partially filled 3d-band (because the Mn^{2+} ion (when it is alone) has the following electronic configuration: $[Ar]3d^5 4s^0$ leading to a half filled 3d-band) so MnO should be a good conductor, but it is an insulator. They attributed the observed high resistivity of such compounds to the scattering on imperfections in those crystals. This explanation was rejected by N. F. Mott who thought that such imperfections can not give so high resistivities as was measured. He then argued that the breakdown of the tight binding method is due to the fact that electron-electron interactions can not be neglected any more [Mott]. In 1963 J. Hubbard gave a quantitative theory in which the electron-electron interaction in crystals with partially filled d- or f-bands is taken into account [Hubb]. He started with a Hamiltonian (in the second quantization formalism) of electrons in the periodic potential of a crystal which also contained electron-electron interaction. The minimal model is:

$$\hat{H} = \sum_{i,j}\sum_{\sigma} T_{ij}\hat{c}^{+}_{i\sigma}\hat{c}_{j\sigma} + \frac{1}{2} I \sum_{i,\sigma} \hat{n}_{i,\sigma}\hat{n}_{i,-\sigma} ,$$

where i and j are counting ionic sites, σ count two possible spin orientations (up and down), $\hat{c}^{+}_{i\sigma}$ ($\hat{c}_{i\sigma}$) is the creation (annihilation) operator for an electron with spin σ and at site i, $\hat{n}_{i,\sigma} = \hat{c}^{+}_{i,\sigma}\hat{c}_{i,\sigma}$ and I is a constant (a matrix element that denotes the Coulomb repulsion between two electrons at the same site). This Hamiltonian is named Hubbard Hamiltonian and materials that are supposed to be good conductors according to the band theory but are insulators due to the strong electron-electron interaction are called Mott-Hubbard insulators. We can see from the form of the Hubbard Hamiltonian that it is a generalization of tight binding method in which the electron-electron interaction only between electrons on the same site is also taken into account. Another name for materials in which electron-electron interaction can not be neglected is systems with strongly correlated electrons. High temperature superconductors for example belong to this class. To see this we can start from the parent compound La_2CuO_4 which contains copper in the formal oxidation state Cu^{2+} with electronic configuration $[Ar]3d^9$, so that this compound should be conductor, but it is an insulator.

Among interesting phenomena observed in transition metal oxides is the effect of colossal magnetoresistance. Magnetoresistance is a measure of how much the resistivity of a substance in the magnetic field differs from the one measured when the field is zero. For most materials this difference remains within 5%. In the year 1988 it was discovered that magnetoresistance of Fe/Cr multi-layers jump to around 50% for magnetic field above 2T [BaBrFe], [BiGrSa]. This effect was named giant magnetoresistance effect (GMR) and was strong enough for applications in electronics, for example in fabrication of magnetic memories. This was not the end of the story because in the year 1995 it was discovered that the material $Pr_{1-x}Ca_xMnO_3$ changes its resistivity by eleven orders of magnitude when placed in the field of around 3T [ToAsMo]. This effect is called colossal magnetoresistance and its origin remains still unclear. Research on manganese oxide $LaMnO_3$ started in 1950 when G. H. Jonker and J. H. van Santen investigated transport and magnetic properties of this and also doped material. They have found that pure $LaMnO_3$ is an antiferromagnetic insulator, but when trivalent La is replaced with a divalent element the resulting compound becomes a ferromagnetic metal [JonSan]. It

follows from electro-neutrality that the doped compound contains manganese in mixed valence states Mn^{3+} and Mn^{4+}. One year later Zener gave a qualitative explanation of the magnetic and transport properties of pure and doped $LaMnO_3$ [Zener]. In this compound manganese ions are far apart and always separated by oxygen ions. For this reason the overlap between wave functions on two neighboring Mn ions is negligible and this leads to a very small exchange interaction. Now Zener postulated that an electron which hops from one Mn-site to the other has its spin always in the same direction and that the Hund's rule coupling is large between electrons on manganese ions. For those reasons the electron can hop between two adjacent Mn ions only if their spins are parallel. In such a way the material can be either a ferromagnetic metal or an antiferromagnetic insulator, which was in agreement with experiments. The mechanism of hopping was proposed as follows: consider the following configuration Mn^{3+}-O^{2-}-Mn^{4+}. The electron from the left manganese ion hops to the oxygen ion while at the same time the electron from the oxygen ion hops to the right manganese ion (all this without altering the electron spins). Such a process Zener called "double exchange". Later this theory was developed in a more detailed, quantitative manner [AndHas], [deGennes]. The interest in doped $LaMnO_3$ has grown also because of the discovery that $La_{2/3}Ba_{1/3}MnO_3$ shows giant magnetoresistance effect [HeWeHo]. It was argued later that double exchange alone can not explain such behavior and that additional interactions have to be included [MiLiSh]. As in the case of high temperature superconductors, those materials are also considered to belong to the class of systems with strongly correlated electrons. In $LaMnO_3$, manganese ion has oxidation number 3+ with the electronic configuration Mn^{3+}: $[Ar]3d^4$ which gives rise to the partially filled d-band, but the material is insulator.

In this thesis we have investigated Raman spectra as well as magnetization, resistance and magnetoresistance at various temperatures of the single crystals of the $SrFeO_{3-\delta}$, $Sr_3Fe_2O_{7-\delta}$ and $CaFeO_3$ compounds. A novel aspect of the work described here is that it was performed on single crystals with controlled oxygen stoichiometry synthesized at the Max Planck Institute for Solid State Research. Prior research on this class of materials was almost exclusively performed on powder samples, where grain boundaries contribute significantly to the physical properties. These compounds are interesting because they contain iron in the unusually high oxidation state +4. Such highly oxidized iron ion has the same electronic configuration as manganese +3 ion in $LaMnO_3$, a material that shows the giant magnetoresistance effect when doped with calcium or strontium.

Part of the data from this thesis is published in the following references:

* P. Adler, A. Lebon, V. Damljanović, C. Ulrich, C. Bernhard, A. V. Boris, A. Maljuk, C. T. Lin and B. Keimer: „Magnetoresistance effects in $SrFeO_{3-\delta}$: Dependence on phase composition and relation to magnetic and charge order", Physical Review B **73**, 094451 (2006).

* A. Maljuk, A. Lebon, V. Damljanović, C. Ulrich, C. T. Lin, P. Adler and B. Keimer: „Growth and oxygen treatment of $SrFeO_{3-y}$ single crystals", Journal of Crystal Growth **291**, 412 (2006).

2. THE COMPOUND $SrFeO_{3-\delta}$

Non-stoichiometric compounds are chemical, solid-state compounds in which the content of one or more constituent elements can vary continuously within a certain range. Such is the case in, for example, wustite whose formula is Fe_xO where $0.833<x<0.957$ or zirconium-oxide whose formula is ZrO_x where $1.700<x<2.004$ [PCb21]. The effect of non-stoichiometry is closely related with defects in the crystal [Qa4]. Defects can be vacancies (an atom is missing from its position in the lattice), interstitials (there is an extra atom in the place where in ideal case there should be no atoms), an atom of one type can replace the atom of another type and so on. Each type of defect has a certain influence on the chemical formula which describes the compound under observation. For example interstitials of atoms of one type will induce excess of the content of atoms of that type in the chemical formula, vacancies of atoms of one type will decrease the content of atoms of that type in the chemical formula and in a similar way the effect of other types of defects can be estimated.

The compound $SrFeO_{3-\delta}$ belongs to the class of non-stoichiometric compounds where the oxygen content is variable. In this compound δ can vary continuously in the range $0\leq\delta\leq0.5$. Experimental proof that this is really the case is given by the phase diagram shown in the figure 2.1 (from [JBMac]). From this diagram we can see that δ varies continuously from 0.5 to 0 because at δ where the left solid curve ends the right solid curve begins (at higher temperature). The lower limit of the perovskite phase expressed by the dashed curve should not be taken literally because after the publication of this paper (in 1965) some more phases were discovered, which will be described later.

From the previous description follows that the type of defects which leads to the non-stoichiometry of $SrFeO_{3-\delta}$ is oxygen vacancies. Now the following questions may appear: where are those vacancies located? Is the crystal structure of $SrFeO_{3-\delta}$ the same for all compositions with the number of vacancies increased monotonically or it is different for different δ? If so, where are the borders where one crystal structure disappears and another appears? and so on… Extensive research on this compound shows that there exist 4 phases of ideal composition in the range $0\leq\delta\leq0.5$, these are: $SrFeO_{2.5}$ ($\delta=0.5$; or equivalently $Sr_2Fe_2O_5$) called brownmillerite, $SrFeO_{2.75}$ ($\delta=0.25$; or equivalently $Sr_4Fe_4O_{11}$) called orthorhombic, $SrFeO_{2.875}$ ($\delta=0.125$; or equivalently $Sr_8Fe_8O_{23}$) called tetragonal and $SrFeO_3$ ($\delta=0$) called cubic perovskite. For all other δ the composition is a mixture of the two nearest ideal phases. This makes the investigations of $SrFeO_{3-\delta}$ a difficult task since it is not straight-forward to assign which physical property

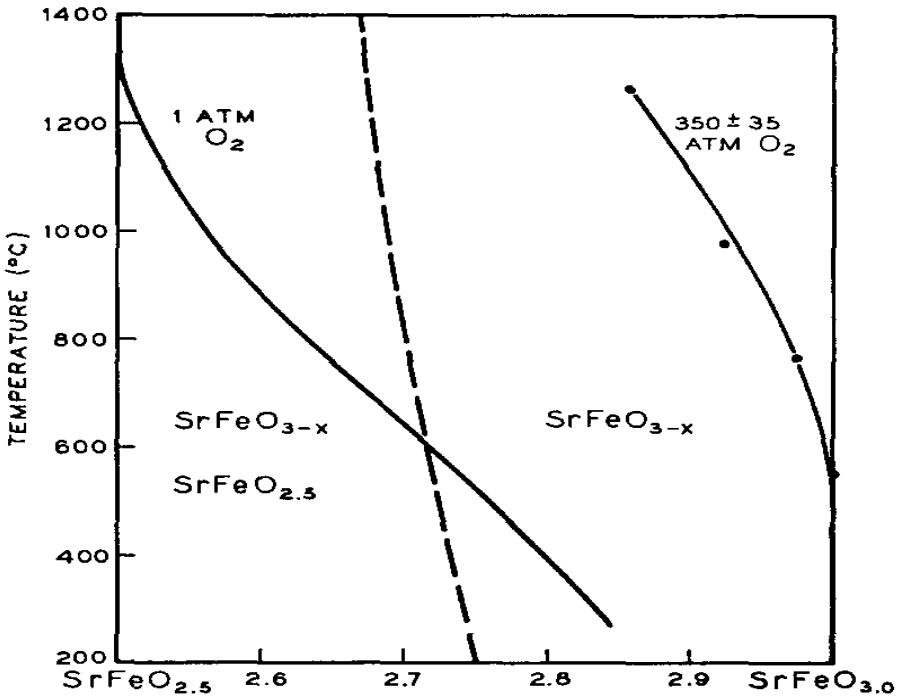

Figure 2.1: Phase diagram (temperature versus composition) of $SrFeO_{3-\delta}$. Left (right) solid line is isobar at 1atm (350atm) of oxygen pressure, dashed line is approximate lower oxygen limit of perovskite phase (1atm=$1.0133\cdot10^5$Pa) (from [JBMac]).

is due to which phase. When the $SrFeO_{3-\delta}$ is heated above a certain temperature (which depends on δ) the crystal structure becomes cubic perovskite with randomly distributed oxygen vacancies. Below this temperature, vacancies are ordered in a manner which will be described for ideal compositions in the part on crystal structures. The typical dependence of this temperature on δ (under the pressure of 1atm) is shown in the figure 2.2 (from [TaKaTaYa]). From this figure Takeda et al. estimated that the oxygen vacancy ordering temperatures at 1atm for ideal phases are 1103K for the brownmillerite phase ($Sr_2Fe_2O_5$), 593K for the orthorhombic phase ($Sr_4Fe_4O_{11}$), 523K for the tetragonal phase ($Sr_8Fe_8O_{23}$) while vacancies in the cubic perovskite phase ($SrFeO_{3-\delta}$) remain disordered down to room temperature [TaKaTaYa] (this estimation was also confirmed in [TaOkNa]). The order-disorder transition in $SrFeO_{3-\delta}$ was also studied in [Gibb1] by Möβbauer spectroscopy, powder X-ray diffraction and magnetic susceptibility measurements, [FoPoGr] by Möβbauer spectroscopy, [MiOkYa] by high temperature gravimetry and high temperature powder X-ray diffraction, [SchCam] by neutron diffraction, [HaBaNo] by heat capacity measurements and [Kosl1] numerically. On the other hand estimations of the room temperature ranges of δ in which single phases exist differs from author to author and can roughly be estimated to be $2.92\leq3-\delta\leq3.00$ for cubic, $2.83\leq3-\delta\leq2.875$ for tetragonal and $2.68\leq3-\delta\leq2.75$ for orthorhombic phase [TaKaTaYa], [NakIid], [FoPoGr], [HaAtKa]. This division should not be taken literally since in most cases every phase contains some minor amount of other phases. For this reason (as have

already been stated) it is important to pay attention to the composition of each particular sample investigated.

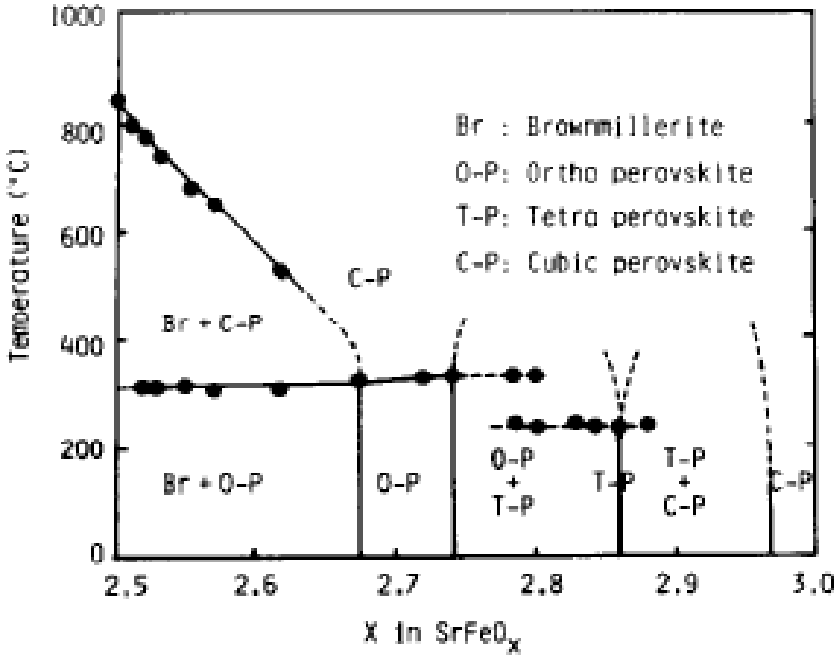

Figure 2.2: Approximate phase diagram showing single phase and coexistence of more phases of $SrFeO_{3-\delta}$ (from [TaKaTaYa]).

Oxygen and strontium in compounds have the usual formal valence state -2 and +2 respectively. From this and electro neutrality it follows that in $SrFeO_{3-\delta}$ iron's valence changes with the change in oxygen content. Still in estimation of valence state of iron, one has to pay attention to the following fact: generally, oxygen vacancies may trap electrons to form so called F-centers (from German Farbzentum i.e. color center. The name came from the property that some single crystals which are usually transparent for light and colorless, gain certain color due to presence of F-centers) [Jm9]. This property can be qualitatively understood in the following naive way: if in a single crystal certain place is "reserved" for the oxygen ion which is negatively charged that means that this crystal "prefers" negatively charged particle in that place. If one oxygen atom is missing from this place electrons are "good candidates" for replacement since they are negatively charged too. By comparing their Möβbauer measurements with results obtained by theromogravimetry Wiβmann and Becker found that electrons are NOT trapped by oxygen vacancies in $SrFeO_{3-\delta}$ meaning that charge is divided completely among Sr, Fe and O ions [WisBec]. This is an important result which can be used in estimations of valence states of Fe ions.

In the following parts, properties and measurement done on different phases of $SrFeO_{3-\delta}$ will be presented.

2.1 PROPERTIES OF AND MEASUREMENTS ON THE CUBIC PHASE

As previously stated, the cubic phase corresponds to the ideal composition $SrFeO_3$. If we start from the usual oxidation states of strontium and oxygen we get from electro neutrality, the oxidation state of iron 4+ which means that the electronic configuration of iron ion when it is alone is Fe^{4+}:[Ar]$3d^4$. Crystal structure (shown and discussed latter) of $SrFeO_3$ is such that iron ions are in the centers of ideal FeO_6 octahedra, meaning that the corresponding crystal field is of symmetry $\underline{O}_h$. As was shown in the Appendix A this crystal field leads to the splitting of five 3d orbitals in lower lying, triply degenerate t_{2g} and higher, doubly degenerate e_g. Three electrons occupy the t_{2g} level with parallel spins according to Hund's rules, while the remaining electron can either occupy the e_g level in a high spin configuration (S=2) or one of the t_{2g} levels in a low spin configuration (S=1). Which of those two possibilities is realized we can find out from Möβbauer spectroscopy and from neutron diffraction experiments. A Möβbauer spectra of $SrFeO_3$ at various temperatures are given in the following figure (from [Gall]):

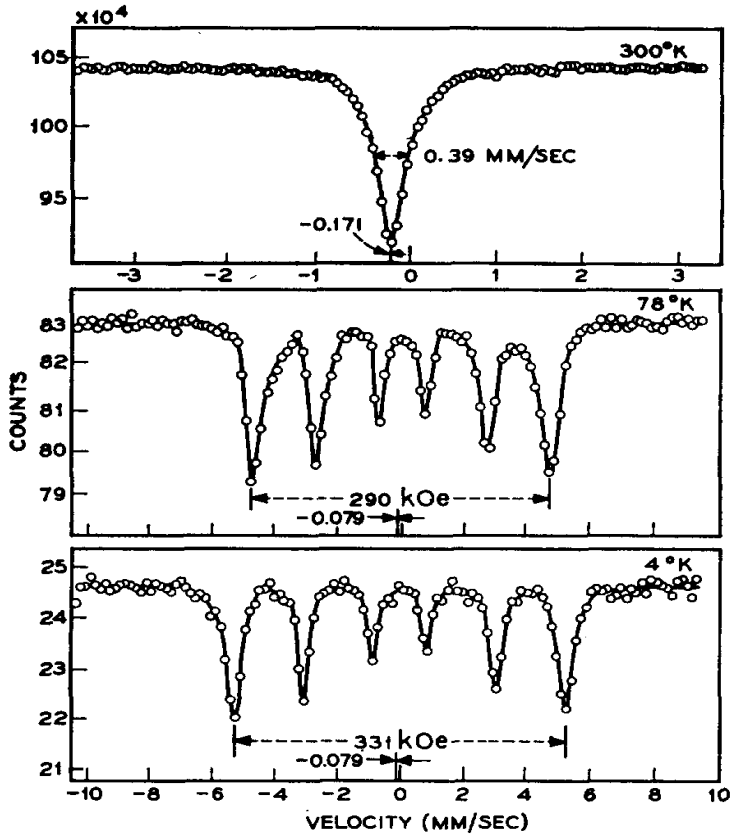

Figure 2.3: Möβbauer spectrum of $SrFeO_3$. Isomer shift is relative to copper. (from [Gall]).

We can see that at 300K the spectrum consists of only one line with an isomer shift of minus 0.171mm/s relative to copper. Gallagher et al. claimed that this isomer shift is much less negative than that expected for Fe^{4+} based on a purely ionic configuration and that this is a sign of increased degree of covalency [Gall]. Below the antiferromagnetic

ordering temperature of around 134K the spectrum consists of one hyperfine sextet with hyperfine magnetic field of 33.1T which corresponds to the Fe^{4+} ions in the high spin state (this value of the magnetic field is in good agreement with the magnetic field of 34T observed in $CaFeO_3$ (see chapter 4 for comparison)). The Möβbauer spectrum shown in figure 2.3 is proof that the oxidation state of Fe remains unchanged down to the lowest temperatures and also that the geometry of environment of Fe ions is unchanged over this temperature range (it is interesting to note here that in recent paper some authors have predicted charge ordering in $SrFeO_3$ based on ab initio cluster model calculations [YuKoIv]. This is inconsistent with above cited experiments). Now the following question may occur: if electrons on Fe-ions in $SrFeO_3$ are in a high spin state, doesn't this induce a Jahn-Teller instability and induce lattice distortions, which are not observed (the fact that $SrFeO_3$ has the ideal cubic perovskite structure down to 4.2K was experimentally verified [JBMac])? The answer can be given in the following experimental fact: $SrFeO_3$ is metallic with a room temperature resistivity value of around 1mΩcm [JBMac] which means that the above picture of localized electrons is not appropriate. Instead of this a picture of 3 localized electrons in the t_{2g} level and the remaining electron itinerant is generally accepted [TaOkNa], [BoFuMi], [MaMoDe]. In favor of this assumption are neutron scattering measurements where the estimated magnetic moment on Fe-ions was found to be 2.7 Bohr magnetons at liquid nitrogen temperature [TaYaWa]. This is in good agreement with the value (3 Bohr magnetons) expected for three electrons with parallel spins in the t_{2g} level.

The crystal structure of $SrFeO_3$ is shown in the following figure:

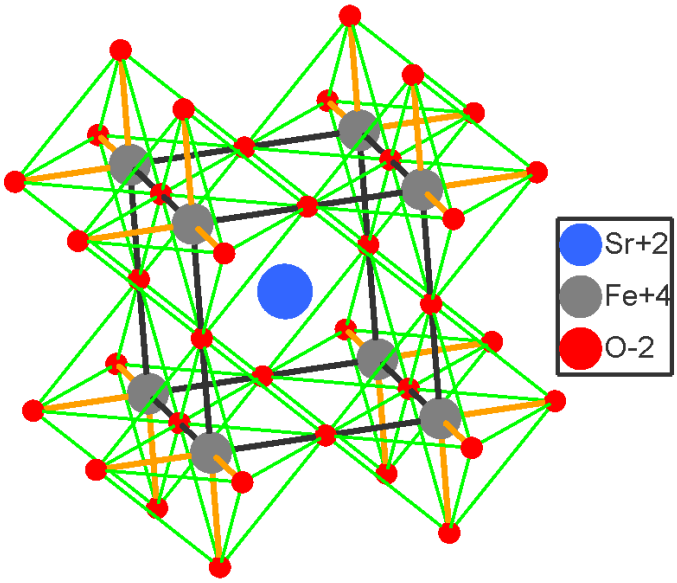

Figure 2.4 (color): Crystal structure of $SrFeO_3$. The black cube denotes the unit cell. The Sr^{2+} ion (blue sphere) is in the center of the unit cell. Spheres of different colors denote different sorts of ions as indicated in the legend. Green lines denote FeO_6 octahedra.

$SrFeO_3$ has the ideal cubic perovskite structure. It belongs to the Pm3m space group (O_h^1 or number 221 in International Tables for Crystallography notation) with lattice constant a=3.851Å at room temperature and pressure [Hodg]. It retains this ideal structure down to the lowest temperature of 4.2K and also up to the pressure of 56GPa [KaNaKu]. The structure consists of ideal corner sharing octahedra with oxygen ions as a link between them. In each octahedron the oxygen-iron distance is equal to 1.9255Å which is exactly half of the lattice constant. Oxygen-iron-next oxygen angles are exactly 90°. All this leads to the site symmetry of Fe ions being $\underline{O}_h$.

The atomic coordinates of an asymmetric unit is given in the table 2.1. From this table one can see that the number of formula units in primitive cell is one (Z=1).

Table 2.1: Fractional coordinates of the asymmetric unit for $SrFeO_3$

Atom	Wyckoff position	x/a	y/a	z/a
Sr	1b	0.5	0.5	0.5
Fe	1a	0	0	0
O	3d	0	0	0.5

Since the volume of the primitive cell is $V=a^3=57.1Å^3$ and molar mass of strontium is M_{Sr}=87.62gr/mol and M_{Fe}=55.847gr/mol, M_O=16gr/mol it follows that the density of $SrFeO_3$ at room temperature and pressure is:

$$\rho = \frac{Z \cdot M_{SrFeO_3}}{V \cdot N_A} = 5.57 \frac{gr}{cm^3}.$$

Concerning the magnetic properties of the cubic phase, Watanabe was first to discover that it is an antiferromagnetic material with Neel temperature around 130K [Wata]. Typical behavior of magnetization with respect to temperature is shown in the figure 2.5 (from [ZhaoZhou]). In this figure we can see an antiferromagnetic transition at around 125K. This temperature is a bit lower than reported in [TaYaWa] and [Wata], probably due to the fact that the sample from Zhao et al. was slightly oxygen deficient (δ was around 0.05). It is established that with decreasing of oxygen content while still in cubic phase, the Neel temperature decreases. On the other hand, with increasing pressure from room value up to more than 17GPa the magnetic ordering temperature increases abruptly to over 400K [KaNaKu]. A second interesting aspect is a hump in the magnetization curves around 65K (indicated with an arrow in the figure 2.5). In their paper, Zhao et al. assigned this hump to the presence of paramagnetic phase carrying Fe^{3+} ions. However this didn't find support in other publications and our investigations show that this hump remains unchanged even in the cubic samples which are annealed at 10 times higher pressure, therefore containing much less other phases, as shown by our Möβbauer measurements (these data will be shown and discussed latter). For that reason the origin of this hump remains an unsolved question.

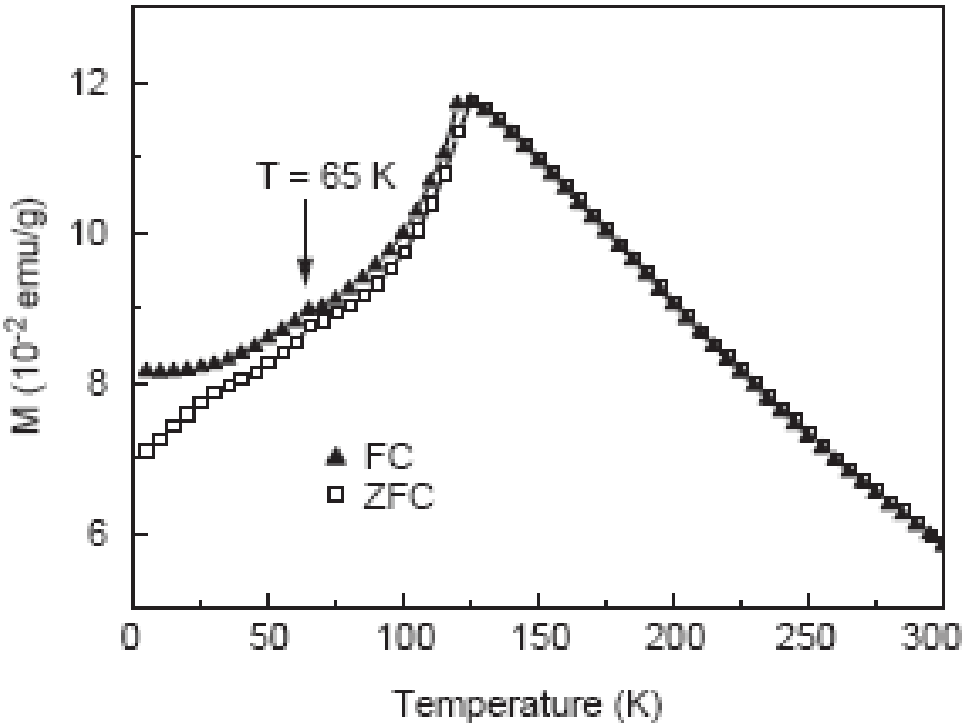

Figure 2.5: Temperature dependence of magnetization of cubic phase in external field of 0.05T. FC-field cooled, ZFC-zero field cooled (from [ZhaoZhou]).

The precise orientation of magnetic moments on Fe-sites in cubic phase was determined for the first time by neutron diffraction measurements on powdered samples by Takeda et al. in 1972 [TaYaWa]. Their result show that below the Neel temperature of 134K, $SrFeO_3$ has a helical magnetic structure (also called antiferromagnetic screw structure or spiral structure [JJ3]) with a helix wave vector parallel to the [111] direction and with the magnitude:

$$\left|\vec{Q}\right| = 0.112 \cdot \sqrt{3} \cdot a^* = 0.112 \cdot \sqrt{3} \cdot \frac{2\pi}{a}$$

where $a^* = \frac{2\pi}{a}$ is the reciprocal lattice parameter, a being the lattice parameter of the cubic perovskite lattice of $SrFeO_3$. Their results were reported at liquid nitrogen temperature (77K). All magnetic moments are perpendicular to the helix wave vector and the angle between magnetic moment at ion which is located at a site with radius vector $\vec{r}$ from the origin of coordinate system, and direction of magnetic moment at the origin is given by:

$$\theta = \vec{Q} \circ \vec{r} \qquad (2.1).$$

This angle depends on the choice of coordinate system's origin. From the equation 2.1 follows that all magnetic moments that belong to one plane which is perpendicular to the helix wave vector are parallel to each other meaning that the order within such a plane is ferromagnetic (for the sketch of helical magnetic structure see figure 4.4, sub sketch "spiral"). In the next such plane magnetic moments are ordered in different direction at an angle given by formula 2.1 and so on. This means that the net magnetization is zero (outside external magnetic field) since all those differently oriented magnetic moments cancel each other when averaged over small but finite volume.

The results of Takeda et al. are confirmed by Oda et al. in 1977 [OdaYaTa]. They investigated single crystals of the oxygen deficient cubic phase $SrFeO_{2.90}$ also by neutron diffraction. Due to oxygen deficiency their sample had a Neel temperature of only 118K but the magnetic order was helical with the helix wave vector parallel to [111] direction as reported in [TaYaWa]. The magnitude of the helix wave vector at liquid helium temperature (4.2K) was found to be

$$\left|\vec{Q}\right| = 0.130 \cdot \frac{2\pi}{a} \cdot \sqrt{3} \qquad (2.2).$$

The electrical conductivity of $SrFeO_3$ was investigated for the first time by MacChesney et al. in 1965 [JBMac]. They have found that this compound shows metallic conductivity with the room temperature value of resistivity around 1mΩcm. From thermoelectric voltage measurements they concluded that the charge carriers which are responsible for the conduction are electrons and from Hall voltage measurements they estimated concentrations of charge carriers of $n>2x10^{21}cm^{-3}$ while the mobility was less than $1.5cm^2/(Vs)$ [JBMac].

In a paper published in the year 2000 Zhao et al. reported for the first time that $SrFeO_3$ shows change of resistivity in the magnetic field, so called magnetoresistance effect [ZhYaZh]. Their compound was slightly oxygen deficient (δ=0.05) but it still belonged to the cubic phase. Investigations of Zhao et al. on same topic were also published, with minor additions, in [ZhMaNg], [ZhZhYa] and [ZhaoZhou]. Their result is shown in the figure 2.6 (from [ZhYaZh]). Magnetoresistance (MR) was defined as $MR = 100 \cdot \frac{\rho(0T) - \rho(9T)}{\rho(0)}$. We can see that outside of the magnetic field temperature dependence of the resistivity shows metallic like behavior ($d\rho/dT>0$) but the value of resistivity remains within the same order of magnitude over the whole temperature range they investigated. With applied magnetic field and at temperatures which corresponds to the hump in the magnetization data (around 65K) the resistivity decreases, producing a magnetoresistance effect of around 15%. Both zero field and field curves show a small hysteresis around that temperature. Zhao et al. assigned the decrease of the resistivity in magnetic field to the suppression of electron-electron correlations and quantum interference effects [ZhYaZh]. In the next chapter the results of our measurements on our samples will be presented

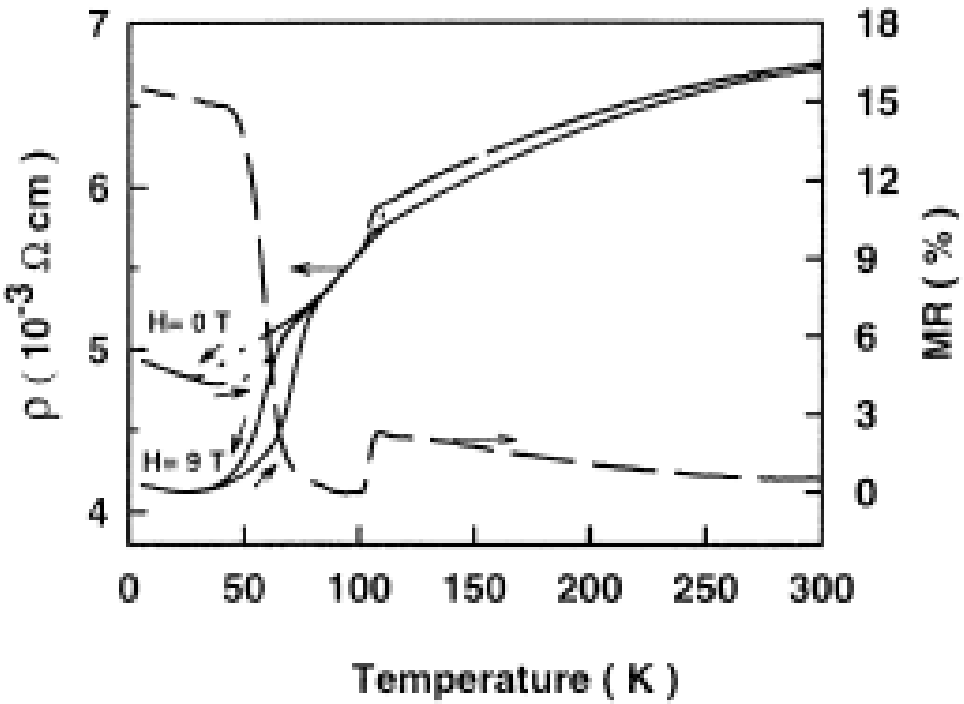

Figure 2.6: Resistivity and magnetoresistance in $SrFeO_{2.95}$ in applied field of 0T and 9T (from [ZhYaZh]).

2.1.1 MEASUREMENTS ON THE CUBIC PHASE

Single crystal samples with different oxygen content were grown and characterized by Maljuk et al. as described in following references [MaStUl] and [MaLeDa]. The crystals were grown by the floating zone method using a four-mirror type infrared image furnace equipped with four halogen lamps with power 500W and 1000W as a heat source. The samples were characterized by thermogravimetry, magnetic susceptibility, Möβbauer, Raman, neutron and synchrotron diffraction experiments. A cubic $SrFeO_3$ single crystal was obtained by post annealing under high oxygen pressure of 5kbar at 400°C (it is interesting to note that another method for obtaining cubic $SrFeO_3$ was reported in [WaFoDe]. They used electrochemical oxidation starting from brownmillerite $SrFeO_{2.5}$ as a working electrode). The mosaicity (full width at half maximum (FWHM) of the rocking curve) determined by neutron scattering experiments of such prepared cubic sample was around 0.5^o [MaLeDa], while the same property measured with synchrotron radiation on another sample was around 0.1^o [MaStUl]. This indicates that the cubic single crystals have a highly ordered lattice. In the following figure the temperature dependence of magnetic susceptibilities of our samples are shown (from [AdLeDa]):

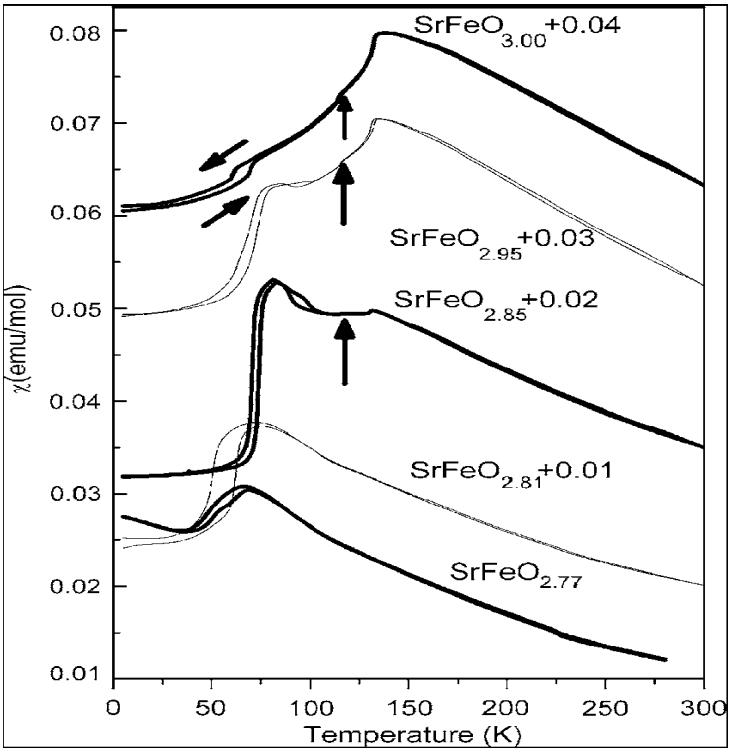

Figure 2.7: Temperature dependence of magnetic susceptibility of $SrFeO_{3-\delta}$ for different δ. Some of the curves were shifted vertically by amounts indicated in the figure. External field is 1T (from [AdLeDa]).

The oxygen content shown by each curve in this figure was determined from thermogravimetry with an accuracy of 0.02. Curves were measured in field cooling and subsequent field heating runs. Let's now concentrate on the curve that belongs to the cubic sample (composition $SrFeO_{3.00}$). We can see an antiferromagnetic transition at around 132K. This value is a little bit lower than that reported (134K), indicating that the sample is not 100% cubic but has very small oxygen deficiency (this is confirmed by our Möβbauer measurements which will be shown and discussed latter). The hump previously reported to occur around 65K (see figure 2.5) is in our case at temperature 60.9K (cooling mode) i.e. 70.1K (heating mode) therefore having hysteresis of 10K. The mean of those two values gives 65.5K which is in good agreement with the value reported earlier (figure 2.5). In addition in the figure 2.7 one can see an additional anomaly at around 115K. This anomaly is marked with a vertical arrow and its origin is still unclear but as will be shown later it is an intrinsic property of the cubic phase. In order to additionally verify quality of our samples it is useful to see their temperature dependence of resistivity and magnetoresistance. This is shown in the following figure (from [AdLeDa]):

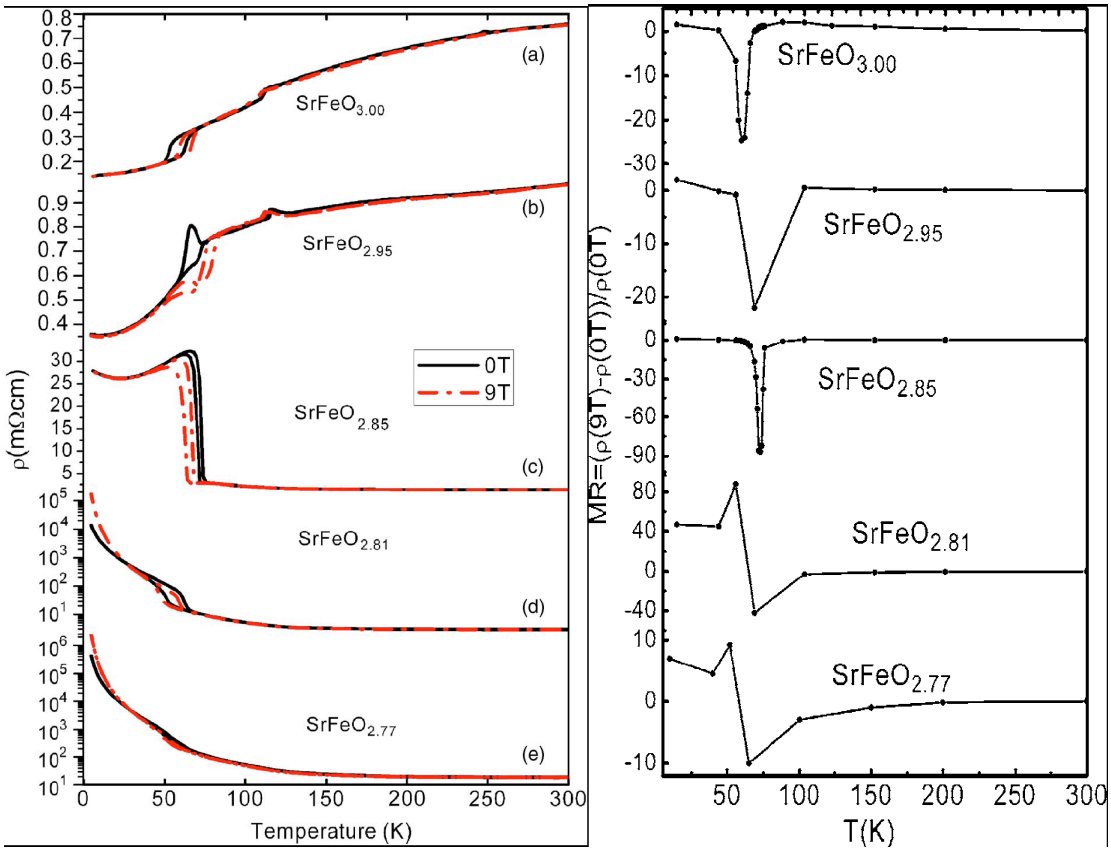

Figure 2.8 (color): Temperature dependence of resistivity in zero magnetic field (black) and in magnetic field of 9T (red) for various $SrFeO_{3-\delta}$ (left) and temperature dependence of the magnetoresistance MR [MR=(ρ(9T)-ρ(0T))/ρ(0T)] for corresponding samples (right) (from [AdLeDa]).

If we now concentrate on cubic $SrFeO_{3.00}$ we can see that, in agreement with earlier reports, it shows metallic conductivity and magneto resistance effect of around -25% at 9T at the temperature that corresponds to unresolved hump (around 65K). In contrast to [ZhYaZh] the resistivity of our cubic sample is an order of magnitude smaller (compare figure 2.6). The remaining parts of experimental data presented in figures 2.7 and 2.8 will be discussed in latter sections where the corresponding phases will be the topic of investigation.

From magnetization data (figure 2.7) we have concluded that antiferromagnetic transition occurs at around 130K, and from this one can derive conclusion that the sample marked with $SrFeO_{3.00}$ is not 100% cubic. Its approximate composition can be derived from Möβbauer spectroscopy. Möβbauer spectra of $SrFeO_{3.00}$ at different temperatures are shown in the following figure (from [AdLeDa]):

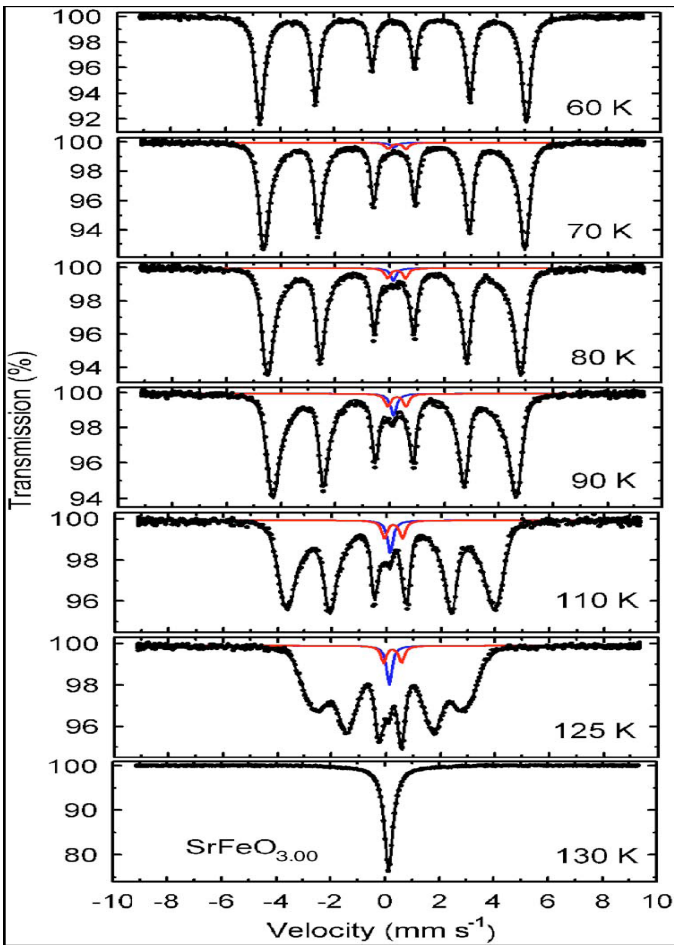

Figure 2.9 (color): Möβbauer spectra of $SrFeO_{3.00}$ (which was annealed under 5kbar) at different temperatures. Blue lines are subspectra of Fe^{4+} (paramagnetic, singlet). Red lines are subspectra of $Fe^{3.5+}$ (paramagnetic, dublet) (from [AdLeDa]).

We can see that already below 125K the hyperfine sextet starts to appear which is the indication of magnetic ordering. Since the spectrum at 130K consists of a single line it follows that magnetic ordering in this sample occurs between 125K and 130K. This is consistent with our magnetization data (figure 2.7). Spectrum at temperatures ≤60K consists of only one hyperfine sextet. On the other hand at temperatures between 70K and 110K there is additional shoulder appearing for the Möβbauer drive velocity close to 0mm/s. This shoulder can be attributed to a small amount of tetragonal phase ($Sr_8Fe_8O_{23}$). From the area ratio of corresponding Lorentzians it is concluded that the actual composition of this sample is 94.6% cubic and 5.4% tetragonal. This is an important conclusion, and it will be shown latter that annealing in 10 times higher pressure drives the content of tetragonal phase below sensitivity limits of Möβbauer measurements. Let's now estimate the oxygen content in the sample from these data. Since the tetragonal phase has equal number of 4+ and 3.5+ Fe ions we can write the following electro neutrality equation (starting from usual oxidation states of oxygen and strontium):

$$2 \cdot (3 - \delta) = 2 + 0.946 \cdot 4 + 0.027 \cdot 4 + 0.027 \cdot 3.5$$

from which follows δ=0.01 which is in a good agreement with thermo gravimetric data.

We now turn to the description of Raman spectra of cubic sample. The spectra for different temperatures are shown in the following figure:

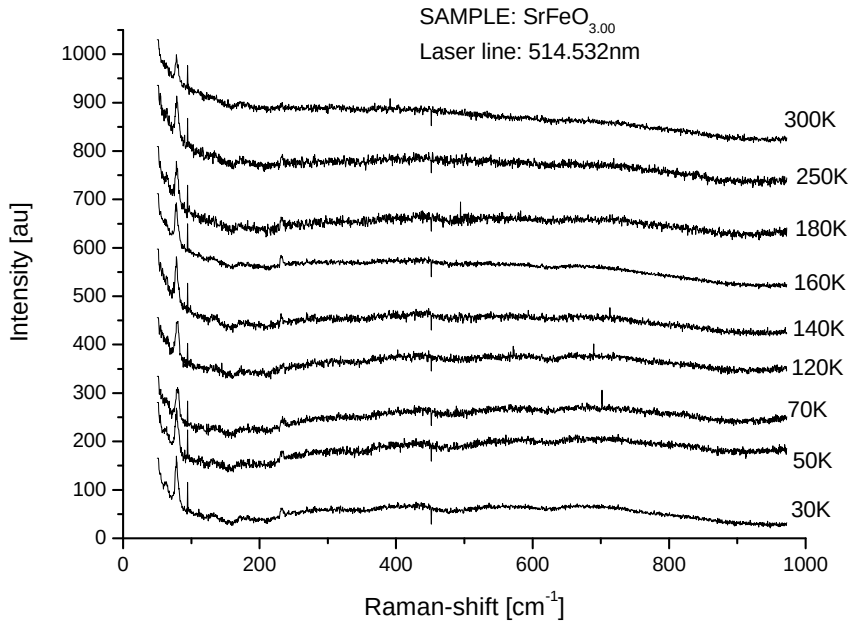

Figure 2.10: Raman spectra of $SrFeO_{3.00}$ sample at different temperatures. Spectra are shifted vertically for clarity and the contribution from cryostats window is subtracted. Incident laser line was green (514.532nm).

Spectra on this figure are accumulated 18 times 5 minutes for each temperature. The final value is an average of those 18 accumulations in order to reduce the noise. The incoming polarization was parallel to [110] direction. The outgoing polarization was summed over all values possible for this back scattering geometry. As was shown in the Appendix A, the mechanical representation at the gamma point in the cubic perovskite $SrFeO_{3.00}$ decomposes in the following way:

$$\Gamma_{meh} = \overbrace{3T_{1u}}^{IR-active} + T_{2u} + \overbrace{T_{1u}}^{acoustic} .$$

From this decomposition we can see that cubic perovskite structure doesn't have any allowed modes in the first order Raman scattering but has three triple-degenerate infra red active phonon modes. One triply degenerate phonon mode is optically silent. Those results are in agreement with our Raman results presented in figure 2.10 where we can see no modes. The absence of any difference between different temperatures goes in favor of assumption that the crystal structure is the same down to the lowest investigated temperature of 4.2K. We have also measured Raman spectra of this sample at a few

temperatures up to 8000cm^{-1} (the maximal range possible with our spectrometer) and have seen no modes. This indicates that the quality of the sample was good, with only minor additional phases below the detection limit of Raman spectroscopy. (This detection limit is of course dependent on which sort of additional phases are present in the sample. But since we have estimated from Möβbauer measurements that the only additional phase is tetragonal and since this phase is not a weak Raman scatterer, as will be shown in chapter about tetragonal phase, we can conclude that the investigated sample was of highly cubic composition).

By analogy with sample preparation of $CaFeO_3$ by high pressure annealing described in chapter 4.2, we have used similar method to obtain cubic $SrFeO_3$ with even higher oxygen content. The cross section of the platinum cup used for this purpose is shown in the following figure:

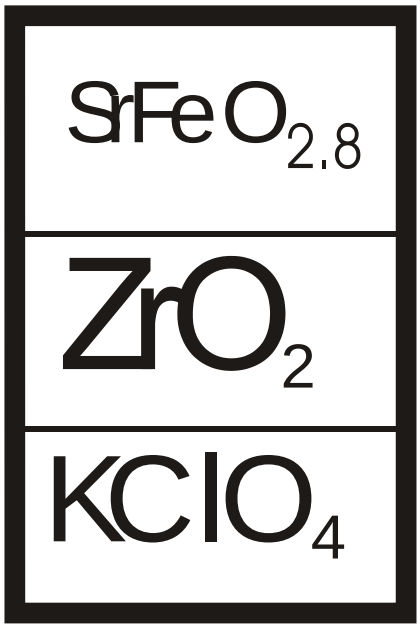

Figure 2.11: Cross section of the cup used for high pressure annealing

We can see that it contains one layer of $KClO_4$ which, as in the case of preparing $CaFeO_3$ serves as an oxygen reservoir, one layer of ZrO_2 which serves as a barrier and one layer of $SrFeO_{2.8}$ starting material which was to be enriched with oxygen (corresponding dimensions and chemical reactions are going to be described in more detail in chapter 4.2). There is one difference with respect to the case of preparation of $CaFeO_3$: while the starting material for obtaining $CaFeO_3$ had the shape of a disk that completely filled the corresponding layer in the cup, the starting material for obtaining $SrFeO_3$ had an irregular shape therefore not fitting appropriately to the corresponding layer. For that reason it was embedded together with a powder of the same material which served to transfer the pressure. Because of that, some samples broke but the enrichment was successful as will be shown latter. We have prepared several samples in this way. Each sample was marked separately and tested by use of magnetization measurements. Sample labels and annealing conditions are shown in the following table:

Table 2.2: Annealing conditions of different samples (1GPa=10kbar)

Sample mark	Annealing pressure	Annealing temperature	Time of annealing
B1	4GPa	600°C	2 hours
B2	4GPa	980°C	40 minutes
B3	4GPa	970°C	2 hours

and the typical measurements of magnetic moments temperature dependence before and after annealing (in this case for the sample B3) in the figure 2.12. From this figure we can see that the oxygen enrichment was successful. The curve for the sample before annealing differs completely from the curve for the sample after annealing. By comparison between figure 2.12 top and figure 2.7 we can estimate that the composition of the starting material was approximately $SrFeO_{2.8}$. From figure 2.12 bottom we can estimate that the antiferromagnetic transition occurs around 140K which is higher than any value reported until now. This means that the composition of the sample is closer to 100% cubic than samples reported till now. We can also see that the hump around 66K is unchanged (in comparison with one in figure 2.7) meaning that it is completely assignable to the cubic phase. The same holds for the anomaly at around 118K.

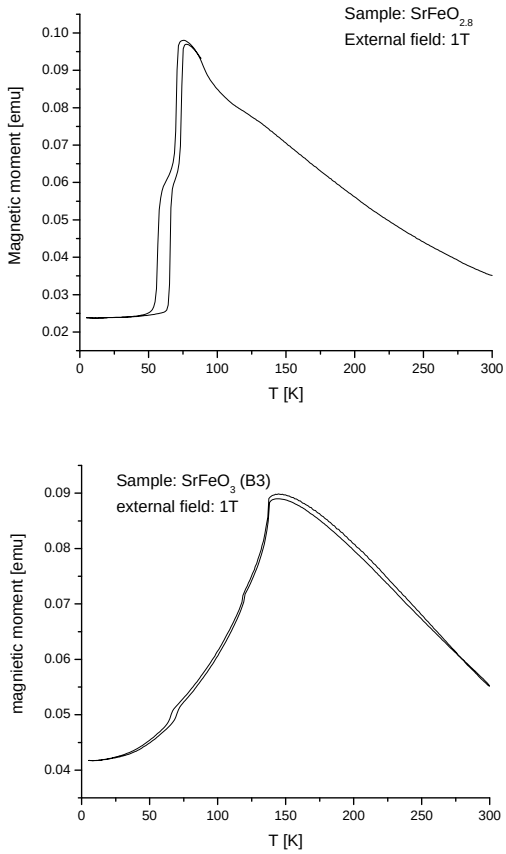

Figure 2.12: Temperature dependence of the magnetic moments for the sample B3 before (top) and after (bottom) high pressure annealing. External field is 1T.

From previous considerations it follows that our three cubic samples (table 2.2) were annealed under approximately ten times higher pressure (40kbar) than cubic samples that were used for our investigations published in [AdLeDa] (5kbar). We saw from Möβbauer measurements that the latter samples contained 5.4% tetragonal phase while remaining part was cubic (figure 2.9 and text related to it). We can ask ourselves are the samples obtained by annealing at pressure of 40kbar more purely cubic than the ones obtained by annealing at 5kbar? Affirmative answer can be given based on the following Möβbauer measurements:

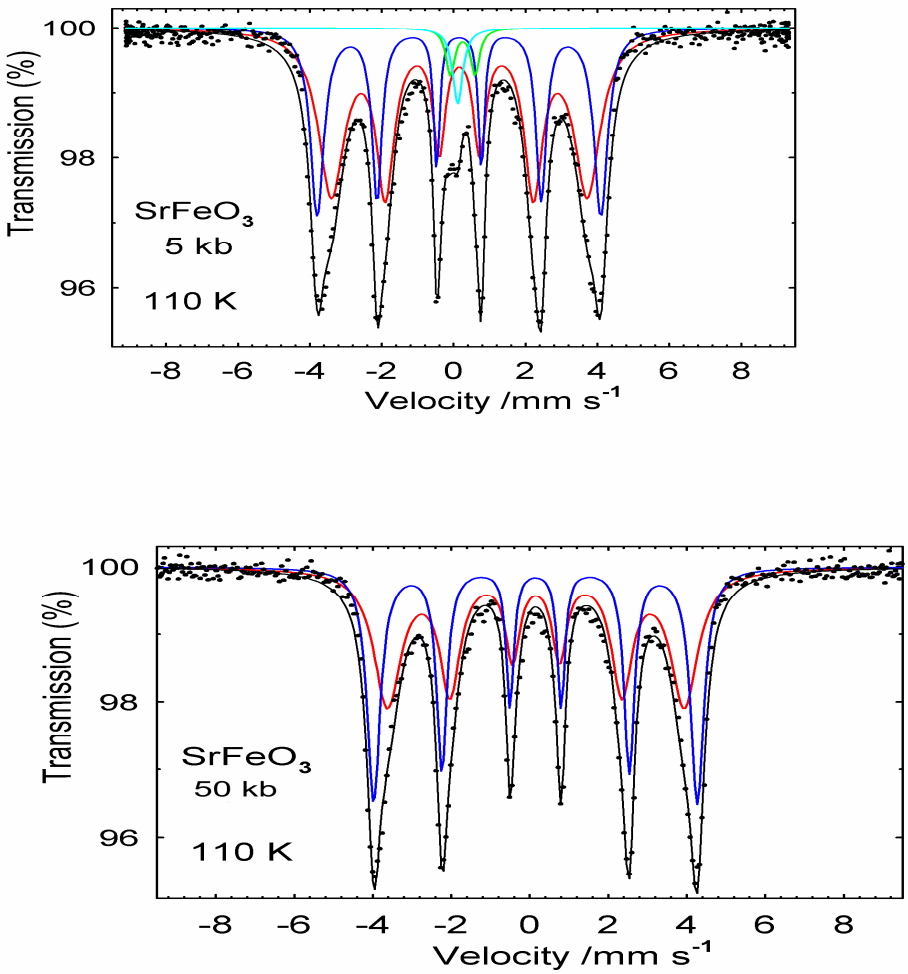

Figure 2.13 (color): Möβbauer spectra at 110K of 5kbar (top) and 40kbar (bottom) annealed sample. The latter sample is B2 (courtesy of Peter Adler).

From this figure we can see that both samples are in the magnetically ordered state at this temperature (110K) but while the sample annealed at 5kbar has a shoulder around velocity equal to zero mm/s (this was discussed before to be a sign of tetragonal phase)

this shoulder completely disappears in 40kbar annealed sample. In this way we can conclude that the latter sample is more close to the ideal cubic composition. This is also in agreement with conclusions drawn from the magnetization measurements (figure 2.12).

2.1.2 LATTICE DYNAMICS CALCULATIONS FOR IDEAL CUBIC $SrFeO_{3.00}$

As was discussed above, the cubic $SrFeO_{3.00}$ structure does not have Raman active phonon modes, but it has three infra red active modes. Those three modes we have really observed in experiment [AdLeDa]. Their energies were measured to be: 172cm^{-1},249cm^{-1} and 559cm^{-1}. In order to assign the observed modes, lattice dynamics calculations were performed. A shell model was used to fit the observed frequencies. In this model each ion in the material is represented by a massless shell and the core. The total charge of an ion is then divided between the core and the shell. Besides "standard" Coulomb interaction between ions, additional terms are given by the so called Buckingham (or Born-Mayer) potential. This is an empirical potential, and it is of the following form:

$$E = A \cdot \exp\left(-\frac{r}{\rho}\right) - \frac{C}{r^6} \qquad (2.3).$$

Here E is the interaction energy between a pair of ions, r is the distance between them and A, ρ and C are constants. Within one ion, the interaction between the core and the shell of this ion is given by the so called spring potential. This potential is of the following form:

$$E = \frac{1}{2} k_2 \cdot r^2 + \frac{1}{24} k_4 \cdot r^4 \qquad (2.4),$$

where this time r is the distance between the center of the shell and the core of the same ion, E is again the energy of interaction and k_2 and k_4 are constants. During the whole calculation the constant k_4 was fixed to zero. The spring potential is added to simulate the polarizability of the ion. We can see from the formula 2.4 that this quantity is isotropic. This is a general property of all atomic ions and atoms. Due to the spherical symmetry of the electric field due to the nucleus there is no preferential direction in which the external electric field will more easily polarize the atom (or the atomic ion) than in the other [Ha10]. Let's see how the polarizability of the atom is related to the constant k_2 from the formula 2.4 (the constant k_4 is assumed to be zero). If the shell charge of the atom (or atomic ion) is q_s then the external electric field E is acting on it with the force q_sE. Opposed to this force is the elastic force whose energy is given by equation 2.4. In our case it is k_2x where x is displacement of the center of the shell and the core. So we have the equation:

$$xk_2 = q_sE.$$

If we multiply this equation with q_s we get: $xq_sk_2=q_s^2E$. Since our system is not necessarily electrically neutral (we are talking about ions) the value of the electric dipole moment p is dependent on where do we put the origin of the coordinate system. If we put the origin of coordinate system in the core then the following equation is valid:

$$p=xq_s$$

but then from the previous equation we get:

$$p=\frac{q_s^2}{k_2}E\overset{def}{=}\alpha E$$

so that for the polarizability of the atomic ion (or atom) we get in this model:

$$\alpha=\frac{q_s^2}{k_2} \qquad (2.5).$$

One can ask oneself where the Coulomb interaction between the core and the shell disappeared in the derivation of the formula 2.5? The answer is that it is assumed that the core is all the time surrounded by its shell and the charge on the shell is homogenously distributed. For this reason the shell produces no electric field in its interior. It is also interesting to note that since shells are in this model massless, the net force on each shell is always zero. This means that the shells are immediately accommodating to the change in ionic configuration. This effect in real crystals corresponds to the Born-Oppenheimer approximation which is valid due to the fact that the electrons (which are in the shell model represented by massless shells) have much smaller mass than the nuclei.

The program that was used for the calculations within the shell model was General Utility Lattice Program (GULP). It calculates crystal properties from the input file in which the elementary cell is given and also parameters for the inter ionic potentials. More about this program and shell model can be found, for example in [GalRoh]. In this work the program was used to calculate all phonon frequencies at the gamma point together with eigenvectors for each phonon. The input parameters were varied until reasonable agreement between calculated and observed frequencies was achieved. The final core and shell charges and the values of spring constants for each ion is given in the following table:

Table 2.3: Core and shell charges and spring constants used in calculation of phonon frequencies and eigenvectors ($e=1.6\cdot10^{-19}C$).

	Core charge [e]	Shell charge [e]	Total charge [e]	k_2[eV/Å^2]	k_4[eV/Å^4]
Sr	0.169	1.831	2	9.50	0
Fe	2.971	1.029	4	915.42	0
O	0.513	-2.513	-2	34.50	0

The final parameters for the Buckingham potential between different ions are given in table 2.4. In this table, r_{min} and r_{max} give the range of application of the corresponding potentials. Before doing the requested calculation, the program first optimizes the structure such that ion positions correspond to the minimum energy. It also calculates the lattice constants. Since in this example, the structure consists only of ions at special positions in the elementary cell, their coordinates were not varied leaving only the cell parameter to be varied. It turned out that the calculated cell parameter (a=3.635Å) was close to the input cell parameter (a=3.851Å).

Table 2.4: Final parameters of Buckingham potential used for the calculation (for the definition of parameters see the formula 2.3).

	A[eV]	ρ[Å]	C[eVÅ^6]	r_{min} [Å]	r_{max} [Å]
O_{shell}-O_{shell}	22764.00	0.1490	0	0	20
Fe_{shell}-O_{shell}	1559.99	0.2990	0	0	20
Sr_{shell}-O_{shell}	1435.65	0.3372	0	0	20

The first three calculated frequencies correspond to three acoustical phonons at the gamma point. Besides these three acoustic phonons there exist four triply degenerate optical modes. The values of their calculated and observed frequencies are given in the following table:

Table 2.5: Calculated and observed frequencies of optical phonon modes

Calculated frequency [cm^{-1}]	172	249	346	529
Observed frequency [cm^{-1}]	172	249	silent	559

We can see that the first two frequencies are reproduced exactly while the difference between the last observed and calculated frequency is 30cm^{-1}. The program had also calculated which eigenvector corresponds to which of these four frequencies. Since these eigenvectors are displacements of ions from the equilibrium position multiplied by the square root of the mass of corresponding atom in order to get the more realistic picture of modes I have multiplied Sr (i.e. Fe) eigenvectors with the square root of (molar mass of oxygen divided by molar mass of Sr (i.e. Fe)). Due to triple degeneracy of each mode if two vectors belong to a certain frequency then any of their linear combinations belong to the same frequency (and to the same irreducible representation). For clarity, particular linear combinations of these modes are depicted in figure 2.14a to 2.14d. The displacement patterns correspond to the mutually orthogonal eigenvectors but are not necessarily normalized.

From the figure 2.14a we can see that to the 172cm^{-1} mode correspond out of phase movements of the heaviest Sr ion on one side and remaining Fe and O ions on the other side. At first glance this looks as if there is much more mass moving to one side (all Fe and O ions in the figure 2.14a) than to the other (only one Sr ion in the figure 2.14a) which would mean that there is a displacement of the center of mass of the primitive cell leading to a translation of the whole crystal. This is not the case because only ions marked with numbers 1 to 5 belong to the drawn cell while other ions belong to the adjacent cells. A careful analysis of this displacement pattern and the masses of the ions shows that the center of mass is not moving. It is also important to notice once more that

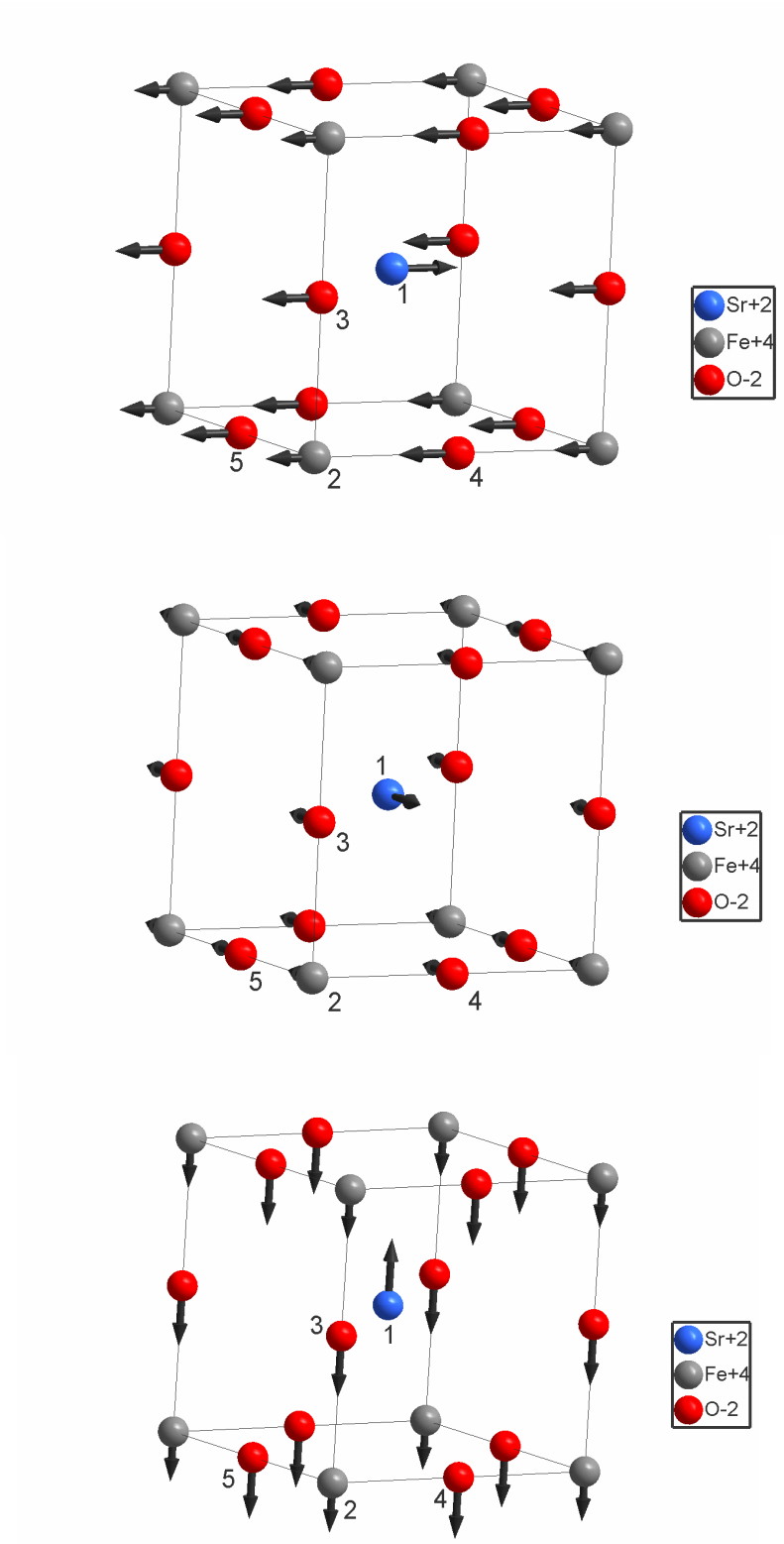

Figure 2.14a (color): Displacement pattern for the 172cm^{-1} mode (T_{1u}; IR).

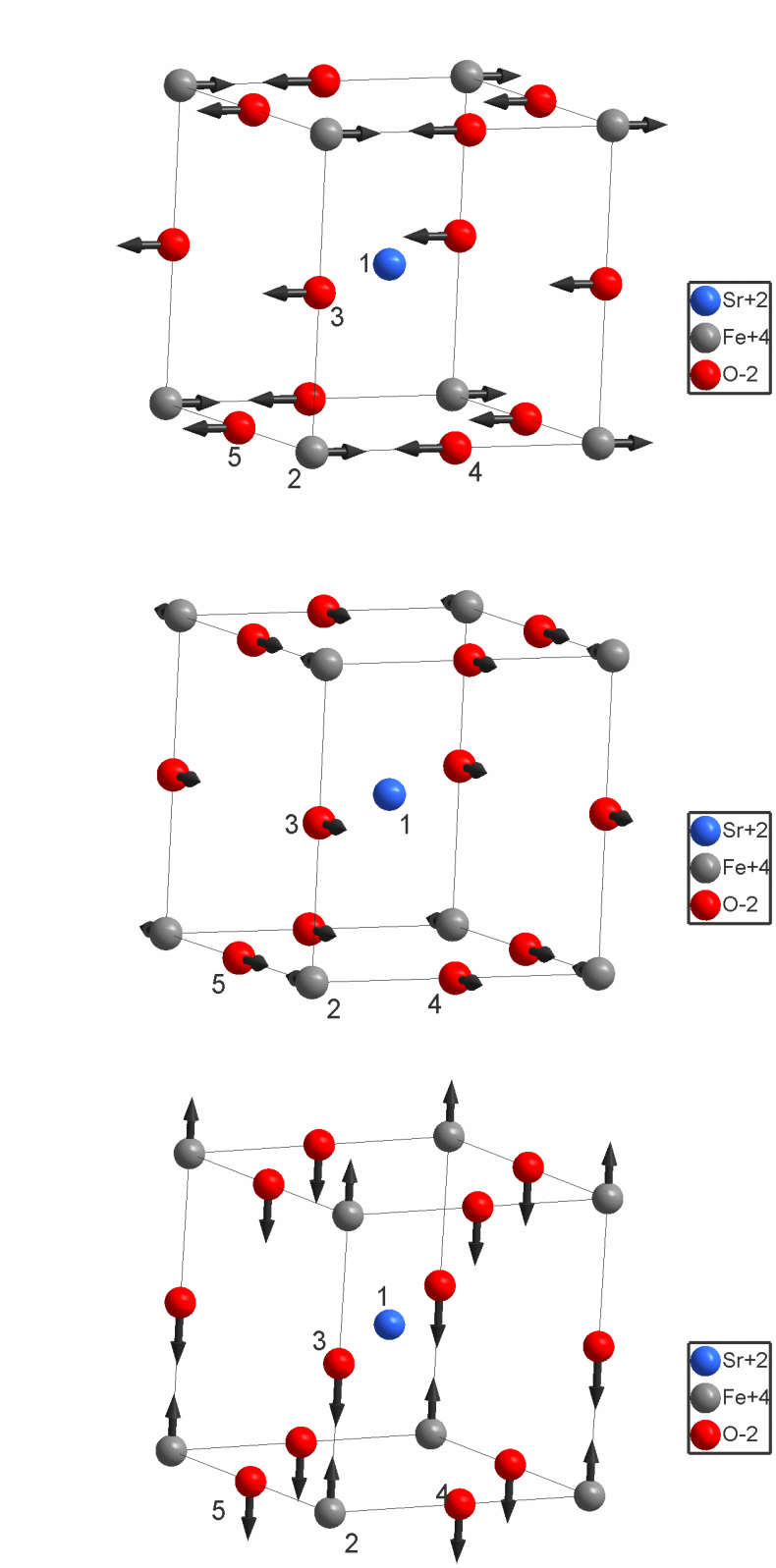

Figure 2.14b (color): Displacement pattern for the 249cm^{-1} mode (T_{1u}; IR).

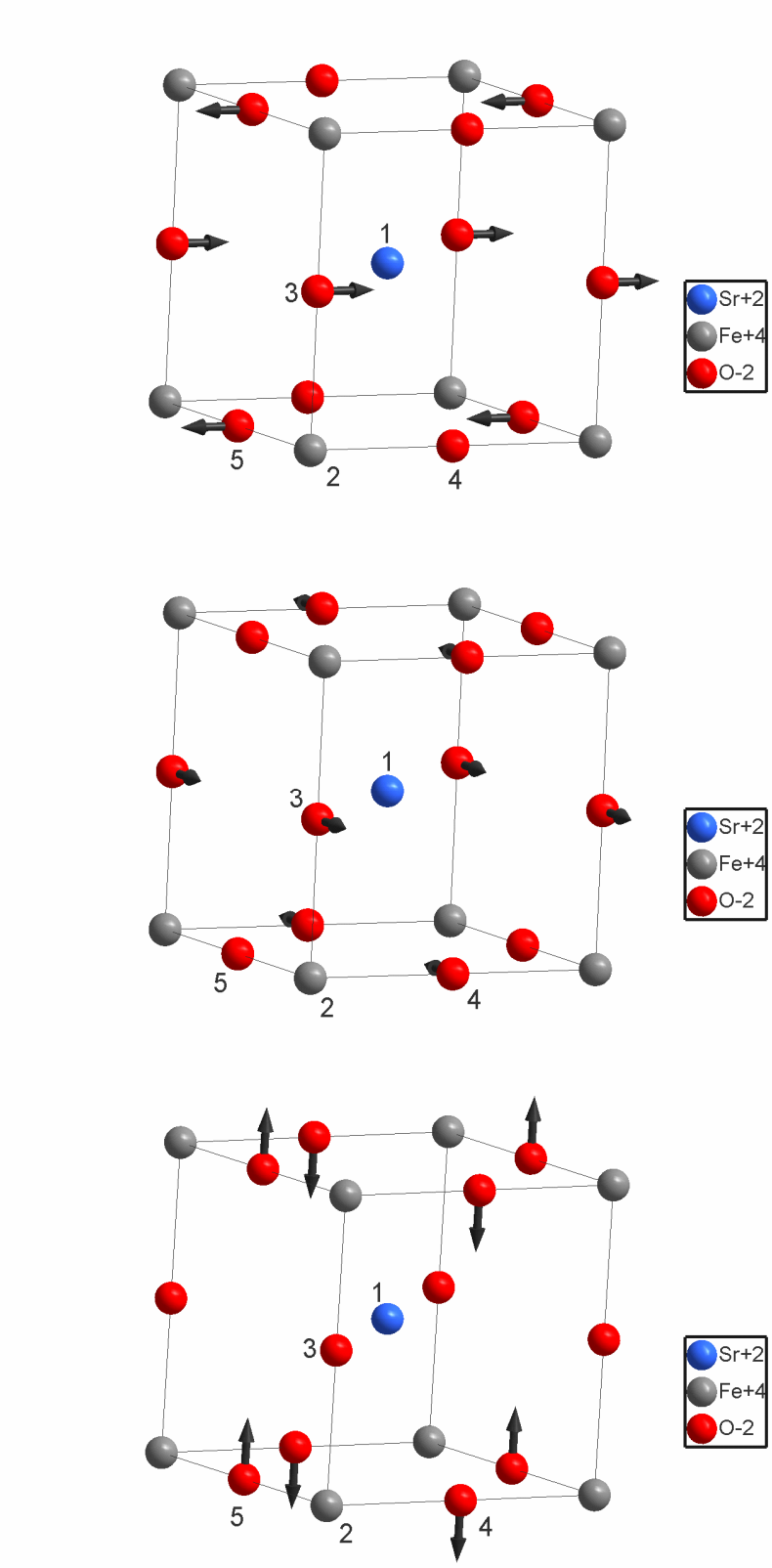

Figure 2.14c (color): Displacement pattern for the 346cm^{-1} mode (T_{2u}; silent).

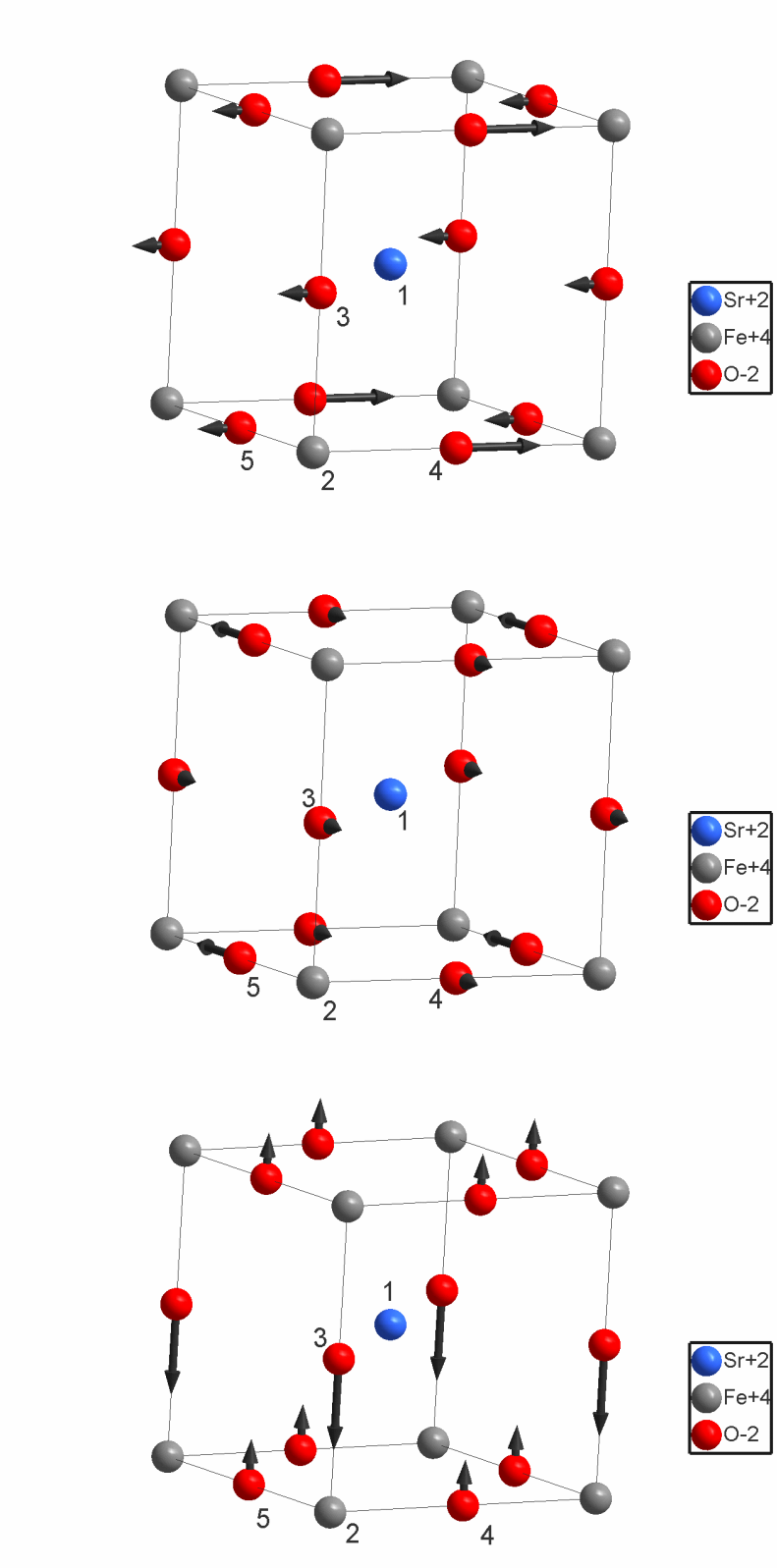

Figure 2.14d (color): Displacement pattern for the 559cm^{-1} mode (T_{1u}; IR).

the three displacement patterns shown in the figure 2.14a are only a basis. Any linear combination of them is also a mode that corresponds to the same frequency. The same comment holds for the other three frequencies too. From the figure 2.14b we can see that the 249cm^{-1} mode corresponds to out of phase movements of Fe ions on one side and remaining O ions on the other. It follows from calculation that displacement of the Sr ion is 20 times smaller than displacements of Fe and O ions. That was too small to be shown in the figure and we can say that Sr ion approximately does not contribute to this mode. In figure 2.14c optically silent mode is shown. Its calculated frequency is 346cm^{-1} and it belongs to the irreducible representation T_{2u} of the point group $\underline{O}_h$. Since this irreducible representation occurs only once in the decomposition of the mechanical representation, the displacement pattern of this mode could be found only from symmetry considerations. Those considerations agreed completely with the GULP calculation. In this mode Sr and Fe ions are not moving due to symmetry arguments. Therefore this mode is assigned only to the oxygen vibrations. Finally, the 529cm^{-1} (measured value: 559cm^{-1}) mode is shown in the figure 2.14d. In this mode Sr and Fe displacements are 100 times smaller than oxygen displacements. Therefore, we can approximately say that Sr and Fe ions do not contribute to the movements in this mode.

If we have overall look at the figure 2.14 we can see the following interesting property: the mode with lowest frequency corresponds to the movements of Sr, Fe and O ions, the next one corresponds to the movements of Fe and O ions while the highest frequency modes correspond to the movements of O ions only. It seems that, as a rule, the heavier ions are involved in the movements in certain mode the lower its frequency is (compared to other modes <u>in the same crystal</u>). Intuitive justification of this rule can be found by observing the case of linear harmonic oscillator with mass m and the elasticity constant k. Its frequency is:

$$\omega = \sqrt{\frac{k}{m}} \, .$$

We can see from this formula that with increasing mass the frequency drops. From the last formula we can see that the correctness of our assignment (figure 2.14) could be experimentally checked if one would substitute Sr ion in $SrFeO_3$ with its isotope. Then the frequency of the lowest energy mode would be most strongly altered since in this mode contribution of Sr ion to the movements is the biggest. This is, however, out of the scope of this thesis.

2.2 PROPERTIES OF AND MEASUREMENTS ON THE TETRAGONAL PHASE

As noted earlier, tetragonal phase corresponds to the ideal composition $Sr_8Fe_8O_{23}$ (i.e. $SrFeO_{2.875}$). If we start with usual oxidation states of Sr and O in compounds, we get from electro neutrality that Fe ions in this compound are in the oxidation state +3.75. Since this number is not integer we can assume that iron ions in $Sr_8Fe_8O_{23}$ are in the mixed valence state. That this is really the case was confirmed in Möβbauer measurements in [FoPoGr], [TaKaTaYa] and [TaOkNa]. From the isomer shift and hyperfine field on Fe sites it is concluded that some Fe ions are in the high spin state with oxidation number +4, while

the rest of the sites have isomer shift and the hyperfine field that are in between high spin Fe^{3+} and high spin Fe^{4+}. For that reason the oxidation state of latter ions are assigned to be $Fe^{3.5+}$. How can we understand this half integer oxidation state? Above cited authors offered the following explanation: this oxidation state corresponds to fast (faster then 10^{-8} s) exchange of electron between Fe^{3+} and Fe^{4+} ions. In other words the following reaction occurs:

$$Fe^{4+}+Fe^{3+} \leftrightarrow Fe^{3+}+Fe^{4+}.$$

Since this reaction is fast in Möβbauer experiments to such pair of sites corresponds effectively two Fe ions in the oxidation state +3.5. Exact position of Fe^{4+} and $Fe^{3.5+}$ ions in $Sr_8Fe_8O_{23}$ together with its crystal structure was determined in the year 2000 [Hodg]. The crystal structure of $Sr_8Fe_8O_{23}$ is shown in the following figure:

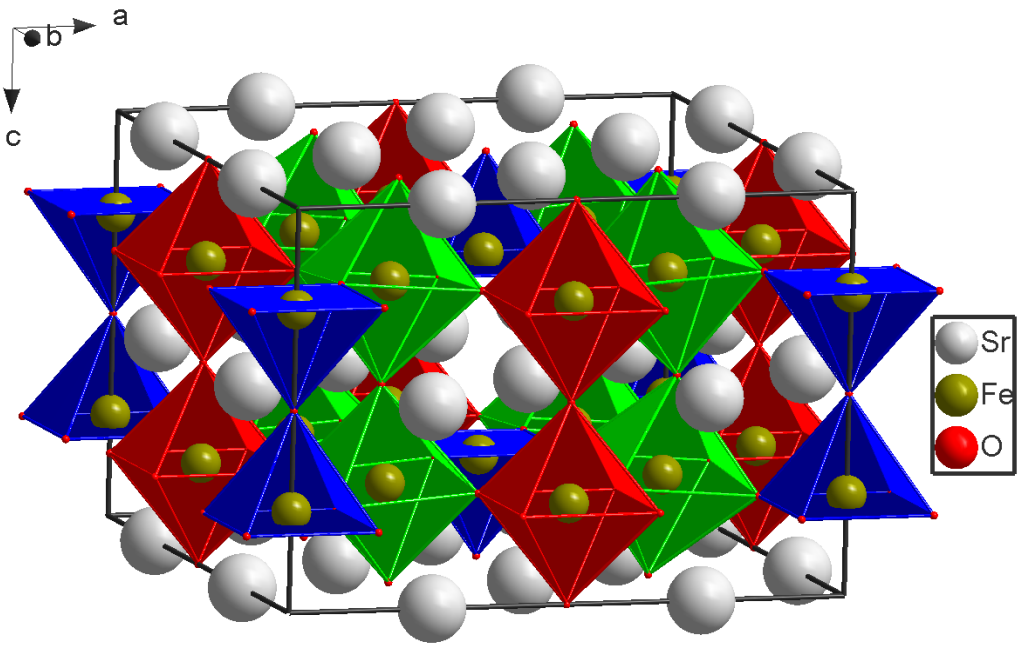

Figure 2.15 (color): Room temperature crystal structure of the $Sr_8Fe_8O_{23}$. Black lines represent unit cell. Oxygen ions (small red spheres) are in the corners of octahedra and pyramids.

This compound belongs to the tetragonal crystal system, space group I4/mmm (D_{4h}^{17}, number 139 in the International Tables for Crystallography), with the lattice constants a=10.929Å and c=7.698Å at room temperature. Each blue pyramid in the figure 2.15 contains one Fe^{4+} ion which is slightly shifted from the center of the pyramids base (square) towards the apical oxygen. This Fe site is denoted by Fe(1) while the apical oxygen is O(1) and four equatorial oxygens are O(2). Those $Fe^{4+}O^{2-}_5$ pyramids are regular in shape leading to the Fe(1) site symmetry $\underline{C}_{4v}$. We can also see that the pyramids are "dimerised" (i.e. they are paired having common apical oxygen) making so

called “bow-tie” units. Each green octahedron in the figure 2.15 contains one $Fe^{3.5+}$ ion in its center. This Fe site is denoted by Fe(2) while apical oxygens are O(3). Those equatorial oxygens of green octahedra which are common to blue pyramids are O(2), while those which are common to red octahedra are O(4). Green octahedra are not perfectly regular. Equatorial oxygen ions make parallelogram such that distance between O(4) ions are smaller than the distance between O(2). In addition apical oxygen ions are inclined such that the symmetry of the Fe(2) site is only $\underline{C}_{2h}$. Finally, each red octahedron in the figure 2.15 contains one Fe^{4+} ion in its center. This Fe site is denoted by Fe(3). Apical oxygen ions are O(5) while equatorial oxygen ions are O(4). Red octahedra are almost perfect, bit elongated along z direction which would lead to the site symmetry $\underline{D}_{4h}$ but if we take in account next nearest neighbors, due to tilting of green octahedra the site symmetry of Fe(3) ions is reduced to $\underline{D}_{2d}$.

If we neglect the slight difference and non ideality of octahedra and pyramids in figure 2.15 and in the same time imagine how ideal cubic perovskite structure would look like we could notice that the structure in figure 2.15 could be obtained from the ideal cubic perovskite structure by regular (i.e. periodic) removal of oxygen, from every second site in c-direction and every second row of octahedra in b-direction. In this way the lattice constants of obtained structure (i.e. structure shown in the figure 2.15) would have the following values: $2\sqrt{2}\cdot a_p \times 2\sqrt{2}\cdot a_p \times 2a_p$, where a_p is the lattice constant of original ideal cubic perovskite lattice. In this way we have seen what the expression “oxygen vacancy ordering” means in $Sr_8Fe_8O_{23}$.

In order to complete the description of the crystal structure of $Sr_8Fe_8O_{23}$, the asymmetric unit is given in the following table:

Table 2.6: Asymmetric unit coordinates for $Sr_8Fe_8O_{23}$ at room temperature.

Atom	Wyckoff position	x/a	y/a	z/c
Sr	8i	0.2577	0	0
Sr	8j	0.2510	0	0.5
Fe	4e	0	0	0.250
Fe	8f	0.25	0.25	0.25
Fe	4d	0.5	0	0.25
O	2b	0	0	0.5
O	16m	0.1190	0.1190	0.2224
O	8h	0.2340	0.2340	0.5
O	16k	0.1237	0.6237	0.25
O	4c	0.5	0	0

From this table we can see that unit cell shown in the figure 2.15 has two formula units (this cell is not primitive but body centered). From this follows that the density of $Sr_8Fe_8O_{23}$ at room temperature is 5.47gr/(cm^3). This is lower than the density of cubic phase (section 2.1) and it can be understood that this is due to the oxygen vacancies.

Concerning magnetic properties of $Sr_8Fe_8O_{23}$, we can refer to the figure 2.7 (the curve that corresponds to the $SrFeO_{2.85}$ sample). We can see an antiferromagnetic transition around 70K and also the small anomaly at the temperature of around 134K. This anomaly is due to the presence of cubic phase which has an antiferromagnetic

transition at this temperature (section 2.1). The exact type of magnetic ordering in $Sr_8Fe_8O_{23}$ has not been reported thus far but this temperature coincides with the temperature where the jump in the resistivity of this material occurs (figure 2.8 left). We can see from the figure 2.8 that above 70K material shows almost metallic conductivity while at 70K the resistivity increases by almost an order of magnitude. At the same temperature a large negative magnetoresistance effect (-90% at 9T) occurs. This effect in $Sr_8Fe_8O_{23}$ was first observed by Lebon et al. in 2003. [LeAdBe]. From their Möβbauer measurements Lebon et al. have concluded that this jump in the resistivity is due to the following charge disproportionation transition:

$$2Fe^{3.5+} \rightarrow Fe^{3+}+Fe^{4+} \text{ at around 70K,}$$

but since the low temperature crystal structure is until now not known, the exact type of charge ordering could not be determined.

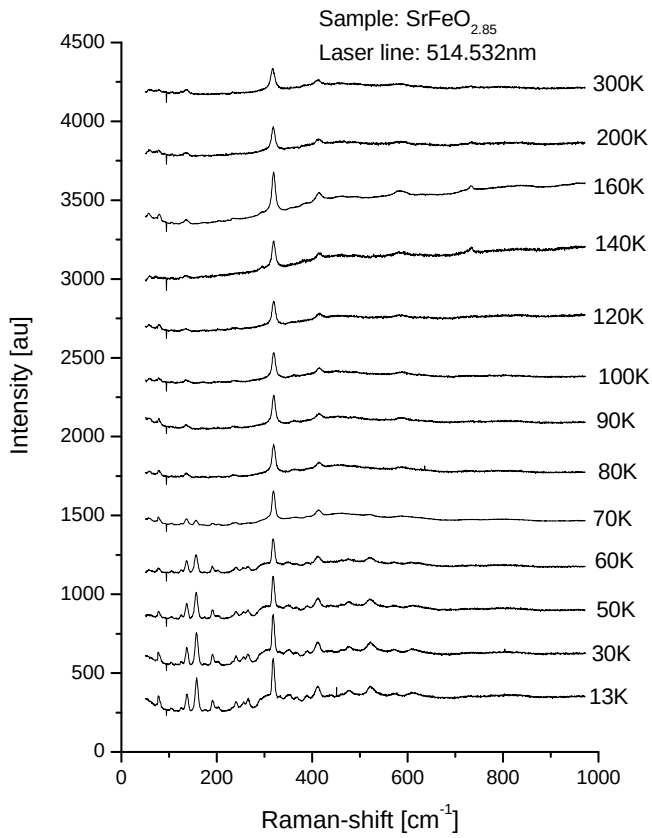

Figure 2.16: Raman spectra of $Sr_8Fe_8O_{23}$ at different temperatures.

Since charge ordering is closely connected with the change of the crystal structure it is possible that this could be seen in the Raman spectra of material in question. For that reason we have performed Raman measurements on the tetragonal phase. From our Möβbauer spectra it was concluded that our sample had nominal composition of

$SrFeO_{2.85}$ (also confirmed by termogravimetry) and that it contained 81% tetragonal and 19% cubic phase [AdLeDa]. Since cubic phase doesn't show any peaks (section 2.1.1) it can be expected that this additional phase will not interfere our Raman measurements. Raman spectra of $Sr_8Fe_8O_{23}$ for different temperatures are shown in the figure 2.16 (spectra were offset vertically for clarity). The wave length of the incident excitation was 514.532nm (green laser line). Spectrum at each temperature was average value of 18 accumulations, 5 minutes each. The setup was used in macro mode, in back scattering geometry. As was shown in the Appendix A, the mechanical representation at gamma point for $Sr_8Fe_8O_{23}$ decomposes in the following way:

$$\Gamma_{meh} = \overbrace{7A_{1g} + 7B_{1g} + 6B_{2g} + 11E_g}^{Raman-active} + \overbrace{12A_{2u} + 19E_u}^{IR-active} + \overbrace{A_{2u} + E_u}^{acoustic} + 3A_{1u} + 6A_{2g} + 7B_{1u} + 6B_{2u}\,.$$

This decomposition is for the room temperature structure and as we can see it has 31 Raman active modes 11 of which are doubly degenerate. If we have a look at the spectra of $Sr_8Fe_8O_{23}$ at 300K (figure 2.16), we can see that out of those 31 modes only 3 modes are present. This shouldn't be surprising because if a mode is symmetry allowed it can happen that due to other reasons its intensity is too small. Again from the figure 2.16 we can see that below the charge and magnetic ordering temperature (70K), several new modes appear. This is then a clear signal that the crystal structure of $Sr_8Fe_8O_{23}$ changes below 70K supporting the charge disproportionation idea proposed in [LeAdBe] and also in [AdLeDa]. Since the three observed modes at 300K do not change their energy below 70K (only their intensity is enhanced) we can conclude that the low temperature, not yet determined space group of $Sr_8Fe_8O_{23}$ is a subgroup of the space group of $Sr_8Fe_8O_{23}$ above 70K. This could then mean that the corresponding phase transition is of the second order.

2.3 PROPERTIES OF AND MEASUREMENTS ON THE ORTHORHOMBIC PHASE

Orthorhombic phase corresponds to the ideal composition $Sr_4Fe_4O_{11}$ (or equivalently, $SrFeO_{2.75}$). This phase was discovered for the first time in the year1975. [ToGrFe]. If we start (as in previous cases) with the usual oxidation states of strontium and oxygen we get, from electro neutrality iron ion in the formal oxidation state +3.5. As in the case of tetragonal phase, this can suggest us that the Fe ions in $Sr_4Fe_4O_{11}$ are in the mixed valence states. Möβbauer measurements show that $Sr_4Fe_4O_{11}$ contains Fe ions both in +3 and +4 oxidation states in equal proportions [TaKaTaYa], [FoPoGr], [Gibb2]. Those measurements also showed that both Fe^{3+} and Fe^{4+} ions are in the high spin state. Also in the above cited references it was shown that the Fe^{3+} sublattice is magnetically ordered below the Neel temperature of around 230K while Fe^{4+} remains disordered down to the lowest measured temperatures. The ordering is antiferromagnetic. A typical dependence of the magnetic susceptibility on the temperature is shown in figure 2.7 (curve that corresponds to the $SrFeO_{2.77}$ sample). Since this sample is a mixture of the tetragonal and the orthorhombic phases, the transition at around 70K can be assigned to the already described magnetic transition in the tetragonal phase. On the other hand, if one looks carefully at this curve, one can see a small change in the slope of the curve at the

temperature of around 230K. This corresponds to the antiferromagnetic ordering of Fe^{3+} ions in $Sr_4Fe_4O_{11}$. When compared to the temperature dependences of magnetic susceptibilities of other antiferromagnetic phases, it can be seen that this curve differs significantly from previous. While previous curves had maximum at the transition temperature of corresponding phases, the curve that corresponds to the $Sr_4Fe_4O_{11}$ doesn't have it. The reason is that this maximum is masked by the contribution of magnetic moments on Fe^{4+} ions, which are co-aligned by the external magnetic field (in the case of the figure 2.7 external field was 1T).

The crystal structure of the $Sr_4Fe_4O_{11}$ has been determined in 2000. [Hodg]. Based on their results this structure is shown in the following figure:

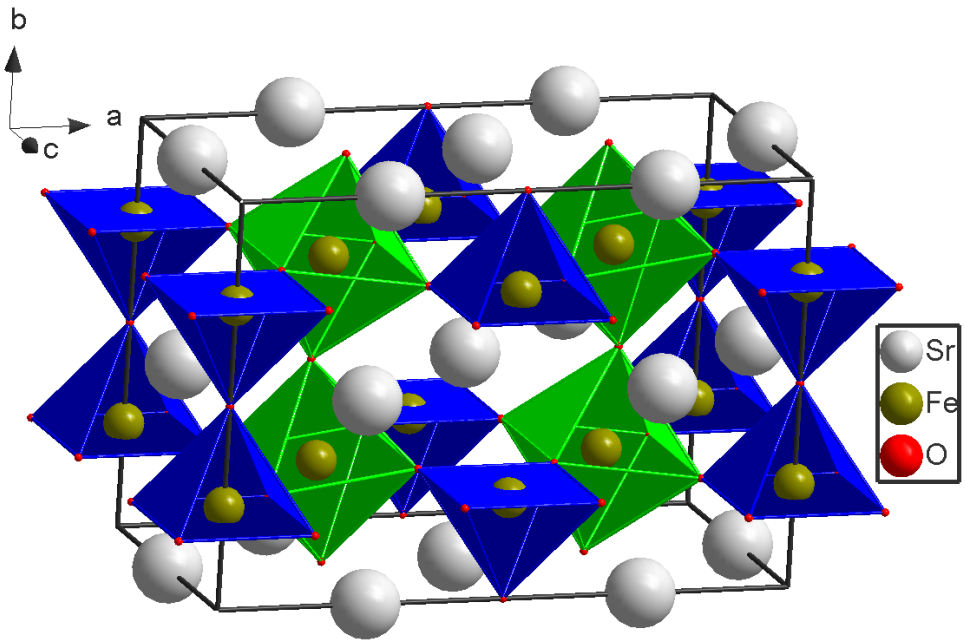

Figure 2.17 (color): Room temperature crystal structure of the $Sr_4Fe_4O_{11}$. Black lines represent the unit cell. Oxygen ions (small red spheres) are in the corners of octahedra and pyramids.

$Sr_4Fe_4O_{11}$ belongs to the orthorhombic crystal system, space group C_{mmm} (D_{2h}^{19} or number 65 in the notation of International Tables for Crystallography). The room temperature lattice constants are a=10.974Å, b=7.702Å and c=5.473Å. Inside every blue pyramid is one Fe^{4+} ion. It is a little bit displaced from the center of the pyramid base towards the apical oxygen. This site is denoted as Fe(1). Apical oxygen is O(1) while equatorial oxygens that belong to the blue pyramids are O(3). The base of each blue pyramid is a rectangle with two opposite sides parallel to a axis equal to 2.625Å, while two opposite sides parallel to c axis are equal to 2.5822Å. All this leads to the site symmetry of Fe(1) site being $\underline{C}_{2v}$. At the center of each green octahedron is one Fe^{3+} ion. The corresponding site is Fe(2). Apical oxygen ions are O(2) while equatorial oxygen ions are O(3). The green octahedra are not ideal, they have a rectangular base and apical

oxygen ions are inclined, as can be seen in the figure 2.17. This leads to the site symmetry of Fe(2) site being $\underline{C}_{2h}$.

It should be noted that the assignment of Hodges et al. which was used here was questioned in [ScHoCa] and [ScJiSc]. They have done neutron diffraction measurements, electron and X-ray diffraction measurements and have claimed that the case of which Fe ion goes to which site is opposite of the one stated in [Hodg]. With such assignment [ScHoCa] have determined the magnetic structure of $Sr_4Fe_4O_{11}$. In their assignment magnetic moments on Fe^{3+} ions are ordered opposite to each other and are directed parallel to the b axis. They have extrapolated the value of the magnetic moment of Fe^{3+} to zero Kelvin to be 3.55 Bohr's magnetons. More over, recent theoretical calculations of Vidya et al. claimed that even not Fe^{3+} lattice was ordered but Fe^{4+} [ViRaFj]. This was criticized by P. Adler in a recent paper [Adler]. For those reasons we will stick to the assignment of Hodges et al.

In order to complete the information on crystal structure in the following table are fractional coordinates of the asymmetric units (the values in the table are taken from [Hodg].):

Table 2.7: Fractional coordinates at room temperature of the asymmetric unit for $Sr_4Fe_4O_{11}$.

Atom	Wyckoff position	x/a	y/b	z/c
Sr	2c	0.5	0	0.5
Sr	2d	0	0	0.5
Sr	4g	0.2588	0	0
Fe	4i	0.5	0.247	0
Fe	4f	0.25	0.25	0.5
O	2b	0.5	0	0
O	4h	0.2695	0	0.5
O	16r	0.3804	0.2761	0.2359

From this table we can see that unit cell has two formula units (unit cell is not primitive but C centered). It therefore follows that the density of $Sr_4Fe_4O_{11}$ at room temperature is 5.38gr/(cm^3). This is less than the room temperature density of tetragonal phase, which is again less than the room temperature density of the cubic phase. This decrease of density, when one goes from cubic, via tetragonal to orthorhombic phase is not accidental. It is closely related to the possibility of obtaining crystal structure of tetragonal phase by regular removement of oxygen from cubic phase, and of obtaining the crystal structure of orthorhombic phase by regular removement of oxygen from tetragonal phase. In this way the volume of the original cell remains approximately constant while having less and less oxygen as one goes through the different phases. It is also possible to obtain the crystal structure of orthorhombic phase directly from cubic. If one looks at the figure 2.17 and at the same time has in mind figure 2.4 one can obtain figure 2.17 by removing one oxygen ion from every second place in the b direction and, with a shift of one layer, in a direction. In this way one obtains the following equality: $a \times b \times c = 2\sqrt{2} \cdot a_p \times 2a_p \times \sqrt{2} \cdot a_p$, where a, b and c are lattice parameters of orthorhombic phase and a_p is the lattice parameter of cubic phase. If we insert for the a_p room temperature value for cubic phase (3.851Å) we get for the orthorhombic phase

a=10.8923Å, b=7.702Å and c=5.4461Å which is in a nice agreement with measured values. Similar agreement holds also for the tetragonal phase.

In order to study the lattice dynamics and eventual change of the crystal structure at temperature above 300K we have performed Raman measurements on a polycrystalline sample. According to our thermogravimetric analysis the sample had the composition $SrFeO_{2.69}$ while Möβbauer spectra show that it is the mixture of 63% orthorhombic and 37% brownmillerite phase [AdLeDa]. As was shown in the Appendix A the mechanical representation in $Sr_4Fe_4O_{11}$ decomposes in the following way:

$$\Gamma_{meh} = \overbrace{6A_g + 6B_{1g} + 5B_{2g} + 4B_{3g}}^{Raman-active} + \overbrace{9B_{1u} + 10B_{2u} + 10B_{3u}}^{IR-active} + \overbrace{B_{1u} + B_{2u} + B_{3u}}^{acoustic} + 4A_u .$$

It follows that the material has 21 non degenerate, Raman active modes and 29 non degenerate, infrared active modes. Raman spectra of $SrFeO_{2.69}$ are shown in the following figure:

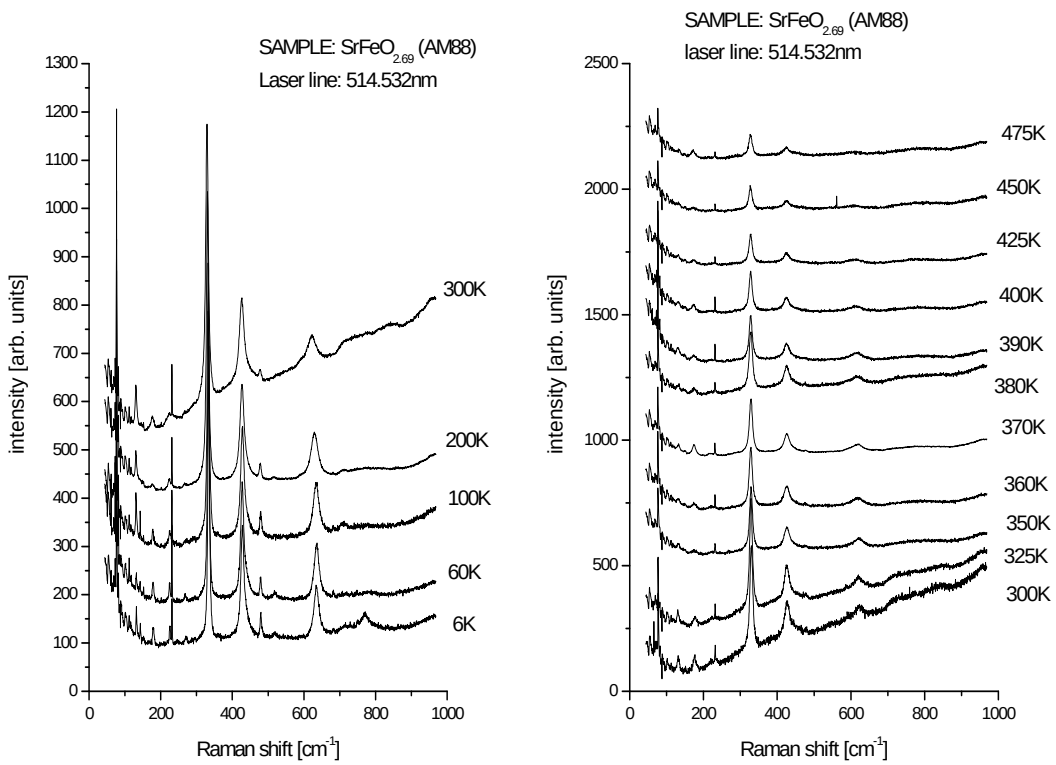

Figure 2.18: Raman spectra of $SrFeO_{2.69}$ at the temperature range 6K to 300K (left) and 300K to 475K (right). Spectra are shifted vertically for clarity.

Spectra were taken in back scattering geometry with the setup used in micro mode. The green laser line (wave length 514.532nm) was used for the excitation. Sample turned out to be polycrystalline but was polished until the surface exposed to the laser radiation was shiny like a mirror. Each spectrum was accumulated 18 times 5 minutes with a final value

being the average of those 18 accumulations. This was done in order to reduce the noise generated in the CCD camera which was additionally cooled with liquid nitrogen. Overall look at the figure 2.18 suggest that in this temperature range (6K to 475K) there is no structural transition. Spectra look very similar, in contrast to the tetragonal phase. This is in agreement with neutron data which show that the orthorhombic phase retains the same structure in the temperature range 300K down to 2K [ScHoCa]. It is also known that around 593K (at room pressure) orthorhombic phase exhibits order-disorder transition, i.e. above this temperature crystal structure is cubic perovskite with randomly distributed vacancies (this was already mentioned at the beginning of chapter 2). We can expect, since cubic perovskite phase showed no peaks, that all peaks in our Raman measurements would disappear when the sample was heated above this temperature. Unfortunately this temperature is far to high for our equipment. If one looks carefully at the spectra in figure 2.18 left, one can see a small peak at around 790cm^{-1} which is present at 6K and absent at all other temperatures. This is assigned to some impurity since repeated measurements on that temperature failed to give the same result (i.e. all other peaks, except that were there). In order to see whether linewidths or energies of observed peaks show any discontinuity at the magnetic transition temperature we have fitted the spectra. Temperature dependency of linewidth and energy of each observed peak showed no significant change at this temperature. The reason for this can be qualitatively given as follows: magnetic transition at 230K concerns only magnetic moments on Fe^{3+} ions, but these ions are sitting on sites with inversion symmetry (this was shown in the part on crystal structure) and therefore they can not contribute to the Raman active phonon modes. On the other hand Fe^{4+} ions are not located on the inversion symmetry centers and therefore they could (in principle) contribute to the movements belonging to a Raman active mode. But since their magnetic moments are not ordered below 230K there is no effect of the transition at this temperature on such modes. For those reasons magnetic ordering in $Sr_4Fe_4O_{11}$ does not influence its Raman spectra.

In addition to the Raman measurements we have performed resistivity measurements on the same sample. It showed semiconducting behavior (monotonically decreasing of the resistance with increasing temperature) which is in agreement with trend existing with increasing δ (figure 2.8 left). Since already below 200K the sample had so big resistance that it couldn't be measured with our setup, the result is not shown here.

3. THE COMPOUND $Sr_3Fe_2O_{7-\delta}$

$Sr_3Fe_2O_{7-\delta}$ is a nonstoichiometric compound in which the oxygen content δ can vary continuously between 0 and 1. If we start from the usual oxidation state for strontium and oxygen we would get, from electro-neutrality for the end member $Sr_3Fe_2O_6$ (δ=1) iron in the oxidation state Fe^{3+} and for the other end member $Sr_3Fe_2O_7$ (δ=0) iron in the oxidation state Fe^{4+}. Möβbauer measurements on the δ=0 compound, however show that this compound exhibits charge disproportionation of the following type: $2Fe^{4+} \rightarrow Fe^{3+} + Fe^{5+}$. This was proposed by Sandra E. Dann et al. in 1993. but the precise temperature of this transition was not determined [DaWeCu2]. This result was confirmed in [Adler] and also in [AdScSy] where this compound was studied at high pressures, and it was determined that the charge disproportionation disappears for pressures higher than circa 20GPa. The precise temperature of the charge disproportionation in $Sr_3Fe_2O_7$ was determined in the year 2000. when its Möβbauer spectrum was studied above room temperature (at room pressure) [KuMoNa1]. Their result is presented in the figure 3.1 (from [KuMoNa1]). We can see from this figure that the peak which is split at 298K and could be fitted with a singlet and a doublet, becomes un split above the 343K and is fitted with a singlet. From their measurements [KuMoNa1] have concluded that the charge disproportionation temperature of $Sr_3Fe_2O_7$, at room pressure is 343K±10K. From the low temperature Möβbauer spectra (at 5K, well below the temperature of antiferromagnetic transition) they have found hyperfine fields of 42.1T and 28.0T which correspond to the Fe^{3+} and Fe^{5+} in the high spin state, respectively. These numbers are in a good agreement with the ones reported by different authors for $CaFeO_3$ (see the beginning of the chapter 4). The same holds for the isomer shifts (relative to the alpha Fe at room temperature). On the other hand from their magnetization measurements they have estimated the effective magnetic moment on Fe^{4+} ion to be $4.3\mu_B$ from where it follows that this ion is in a high spin state also (above the charge disproportionation temperature).

One of the first attempts to determine the crystal structure of $Sr_3Fe_2O_7$ was published in 1973. [LuMiSl1] where the primitive tetragonal cell was proposed. One year later the same authors proposed that $Sr_3Fe_2O_7$ is a polymorphous material with three phases (which they called alpha, beta and gamma) [LuMiSl2]. Those results were not supported by other, later investigations which were mutually consistent. Sandra E Dann et al. using powder neutron diffraction, have determined that $Sr_3Fe_2O_7$ belongs to the space group I4/mmm (D_{4h}^{17} or number 139 in the notation of International Tables for Crystallogra-

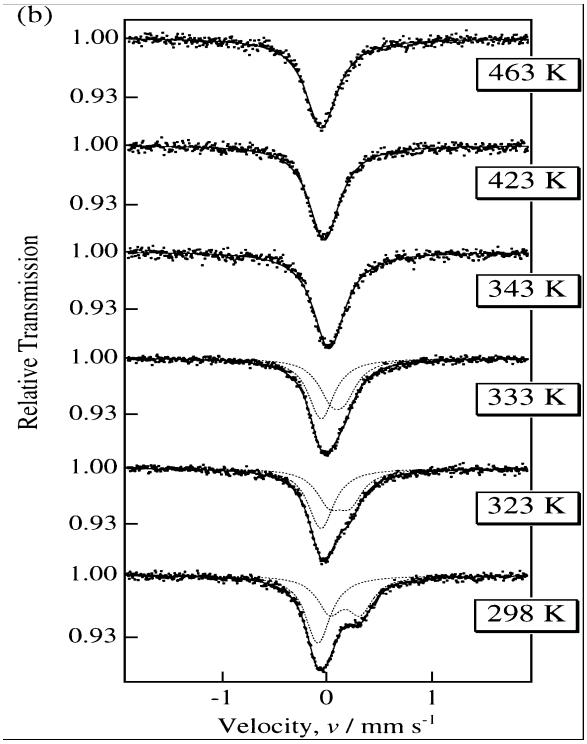

Figure 3.1: Möβbauer spectrum of $Sr_3Fe_2O_7$ above room temperature (from [KuMoNa1]).

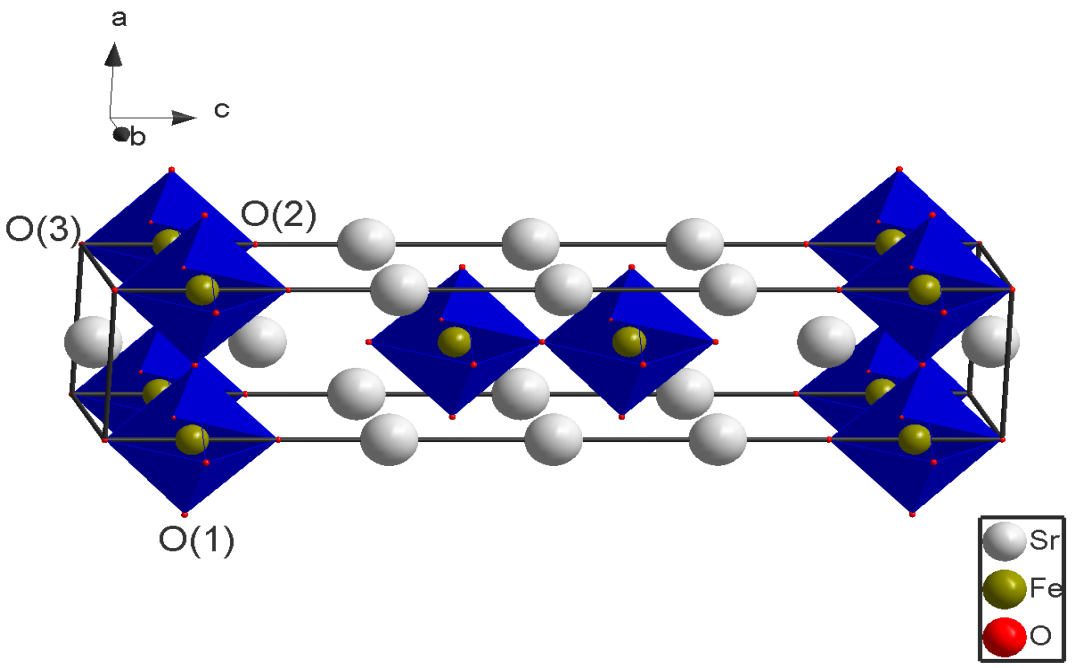

Figure 3.2 (color): Crystal structure of $Sr_3Fe_2O_7$. Black lines represent unit cell. Oxygen ions (small red spheres) are in the corners of octahedra shown. Note that due to tetragonal symmetry a- and b- directions are indistinguishable.

phy) with the room temperature lattice parameters a=3.8526Å and c=20.1490Å [DaWeCu1]. Based on their results the crystal structure of $Sr_3Fe_2O_7$ is shown in the figure 3.2. We can see that the structure belongs to the tetragonal crystal system and it consists of layers of FeO_6 octahedra, separated by SrO layers. For this reason the system can be considered as quasi-two-dimensional. The octahedra are not perfectly regular. For example the Fe-O(1) distance is 1.9271Å, while the Fe-O(2) distance is 1.9363Å and Fe-O(3) distance is 1.9585Å. Also the angles O(2)-Fe-O(1) and O(1)-Fe-O(1) are not exactly 90° leading to the site symmetry occupied by Fe ions being $\underline{C}_{4v}$. This means that, among other things, Fe ions are not located on inversion centers. Dann et al. investigated the room temperature crystal structure of four samples with different oxygen content. They found that (in contrast to the $SrFeO_{3-\delta}$ system where the oxygen vacancies are ordered (see chapter 2)) oxygen is partially missing from the site which connects two neighboring octahedra (in the c-axis direction) i.e. the O(3) site. The other two oxygen sites have occupancy 1 [DaWeCu1]. They also found that with increasing oxygen content the lattice constant a linearly decreases. This property can be used for the estimation of the oxygen content in other samples of $Sr_3Fe_2O_{7-\delta}$. Crystal structure investigations at low temperatures [MoKaKo1] and high pressures [RoMaPa] have shown that it remains the same down to the temperature of 18K (at room pressure) and up to the pressure of 40GPa (at room temperature). On the other hand thermodynamic [MoFoPr] and neutron scattering [PrMoCu] investigations of this system at temperatures above 673K show that also other two types of oxygen sites can then become partially occupied. In order to complete the description of the crystal structure of $Sr_3Fe_2O_7$ the fractional coordinates of the asymmetric unit are shown in the following table (table was made according to the data published in [DaWeCu1]):

Table 3.1: Fractional coordinates of the asymmetric unit for $Sr_3Fe_2O_7$.

Atom	Wyckoff position	x/a	y/a	z/c
Sr(1)	2b	0	0	0.5
Sr(2)	4e	0	0	0.3170
Fe	4e	0	0	0.0972
O(1)	8g	0	0.5	0.0945
O(2)	4e	0	0	0.1933
O(3)	2a	0	0	0

From this table we can see that the conventional crystallographic unit cell contains two formula units (this unit cell is not primitive but body centered). From this it follows that the density of $Sr_3Fe_2O_7$ at room temperature is 5.4gr/(cm^3). Another interesting thing follows from the table 3.1. Contrary to the case of $CaFeO_3$ below the charge ordering temperature which contained two crystallographic non equivalent types of sites (chapter 4), $Sr_3Fe_2O_7$ contains only one type of sites even below the charge ordering temperature. This presents difficulty in determination of the exact charge ordering in this material. In the literature explanations for this are given saying that the time scale which corresponds to the charge ordering is smaller than the time scale appropriate for Möβbauer spectroscopy (approximately 10^{-8}s) but larger than the time scale that corresponds to neutron scattering (approximately 10^{-18}s) [DaWeCu2]. Finally, it can be mentioned that

$Sr_3Fe_2O_7$ is also called Ruddlesden-Popper phase due to the fact that it is isostructural with $Sr_3Ti_2O_7$ which was first described in 1958. [RudPop].

Concerning the magnetic properties it was established that $Sr_3Fe_2O_{7-\delta}$ is an antiferromagnet with a Neel temperature which depends strongly on oxygen content. In this way the Neel temperature decreases from slightly above 300K for $Sr_3Fe_2O_6$ to 0K for $Sr_3Fe_2O_{6.5}$ and then increases again to approximately 130K when the oxygen content is increased to $Sr_3Fe_2O_{6.90}$ [GaMacBu]. The antiferromagnetic transition around 110K was found also in [DaWeCu2] and [Adler] while based on Möβauer measurements it was estimated that the Neel temperature of $Sr_3Fe_2O_7$ is 120K±2K and that this material "might have a helical structure" [KuMoNa1] and [KuMoNa2]. On the other hand calculations based on the tight-binding linear muffin-tin orbital method (in the local spin density approximation of density functional theory) predicted that the $Sr_3Fe_2O_6$ compound is a G-type antiferromagnet (this means that the neighboring spins are ordered antiparallel in all three directions) [ZaKoKo1] and [ZaKoKo2].

It was also established that the electric transport properties of $Sr_3Fe_2O_{7-\delta}$ are semiconducting below the charge ordering temperature while above this temperature the material is metallic [KuMoNa1]. The temperature dependence of the conductivity does not follow the Arrhenius-type law (this law states that $\sigma = A\exp\left(-\frac{E_a}{k_B T}\right)$ where σ is conductivity and E_a is activation energy) while in a limited low-temperature range it follows the Mott variable range hopping law ($\sigma = A\exp\left(-\left(\frac{T_0}{T}\right)^{\frac{1}{4}}\right)$) [Adler], [MoPrAs].

At high pressures the material exhibits a semiconductor-metal transition above circa 20GPa [RoMaPa], [AdScSy], while in the high magnetic field the magnetoresistance remains within 4% (at temperature of 10K and magnetic field of 7T) [GhoAdl]. In the next section our own measurements on $Sr_3Fe_2O_{7-\delta}$ single crystal will be presented.

3.1 MEASUREMENTS ON $Sr_3Fe_2O_{7-\delta}$

All measurements were performed on one single crystalline sample from the batch whose growth was described in [MaStUl]. The crystals were grown by the floating zone method on the apparatus equipped with four mirrors with four 1000W halogen lamps as a heat source. X ray diffraction analysis showed that samples which were grown under a pulling rate of 1-2mm/h had very good mosaicity (FWHM was less then 0.03^o). Thermogravimetric analysis showed that the samples grown under oxygen pressure of 3 bar (1MPa=10bar) had oxygen content of 6.76 which means that the chemical formula of the sample was $Sr_3Fe_2O_{6.76}$.

It was reported in the literature that this material is sensitive to the air probably due to the reaction with water or carbon dioxide from the air [PraMan]. For this reason the sample was kept in the desiccator under argon atmosphere and was in contact with air only for short time necessary for transferring the sample from the desiccator to the setup. It turned out that the sample didn't change his properties even after long period.

In order to accommodate the shape of the sample to match nicely to our requirements and setups used the sample was cut such that it had the shape of rectangular parallelepiped with the following dimensions: l_1=2.2mm along c-axis, l_2=2.5mm along b-axis and l_3=1.6mm along a-axis (as was mentioned in the part of crystal structure, due to the tetragonality of the system a- and b-axes are indistinguishable). Regularity of samples shape made manipulation with it easier.

Temperature dependence of the magnetic moment of the sample measured in the external magnetic field of 1T along all three crystallographic axes is shown in the following figure:

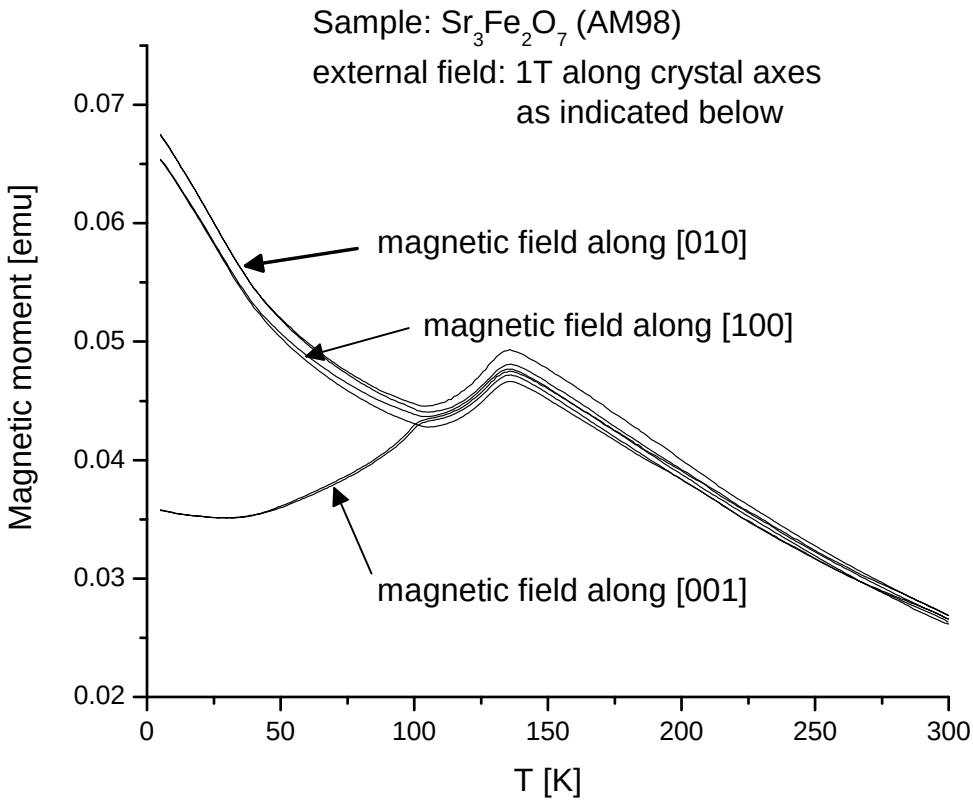

Figure 3.3: Temperature dependence of the magnetic moment of $Sr_3Fe_2O_{7-\delta}$ in the external field of 1T along all three crystallographic axes (1emu=10^{-3}Am^2).

We can see from this figure that above Neel temperature (which from the figure can be estimated to be around 140K) the magnetic susceptibility tensor is isotropic. In the Appendix A it was shown that crystal symmetry requires the magnetic susceptibility tensor to be isotropic in the ab-plane with in general case different value along c axis. The results above the Neel temperature are special case of this requirement where e=f (section A.2). Below the Neel temperature formula for the magnetic susceptibility tensor in the section A.2 is nicely confirmed. We can see that the magnetic moments along a- and b-directions are equal and different than the magnetic moment along the c-axis. The

slight difference between magnetic moments along a- and b-directions could be due to a slight error in the cutting directions of the sample. That error can cause that the magnetic field is not exactly in the ab-plane. After completing the measurements but prior to completion of this thesis I became aware of similar measurements on $Sr_3Fe_2O_{7-\delta}$ compound published in 2002. [MoKaKo2]. Those authors have measured the temperature dependence of the magnetic moment along the [100], [110] and [001] crystallographic directions on the compound that was more oxygen deficient than ours (according to their paper, they have claimed that the single crystalline sample was of the composition $Sr_3Fe_2O_{6.5}$). Apart from the observed divergence of the magnetic susceptibility at very low temperatures their data are in complete accordance with our presented in the figure 3.3. Moreover similarity of magnetic moment measured along [110] direction with the one measured along [100] direction shows that the magnetic susceptibility tensor is indeed isotropic in ab-plane, as predicted by group theory. This is an example how discrete symmetry of the crystal induces continuous symmetry of one of its physical properties: although the symmetry of the directions (point group of the crystal) has only few, discrete symmetry operations the magnetic susceptibility is the same along <u>any</u> direction in the ab-plane.

Another conclusion can be drawn from the figure 3.3. If the magnetic moments on Fe-ions in $Sr_3Fe_2O_7$ are ordered antiferromagnetically then it follows from this figure that they are aligned parallel to the c-axis. The reason for this is that the magnetic susceptibility is bigger when the field is applied perpendicular to such ordered magnetic moments than when this field is parallel since it is easier to tilt magnetic moment than to completely reverse their direction. Exact type of magnetic ordering could be determined in neutron experiments on single crystals.

In order to investigate the charge transport properties of $Sr_3Fe_2O_7$ we have measured temperature dependence of the resistivity and magnetoresistance of our sample. Since we had a single crystal it was in principle possible to measure the components of the resistivity tensor. As in the case of the magnetic susceptibility tensor, the crystal symmetry requires resistivity tensor to be isotropic in the ab-plane, therefore having only two independent components to be measured (section A.2, formula A.2.7). This property made our sample a good candidate for applying the so called Montgomery method for measuring resistivities along crystal axes [Mont]. In this method single crystal is cut along crystallographic axes such that it has a shape of rectangular parallelepiped, as we did with our sample. Then four point-like electrodes are attached to the corners of (100) face of the sample (this should correspond to the bc-plane). Now current I is pushed through two adjacent electrodes and voltage V is measured across other two electrodes. The ratio V/I is calculated (let's denote this ratio with R_1; it has dimensions of the resistance but it is not a resistance in the sense used in electronics). Then the configuration of V/I measurement is rotated by 90° (that can be done without touching the electrodes from measurement of R_1). Let's denote corresponding V/I ratio with R_2. The parameters a and b (formula A.2.7, section A.2) are then calculated from R_1 and R_2 by not so simple means as described in [Mont]. The advantage of this method is that it requires only one sample (in our case) with only one cutting. It is based on the papers of L. J. van der Pauw in which he developed a formula (based on conformal mapping of (two dimensional) complex plane) that relates resistivity of isotropic material which is flat but otherwise has arbitrarily shape and corresponding voltage-current ratios [Pauw1]

and in which he extended derivation for the flat (but arbitrarily shaped) anisotropic material [Pauw2]. Unfortunately due to the cracks in the sample several attempts to apply this method were unsuccessful. Unavoidable cracks in the sample (mostly perpendicular to the c-axis, due to the layered structure of the material) caused voltage-current ratios to be too high for our setup. For that reason we used "standard" four-point method (described in the section 4.3) and then we have estimated the value of resistivity from the infra red measurements. Infra red measurements are insensitive to sample cracks because they are optical measurements. According to IR measurements of A. V. Boris our sample was semiconducting in the ab-plane and insulating along c-axis [Boris]. Our resistivity measurements in ab-plane in zero field (black line) and in the field of 8T (red line) and fitted to the infra red measurements (three black squares with error bars) are shown in the following figure:

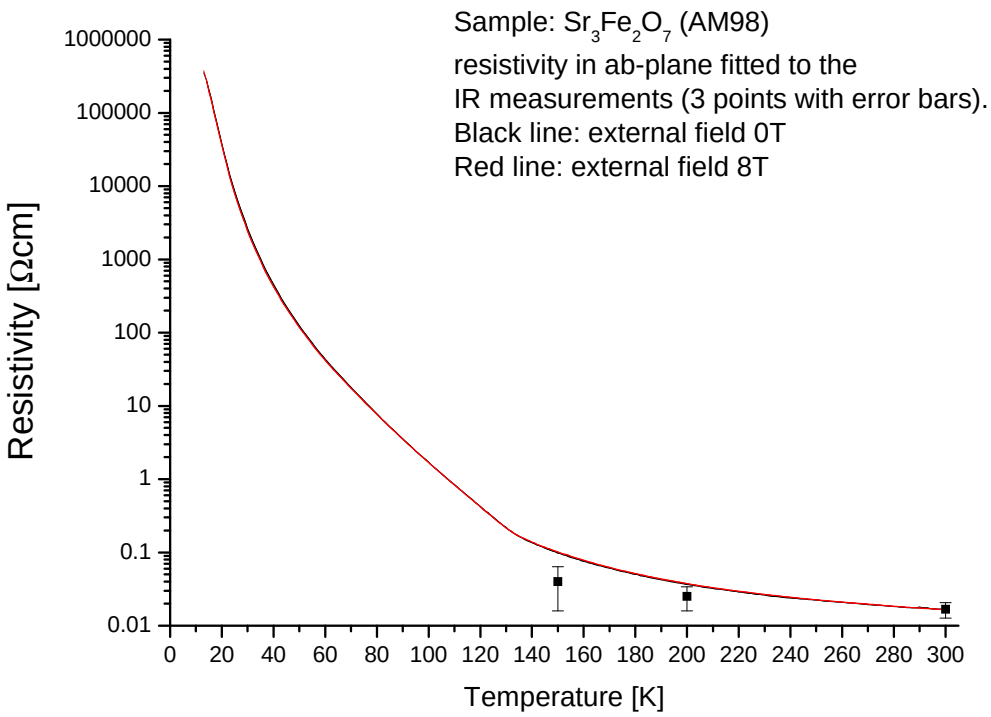

Figure 3.4 (color): Temperature dependence of the resistivity in the magnetic field of 0T (black) and 8T (red) of $Sr_3Fe_2O_{7-\delta}$. Three spots with error bars are values obtained from infra red measurements.

We can see from this figure that the material is semiconducting below room temperature with the resistance that increases by almost seven orders of magnitude when the temperature is reduced from room value to 10K. At the temperature that corresponds to antiferromagnetic transition (around 140K, figure 3.3) the slope of the curve changes which can suggest that some interaction occurs between the conduction electrons and the magnetic moments on Fe-ions. Finally it is apparent from figure 3.4 that a

magnetoresistance effect is not present in this compound. Careful analysis shows that the magnetoresistance effect remains within 4%. This is in accordance with results of earlier investigations (for example [GhoAdl]).

Isothermal variations of the resistivity with respect to magnetic field are shown in the following figure:

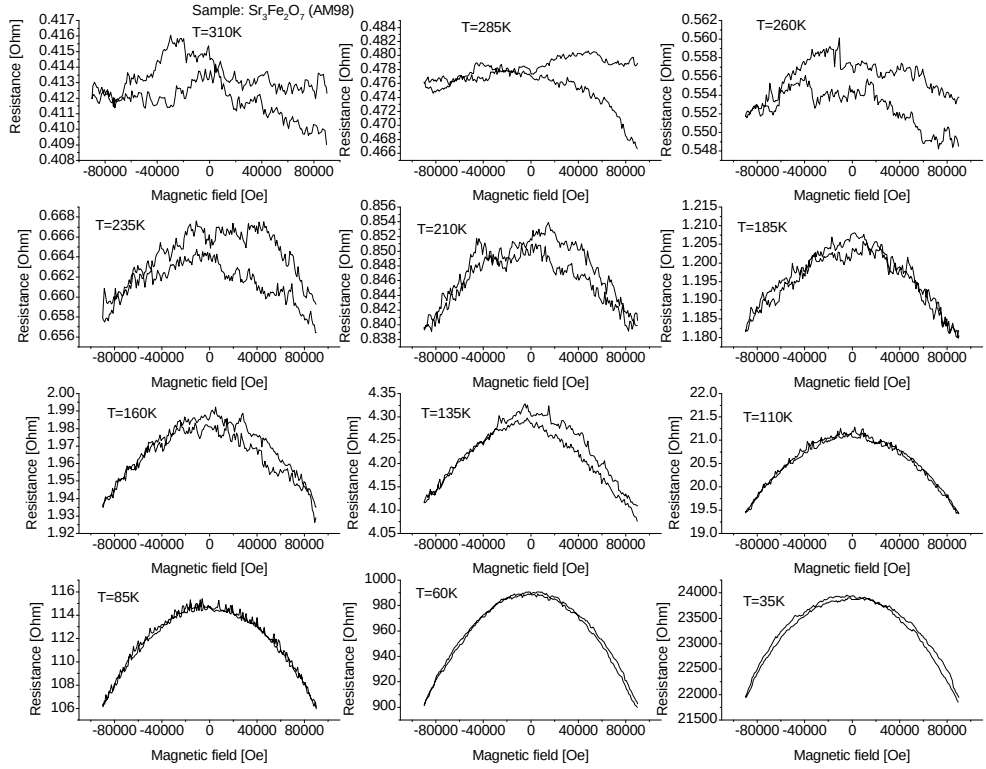

Figure 3.5: Magnetic field dependence of the resistivity of the $Sr_3Fe_2O_{7-\delta}$ for various temperatures. Magnetic field is from the range -9T to 9T.

From this figure we can see that as the temperature gets lower, the resistivity versus magnetic field curve becomes more and more symmetric. This can be mathematically denoted in the following way:

$\rho(-\vec{H},T) = \rho(\vec{H},T)$ as the temperature T gets lower,

and can be qualitatively explained that this property is due to the fact that $Sr_3Fe_2O_7$ is centrosymmetric. Due to the inversion symmetry any two opposite directions are equivalent. The absence of symmetry in resistivity versus magnetic field dependence at higher temperatures can be attributed to the poor signal to noise ratio.

In order to search for the possible influence of the magnetic and charge ordering on the lattice dynamics we have performed Raman measurements on the same sample. Raman spectra of $Sr_3Fe_2O_{7-\delta}$ are shown in the following figure:

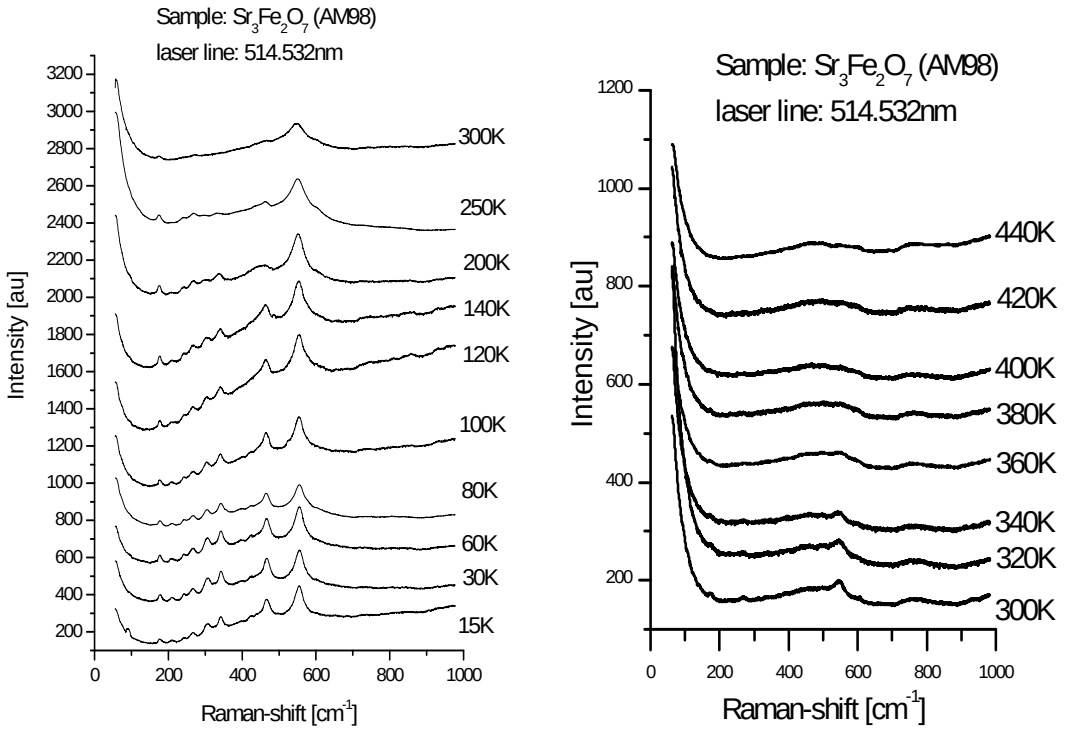

Figure 3.6: Raman spectra of $Sr_3Fe_2O_{7-\delta}$ for temperature range 15K to 300K (left) and 300K to 440K (right). Polarization of incident photons is parallel to the c-axis. Spectra are offset vertically for clarity.

The incident laser light was green (λ=514.532nm), the polarization of the incident light was parallel to the c-axis. The spectrum was measured in the back-scattering geometry, without analyzer which means that summing was performed over outgoing polarizations. In the Appendix A the form of the Raman tensor was described (section A.4). From this form it can be inferred that geometry used allowed us to measure phonons of A_{1g} and E_g symmetry. We can see that below 300K the spectrum can be resolved into eight peaks, while above this temperature peaks are absent. Since around this temperature there are no transitions reported, we can assign this disappearance of peaks to thermal smearing (with increasing temperature the intensity of the peak decreases while their line widths increase). The eight, low temperature peaks, when fitted show no changes in line width nor in intensities at the magnetic transition temperature. As was shown in the Appendix A (section A.3) the mechanical representation of $Sr_3Fe_2O_7$ at the gamma point decomposes in the following way:

$$\Gamma_{meh} = \overbrace{4A_{1g} + B_{1g} + 5E_g}^{Raman-active} + B_{2u} + \overbrace{5A_{2u} + 6E_u}^{IR-active} + \overbrace{A_{2u} + E_u}^{acoustic} .$$

From this decomposition it follows that $Sr_3Fe_2O_7$ has 10 Raman active modes (5 of them being double degenerate), 11 infra red active modes (6 of them being double degenerate) and one non-degenerate silent mode.

Since this material exhibits charge-ordering (and metal to semiconductor transition) at approximately 340K it can be expected that at this temperature the number of free charge carriers changes significantly. This might be seen in the electronic Raman scattering, i.e. scattering from free carriers. The formula for such a process is:

$$I \propto \exp\left(-\frac{w^2}{q^2 \cdot v_{th}^2}\right)$$

where $v_{th}^2 = \frac{2k_B T}{m^*}$ is square of the thermal velocity of electrons, m^* is the electron effective mass, k_B is Boltzmann constant, T is the temperature, w is the angular frequency calculated from the frequency of incident light (Raman-shift) and $\vec{q} = \vec{k}_{in} - \vec{k}_{sc}$ is the difference between the wave vectors of incident and scattered radiation [Jl47/1], [Jl47/3], [Jl47/4]. We can see that the formula is Gaussian centered at w=0. For this reason the tails of spectra near w=0 (figure 3.6) were fitted with this formula. No significant changes in parameters were found, leading to the conclusion that the charge-ordering transition is not seen in our data.

In order to test whether phonons of B_{1g} symmetry can be seen we have performed another Raman experiment in the back-scattering geometry, with the wave vector of incident radiation being parallel to the c axis (i.e. [001] direction). The result is shown in the following figure:

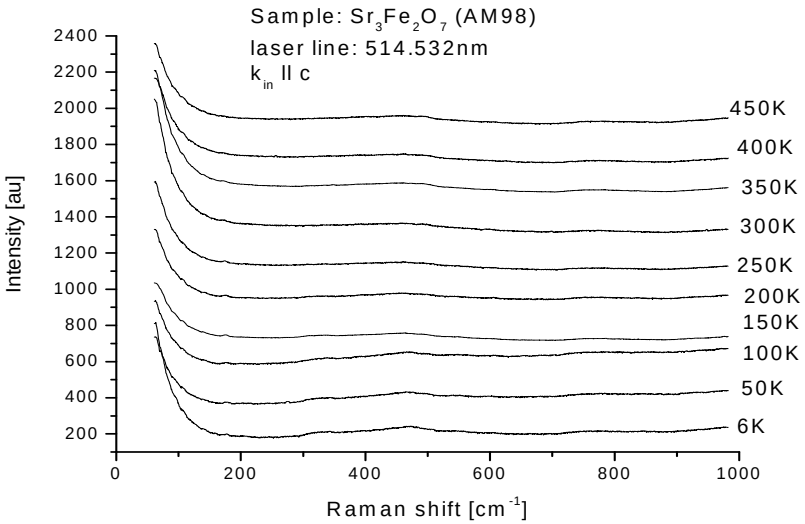

Figure 3.7: Raman spectra of $Sr_3Fe_2O_{7-\delta}$ (k_{in} parallel to c-axis) for temperature range 6K to 450K. Spectra are offset vertically for clarity.

The polarization of the incident light was parallel to a-axis, analyzer was not used, meaning that it should be summed over outgoing polarizations (of course, keeping in mind that in each case polarization of linearly polarized light is perpendicular to the wave vector). From the section A.4, where the form of the Raman tensor is described we can see that this geometry allows us to observe phonons of A_{1g} and B_{1g} symmetry. From the figure 3.7 it can be seen that modes are absent. When comparing figures 3.6 and 3.7 the following question can appear: in the figure 3.6 there are eight peaks in the scattering geometry that allows phonons of A_{1g} and E_g to be observed. In the figure 3.7 there are no peaks in the scattering geometry that allows phonons of A_{1g} and B_{1g} symmetry to be observed. Could we conclude than that all eight peaks are of E_g symmetry? The answer to this question is no. The reason is contained in the formula for the Raman tensor that corresponds to the mode A_{1g} (section A.4). In the case of figure 3.6 we are observing matrix element "b", while in the case of figure 3.7 we are observing matrix element "a". Nobody said that both of them must be different than zero. It will be shown later that our polarization analysis (where the analyzer was used) shows that none of the peaks is of E_g symmetry.

In order to check whether there is a contribution from the Raman scattering of free electrons we have fitted low energy tail of spectra in the figure 3.7 with the same Gaussian as we did in the case of the figure 3.6. The line width and the position were temperature independent leading to the conclusion that it is not of the electronic origin.

Lattice dynamics calculations were performed in order to make the assignment of peaks that appeared in the spectra shown in the figure 3.6. The program used was the same as described in the case of cubic $SrFeO_3$ (section 2.1.2). Since the procedure was already described in the section 2.1.2 we are going immediately to show the final values of parameters. The final core and shell charges and the values of spring constants for each ion are given in the following table:

Table 3.2: Core and shell charges and spring constants used in calculation of phonon frequencies and eigenvectors ($e = 1.6 \cdot 10^{-19} C$).

	Core charge [e]	Shell charge [e]	Total charge [e]	k_2[eV/Å^2]	k_4[eV/Å^4]
Sr1	-1.6	3.5	1.9	10.17	0
Sr2	-1.6	3.5	1.9	12.16	0
Fe	0.8	3.0	3.8	510.93	0
O1	1.1	-3.0	-1.9	41.01	0
O2	1.1	-3.0	-1.9	43.12	0
O3	1.1	-3.0	-1.9	45.00	0

We can see from this table that total charges of ions are close to their ideal values (+2 for strontium, -2 for oxygen and +4 for iron) which means that the charge ordering in this compound was not taken into account. The reason for this is the presence of only one crystallographic family of sites which occupies iron ion. Apart from parameters from table 3.2, the Buckingham potential was used between strontium shells and oxygen shells, between iron shells and oxygen shells and between oxygen shells and oxygen shells. Their final values are shown in the following table:

Table 3.3: Final parameters of Buckingham potential used for the calculation (for the definition of parameters see the formula 2.3 section 2.1.2)

	A[eV]	ρ[Å]	C[eVÅ^6]	r_{min}[Å]	r_{max}[Å]
$Sr1_{shell}$-$O1_{shell}$	1090.85	0.3366	0	0	10.0
$Sr1_{shell}$-$O2_{shell}$	1080.0	0.3366	0	0	10.0
$Sr1_{shell}$-$O3_{shell}$	1070.49	0.3366	0	0	10.0
$Sr2_{shell}$-$O1_{shell}$	1081.55	0.3366	0	0	10.0
$Sr2_{shell}$-$O2_{shell}$	1080.21	0.3366	0	0	10.0
$Sr2_{shell}$-$O3_{shell}$	1221.10	0.3366	0	0	10.0
Fe_{shell}-$O1_{shell}$	1300.84	0.3279	0	0	10.0
Fe_{shell}-$O2_{shell}$	1575.20	0.3279	0	0	10.0
Fe_{shell}-$O3_{shell}$	1766.09	0.3279	0	0	10.0
O_{shell}-O_{shell}	22764.0	0.1490	20.37	0	12.0

In the last row of this table "O_{shell}-O_{shell}" means that the corresponding parameters are equal between all nine combinations of oxygen shell pairs (O1-O1, O1-O2 and so on). On the basis of those parameters program has calculated the crystal structure that corresponds to the energy minimum and compared the initial and final values of fractional coordinates. It turned out that the agreement between them was better than 6% for each fractional coordinate.

In order to draw output eigenvectors one needs a transformation matrices from the primitive basis to the conventional (in this case I-centered). For this we need a relation between vectors that form primitive basis and vectors that form I-centered basis. This relation vas given in the output file of the GULP calculation, from where it follows that the final transformation is:

$$\begin{pmatrix} x' \\ y' \\ z' \end{pmatrix}_P = \begin{pmatrix} 0 & 1 & 1 \\ 1 & 0 & 1 \\ 1 & 1 & 0 \end{pmatrix} \cdot \begin{pmatrix} x \\ y \\ z \end{pmatrix}_I \quad \text{which is equivalent to} \quad \begin{pmatrix} x \\ y \\ z \end{pmatrix}_I = \begin{pmatrix} -0.5 & 0.5 & 0.5 \\ 0.5 & -0.5 & 0.5 \\ 0.5 & 0.5 & -0.5 \end{pmatrix} \cdot \begin{pmatrix} x' \\ y' \\ z' \end{pmatrix}_P .$$

Here index P (i.e. I) shows that the column refers to the primitive (i.e. I-centered) basis. Those matrices are the same as the ones used by program Crystal (this is a program for ab-initio calculations of crystal properties) [Crys]. By using the relation between primitive and conventional basis I have found which atoms in the conventional unit cell are equivalent (i.e. their positions differ by a vector from the direct lattice) and which are used in the GULP output. The result is shown in the figure 3.8. I have used this figure for drawing displacement pattern. The data treatment procedure of the output file was already described in the case of $SrFeO_3$ (section 2.1.2). Here one can add that the irreducible representation to which particular phonon belongs had to be determined by hand, since the program does not do it.

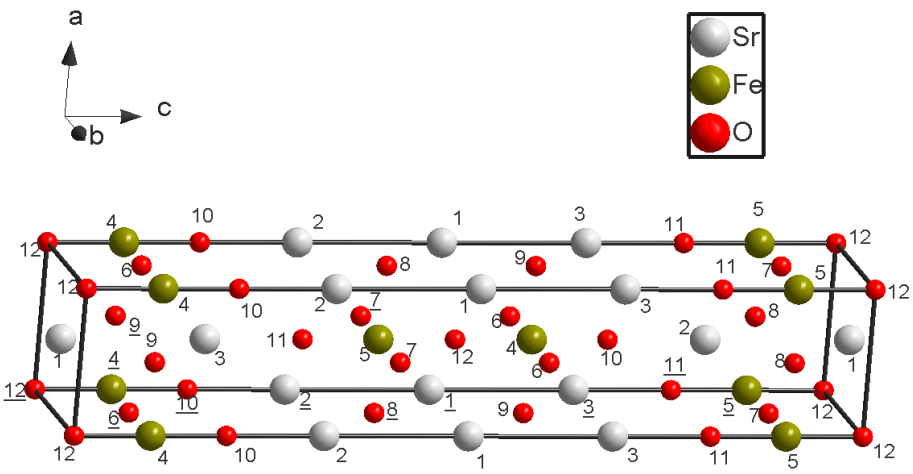

Figure 3.8 (color): Numbering scheme of atoms in $Sr_3Fe_2O_7$ conventional cell used by GULP. Underlined numbers denote atoms that appear in the output file. The rest numbers show which atoms are mutually equivalent.

The result of the calculation is shown in the figure 3.9. All modes except three acoustical are shown. Modes are grouped on the basis of which irreducible representation they belong to, starting with Raman active. Double degenerate modes are shown in the upper parts of page, while non degenerate modes are shown in lower parts of page. Within one irreducible representation, modes are arranged in increasing frequency. In some cases displacement vector of a certain ion was smaller than the symbol that denotes this ion. Those displacements are therefore neglected. It follows from figure 3.9 that the decomposition of mechanical representation at gamma point for $Sr_3Fe_2O_7$ (section A.3.3) was correct. We can also see that all non degenerate modes involve movements of ions along c-axis while all degenerate modes involve movements of ions perpendicular to c-axis. Displacement patterns (but not frequencies) of B_{1g} and B_{2u} modes could be found only from symmetry considerations since they appear exactly once in the decomposition of the mechanical representation. Those displacements found by group projector method (by use of Bilbao Crystallographic Server) and numerically (by use of program GULP) agreed completely with each other.

Important and crucial step in assignment of phonons to the peaks is experimental determination of the symmetry of each Raman active phonon mode (more precisely, only those which are observable). For those reasons we have to use the form of Raman tensor that corresponds to each Raman active irreducible representation. This form is described in the section A.4 together with the formula that relates intensity of Raman signal, Raman tensor and the polarizations of incident and scattered photons. From those formulae we can conclude that so called (z,z) polarization (the first letter in brackets denotes polarization of the incident photon while the second denotes polarization of outgoing

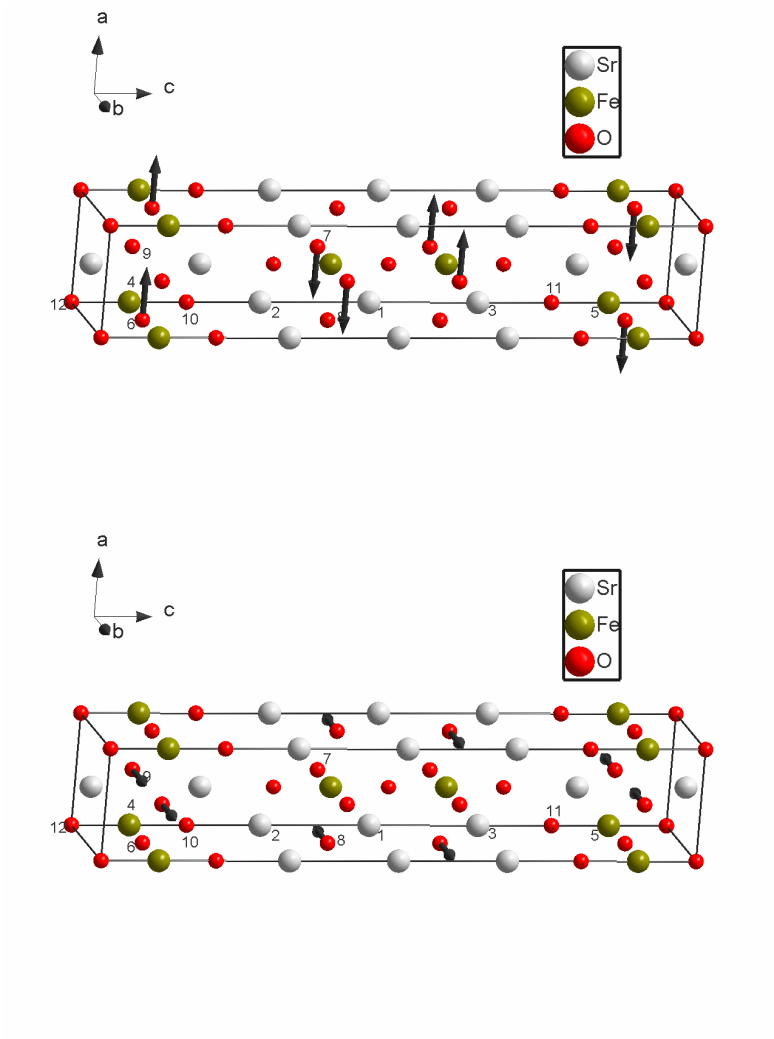

Figure 3.9a (color): Displacement pattern for the 34cm^{-1} mode (E_g; Raman active).

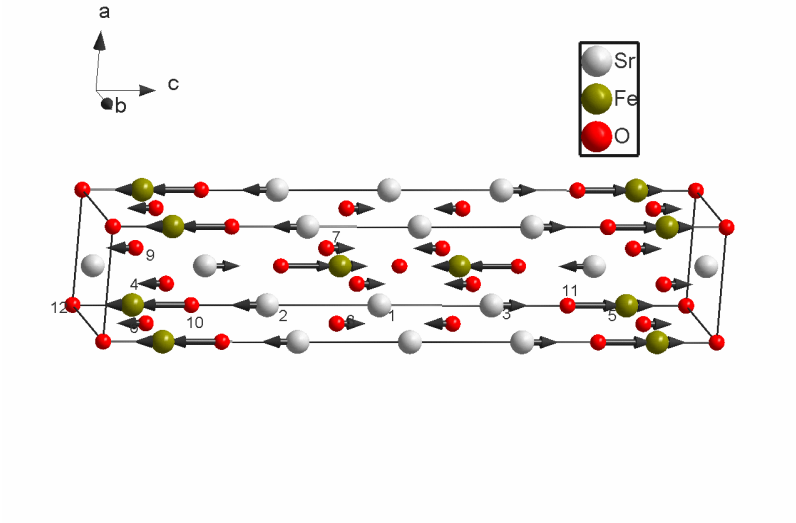

Figure 3.9b (color): Displacement pattern for the 97cm^{-1} mode (A_{1g}; Raman active).

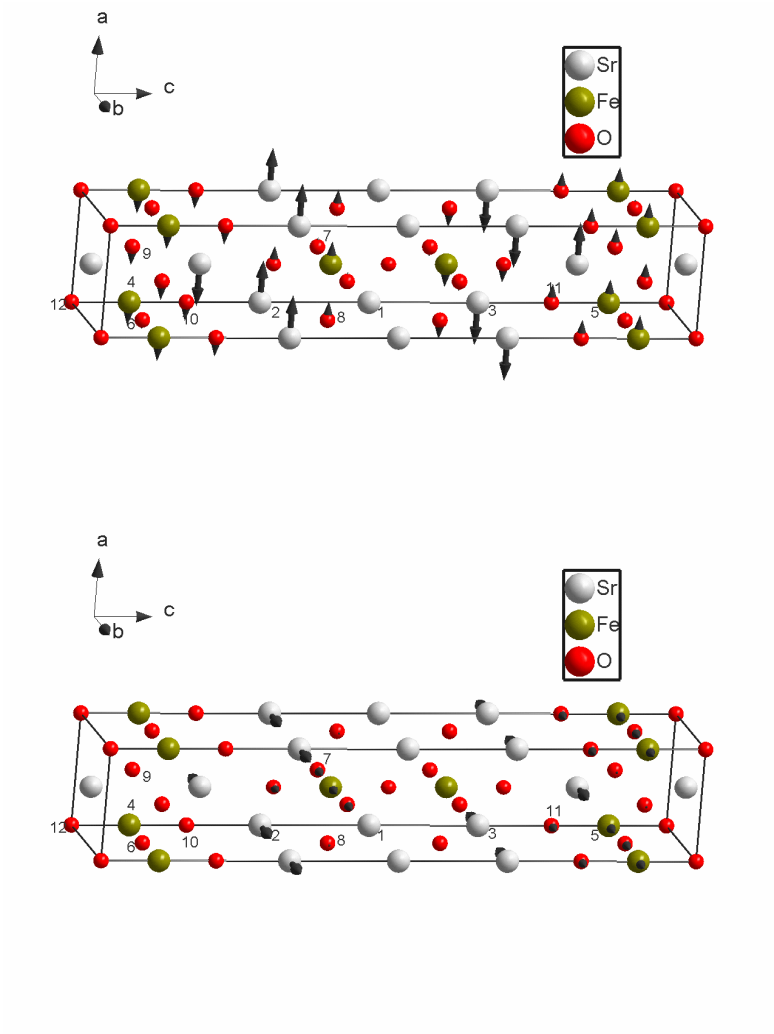

Figure 3.9c (color): Displacement pattern for the 83cm^{-1} mode (E_g; Raman active).

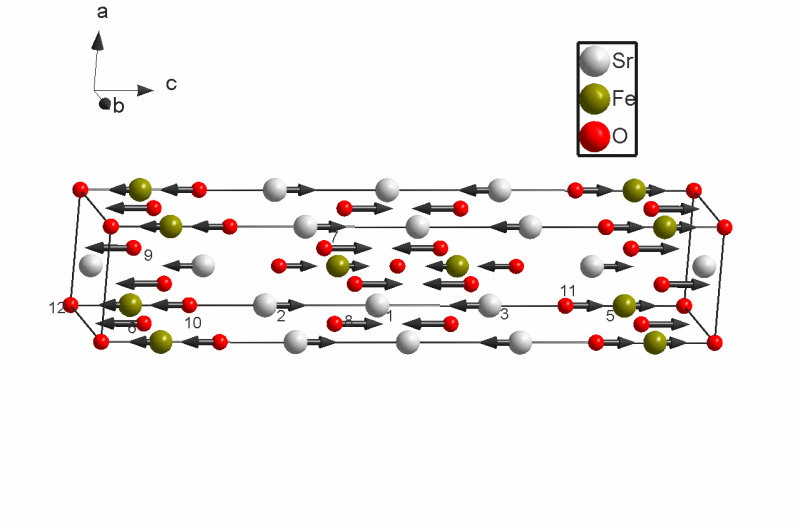

Figure 3.9d (color): Displacement pattern for the 144cm^{-1} mode (A_{1g}; Raman active).

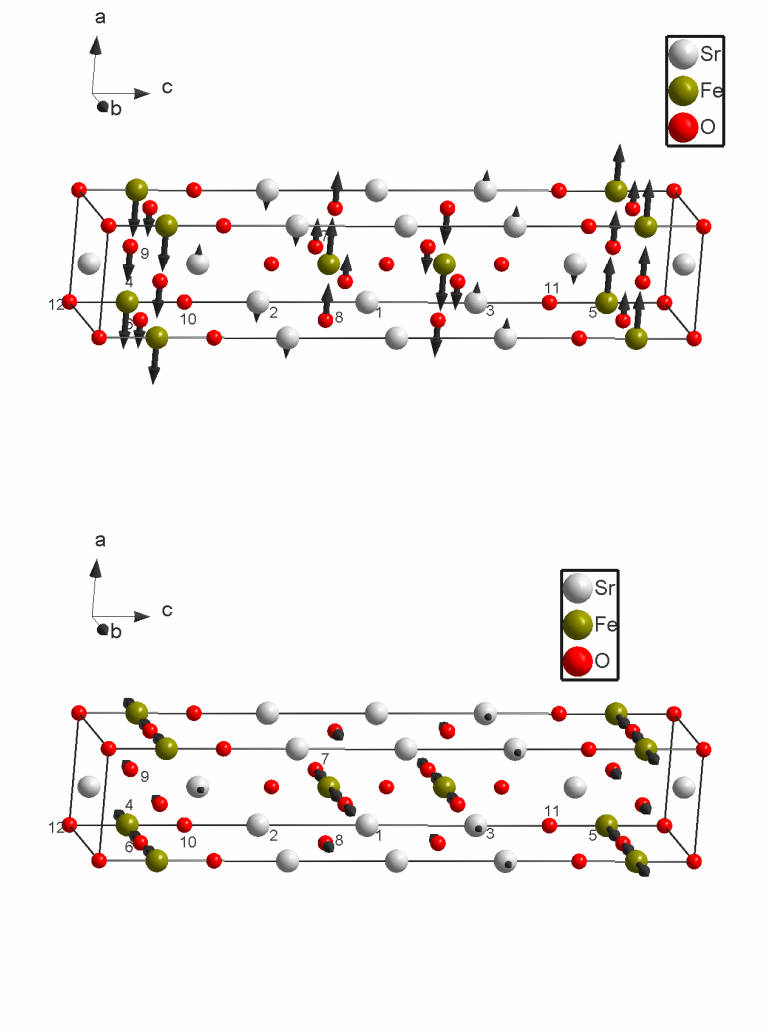

Figure 3.9e (color): Displacement pattern for the 163cm^{-1} mode (E_g; Raman active).

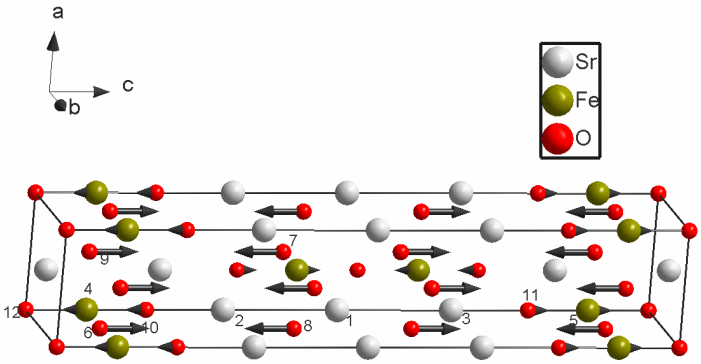

Figure 3.9f (color): Displacement pattern for the 317cm^{-1} mode (A_{1g}; Raman active).

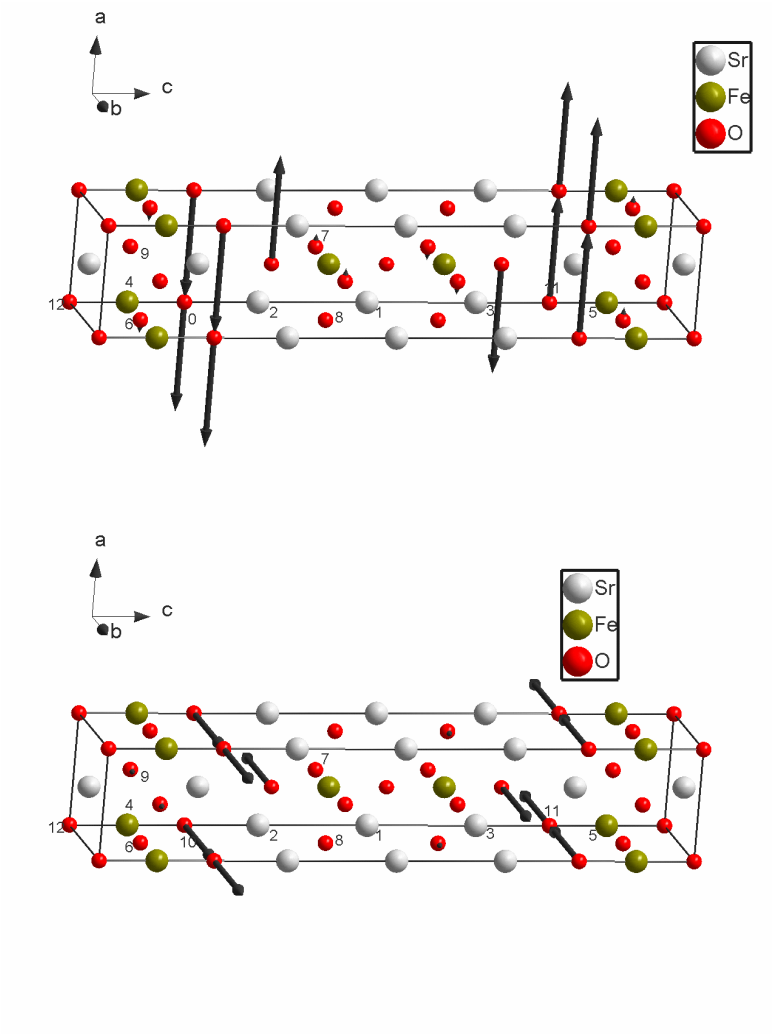

Figure 3.9g (color): Displacement pattern for the 601cm^{-1} mode (E_g; Raman active).

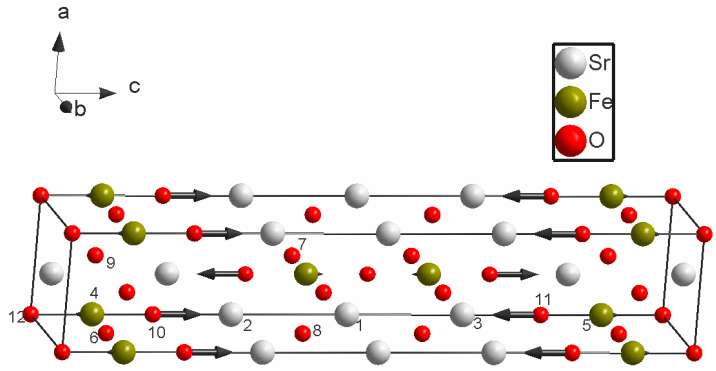

Figure 3.9h (color): Displacement pattern for the 472cm^{-1} mode (A_{1g}; Raman active).

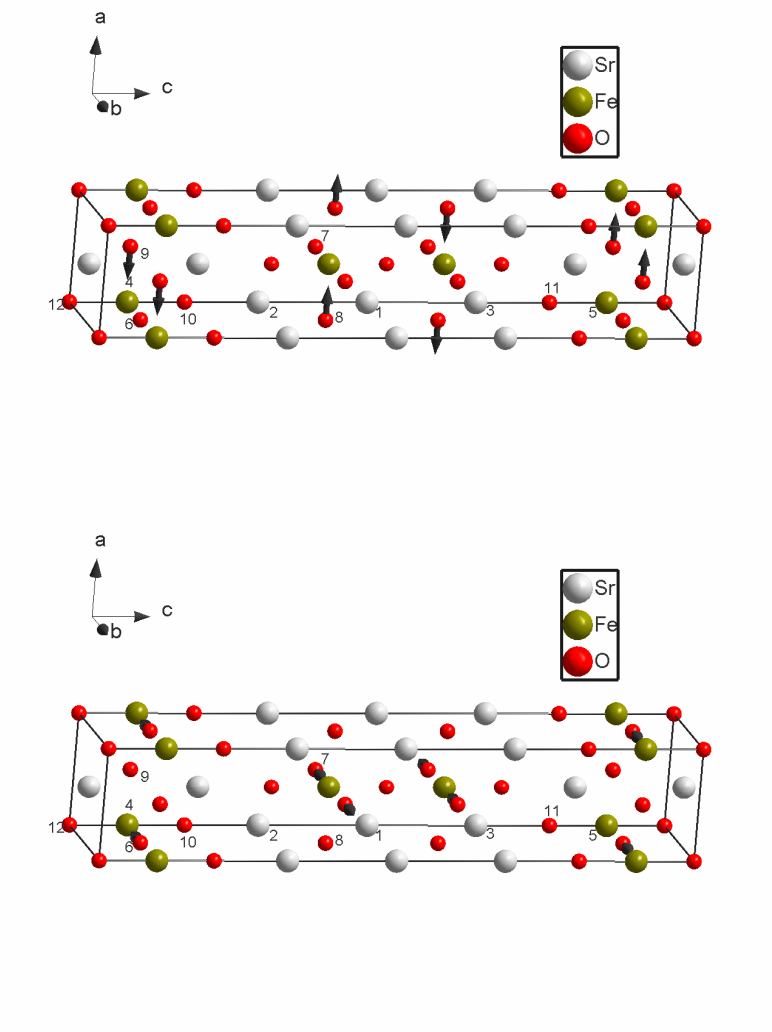

Figure 3.9i (color): Displacement pattern for the 725cm^{-1} mode (E_g; Raman active).

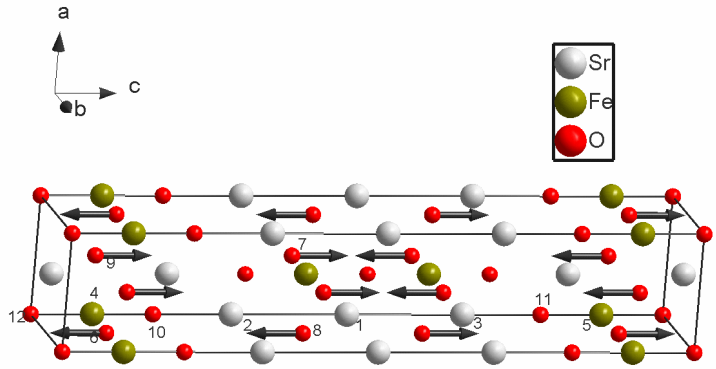

Figure 3.9j (color): Displacement pattern for the 128cm^{-1} mode (B_{1g}; Raman active).

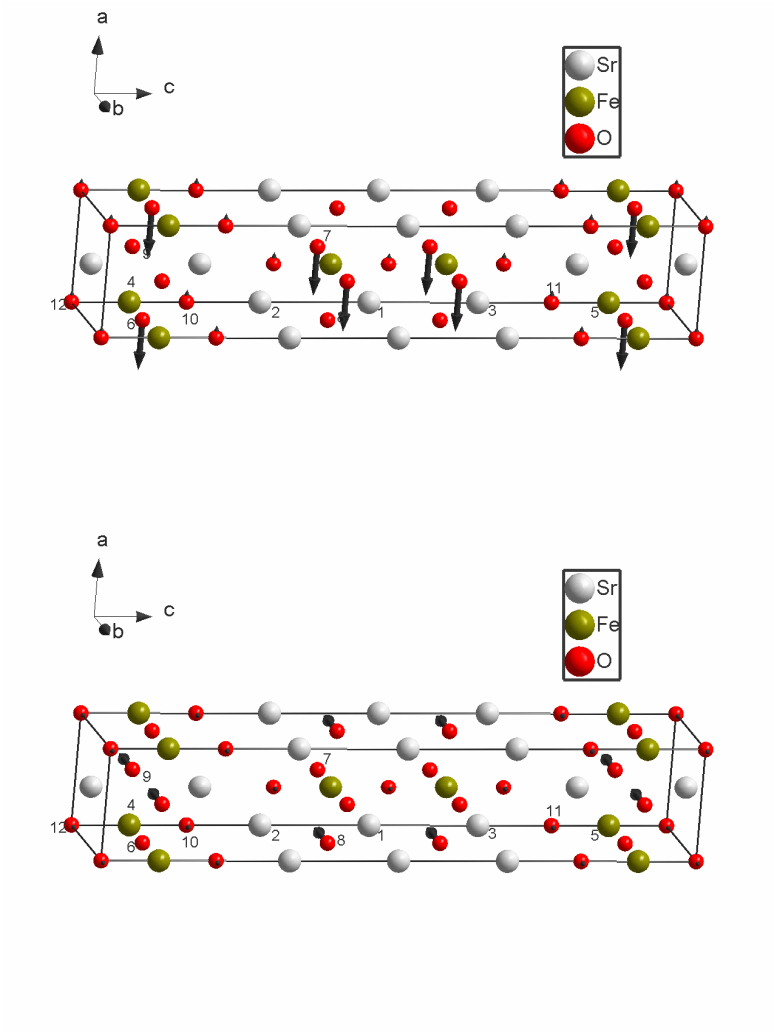

Figure 3.9k (color): Displacement pattern for the 53cm^{-1} mode (E_u; IR-active).

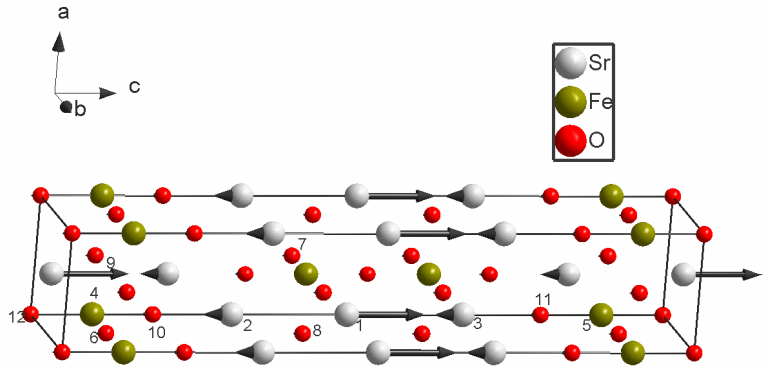

Figure 3.9l (color): Displacement pattern for the 113cm^{-1} mode (A_{2u}; IR-active).

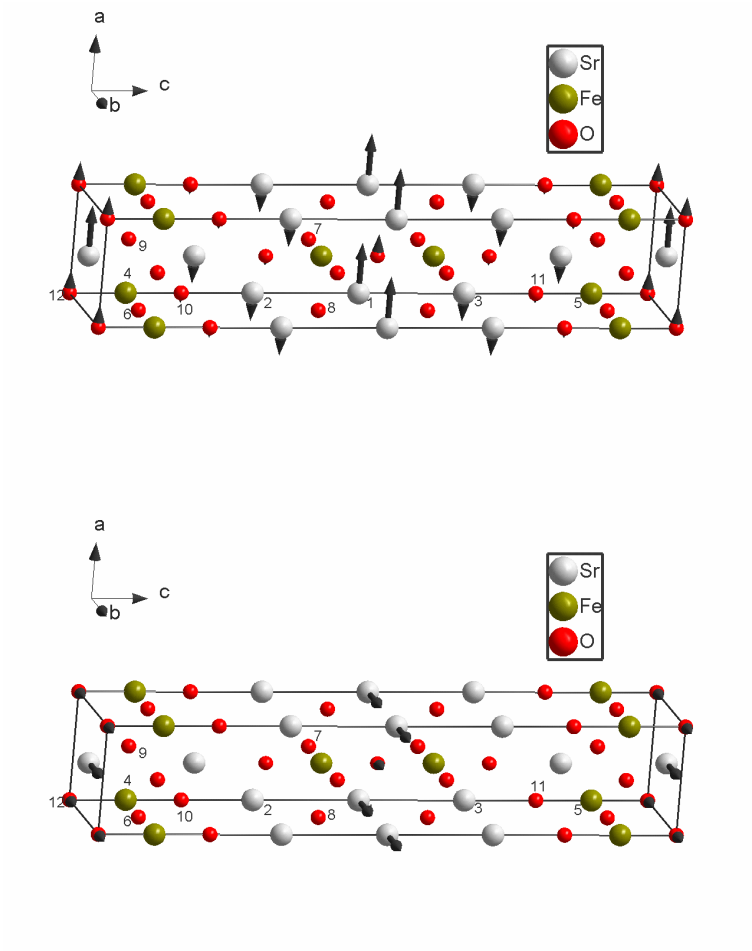

Figure 3.9m (color): Displacement pattern for the 107cm^{-1} mode (E_u; IR-active).

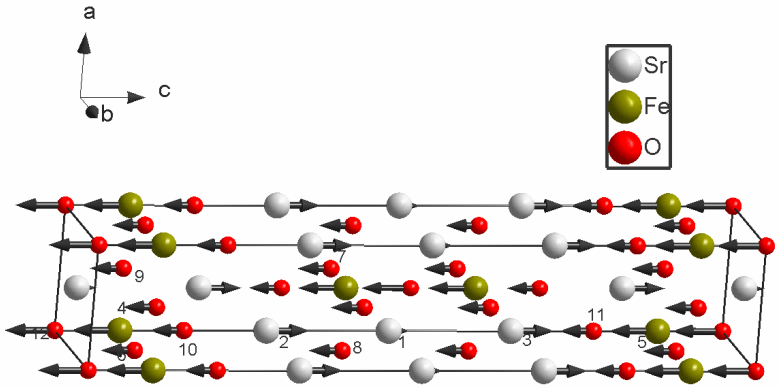

Figure 3.9n (color): Displacement pattern for the 178cm^{-1} mode (A_{2u}; IR-active).

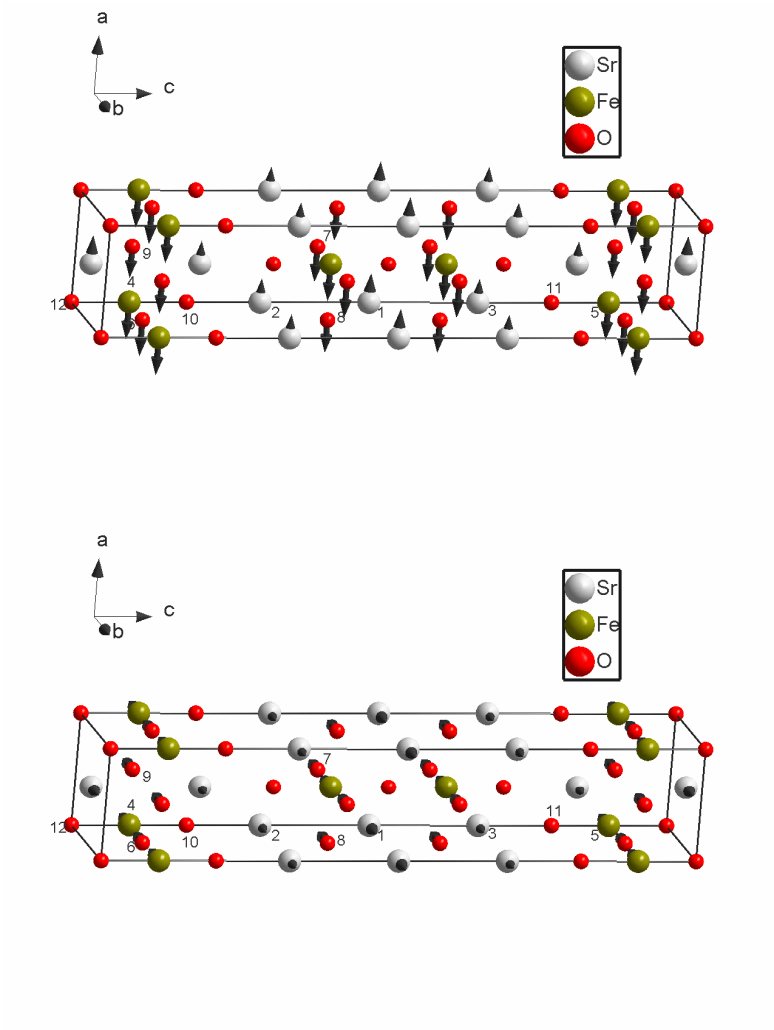

Figure 3.9o (color): Displacement pattern for the 158cm^{-1} mode (E_u; IR-active).

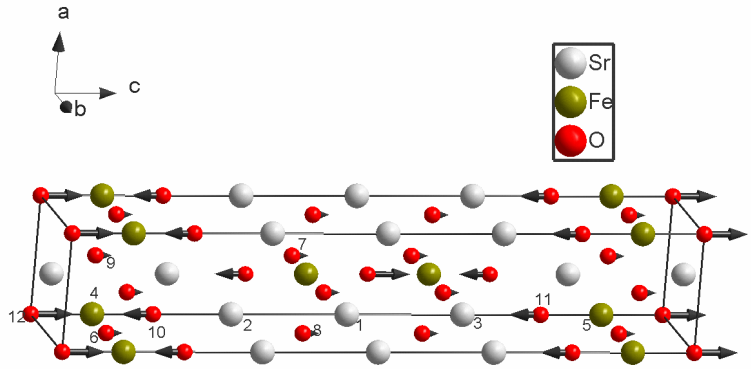

Figure 3.9p (color): Displacement pattern for the 488cm^{-1} mode (A_{2u}; IR-active).

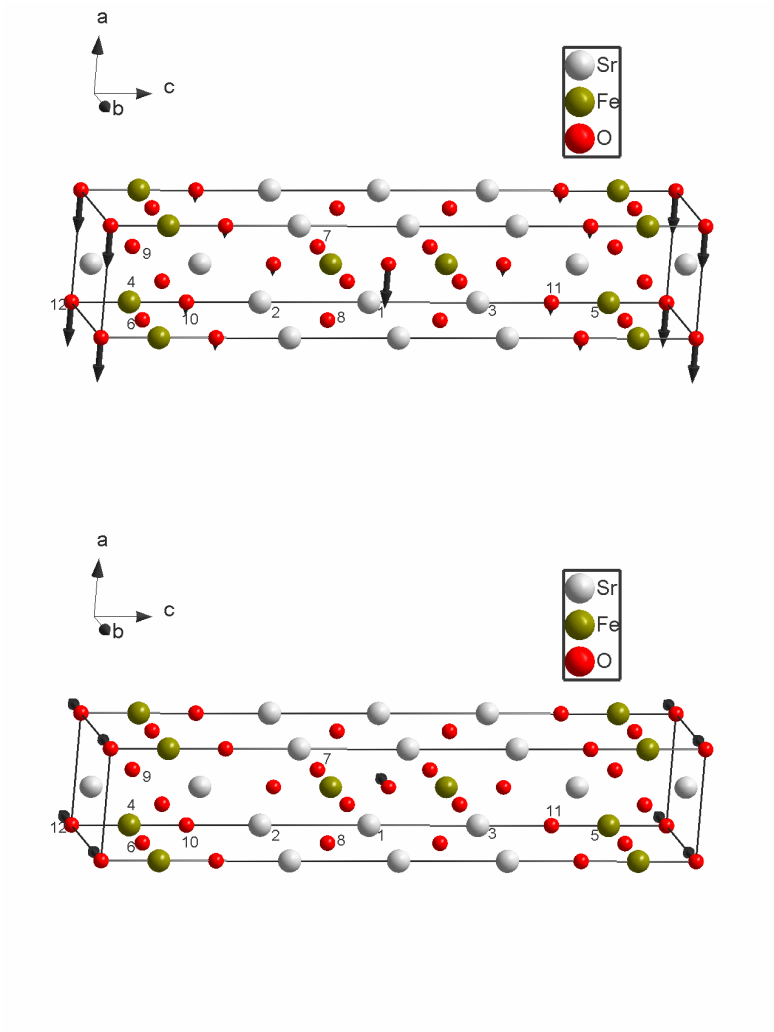

Figure 3.9q (color): Displacement pattern for the 389cm^{-1} mode (E_u; IR-active).

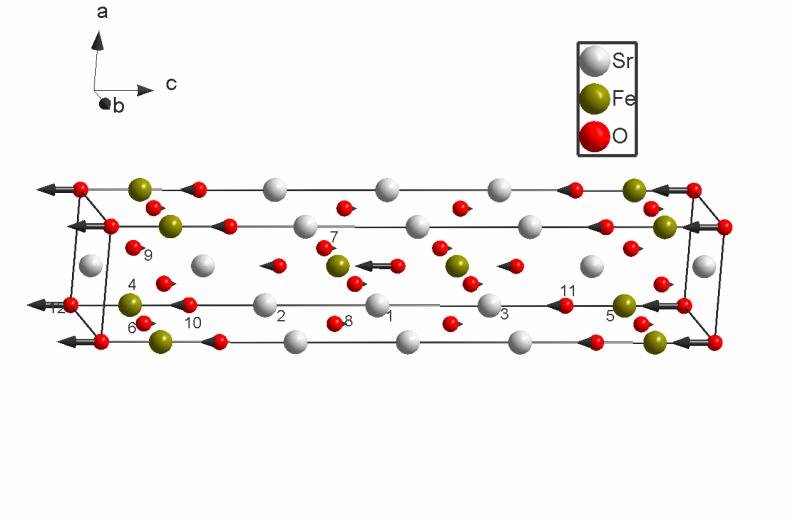

Figure 3.9r (color): Displacement pattern for the 532cm^{-1} mode (A_{2u}; IR-active).

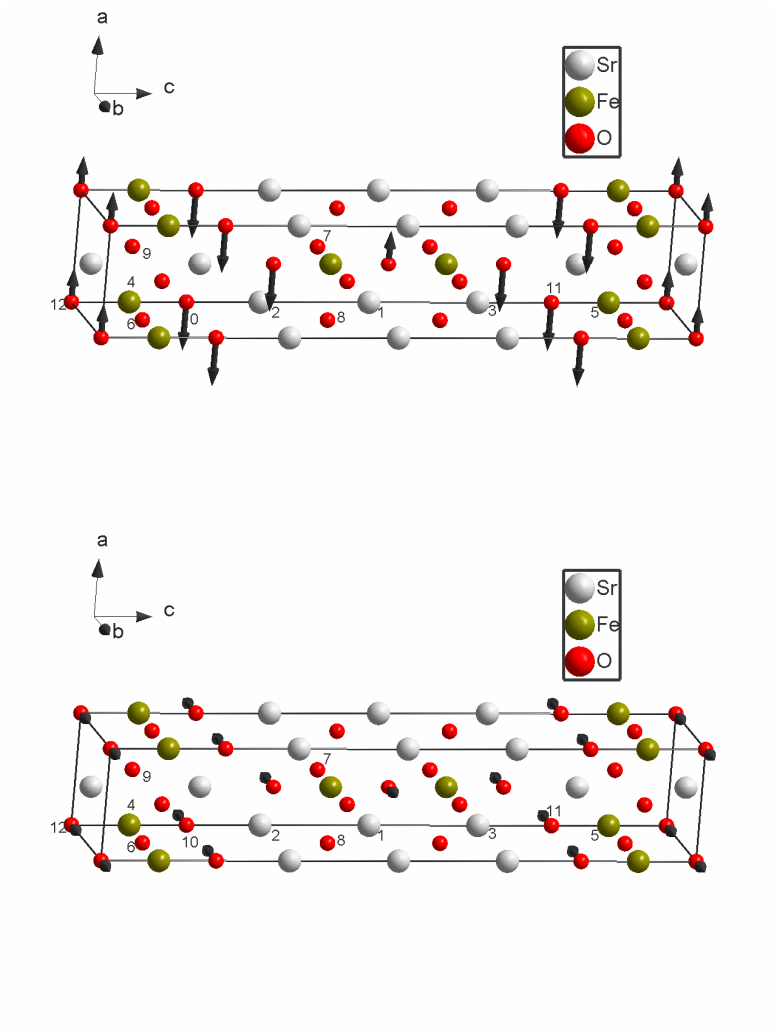

Figure 3.9s (color): Displacement pattern for the 463cm^{-1} mode (E_u; IR-active).

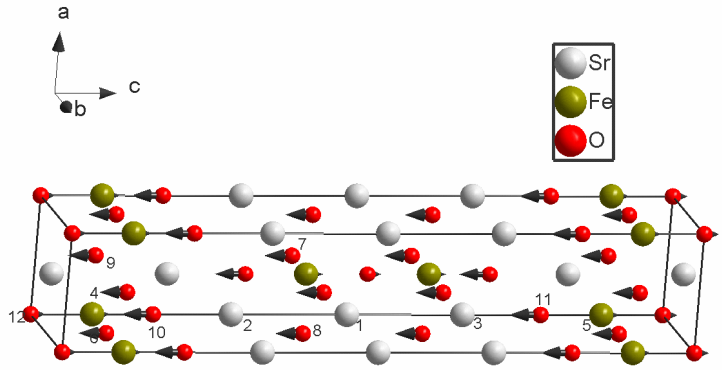

Figure 3.9t (color): Displacement pattern for the 623cm^{-1} mode (A_{2u}; IR-active).

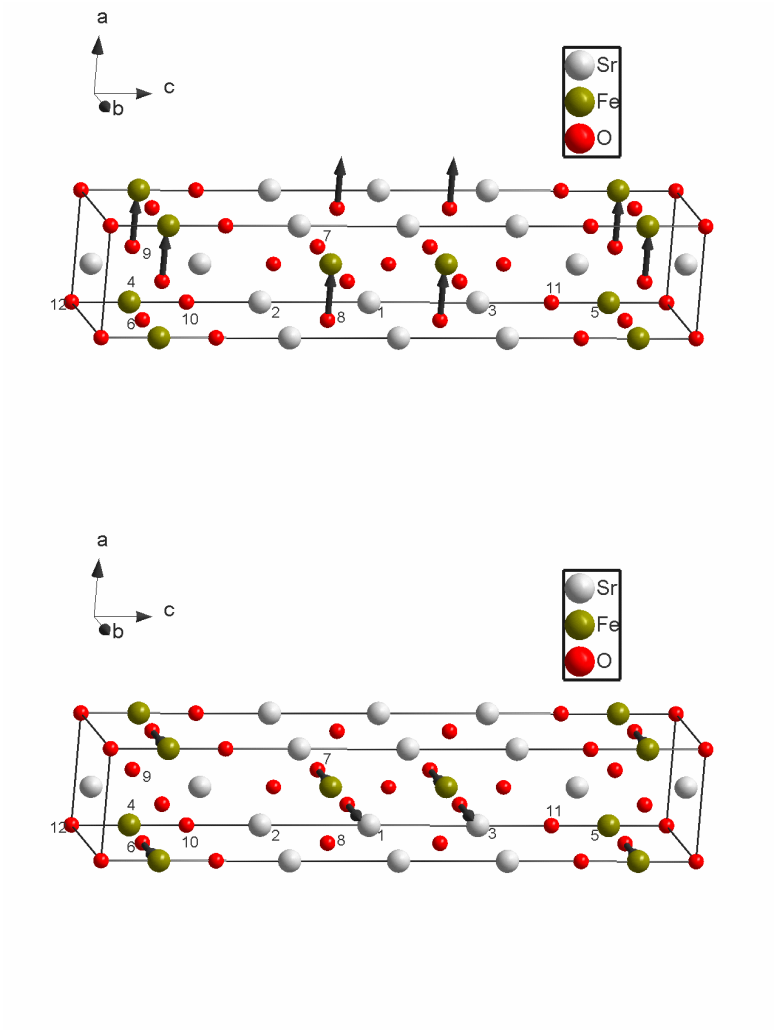

Figure 3.9u (color): Displacement pattern for the 723cm^{-1} mode (E_u; IR-active).

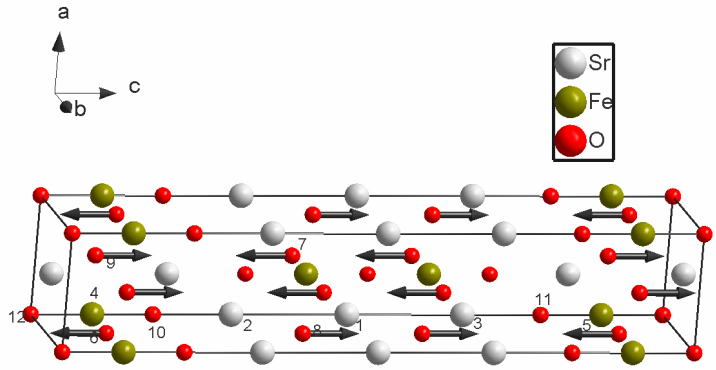

Figure 3.9v (color): Displacement pattern for the 126cm^{-1} mode (B_{2u}; silent).

photon) allows us to see only phonons of A_{1g} symmetry, (y,y) polarization phonons of A_{1g} and B_{1g} symmetry while (z,y) polarization allows us to see only modes of E_g symmetry. In order to investigate symmetry properties of observed peaks we have performed a polarization analysis in which apart from the polarization of incident photons, the polarizations of outgoing photons were measured, by help of an analyzer. The result is shown in the following figure:

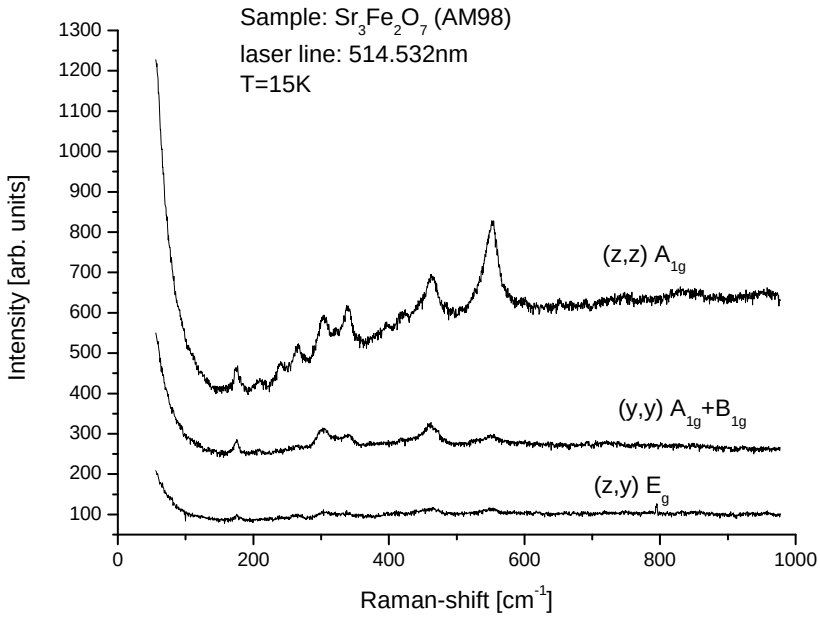

Figure 3.10: Polarization dependence for $Sr_3Fe_2O_{7-\delta}$ at 15K.

From this figure it can be derived by fitting procedure that the peaks are of following energies: 177cm^{-1}, 210cm^{-1}, 242cm^{-1}, 266cm^{-1}, 306cm^{-1}, 342cm^{-1}, 466cm^{-1} and 554cm^{-1}. Those energies together with calculated energies of the Raman active modes are given in the following table:

Table 3.4: Calculated and observed phonon energies

Calculated frequencies [cm^{-1}]	34 E_g	83 E_g	97 A_{1g}	128 B_{1g}	144 A_{1g}	163 E_g	317 A_{1g}	472 A_{1g}	601 E_g	725 E_g
Observed frequencies [cm^{-1}]	177	210	242	266	306	342	466	554		

We can also see that all eight observed peaks are of A_{1g} symmetry, the result which is in contradiction with the decomposition of mechanical representation, where only four A_{1g} peaks are possible. Such result could be explained if one assumes that higher energy modes are due to second- or higher-order Raman scattering, but energies of those peaks rule out this possibility since they can not be obtained as a sum of energies of lower energy peaks. If one compare measured peak energies with one obtained by lattice

dynamics calculation (figure 3.9) one can see that in some of them both energy and symmetry agree. Such is the case for example, with 144cm^{-1} mode (figure 3.9d) which can be assigned to the measured 177cm^{-1} mode the difference being less then 19%, 317cm^{-1} mode (figure 3.9f) which can be assigned to the measured 306cm^{-1} mode with the difference less then 4% and finally 472cm^{-1} mode (figure 3.9h) which can be assigned to the measured 466cm^{-1} mode with the difference being less then 2%. No matter of that, discrepancy between number of observed and calculated modes of A_{1g} symmetry lead to the possibility that in this particular sample, the crystal structure does not correspond to the one reported in the literature. It is possible that oxygen vacancies are ordered and that they form superstructures similar to the case of $SrFeO_{3-\delta}$ (see chapter 2). At the end let us see something that can at a first glance seem to be a contradiction: how come in the figure 3.10 we see less modes in the A_{1g}+B_{1g} geometry, then in A_{1g}? The answer is again given in the form of Raman tensor. In the A_{1g} geometry ((z,z) polarization) we are measuring element "b" while in A_{1g}+B_{1g} geometry ((y,y) polarization) we are measuring element "a" of Raman tensor (section A.4). Those two elements are in general case different.

3.2 MAGNETIC STRUCTURE OF $Sr_3Fe_2O_{7-\delta}$

In this chapter our results on magnetic structure determination of $Sr_3Fe_2O_{7-\delta}$ will be shown. In this experiment we used different sample than the one we used for all previous experiments, but it was from the same batch.

The experiment used for the magnetic structure determination was neutron scattering. This is a powerful technique for both crystal structure and magnetic structure determination. In this technique neutrons, with well defined momentum $\hbar\vec{k}_{in}$ and energy $E_{in} = \frac{\hbar^2 \vec{k}_{in}^2}{2m_n}$ ($m_n = 1.675\times10^{-27}\,kg$ is the mass of the neutron) are directed towards the sample. Because of the interaction with the sample the incident neutron beam is scattered and the momentum of the outgoing neutrons $\hbar\vec{k}_{out}$ as well as their energy $E_{out} = \frac{\hbar^2 \vec{k}_{out}^2}{2m_n}$ are measured. If the outgoing energy is equal to the incident energy of the neutrons we are speaking about elastic scattering. From the relationship between energy and the wave vector of neutrons it follows that in elastic scattering the modules of wave vector of the incident and the scattered neutrons are the same i.e. $\left|\vec{k}_{in}\right| = \left|\vec{k}_{out}\right|$. If the energy of outgoing neutrons is different from the energy of incident neutrons we are speaking about inelastic scattering. Elastic scattering is used when the crystal and magnetic structure of material have to be determined, while inelastic scattering measures the dispersion relations of elementary excitations (phonons, magnons…) in the material. For the purpose of magnetic structure determination we consider here only elastic neutron scattering.

The reason why the incident neutron beam is deflected from its original direction is that neutrons from the beam interact with the sample. Since the charge of the neutron is zero this interaction is not Coulomb. Interaction between neutrons and the sample proceeds via two mechanisms: the first is the strong interaction between the neutron and

the nuclei. This interaction has very short range ($\approx 10^{-15} m$) and is described by the so called Fermi pseudopotential:

$$V(\vec{r}) = \frac{2\pi\hbar^2}{m_n} b\delta(\vec{r})$$

where b is a phenomenological parameter with dimension of length and it is dependent on the type of nucleus with which the neutrons interact as well as the type of the isotope to which this nucleus eventually belongs and also the total spin of the nucleus. Due to those variations we can divide the total scattering into so called coherent (i.e. the scattering that occurs from the sample in which all b's are equal to some mean value $\bar{b}$) and incoherent (i.e. the scattering due to the fluctuation of the parameter b from one nucleus to the other) parts. Consider now a single crystal in which neutrons from the incident beam interact with the nuclei only by the strong force described by the Fermi pseudopotential. Starting from Fermi's Golden Rule one obtains after lengthy calculations the following formulae for the coherent and incoherent scattering cross sections of such system [Jn15]:

$$\left(\frac{d\sigma}{d\Omega}\right)_{coh} = \frac{\sigma_{coh}}{4\pi} N \frac{(2\pi)^3}{V_0} e^{-2W} \sum_{\vec{\tau}} \delta(\vec{k} - \vec{\tau})$$

$$\left(\frac{d\sigma}{d\Omega}\right)_{inc} = \frac{\sigma_{inc}}{4\pi} N e^{-2W} .$$

In those formulae N is the number of unit cells in the investigated single crystalline sample, V_0 is the volume of the unit cell, $\sigma_{coh} = 4\pi(\bar{b})^2$, $\sigma_{inc} = 4\pi(\overline{b^2} - (\bar{b})^2)$, $\vec{k} = \vec{k}_{in} - \vec{k}_{out}$ is so called scattering vector, $\vec{\tau}$ is a vector of the reciprocal lattice, summing is performed over the whole reciprocal lattice and W is the so called Debye-Waller factor. Due to thermally excited lattice vibrations this factor is temperature dependent and also depends on the scattering vector. At low temperatures the dependence of this factor on the scattering vector is weak. From the formula on the coherent scattering cross section it follows that it is different then zero only when the scattering vector coincides with a vector from the reciprocal lattice. In this way we can determine the crystal structure from the positions of peaks while incoherent scattering gives rise to the background. It also follows from the first formula that the bigger sample we have the higher intensity of peaks will be observed. For this reason very small samples can not be investigated by neutron scattering so if the single crystals grown are not of sufficient size then more of them have to be co-aligned on the same sample holder (usually Al plates). Fortunately in our case the grown sample was big enough for our purposes.

A second origin of interaction between neutrons from the beam and the sample is the magnetic moment of the neutron. It interacts via magnetic dipole – magnetic dipole interaction with the magnetic moments of the electrons in the sample and the magnetic moments of the nuclei in the sample. This last interaction can be neglected because the magnetic moment of the nucleus is much smaller than the magnetic moment of the

electron due to the fact that the mass of the nucleus is much larger than the mass of the electron. Apart from the interaction with the magnetic moment of the electrons, neutrons also interact with the magnetic field produced by the motions of the electron. The total potential of interaction is [Jn15]:

$$V_{mag} = -\vec{\mu}_n \circ \vec{B}$$

$$\vec{B} = \frac{\mu_0}{4\pi}\left\{ curl\left(\frac{\vec{\mu}_e \times \vec{R}}{R^3}\right) - \frac{2\mu_B}{\hbar}\frac{\vec{p}\times\vec{R}}{R^3}\right\}$$

where $\vec{R}$ is the radius vector between neutron and electron, $\vec{\mu}_n$ is the magnetic moment of the neutron, μ_0 is the magnetic permeability of vacuum, μ_B is the Bohr magneton, $\vec{\mu}_e$ is the magnetic moment of the electron and $\vec{p}$ is the momentum of the electron. We can see that the first contribution to the magnetic field of the electron at the point where the neutron is, is due to the spin of the electron and the second is due to the motion of the electron. This last contribution comes from the Biot-Savart law. Again by applying Fermi's Golden Rule and after a lengthy calculation one can obtain the cross section for magnetic scattering. In the course of the calculation one has to average over polarization of incident neutrons and sum up over the polarization of outgoing neutrons. This is because we are dealing with an experiment in which the polarization of the neutrons is not measured (i.e. the polarization analysis is not performed). Obtained formula is complicated and can be significantly simplified when particular ordering patterns of magnetic moments are considered. In every case analogous division into coherent and incoherent scattering does not appear since there are no fluctuations in the value of magnetic moment when different ions of the same type are considered. In the case of the magnetic neutron scattering from a ferromagnetic crystal we have [Jn15]:

$$\left(\frac{d\sigma}{d\Omega}\right)_{fm} = \left(\frac{\gamma r_0}{2\mu_B}\right)^2 N \frac{(2\pi)^3}{V_0}\sum_{\vec{\tau}} e^{-2W}\delta(\vec{k}-\vec{\tau})\left|\hat{\vec{\tau}}\times\left(\vec{M}(\vec{\tau})\times\hat{\vec{\tau}}\right)\right|^2 .$$

Here $r_0 = \frac{\mu_0 e^2}{4\pi m_e}$ is the classical electron radius, $\gamma = 1.913$ is a positive constant, $\hat{\vec{\tau}}$ is a unit vector in the direction of $\vec{\tau}$ and $\vec{M}(\vec{\tau}) = \int_{cell}\left\langle \vec{M}'(\vec{r})\right\rangle e^{i\vec{\tau}\circ\vec{r}} d^3\vec{r}$ is a Fourier transform of the mean value of the magnetization of a ferromagnetic crystal. All other values are given before. We can see from this formula that in the case of magnetic scattering from ferromagnetic crystal the magnetic peaks appear at the same positions as the nuclear ones. This is because the magnetic unit cell is the same as the nuclear unit cell. In spite of that there are several means to distinguish magnetic from nuclear neutron scattering in this case. The first is that magnetic nuclear scattering is strongly temperature dependent and disappears above the Curie temperature of a ferromagnet while nuclear scattering is almost temperature independent (provided that there is no structural phase transition in

the temperature range investigated), the second is that intensity of magnetic peaks decreases with increasing $|\vec{\tau}|$ while that of the nuclear peaks remains constant. The third way is the behavior in an external magnetic field. The magnetic scattering pattern notably changes with applying magnetic field while nuclear scattering remains constant.

If the scattering system is antiferromagneticaly ordered then the magnetic unit cell is twice as large as nuclear unit cell. Formula for the scattering cross section involves sum over delta functions centered at the reciprocal lattice points of the magnetic lattice [Jn15]. This means that in between peaks of nuclear scattering, additional peaks appear when antiferromagnetic order is present. Those peaks are due to the magnetic scattering.

Finally (and most important for this chapter) is the case of a helical spin arrangement. In the helix configuration described by the helix vector $\vec{Q}$ the components of the spin of the n-th ion at the position $\vec{r}_n$ from the origin of the coordinate system is [Naga]:

$$S_{nx} = A\cos\left(\vec{Q}\circ\vec{r}_n + \alpha\right);\ S_{ny} = B\cos\left(\vec{Q}\circ\vec{r}_n + \beta\right);\ S_{nz} = C\cos\left(\vec{Q}\circ\vec{r}_n + \gamma\right)$$

where A, B, C, α, β and γ are arbitrary real constants. This structure is alternatively called screw structure because the rotation of the spins increases when the point of observation is moved along the helix vector. If the rotation plane is perpendicular to the helix vector the structure is called proper screw structure, while if the rotation plane is parallel to the helix vector the structure is called cycloidal structure. We can see that the description of a helix configuration includes ferromagnetic order (for this case $\vec{Q} = 0$) as well as antiferromagnetic order (for this case $\vec{Q}$ is on the border of the first Brillouin zone) as special cases. In general case of helical ordering described by the helix vector $\vec{Q}$ the formula for the neutron scattering cross section is [Jn15]:

$$\left(\frac{d\sigma}{d\Omega}\right)_{helix} = (\gamma r_0)^2 \left[0.5gF(\vec{k})\right]^2 e^{-2W} I$$

$$I = \frac{N}{4}\frac{(2\pi)^3}{V_0}\left\langle\vec{S}\right\rangle^2\left(1+\hat{\vec{k}}_z^2\right)\sum_{\vec{\tau}}\left[\delta(\vec{k}+\vec{Q}-\vec{\tau})+\delta(\vec{k}-\vec{Q}-\vec{\tau})\right].$$

Here γ is again a positive constant equal to 1.913, g is the Lande factor, $F(\vec{k})$ is the magnetic form factor, $\hat{\vec{k}}_z$ is a z-component of a unit vector in the direction of the scattering vector, $\left\langle\vec{S}\right\rangle$ is the thermal average of the spin operator of an ion which carries the magnetic moment. We can see from those formulae that the condition for a peak to appear in the magnetic scattering by crystal with helical ordering of spins is:

$$\vec{k} = \vec{\tau} \pm \vec{Q}$$

where $\vec{\tau}$ is a vector from the nuclear reciprocal lattice. This means that every nuclear peak is accompanied by two magnetic satellites placed at the "distance" $\pm\vec{Q}$ from it. Due to the $\vec{k}$ dependence of the magnetic form factor those satellite peaks do not have to be of the same intensity. This last paragraph is of extreme importance for understanding our neutron scattering data.

The neutron scattering experiments are performed in the following way. The "white" neutron beam (i.e. the beam with continuous distribution of neutrons with respect to energy) from the source (source can be either nuclear reactor or the spallation source) is directed on the single crystal which serve as a monochromator. Due to the Bragg diffraction only neutrons with selected wavelength are diffracted and continue towards the sample. This selected wavelength depends on the relative orientation of incoming and outgoing beams and the single crystal (monochromator). Mostly used single crystals for this purpose are silicon or pyrolytic graphite. After monochromator the beam is directed towards the sample. After diffraction from the sample the outgoing beam falls on another single crystal which serves as an analyzer. The requirements on this single crystal are the same as in the case of monochromator. The desired mode of the analyzer is achieved by rotation of the analyzer with respect to the beam. After the analyzer the beam is directed towards the detector. The just described configuration is called triple axis spectrometer because it has three degrees of freedom (angle of the monochromator, angle of the sample and angle of the analyzer) where every degree is an angle (from some reference point) of rotation around one of three corresponding axes.

Our measurements were done on the instrument RITA-2 in the Paul Scherer Institute in Villigen, Switzerland. Word RITA stays for "reinvented triple axis spectrometer" and it is a slight modification of a standard triple axis spectrometer. One of modifications is that both analyzer and monochromator are not made from one part but they consist of 7 vertical blades, each can be rotated around its vertical axis. In this way they can be arranged to form curved surface which increases the focusing of the beam and in that way the beam intensity at the sample. In this facility the spallation source serves for obtaining neutrons. Protons are accelerated in an accelerator up to the energy 590MeV and then collide with the lead (Pb) target. What happens then is a very complicated process. The Pb nuclei are disintegrated into a bunch of neutrons, protons and residual nuclei. This disintegration occurs in many ways. In order to have a rough picture of this process let's mention that Gloris et al. identified 127 different disintegration channels [GlMiSu], [Glor]. That means that there are 127 different ways for spallation of lead to occur. Such reactions are for example ${}^{nat}Pb(p;11p,xn)^{172}Hf$ or ${}^{nat}Pb(p;19p,xn)^{153}Gd$. Those formulae mean that the particles which are left from the semi colon (i.e. proton and lead) entering reaction while those which are right from it are the reaction products. The number x (i.e. the number of the obtained neutrons) has to be determined for each reaction separately. For this reason it is necessary to know the composition of natural lead. It consists of 1.4% ${}^{204}Pb$, 24.1% ${}^{206}Pb$, 22.1% ${}^{207}Pb$ and 52.4% ${}^{208}Pb$. If we consider spallation of the ${}^{207}Pb$ nucleus and if we assume the conservation of baryon number B (this number is equal to the one third of the difference of the number of quarks and anti-quarks and since both proton and neutron consist of three quarks it follows that B=1 for proton and neutron) we get x=25 for the first reaction and x=36 for the second. This means that only one proton, if it causes spallation of the

^{207}Pb gives 25 neutrons in the first case i.e. 36 neutrons in the second case. This is a huge number but one has to keep in mind that due to the smallness of the cross section for the corresponding reaction not every proton which hits the target will cause spallation. Some calculations and also experiments on neutron production by proton bombardment of lead targets predict that Pb target of cylindrical shape with 20cm diameter and 60cm length for the proton energies of around 500MeV will give approximately 10 neutrons per incident proton [LonWon]. These lines served to give a rough description of how neutrons are provided at the PSI spallation source. Concerning the detection of neutrons a container filled with ^{3}He serves for that purpose. Since the neutron has charge zero it is difficult to detect it and the idea is that neutrons after hitting the detector are "converted" to some charged particles. This is really the case since in the He-detector the following reaction occurs:

$$n + {}^{3}He \rightarrow {}^{3}H + p + 0.764 MeV$$

i.e. a neutron hits the nucleus of helium-3 and this produces tritium, a proton and energy of 764keV. This proton is then easier to detect.

Our results on elastic neutron scattering on $Sr_3Fe_2O_{7-\delta}$ for different temperatures are shown in the following figure:

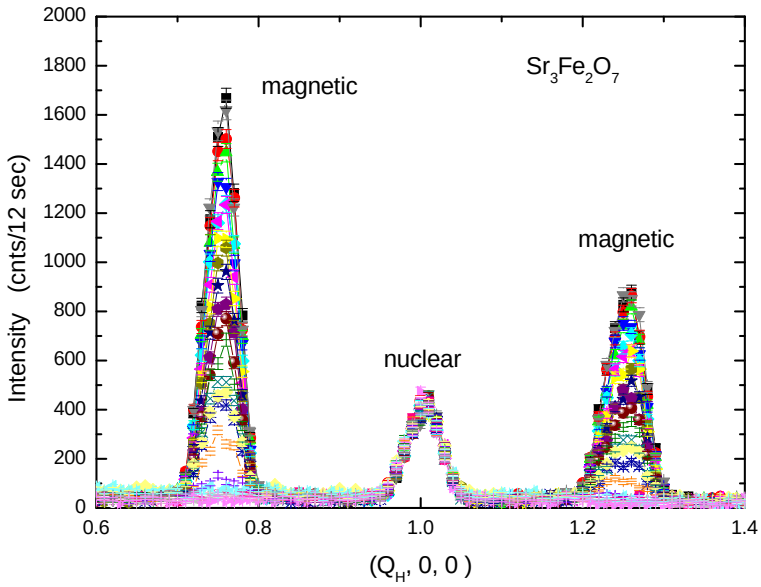

Figure 3.11: Elastic neutron scattering on $Sr_3Fe_2O_{7-\delta}$ at various temperatures.

For better understanding of our data one has to keep in mind that the reciprocal lattice of body centered tetragonal lattice is all-face centered tetragonal. Careful analysis of the crystal structure of $Sr_3Fe_2O_{7-\delta}$ shows that the reciprocal lattice basis vectors of conventional cell are:

$$\vec{a}^* = \frac{4\pi}{a^2}\vec{a}\,;\ \vec{b}^* = \frac{4\pi}{a^2}\vec{b}\,;\ \vec{c}^* = \frac{4\pi}{c^2}\vec{c}\,.$$

In these formulae $\vec{a}$, $\vec{b}$ and $\vec{c}$ are basis vectors of conventional unit cell of direct lattice (see figure 3.2). Figure 3.11 presents elastic scattering around nuclear peak (1,0,0) in the a-direction. We can see that this nuclear peak is accompanied by two magnetic satellites. Their intensity decreases with increasing temperature and goes to zero above magnetic transition temperature (around 140K). In the same time the nuclear peak remains unchanged. From what we have learned about elastic magnetic neutron scattering we can conclude that the type of magnetic order in $Sr_3Fe_2O_{7-\delta}$ is helical with the helix vector equal to

$$\vec{Q} = 0.25 \cdot \vec{a}^*\,.$$

We can not, on the basis of these data, conclude which type of helical order is present. This remains an open question.

The temperature dependence of the intensity of magnetic peaks is given in the following figure:

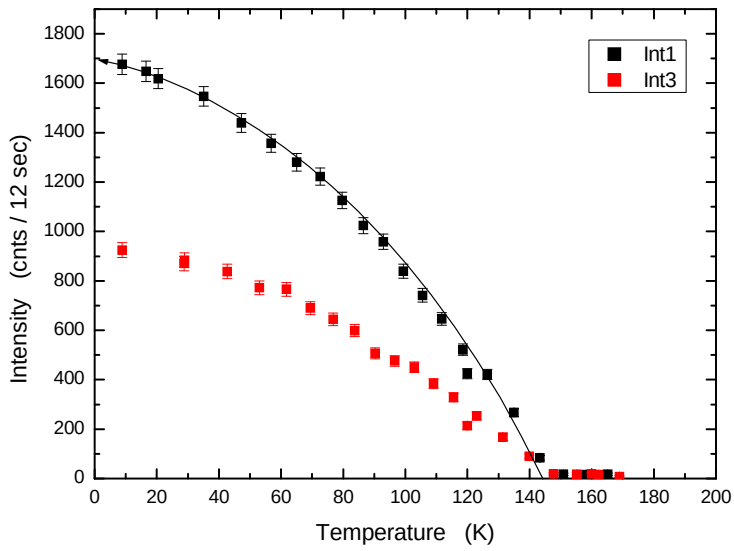

Figure 3.12 (color): Temperature dependence of the intensity of magnetic peaks. Black squares – left magnetic peak, red squares – right magnetic peak (fig. 3.11).

This figure confirms assumption that those peak are of magnetic origin. The difference in intensities can be assigned to the difference in the magnetic form factor for given two positions in the reciprocal space.

The examined magnetic structure of $Sr_3Fe_2O_{7-\delta}$ could be related to the reported magnetic structure of $SrFeO_3$ and $CaFeO_3$ materials. It is experimentally verified that both $SrFeO_3$ [AbZaOk] as well as $CaFeO_3$ [MaMiFu] have negative charge transfer energy Δ (this energy is defined as energy necessary to transfer an electron from the oxygen to the iron site). M. Mostovoy has shown theoretically that in this case double exchange favors helical ordering of magnetic moments [Mos1], [Mos2]. Analysis of X-ray absorption and photoelectron spectra shows that also $Sr_3Fe_2O_7$ has negative charge transfer energy [AbAsPr], [AbAsMo], [AbMoPr]. This can then explain observed helical magnetic structure of this material.

4. THE COMPOUND $CaFeO_3$

The compound $CaFeO_3$ was first synthesized in 1970 by high pressure annealing [KaMiMi.]. At that time it was believed that it was a new cubic perovskite with lattice constant of 3.770Å but as we will see later the crystal structure is, strictly speaking, different. If we start with the usual oxidation states of Calcium: Ca^{2+} and Oxygen: O^{2-}, from electrical neutrality we can conclude that the oxidation state of Iron is: Fe^{4+}. The electronic configuration of this ion is: Fe^{4+}: [Ar]$3d^4$, where [Ar] means the electronic configuration of the noble gas Argon. In the crystal this in free space five fold degeneracy is lifted by the influence of the crystal field. If the crystal field were of cubic symmetry (point group $\underline{O}_h$) the splitting would be into lower lying, triply degenerate t_{2g} and higher, doubly degenerate, e_g level. (Strictly speaking the site symmetry of Fe^{4+} site is $\underline{C}_i$ and as was shown in the Appendix A this leads to splitting into 5 non degenerate levels). Since this involves orbital degeneracy of the ground state we can apply the Jahn-Teller theorem that states that if the ground state of the system is orbitaly degenerate the system is unstable with respect to movement of the nuclei, and the lattice suffers a distortion [JahTel], [Jahn]. However, instead of showing Jahn-Teller instability, the system shows charge ordering $2Fe^{4+} \rightarrow Fe^{3+} + Fe^{5+}$ at T=290K as was inferred by Mössbauer measurements [TaNaTa], [DaDeFa]. The Mössbauer spectrum of $CaFeO_3$ for three different temperatures is shown in the figure 4.1 (from [DaDeFa]). From this figure we can see that at a temperature of 293K which is above the charge ordering transition at 290K the Mössbauer spectrum consist of only one line with isomer shift of δ=0.044mm/s (relative to α-Fe) which corresponds to Fe^{4+} ions. At the temperature of 125K, which is below the charge ordering temperature but above the magnetic ordering temperature (at about 120K), the spectrum consists of two lines corresponding to the "Fe^{3+}" and "Fe^{5+}" ions, while at 4.2K, well below the magnetic ordering temperature, the spectrum consists of two magnetic hyperfine sextets with isomer shifts δ_1=0.30mm/s and δ_2=0.026mm/s which correspond to the Fe^{3+} and Fe^{5+} ions, respectively. We can see that strictly speaking, the charge disproportionation reaction at 290K should be written in the following way: $2Fe^{4+} \rightarrow Fe^{(4-\varepsilon)+} + Fe^{(4+\varepsilon)+}$, where ε rises from 0 to 1 when the temperature is lowered from 290K to around 4K. The effective magnetic fields (also called hyperfine fi-

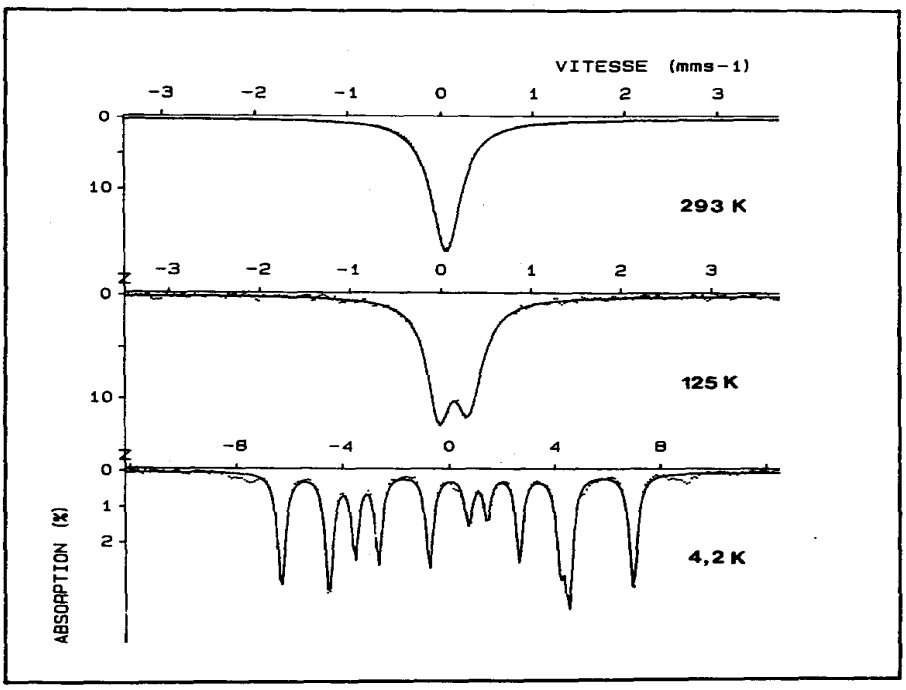

Figure 4.1: Mössbauer spectrum of $CaFeO_3$ at various temperatures (vitesse = velocity; from [DaDeFa]).

elds) at 4.2K are 41.8T at Fe^{3+} site and 28.4T at Fe^{5+} site as inferred from the Mössbauer spectrum at this temperature. Those fields correspond to the Fe^{3+} and Fe^{5+} ions in the high spin (S=5/2 and S=3/2 respectively) state. On the other hand, the observed hyperfine magnetic field of circa 34T [TaNaTa] corresponds to Fe^{4+} in the high spin (S=2) state. From this follows that the charge disproportionation in $CaFeO_3$ can be schematically shown like in the following figure:

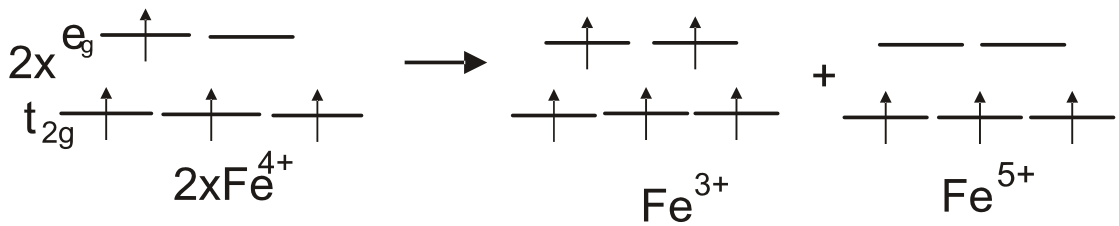

Figure 4.2: Charge disproportionation in $CaFeO_3$ (horizontal lines are energy levels, vertical arrows represent electrons together with their spin).

From this figure it follows that the orbital degeneracy of the electron subsystems ground state, which is present because of the Fe^{4+} ions above charge ordering temperature, is completely removed below the charge ordering transition (where instead of Fe^{4+} ions we have non-degenerate, and therefore Jahn-Teller inactive, high spin Fe^{3+} and Fe^{5+} ions), therefore removing the Jahn-Teller instability. However, this figure is only approximately

valid, since Fe ions (both below and above charge ordering) are not in the crystal field of exactly cubic symmetry.

Concerning the magnetic properties of $CaFeO_3$ it is well known that there is an antiferromagnetic transition at 115K as can be seen in the figure 4.3 (from [TaKaKa]). In this figure, the temperature dependence of the magnetic susceptibility of $Ca_{1-x}Sr_xFeO_3$ for x equal to 0; 0.1 and 0.2 is shown. We can see that the three curves are similar, showing an antiferromagnetic transition at Neel temperature a bit higher than 100K. The exact magnetic ordering of magnetic dipole moments of Fe ions in $CaFeO_3$ is still an open question. While Kawasaki et al., based on neutron scattering measurements, have found that the magnetic structure is helical, with a propagation vector $\vec{k}$ parallel to [111] direction, length of the propagation vector $\left|\vec{k}\right| = 0.161a^*$ (where a^* is the main diagonal of a cube) and angle between spins of nearest neighboring Fe ions circa 60°, Woodward et al., based also on the neutron scattering experiments proposed two models, both equally probable according to their data [KaTaKa], [WoCoMo]. The first one is consistent with Kawasaki et al. while for the second they have proposed a sinusoidal structure with propagation vector along [111] direction and amplitude of 3.5 Bohr magnetons for Fe^{5+} and 5 Bohr magnetons for Fe^{3+}. Their models are shown in the figure 4.4 (from [WoCoMo]).

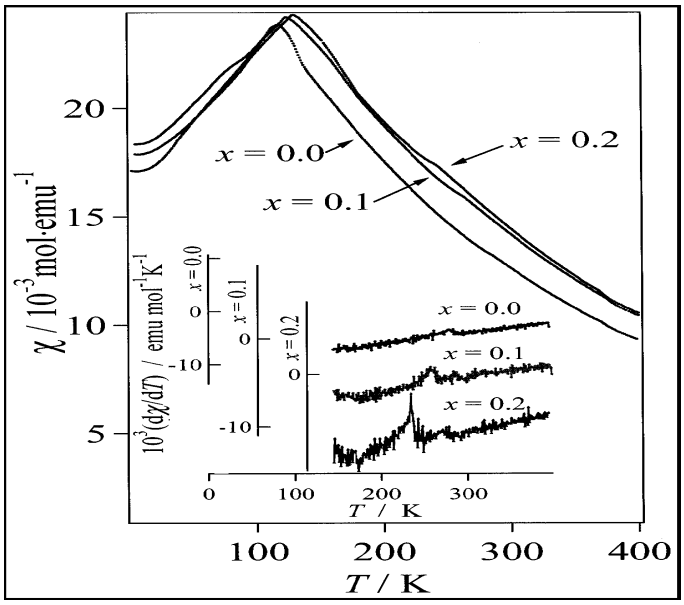

Figure 4.3: Temperature dependence of the magnetic susceptibility of $Ca_{1-x}Sr_xFeO_3$ (from [TaKaKa]).

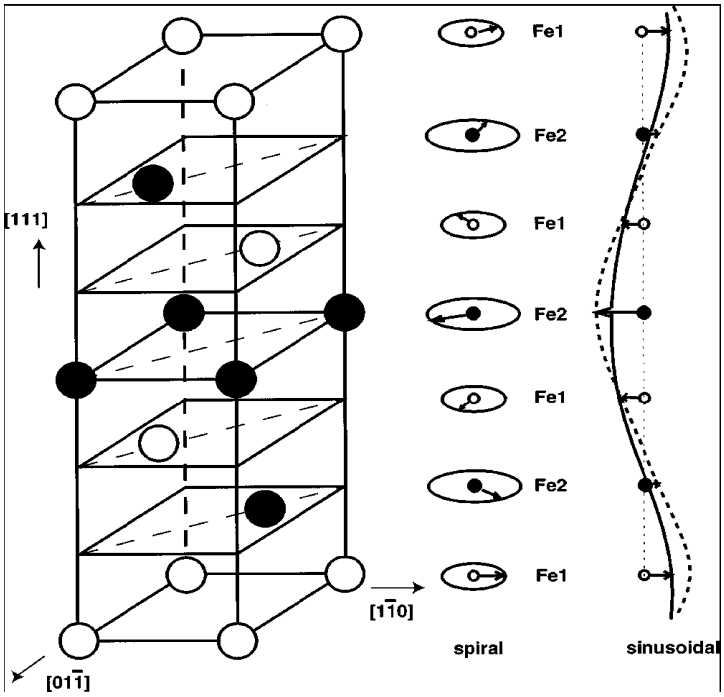

Figure 4.4: Proposed models of magnetic ordering in $CaFeO_3$ (from [WoCoMo]).

The spin values of Fe ions in their spiral model that came out of fit are 2.5 Bohr magnetons for Fe^{5+} ("Fe1") and 3.5 Bohr magnetons for Fe^{3+} ("Fe2"). Those values are somewhat lower then the values (3 Bohr magnetons for Fe^{5+} and 5 Bohr magnetons for Fe^{3+}) expected for high spin states and they have considered them as an indication of considerable degree of covalency. We can also see from the spiral at the figure 4.4 that the angle between spins on nearest neighboring Fe ions is almost 60° as was found by Kawasaki et al.

Since charge ordering involves changes in the electronic states one could expect that at this temperature resistivity will change considerably. That this is really the case in the $CaFeO_3$ is confirmed by experiments. Typical behavior of the resistivity with changing the temperature is shown in the figure 4.5 (from [KaTaKa]). In this figure temperature dependence of the resistivity for $CaFe_{1-x}Co_xO_3$ (x is equal to 0; 0.03; 0.1 and 0.4) and $SrFe_{1-x}Co_xO_3$ (x is equal to 0 and 0.4) is shown, but let's concentrate on $CaFeO_3$. We can see that above the charge ordering transition, this compound is metallic with resistivity around 10 mΩcm. Below the charge ordering transition the compound shows semiconducting behavior with increasing of resistivity by four orders of magnitude when the temperature is decreased from 290K to approximately 50K. First-principles spin-polarized electronic band structure calculations [WhKoVi] show that the value of a gap between conduction and valence bands is of the order of 1eV in the charge ordered state.

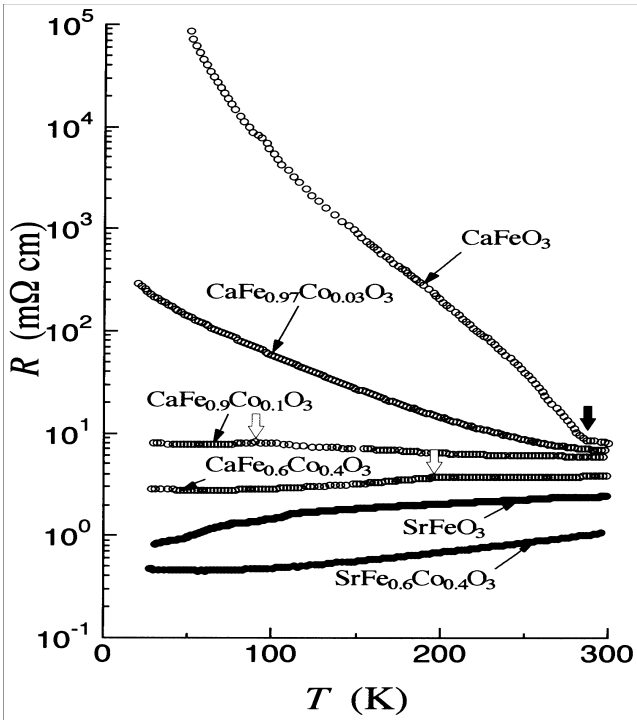

Figure 4.5: Temperature dependence of the resistivity. Vertical black arrow marks the onset of the charge disproportionation in $CaFeO_3$ (from [KaTaKa]).

4.1 THE CRYSTAL STRUCTURE OF $CaFeO_3$

The crystal structure of $CaFeO_3$ was determined experimentally by X-ray and neutron scattering [TaKaKa] and simultaneously and independently by Woodward et al. [WoCoMo]. Those works appeared in the year 2000, so it took more than 20 years after discovery of charge ordering in this compound until exact type of ordering was determined. In this chapter the crystal structure of $CaFeO_3$ will be described on the basis of the results published in the above cited references.

Above the charge ordering temperature at 290K, $CaFeO_3$ adopts the $GdFeO_3$ type structure which belongs to the orthorhombic crystal system, space group Pbnm (D_{2h}^{16} or number 62 in the notation of International Tables for Crystallography). This structure is shown in the figure 4.6. The lattice constants are a=5.32630Å, b=5.35270Å and c=7.53986Å at room temperature. We can see from the figure 4.6 that the crystal structure of $CaFeO_3$ above the charge ordering transition can be derived from the ideal perovskite structure by a small rotation of the FeO_6-octahedra around the c-axis together with out of phase tilting around the a-axis. On the other hand the FeO_6-octahedra are not ideal (possessing $\underline{O}_h$ symmetry) but are distorted. The distance between the apical Oxygen ("O2") and Fe ions is 1.9193Å, while the distances between the equatorial oxy-

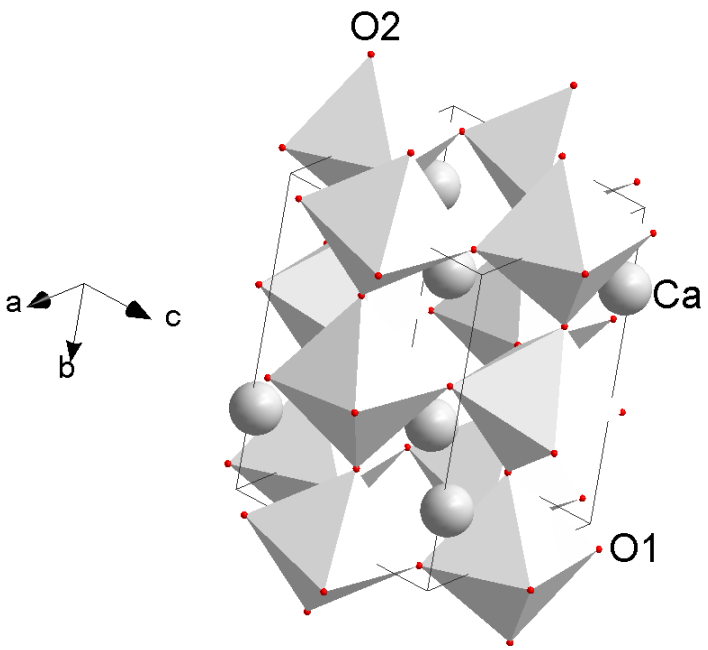

Figure 4.6 (color): Crystal structure of $CaFeO_3$ above the charge-ordering transition. Fe ions are in the centers of octahedra shown (FeO_6-octahedra). Black lines denote unit cell.

gens ("O1") and the Fe ions are 1.9326Å and 1.9158Å. The equatorial angles O1-Fe-O1 are 90.784° and 89.216° which, when summed up, give exactly 180°. From this description it follows that the symmetry of the FeO_6-octahedra would be $\underline{C}_{2h}$ but since the octahedra are tilted around the a-axis the symmetry of Fe-sites is reduced to $\underline{C}_i$.

In order to complete the information about the crystal structure of $CaFeO_3$ above the charge ordering temperature the fractional coordinates of the asymmetric unit are shown in the following table [WoCoMo]:

Table 4.1: Fractional coordinates of the asymmetric unit for $CaFeO_3$ at room temperature.

Atom	Wyckoff position	x/a	y/b	z/c
Ca	4c	0.9950	0.0328	0.25
Fe	4b	0	0.5	0
O1	8d	0.7129	0.2858	0.0327
O2	4c	0.0663	0.4908	0.25

From this table we can see that the number of formula units in the primitive cell is 4 (Z=4). Since the volume of the primitive cell is V=abc=214.61Å^3 we can conclude that the density of $CaFeO_3$ at room temperature is $\rho = \frac{Z \cdot M_{CaFeO_3}}{V \cdot N_A} \approx 4.46 \frac{gr}{cm^3}$. In this

formula N_A is Avogadro's number and M_{CaFeO_3} is molar mass of $CaFeO_3$ which is equal to 143.927gr/mol according to the values taken from the Periodic System of Elements. The above calculated density is of interest when the magnetization measurements are discussed.

Below the charge ordering transition $CaFeO_3$ adopts a monoclinic structure, space group $P2_1/n$ (C_{2h}^5 or number 14 in International Tables for Crystallography). At 15K the cell parameters are a=5.31182Å, b=5.34775Å and c=7.52058Å with a monoclinic angle $\beta=90.065^o$ which means that the structure deviates slightly from orthorhombic. In figure 4.7 the crystal structure is shown (from [TaKaKa]). We can see that it consists of corner sharing FeO_6 octahedra which are not identical to each other but are divided into two groups: larger ("Fe2-O" where Fe2 site corresponds to Fe^{3+}) in the figure denoted with light color and smaller ("Fe1-O" where Fe1 site corresponds to Fe^{5+}) in the figure denoted with dark color. Although it is not easy to see the difference between those two groups of octahedra from the figure we can refer to the average Fe-O distance which is approximately 1.97Å for Fe2-O bound and 1.87Å for Fe1-O bound. It is then possible to qualitatively connect the size of the octahedra with the formal valence states of the corresponding Fe ions: since the Fe^{5+} ion has fewer electrons than the Fe^{3+} ion, it is smaller and therefore it belongs to the smaller FeO_6 octahedra. We can also see from the figure that the charge ordering of Fe^{3+} and Fe^{5+} ions is of the rock-salt type.

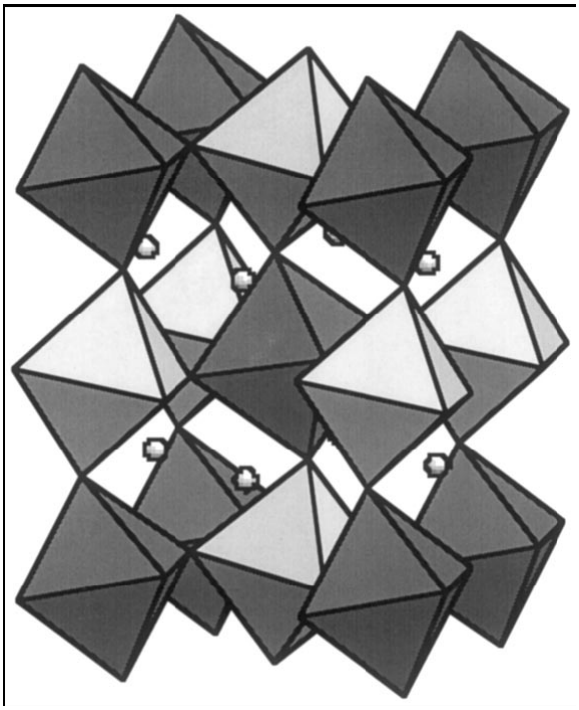

Figure 4.7: Crystal structure of $CaFeO_3$ below the charge ordering temperature. Dark octahedra are $Fe^{5+}O_6$ while light octahedra are $Fe^{3+}O_6$. Fe ions are located in the centers of octahedra and O ions at corners. Small spheres are Ca ions (from [TaKaKa]).

As can be seen from Fe-O bond distances and O-Fe-O angles (table VI in [WoCoMo]) the octahedra are not regular, similar to the case of $CaFeO_3$ above charge ordering transition. This irregularity together with the static tilting of the octahedra reduces the site symmetry of Fe ions again to $\underline{C}_i$. The distance between Fe1 and equatorial O (denoted with O1 and O2) are 1.853Å and 1.870Å respectively, while the distance between Fe1 and apical Oxygen (denoted by O3) is 1.894Å. On the other hand the distance between Fe2 and equatorial Oxygen is 1.997Å for O1 and 1.971Å for O2, while the distance between Fe2 and apical Oxygen (O3) is 1.953Å. These data confirm the idea that the octahedra are not regular but distorted. Also in the favor of this assumption goes the fact that equatorial angles O1-Fe1-O2 are 89.9^o and 90.1^o, the equatorial angles O1-Fe2-O2 are 89° and 91° while the angle between apical Oxygen-Fe bond and corresponding equatorial FeO_4 plane is not exactly 90° in both cases. This means that the deviation of the shape of octahedra from ideal is bigger below charge ordering transition than above.

The fractional coordinates of the asymmetric unit for $CaFeO_3$ at 15K is shown in the table 4.2. From this table we can conclude that as in the case above charge ordering, the low temperature structure contains 4 formula units in the primitive cell (Z=4). Since the volume of the elementary cell is equal to $V=acb\sin(2\pi-\beta)\approx 213.63Å^3$ we can conclude that the density of $CaFeO_3$ at 15K is equal to:

$$\rho = \frac{Z \cdot M_{CaFeO_3}}{V \cdot N_A} \approx 4.47 \frac{gr}{cm^3}.$$

Table 4.2: Fractional coordinates of the asymmetric unit for $CaFeO_3$ at 15K.

Atom	Wyckoff position	x/a	y/b	z/c
Ca	4e	0.9936	0.0371	0.2511
Fe1	2d	0.5	0	0
Fe2	2c	0	0.5	0
O1	4e	0.300	0.720	-0.0330
O2	4e	0.219	0.206	-0.0318
O3	4e	0.0761	0.4927	0.254

From comparison of tables 4.1 and 4.2 we can see that Wyckoff position of Fe ions splits into two below charge ordering transition therefore making place for two different oxidation states of iron. Another observation is that the volume of primitive cell of $CaFeO_3$ at 300K doesn't differ much from the volume at 15K (the difference being only 0.5%) although there is a change of the crystal structure between those two temperatures. Moreover there is no any anomaly in the dependence of unit cell volume with temperature. This dependence is shown in the figure 4.8 (from [WoCoMo]):

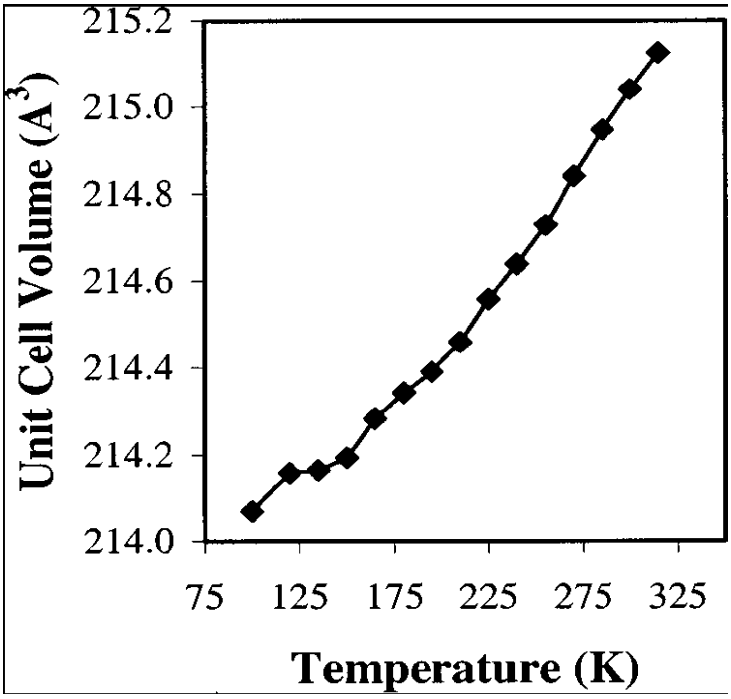

Figure 4.8: Temperature dependence of the unit cell volume of $CaFeO_3$ (from [WoCoMo]).

We can see from this figure that the dependence is almost linear without any significant change at the charge ordering temperature 290K. Similar behavior is shown by temperature dependence of lattice constants a, b and c in the temperature range from 75K to 320K again with no anomaly at 290K. These results can be considered as proof that the charge ordering phase transition in $CaFeO_3$ is of the second (or higher) order. On the other hand, the monoclinic angle β shows almost temperature independent value (90.06^o) below charge ordering transition with sudden decrease to exactly 90° at 290K. This is then another indication of the change of crystal symmetry at this temperature.

4.2 SAMPLE PREPARATION AND CHARACTERIZATION

The aim of this section is to describe how we have obtained the $CaFeO_3$ samples. In order to obtain $CaFeO_3$ we have prepared a platinum crucible like in the figure 4.9. The cup had cylindrical shape with dimensions shown in the figure. This platinum crucible contained one layer of $KClO_4$, one layer of ZrO_2 and one layer of $CaFeO_{2.5}$ single crystal as shown in the figure 4.9. The system was then subjected to high pressure (around 4GPa) and high temperature (around 1000^oC) for about 2 hours. Several samples were prepared in this way under slightly different annealing conditions. Each sample was therefore marked with different numbers. The sample numbers and the annealing conditions are summarized in the table 4.3.

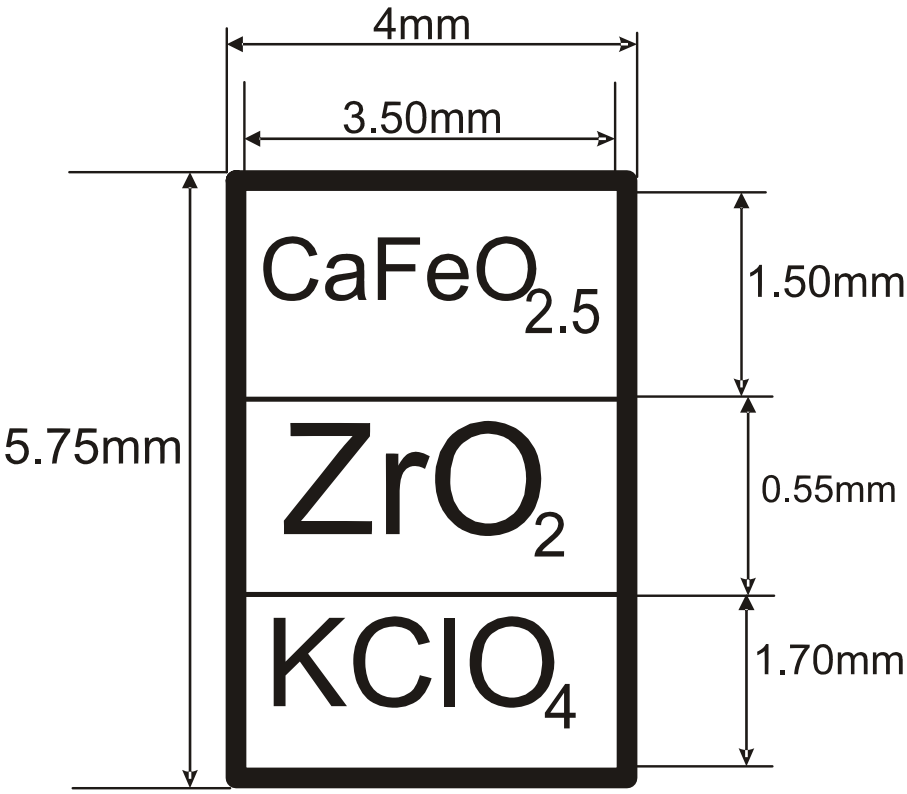

Figure 4.9: Cross section and dimensions of platinum cup that was used for sample preparation.

Table 4.3: Annealing conditions of different samples (1GPa=10kbar).

Sample Mark	Annealing Pressure	Annealing Temperature	Time of Annealing
Sample #1	4GPa	925°C	2 hours
Sample #2	4GPa	850°C	2 hours
Sample #5	4GPa	1000°C	2 hours
Sample #6	4GPa	1000°C	2 hours
Sample #9	4GPa	1000°C	1 hour

The idea of obtaining $CaFeO_3$ from $CaFeO_{2.5}$ is the following: under the annealing pressure and temperature, the $KClO_4$ will release oxygen, which will move through the ZrO_2 barrier by diffusion and then enrich $CaFeO_{2.5}$ to become $CaFeO_3$. The reason why this works is that $KClO_4$ when heated over some temperature, decomposes into KCl and oxygen. This temperature depends slightly on the pressure applied and at 4GPa, it is approximately 550°C. Precisely speaking, the following reaction occurs:

$$KClO_4(solid) \xrightarrow{\sim 550^o C} KCl(solid) + 2O_2(gas).$$

Since annealing occurs at much higher temperature (table 4.3) we can expect that all $KClO_4$ decomposes and then we have oxygen gas as the only "candidate" for diffusion through ZrO_2 barrier which is intact at this temperature and serves as a protection of $CaFeO_{2.5}$ from contamination with K or Cl. (ZrO_2 is chosen because it is stable up to 2400^0C, it is chemically inert and it has high fracture toughness and high hardness.) On the other hand the annealing conditions are such that $CaFeO_{2.5}$ remains in the crystalline state since it melts at around 1454^oC. Later it will be shown that there exist three experimental proofs that the oxygen enrichment of our samples was successful but let's first say few words about our starting material, $CaFeO_{2.5}$ single crystal. $CaFeO_{2.5}$ (or equivalently $Ca_2Fe_2O_5$) has a brownmillerite structure. It belongs, at room temperature, to the orthorhombic space group P_{cmn} (D_{2h}^{16}; 62) with cell parameters a=5.5946Å, b=14.8273Å and c=5.4307Å [BeErHu]. The structure consists of alternating layers of FeO_6 octahedra and FeO_4 tetrahedra that are elongated along the b axis, with O(2) as a link between the two layers. Above approximately 700^oC the crystal structure changes such that it belongs to the space group I_{cmm} (D_{2h}^{28}; 74) which is also orthorhombic. Although there is a change of crystal structure, the unit cell parameters vary linearly and continuously with temperature, suggesting a second order phase transition. The $Ca_2Fe_2O_5$ single crystals for our experiments were grown by A. Maljuk and the growth was described in [MaStLi]. $Ca_2Fe_2O_5$ single crystal was grown by floating zone method, using a four-mirror type infrared image furnace equipped with four 500W halogen lamps as a heat source. The obtained single crystal had cylindrical shape, with length of 4cm and was therefore cut into small disks to match our high pressure annealing apparatus. The growth direction (i.e. the axis of the cylinder) was found to lie close to the [0 1 4] axis. Powder X-ray diffraction showed no impurity phases and the X-ray rocking curve had full width at half maximum of only 0.065^o indicating that the crystal was of good quality. (Also one has to mention that our Laue X-ray diffraction photos showed plenty of clear spots without any smearing which also goes in favor of the statement that the $Ca_2Fe_2O_5$ single crystals were good.) From the thermo-gravimetric method (TG) the oxygen content was determined to be X=4.96±0.04 for the formula $Ca_2Fe_2O_X$.

Now let's go back to the sample preparation. One can ask the natural question, how do we know that the oxygen enrichment was successful? In order to prove this we have performed a series of experiments on annealed samples. First among them was powder X-ray diffraction. Samples #1 and #2 (table 4.3) were taken out of the cup and then ground and then the two capillaries were filled, the first with sample #1 and the second with sample #2 powder. Then we compared the result with the diffractogram calculated for the case of $CaFeO_3$. The result is shown in the figure 4.10:

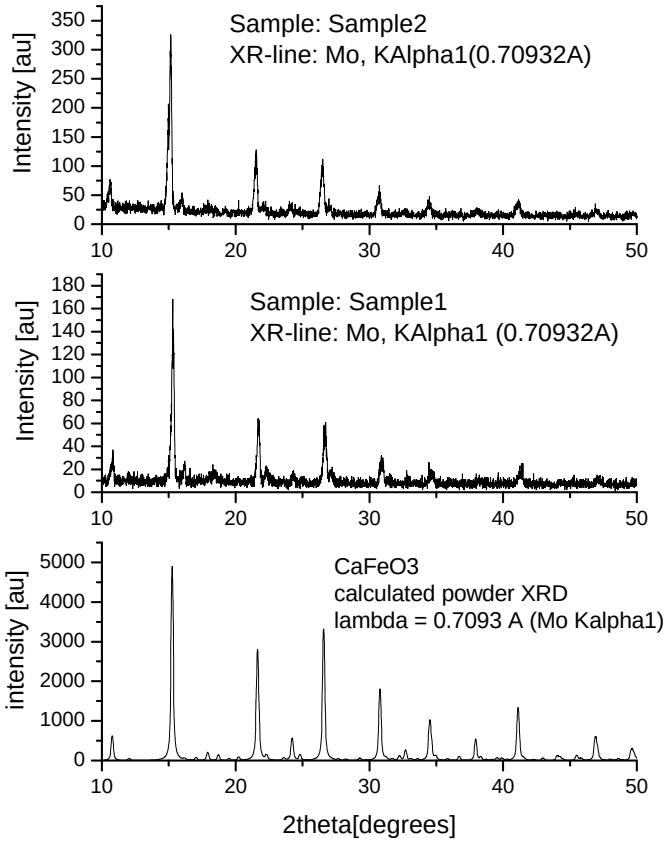

Figure 4.10: Powder X-ray diffraction pattern for the sample#2 (up), sample#1 (middle) and calculated for $CaFeO_3$ (bottom) at room temperature.

Room temperature X-ray powder diffraction data were collected on a Stoe Stadi-P Powder Diffractometer with Johannson Ge-(111) Monochromator. Counting time was 2 hours of Mo-Kalpha1 radiation (wavelength λ=0.70932Å) and the scattering angles were measured with a step size of 0.01^o. The powder samples were placed in the lithiumborate glass capillaries (Hilgenberg glass No. 50) with the diameter of 0.30mm. The capillaries were rotated around their axes in order to "increase randomness" of small crystallites orientations within the capillary. The calculated diffraction pattern for $CaFeO_3$ at room temperature (figure 4.10 bottom) was obtained by use of the program Atoms. From figure 4.10 we can see that the agreement between the measured and calculated diffraction patterns is very good. Both the peaks positions and their relative intensities match well with these expected for $CaFeO_3$ at room temperature. Also diffraction patterns between sample#1 and sample#2 are very similar. From table 4.3 we can see that the only difference between annealing conditions of those two samples is that sample#1 is annealed at the temperature that is 75^oC higher than the temperature of annealing for sample#2. Does this small difference influence our measured data? If one looks carefully at the figure 4.10 one can see that the peak at approximately 15° (the most intense peak of diffraction pattern shown) exhibits a small splitting for sample#2, while for sample#1 this splitting vanishes and the peak looks more similar to that expected for $CaFeO_3$ (bottom of

the figure 4.10). One can connect this effect with assumption that due to the difference in annealing temperature, oxygen deficiency is bigger in sample#2 and then oxygen vacancies can produce more lattice distortions, which would then lead to the splitting of this peak. The observed agreement between the measured and calculated patterns is one of the proofs that the oxygen enrichment was successful.

The next experiment which was done in order to see whether the oxygen enrichment was successful was to measure the temperature dependence of the magnetic moment of the sample before and after annealing. Those measurements were performed with a Physical Properties Measurement System (PPMS, Quantum Design, model 6000), in field cooling and subsequent field heating runs with an applied field of 1T (or equivalently 10000Oe). The results of the measurements are shown in figure 4.11. From this figure we can see that before annealing (figure 4.11 up) our starting material $Ca_2Fe_2O_5$ has two magnetic transitions. After annealing (figure 4.11 bottom) the magnetization curve looks completely different than before annealing, and shows an antiferromagnetic transition at around 120K, similar to that found in the literature (figure 4.3).

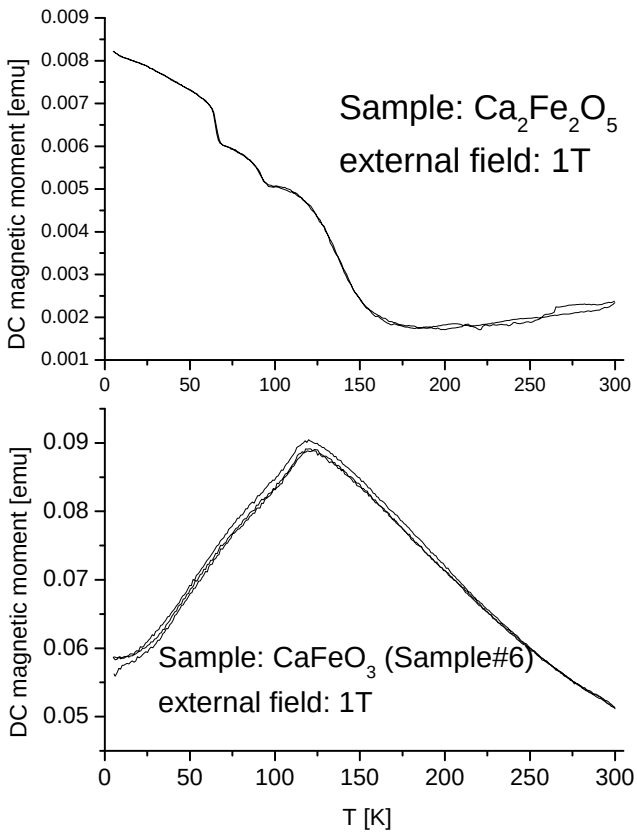

Figure 4.11: Temperature dependence of the magnetic moment of the sample before (top) and after (bottom) annealing.

Let's now extract the value of the spin of Fe ion in $CaFeO_3$ at room temperature from the temperature dependence of the magnetic moment of the sample (figure 4.11 bottom). For this we need, among other things, the number of moles in the sample. If we start from dimensions of the sample which are described in the beginning of section 4.2, we can see that the volume of the sample is

$$V = \left(\frac{d}{2}\right)^2 \pi h = \left(\frac{3.5mm}{2}\right)^2 \pi 1.5mm = 14.43mm^3 = 0.01443cm^3 .$$

Now, since the density of the sample (which was calculated earlier) is 4.46gr/(cm^3) we have the mass of the sample

$$m = \rho V = 0.064gr .$$

Since the molar mass of the $CaFeO_3$ is (also calculated earlier) M=143.927gr/mol we have for the number of moles

$$N_m = \frac{m}{M} = 4.47 \cdot 10^{-4} mol .$$

If we now divide value of magnetic moment of the sample with number of moles in the sample and with value of external magnetic field in Oersted (Oe) we get the molar magnetic susceptibility χ_m. Here we will use the following formula for the temperature dependence of χ_m (Curie law for paramagnet):

$$\chi_m = \frac{C_m}{T} , \qquad (4.1)$$

where T is temperature and C_m is a constant. It is important to note that although we have divided magnetic moment of the sample (unit: emu) with the number of moles (unit: mol) and with applied magnetic field (unit: Oersted) to get the molar magnetic susceptibility the unit of this susceptibility is not emu/(molOe) but only emu/mol. For some reasons people do not write unit Oe. From this it follows that the constant C_m has the following units: (emuK)/mol. Another important issue is that the formula 4.1 is valid for paramagnet. Our sample can be approximated by paramagnet only for temperatures which are higher enough then the Neel temperature but then the difference between measured temperature and Neel temperature has to enter into 4.1 instead of T. In other words our sample above its Neel temperature is described by the curve which is the curve 4.1 "shifted to the right" for Neel temperature. No matter of that, the slope of the curve remains the same. If we now plot one over molar magnetic susceptibility versus temperature, the slope of this curve is reciprocal of C_m. So from our data it follows:

the slope of the curve=0.28mol/(emuK).

From this it follows that the constant C_m is:

$$C_m = \frac{1}{0.28}\frac{emu \cdot K}{mol} = 3.57\frac{emu \cdot K}{mol}.$$

When C_m is given in emuK/mol then we can use the following formula for so called "effective Bohr magneton number" p_{eff} [McElf]:

$$p_{eff} = 2.82 \cdot \sqrt{C_m} \tag{4.2}$$

p_{eff} is then given in units of Bohr magneton μ_B. Formulae 4.1 and 4.2 will be derived latter. In this place one has to say that p_{eff} is given by the following formula [Ja52]:

$$p_{eff} = g \cdot \sqrt{J(J+1)} \cdot \mu_B, \tag{4.3}$$

where g (Lande factor) is equal to:

$$g = \frac{3}{2} + \frac{1}{2} \cdot \frac{S(S+1) - L(L+1)}{J(J+1)}. \tag{4.4}$$

Here S is total spin of the ion, L total orbital angular momentum of the ion and $\vec{J} = \vec{L} + \vec{S}$ is total angular momentum of the ion. Now let's go back to our calculation. We have determined the constant C_m to be 3.57emuK/mol. From formula 4.2 we have p_{eff} to be:

$$p_{eff} = 2.82 \cdot \sqrt{3.57} \cdot \mu_B = 5.33\mu_B.$$

On the other hand the eigenstates of the Fe ion in $CaFeO_3$ are non degenerate (this was shown in the Appendix A). In this case L=0 (this will also be shown latter) so that J=S and g=2. From all this and formula 4.3 follows:

$$5.33 = 2 \cdot \sqrt{S(S+1)}.$$

If we now take square of this equation we get the following quadratic equation:

$$S^2 + S - 7.1 = 0,$$

with the

$$S = \frac{-1 + \sqrt{1 + 4 \cdot 7.1}}{2} \approx 2.2$$

as the only positive solution. So finally, we have got from our magnetization measurements that at 300K the total angular momentum of Fe-ion (which is, because of L=0, equal to the total spin of the Fe-ion) is S=2.2 which is in good agreement with the

value estimated from Mössbauer measurements and with the value estimated from energy diagrams (high spin state): S=2.

Let's now show how we can obtain formulae 4.1, 4.2 and 4.3. For this purpose we can consider N noninteracting, equal ions, each with magnetic moment $\vec{\mu} = g\vec{J}\mu_B$ in the homogenous external magnetic field H (g is the Lande factor given by the formula 4.4 and μ_B is, as before, Bohr magneton. J is total angular momentum of the ion). By applying standard methods of statistical physics we get for the temperature dependence of the magnetization along z axis (direction of the magnetic field) of this system:

$$m_z = Ng\mu_B\left[(J+\frac{1}{2})cth\left((J+\frac{1}{2})\frac{g\mu_B H}{k_B T}\right)-\frac{1}{2}cth\left(\frac{g\mu_B H}{2k_B T}\right)\right].$$

Let's now consider the case:

$$x \overset{def}{=} \frac{g\mu_B H}{k_B T}; |x| << 1.$$

the previous formula can be approximated to give:

$$m_z = N\frac{(g\mu_B)^2}{3}\frac{J(J+1)}{k_B T}H \text{ for } \left|\frac{g\mu_B H}{k_B T}\right| << 1 \qquad (4.5).$$

To get the molar magnetic susceptibility χ_m we have to divide m_z with number of moles in the system (this is equal to N/N_A where N_A is Avogadro's number) and with magnetic field H. In this way we get:

$$\chi_m = \frac{N_A}{3k_B}\frac{(g\mu_B)^2 J(J+1)}{T} \text{ for } \left|\frac{g\mu_B H}{k_B T}\right| << 1,$$

which is the same as formula 4.1 with the constant C_m equal to:

$$C_m = \frac{N_A}{3k_B}p_{eff}^2 \text{ where } p_{eff} \overset{def}{=} g\mu_B\sqrt{J(J+1)}.$$

In this way we have proved formulae 4.1 and 4.3. In order to get formula 4.2 we have to rearrange previous equalities to get:

$$g\sqrt{J(J+1)} = \sqrt{\frac{3k_B}{N_A\mu_B^2}}\cdot\sqrt{C_m}.$$

Since Boltzmann constant is equal to k_B=1.3806505x10^{-23}J/K, Avogadro's number is equal to N_A=6.022x10^{23}1/mol, Bohr's magneton is equal to μ_B=9.274x10^{-24}J/T and since 1emu=10^{-3}Am^2, 1T=10^{4}Oe and 1J=1Am^{2}T=10^{7}emuOe we have

$$\sqrt{\frac{3k_B}{N_A\mu_B^2}} \approx 0.89426 \cdot \sqrt{\frac{mol}{K} \cdot \frac{T^2}{J}} = 0.89426 \cdot \sqrt{\frac{mol}{K} \cdot \frac{10^8 Oe^2}{10^7 emuOe}} \approx 2.83 \cdot \sqrt{\frac{mol \cdot Oe}{emu \cdot K}}$$

In this way we have proved the formula 4.2. At the end let's see weather the inequality from the equation 4.5 is fulfilled. In our experiment H=1T and temperature was around 300K so that:

$$\frac{g\mu_B H}{k_B T} = \frac{2 \cdot 9.274 \times 10^{-24} \frac{J}{T} \cdot 1T}{1.3806505 \times 10^{-23} \frac{J}{K} \cdot 300K} \approx 4.5 \times 10^{-3}$$

which means that it is indeed much less then one.

Now let's prove that when the energy level of an electron in the ion influenced by the crystal field is non degenerate then orbital angular momentum in that state is zero (this effect is called quenching of orbital angular momentum) [Jc177]. The Schrödinger equation of this system is:

$$\hat{H}\psi = E\psi$$

where $\hat{H} = -\frac{\hbar^2}{2m}\Delta + V(\vec{r})$ is a real operator (i.e. operator that doesn't contain complex numbers. It is assumed that the system is outside magnetic field.). If we take complex conjugation of the last equation we get, due to reality of Hamiltonian:

$$\hat{H}\psi^* = E\psi^*$$

which means that ψ and ψ^* belong to the same energy level. Since this level is non degenerate ψ and ψ^* are linearly dependent, i.e.:

$$\psi = a\psi^*$$

where a is a complex number. If we take complex conjugation of the last equation we get:

$$\psi^* = a^*\psi .$$

Now, from the last two equations we get:

$$\psi = a\psi^* = aa^*\psi = |a|^2\psi$$

from which it follows that modulus of a is one. That means $a = e^{i\varphi}$ where $\varphi \in [0,2\pi]$. From this it follows:

$$\psi = e^{i\varphi}\psi^*.$$

If we multiply the last equation with $e^{-i\frac{1}{2}\varphi}$ we get:

$$e^{-i\frac{1}{2}\varphi}\psi = e^{i\frac{1}{2}\varphi}\psi^*.$$

Now let's consider the function:

$$\phi \overset{def}{=} e^{-i\frac{1}{2}\varphi}\psi.$$

It is solution of our Schrödinger equation that corresponds to the energy level E and it satisfies the following equation:

$$\phi = \phi^*$$

which means that it is real. In this way we have proven that every non degenerate solution of our Schrödinger equation (that corresponds to real Hamiltonian) is up to a phase factor real. From this it follows that the diagonal matrix element of the angular momentum operator in the state described by the above mentioned function ψ:

$$\int_{R^3} \psi^*(\vec{r})\hat{\vec{L}}\psi(\vec{r})d^3\vec{r} = -i\hbar\int_{R^3}\phi(\vec{r})(\vec{r}\times\nabla)\phi(\vec{r})d^3\vec{r}$$

is purely imaginary. On the other hand, since the angular momentum operator is Hermit this matrix element should be real. That is possible only if it is zero. In this way we have proved that in non degenerate state of the electron that belongs to ion in the crystal field, the orbital angular momentum is quenched. With this we have completed analysis of magnetization measurements on $CaFeO_3$.

The last experiment which was done in order to see whether the oxygen enrichment was successful was a measurement of the temperature dependence of the resistance of the sample after annealing. This is shown in figure 4.12:

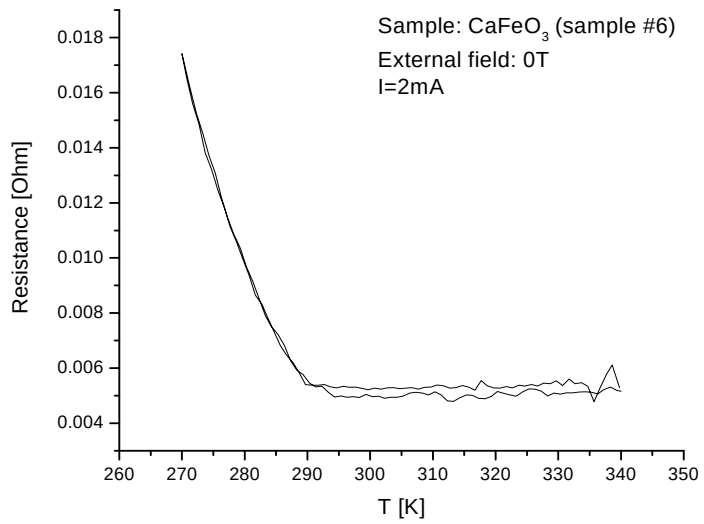

Figure 4.12: Temperature dependence of the resistance of the sample $CaFeO_3$ (sample#6) around charge ordering temperature.

The measurement was done in the same apparatus as the magnetization measurements. The driving current was kept constant at the value of 2mA and the corresponding change in the voltage was measured. The measurement was done without external magnetic field. We have used Chromium-Gold electrodes with thickness of 200Å for Chromium and 3000Å for Gold as a medium for contact. From figure 4.12 we can see that there is a clear metal to insulator transition exactly at T=290K, the temperature that agrees with the one taken from the literature (see figure 4.5). This is then another proof that the oxygen enrichment was successful. We have also measured the temperature dependence of the resistance of the sample for a wider range of temperatures and in the external magnetic field in order to see whether there is any magneto-resistance effect. The results will be shown in the next section where Raman measurements will also be shown.

4.3 RESISTIVITY, MAGNETORESISTANCE AND RAMAN MEASUREMENTS ON $CaFeO_3$

The temperature dependence of the resistance of $CaFeO_3$ with and without external magnetic field is shown in figure 4.13. Strictly speaking what we have measured is not the resistance but voltage to current ratio on different electrodes that are attached in the sample. This ratio has the same units as the resistance. The method applied is called four points method and below it will be shown more precisely how this was done. From figure 4.13 we can see that above charge ordering temperature the sample is metallic ($d\rho/dT>0$ where ρ is the resistivity) while below charge ordering temperature it is semiconducting ($d\rho/dT<0$) therefore having metal to semiconductor transition at this temperature. The behavior of the temperature dependence of the resistivity in the case of metals and semiconductors can be qualitatively explained in the following way. In metals electron-phonon interaction is dominant for the phenomenon of resistivity. With decreasing tem-

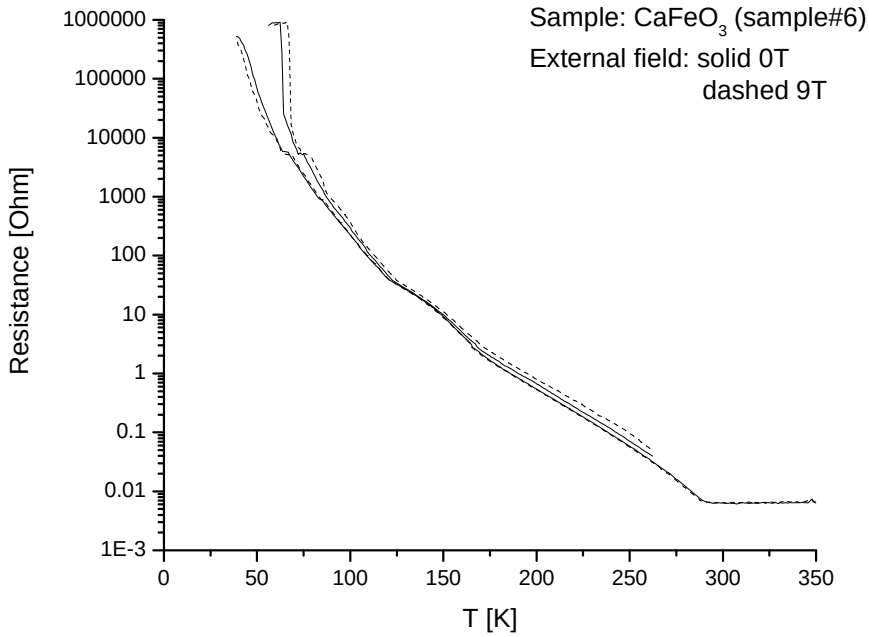

Figure 4.13: Temperature dependence of the resistance for $CaFeO_3$ without (solid line) and in the magnetic field (dashed line) of 9T.

perature the phonons are less excited and therefore resistivity is smaller so that $d\rho/dT>0$. This effect is negligible in semiconductors. Here with decreasing temperature the number of thermally excited electrons from valence to the conducting band is smaller therefore leading to smaller number of charge carriers. The conclusion is that resistivity of semiconductor is bigger when temperature is reduced which means $d\rho/dT<0$. From figure 4.13 we can see that there is no big difference on resistance when magnetic field is applied. The dashed curve (measurement at 9T) follows closely the solid curve (measurement at 0T). This means that the magnetoresistance effect (change of the resisitivity when the magnetic field is applied) is absent.

Next question could be how we can get the resistivity from the resistance? Since the sample had the shape of the disk as described at the beginning of the section 4.2 and four electrodes attached were of known dimensions we can only estimate resistivity. This can be done in the following way. In the figure 4.14 is shown schema of the positions of the electrodes on the sample surface as was in reality. The electrodes were placed on equal distance between each neighbors. The length of the electrodes was L=3mm. Sample's surface was first polished and then one layer of chromium was evaporated. Its thickness was 200Å. On top of the chromium layer, gold layer was evaporated. The thickness of gold layer was 3000Å. Outer two electrodes were used for the current excitation, while voltage was measured between two inner electrodes. The ratio between this voltage and exciting current is then called "resistance" and is shown in figure 4.13. External magnetic field was perpendicular to the plane of scheme presented in the figure

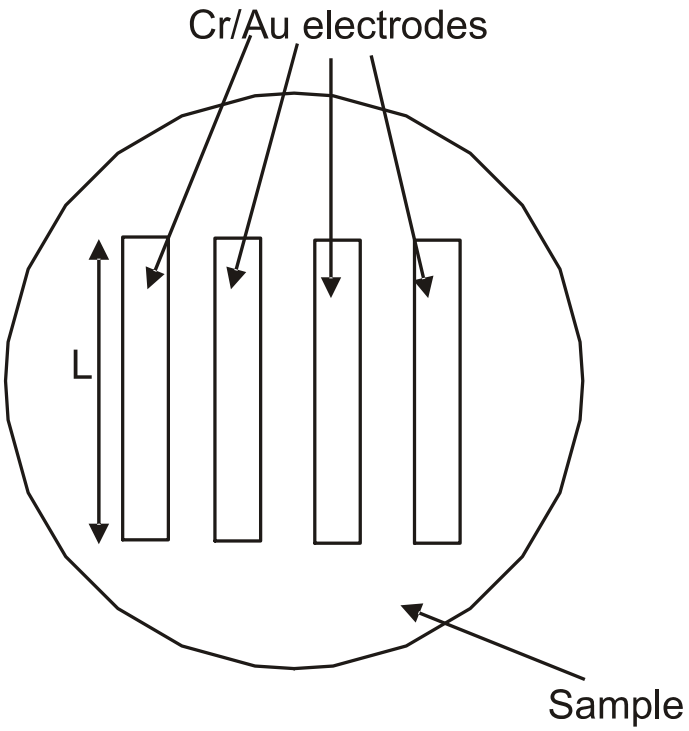

Figure 4.14: Position of the chromium-gold electrodes on the sample surface (top view).

4.14. After calculation for slightly different geometry we get the following formula for the resistivity from the "resistance" (for the derivation see the Appendix B):

$$\rho = \frac{V}{I} \cdot \frac{L\pi}{\ln 4} \qquad (4.6).$$

We can estimate from figure 4.13 that at 300K voltage current ratio is around 0.006Ohm. Since L was 3mm we have for the estimation of resistivity of $CaFeO_3$ at 300K the following value:

$$\rho = 6 \cdot 10^{-3}\,\Omega \frac{3mm\pi}{\ln 4} \approx 4m\Omega cm \text{ (estimation from our measurements).}$$

Let's compare it with the value other people obtained. For example we can use already cited paper of Kawasaki et al. From figure 4.5 we get (T=300K):

$$\rho \approx 8m\Omega cm \text{ (from Kawasaki et al.).}$$

We can see that the agreement is good in spite of all these approximations we have made.

The next experiment we have done was measurement of Raman spectra on $CaFeO_3$. Since there is a charge-ordering transition with change in crystal structure at 290K one could expect that this can be seen in Raman spectra (usually with reduction of

the crystal symmetry previously forbidden modes become allowed and this results in appearance of additional peaks in the Raman spectra below corresponding temperature. As was shown in the chapter 2 this was the case, for example, with $SrFeO_{2.85}$ compound). In favor of this assumption goes the classification of phonon modes at the gamma point for the crystal above and below the charge-ordering temperature. According to the results obtained the Appendix A we get for this classification (i.e. decomposition of the mechanical representation at the gamma point) the following:

$$\Gamma = \begin{cases} 8A_u + \overbrace{7A_g + 7B_{1g} + 5B_{2g} + 5B_{3g}}^{Raman-active} + \overbrace{7B_{1u} + 9B_{2u} + 9B_{3u}}^{IR-active} + \overbrace{B_{1u} + B_{2u} + B_{3u}}^{Acoustic}; T > 290K \\ \underbrace{12A_g + 12B_g}_{Raman-active} + \underbrace{17A_u + 16B_u}_{IR-active} + \underbrace{A_u + 2B_u}_{Acoustic}; T < 290K \end{cases}$$

We can see that above charge ordering transition temperature $CaFeO_3$ has 24 non degenerate Raman-active modes which is also the case below this temperature. This however doesn't mean that all 24 modes must appear in the experiment. The intensity of some of the modes can be low for some other reasons. This decomposition means only that those modes are not forbidden by symmetry. Next expectations can be that also electronic background will change, since charge-ordering transition means also change in the electronic states. Also it is interesting to check whether the magnetic transition at around 120K will influence the energy, intensity or line width of observed peaks. Surprisingly our measurements show opposite. The Raman spectra of $CaFeO_3$ for various temperatures ranging from 20K till the room temperature are shown in the figure 4.15. We can see from this figure that spectra below and above charge ordering temperature at 290K look the same. There is no change in electronic background and there are no additional peaks. On the other hand the number of peaks is much less than allowed by group theory. We can basically distinguish only two peaks, one around 260cm^{-1} and second around 735cm^{-1}. The peaks are of relatively low intensity (as compared to the starting material $Ca_2Fe_2O_5$, whose spectra will be shown later). Due to this low intensity we couldn't avoid interference on measured spectra from the glass of the cryostats window. Since laser before hitting the sample surface goes through a window of the cryostat the measured spectrum is always sum of Raman spectra from the sample and Raman spectra from the glass of this window. If the sample is strong Raman scatterer (i.e. if the signal from the sample is strong) then the signal from the glass of the cryostats window is negligible. However if the sample is weak Raman scatterer as in our case, then the signal from the glass will be clearly seen on the spectra. In the figure 4.15 we have subtracted the contribution from the cryostats window. This contribution can be determined by measuring the Raman spectra of empty cryostat. (The contribution from the cryostats window could be diminished by placing the sample deeper inside the cryostat, more further from the cryostats window. In that way, since sample is in the focus of collecting lens of the spectrometer, the cryostats window will be more away from the focus, therefore giving less signal. Unfortunately in this way the signal from the sample is also weaker because the accepting angle of the collecting lens is smaller. Therefore the choice of the distance between the sample and the cryostats window is a matter of compromise). In order to see weather the charge-ordering and magnetic transitions influence the line width, energy or intensity of observed peaks we have

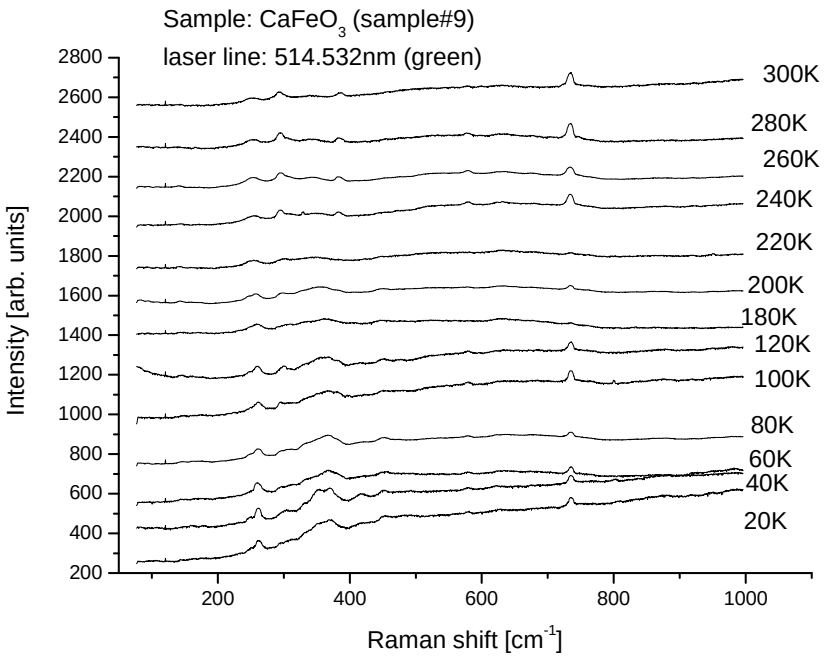

Figure 4.15: Raman spectra of $CaFeO_3$ for different temperatures. Spectra are shifted vertically for clarity. The contribution from the cryostats window is subtracted. Incident laser line was green (λ=514.532nm).

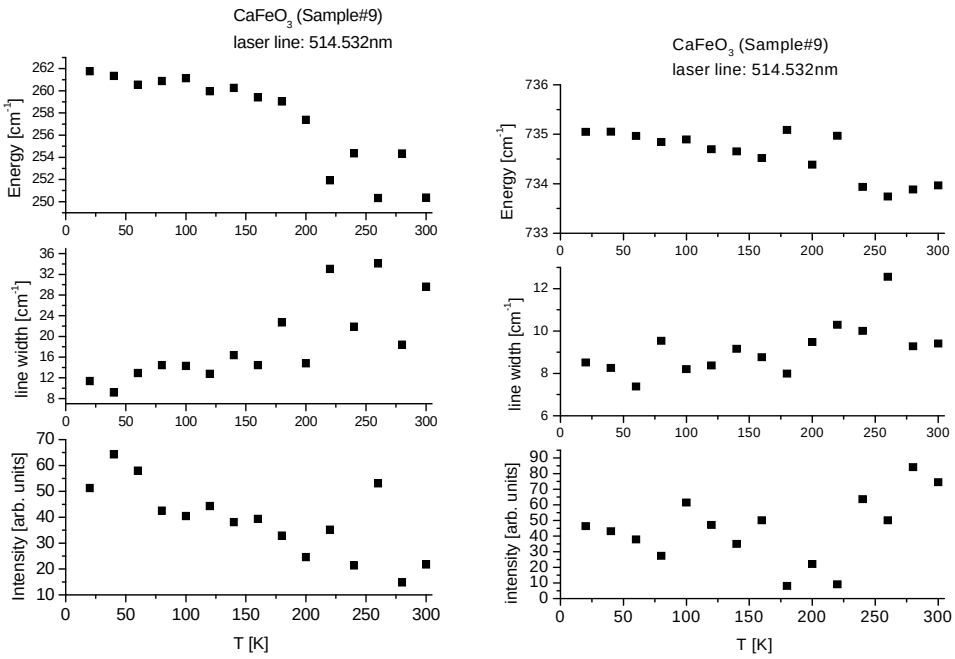

Figure 4.16: Temperature dependence of the energy, line width and intensity of observed peak at 262cm^{-1} (left) and 735cm^{-1} (right).

performed analysis of those parameters dependence on the temperature. The result is shown in the figure 4.16. From this figure one can see that at magnetic transition temperature (around 120K) and at charge-ordering temperature (290K) there are no significant changes in energy, line width or intensity of observed peaks. It is important to note that the intensity of the peak is usually very difficult to follow since it is sensitive not only to sample properties but also to the experimental conditions (for example positions and orientation of mirrors, lenses or plasma filter in the setup). That's why the absolute value of the intensity (unit: counts) has to be taken with caution.

The line widths of both peaks show usual behavior for phonons in the first order Raman scattering: monotonic increase in line width with increasing temperature. This behavior can be qualitatively explained in the following way: when the temperature is raised the more phonons are excited and therefore the phonon-phonon interaction due to anharmonic effects is stronger. This leads to opening of more channels for phonon decay so that the life time of the phonon is shorter. Since the phonon line width is inversely proportional to the phonon life time its value rises with increasing temperature.

How could we explain all those results of our Raman measurements? We can try to understand them in the following way: similarity between Raman spectra above and below charge ordering temperature could be explained if one remember the crystal structure and lattice parameters changes across this temperature (section 4.1). It was shown earlier that lattice parameters and the unit cell volume show small and continuous change across charge ordering temperature. On the other hand monoclinic angle is very close to 90°. For this reason the change in the crystal system (from orthorhombic to monoclinic) is small. This can also be said for the atomic positions. If one compares numbers in tables 4.1 and 4.2 one can see that most of them are very similar. Maybe this small change in the crystal structure is the reason why the spectra below and above charge ordering temperature look so similar.

The absence of any change in peak parameters at charge ordering and magnetic transition temperatures might be explained in the following way. Charge and magnetic order are closely connected with Fe ions (charge order is change in number of electrons in Fe ions while the magnetic order is ordering of magnetic moments on Fe ions). But Fe ions are fixed (they do not move) in Raman active phonons. This is because they are sitting on the center of inversion symmetry of the $CaFeO_3$ both above and below charge ordering transition. For this reason the observed peaks (if they are due to phonons in the first order Raman scattering) are involving movements of Ca or O ions which are insensitive to those changes since they are not involved. That's why the change in energy, line width and intensity of those peaks at charge and magnetic ordering temperatures is absent. (As a small digression let's see why if an ion is located in the center of inversion symmetry it must not move in Raman active phonon (in first order Raman scattering). Let's denote the shift of this ion from it's equilibrium position with the radius vector $\vec{r}$. It can be shown (not so easy) that in the crystal with inversion symmetry necessary (but not sufficient) condition for phonon to be active in the first order Raman scattering is that irreducible representation to which this phonon belongs must be "gerade" (i.e. to have suffix "g" in it's name). When we apply inversion symmetry to our observed ion its radius vector transforms to $-\vec{r}$. Since this transformation must be "gerade" it follows $\vec{r} = -\vec{r}$ and this is possible only if $\vec{r} = 0$. In this way we have proven that in the crystal with inversion symmetry ion that is positioned on it should stay on its equilibrium

position all the time if the phonon mode to which it belongs, belongs to the “gerade” irreducible representation. Since Raman active irreducible representations are always “gerade” this proves our initial statement).

And finally let’s try to explain why the peaks were of very low intensity. The reason for this could be find in slight deviation of $CaFeO_3$ crystal structure from ideal cubic perovskite. Since in ideal cubic perovskite there are no Raman active phonons (that was shown in the Appendix A) this could explain low intensity of observed peaks in our case.

At the end let’s note that in the literature there is only one paper on Raman scattering in $CaFeO_3$ published in [GhKaSe]. Their spectra, for the same laser line as in our case, are shown in figure 4.17 (from [GhKaSe]). We can see that their result is completely different than our. They have observed eight peaks and have done lattice dynamics calculations in order to assign them. According to their paper first five peaks are various movements of oxygen ions while Ca and Fe ions remain still. The remaining three peaks are due to second order Raman scattering. We can see that as the only similarity to our result there is no difference in spectra below and above charge ordering transition. In order to see weather our (or their) measured spectra are maybe due to some remainings of the initial material we have performed measurement of Raman spectra on $Ca_2Fe_2O_5$ at various temperatures. The result is shown in the figure 4.18.

.

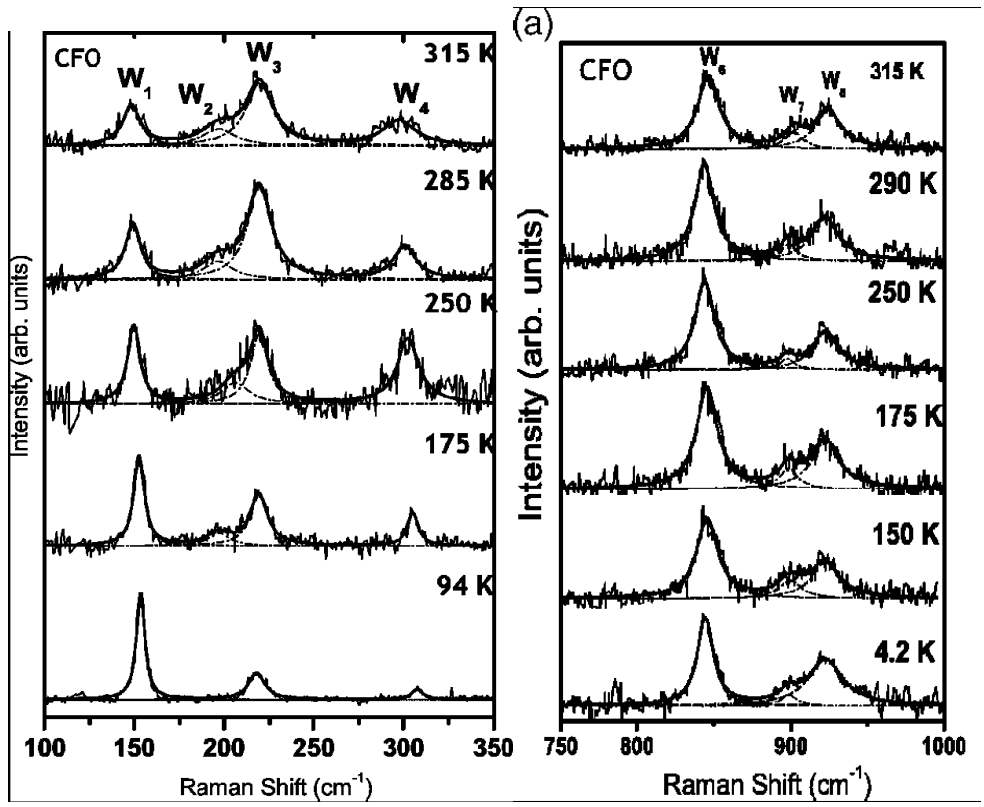

Figure 4.17: Raman spectra of $CaFeO_3$ according to Ghosh et al (from [GhKaSe]).

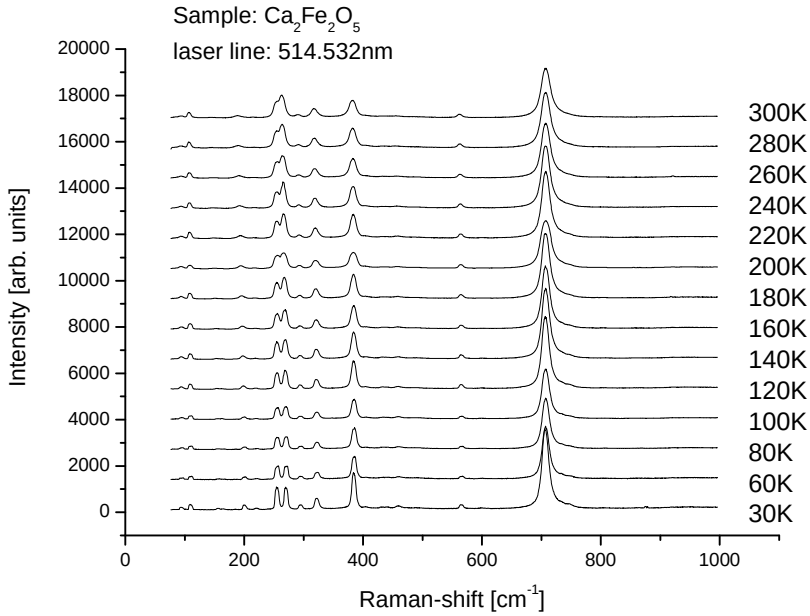

Figure 4.18: Raman spectra of $Ca_2Fe_2O_5$ (λ=514.532nm).

Careful analysis of the positions of observed peaks gives that there is no similarity between our results on $CaFeO_3$, their results and our results on $Ca_2Fe_2O_5$. Therefore measured spectra on $CaFeO_3$ are not due to the remaining phase of starting material. Next what could be checked is Raman spectra of compounds that might appear in the process of sample preparation. Fortunately, for all those compounds Raman spectra already exist in the literature. In that way it has been shown that Raman spectra of $KClO_4$ (from [ToPoPo]), ZrO_2 (from [IshSak]), $CaCO_3$ (from [BeKuUb] and [NicEll]), α-Fe_2O_3 (from [MaMeHu], [AdaHar], [HarAda], [MaBaMe] and [TaFuKo]), magnetite Fe_3O_4 (from [SheLaz1], [SheLaz2], [GaTaRo] and [GuSoMe]) and CaO ([Ke] and [KeMaTo]) don't show any similarity with measured spectra of $CaFeO_3$. Therefore the possibility that measured spectra of $CaFeO_3$ come from some impurity or additional phase is ruled out and the discrepancy between our results and results from Ghosh et al remains an open question.

5. CONCLUSIONS AND OUTLOOK

We have examined single crystals of $SrFeO_{3-\delta}$, $Sr_3Fe_2O_{7-\delta}$ and $CaFeO_3$, compounds that contain iron in the oxidation state +4 which is isoelectronic with the Mn^{3+} ion in $LaMnO_3$, the material that shows the giant magnetoresistance effect when doped with calcium or strontium.

$SrFeO_{3-\delta}$ is non stoichiometric compound which has four phases: cubic (for δ=0), tetragonal (for δ=0.125), orthorhombic (for δ=0.25) and brownmillerite (for δ=0.5). For other values of δ the system is phase mixture. We have measured Raman spectra of cubic phase (obtained by annealing at 5kbar pressure) at temperatures between 30K and 300K. The spectra show no modes as expected from symmetry considerations. This indicates the quality of our sample and is in agreement with earlier investigations where no changes of crystal structure in this temperature range are reported. We have also obtained single crystals of cubic phase by annealing at 40kbar pressure using $SrFeO_{2.8}$ single crystal as a starting material and $KClO_4$ as an oxygen source. Comparison of magnetization curves for the sample before and after annealing indicates that the oxygen enrichment was successful. Comparison of Möβbauer spectra of this sample and the sample annealed at 5kbar shows that the former is more close to the ideal composition. The same conclusion follows from the magnetization curve. In addition to experiments we have performed lattice dynamics calculations in order to assign modes obtained in infra-red measurements. All three observed frequencies are accurately reproduced. Every frequency is triply degenerate, the lowest one corresponds to the out of phase movement of strontium ions from one side and the iron and oxygen ions on the other, the next one corresponds to the out of phase movements of iron and oxygen ions (with negligible movements of strontium ions) while the highest observed mode corresponds to the movements of oxygen ions only (with negligible motions of strontium and iron ions). The only optically silent, triply degenerate mode could be found (apart from its frequency) directly from the symmetry arguments. In this mode iron and strontium motions are forbidden by symmetry. This result also came out of calculation giving agreement between numerical solution and the one obtained analytically by group projector method. The topic of future work could be measurements of infra-red spectra of different samples of the cubic phase where the content of certain isotopes of strontium, iron or oxygen is known. The eventually observed shifts in frequencies of those modes could show if our assignment was correct. We have measured Raman spectra of tetragonal phase for temperature range 13K to 300K. Spectra clearly show additional modes below 70K, the

temperature that corresponds to the charge ordering transition reported in the literature. This is another experimental proof of crystallographic transition in this compound. The topic of future work could be experimental determination of the low temperature crystal structure as well as the magnetic structure of this compound using neutron scattering experiments. We have measured Raman spectra of the orthorhombic phase for the temperature range 6K to 475K. The sample was polycrystalline. In contrast to the tetragonal phase the spectra are similar over the whole temperature range. This is in agreement with the fact that no structural change is reported for these temperatures. In order to assign observed modes future experiments could be done on single crystalline samples, with polarization analysis. After this the lattice dynamics calculations could be performed.

In non-stoichiometric compound $Sr_3Fe_2O_{7-\delta}$ the oxygen content can vary in the range $0 \leq \delta \leq 1$. In contrast to the $SrFeO_{3-\delta}$ where oxygen vacancies are ordered, in this compound similar effect was not reported. We have measured magnetic moment of this compound along all three crystallographic axes. The magnetization in the ab-plane is isotropic as expected from the symmetry. Our neutron scattering experiments show that this material has helical structure with the helix vector parallel to the a-direction. Future experiments by neutron scattering could determine to which type of helix this compound belongs. We have measured resistivity and magnetoresistance of this material in the ab-plane. Both curves show change in slope at the magnetic transition temperature. The magnetoresistance remains within 5% in agreement with the results published thus far. Infra-red measurements show that the material is insulating along the c-axis. This could than explain failure of the Montgomery method which we applied first. We have measured Raman spectra on single crystal of this compound in the temperature range 6K to 450K with incident photon wave vector perpendicular and parallel to the c-axis. The first case allowed us to observe phonons of A_{1g} and E_g symmetry, the second those of A_{1g} and B_{1g}. In the first case we have observed 8 modes below 300K. In order to assign the observed modes we have performed lattice dynamics calculations. The optimal input parameters were achieved because the relaxed structure differed only slightly from the one reported in the literature. All 33 modes are presented. The doubly degenerate modes involve movements of ions perpendicular to the c-axis while non degenerate involve movements of ions along c-axis. In order to determine symmetry of observed modes we have performed polarization analysis. It turned out that all 8 peaks were of A_{1g} symmetry. This is in contradiction with the fact that the maximum number of A_{1g} modes that can be observed for this structure is 4. Future work should provide information whether the actual crystal structure differs from the one reported in the literature.

Similar to the case of cubic $SrFeO_3$ we have obtained $CaFeO_3$ single crystals by high pressure annealing of $CaFeO_{2.5}$ single crystals with $KClO_4$ as an oxygen source. In order to test whether the oxygen enrichment was successful we have measured powder X-ray diffraction and have found that the diffractogram of the annealed samples match the one expected for the crystal structure of $CaFeO_3$ published in the literature. Positive results came out of magnetization measurements and measurements of resistivity across the charge-ordering transition too. These were three experimental proofs that the oxygen enrichment was successful. The estimated value of the magnetic moment of Fe-ions agreed with the one reported. We have measured the resistivity and magnetoresistance of this material and have found that the magnetoresistance effect was absent. We have

estimated the resistivity of the sample at room temperature from voltage-current ratio and have found reasonable agreement with the one published in the literature. In addition we have measured Raman spectra of this material for the temperature range 20K to 300K. The spectra look similar through charge ordering and differ with the only one report that is in the literature. Future work should decide which spectra are correct.

APPENDIX A. GROUP-THEORETICAL CONSIDERATIONS RELATED TO THIS WORK

In this chapter consequences inferred from the group theory for the materials properties will be shown. These include splitting of d-orbitals in the crystal field of a given symmetry, consequences of crystal symmetry for the magnetic susceptibility and electric resistivity tensors, classification of phonon modes of a crystal, prediction of their Infra-Red and Raman activities and prediction of the "shape" of the Raman tensor for a given phonon. It is assumed that the reader of these pages is familiar with basic concepts of group theory and theory of vector spaces.

A.1 SPLITTING OF d-ORBITALS OF THE Fe ION IN A CRYSTAL FIELD OF A GIVEN SYMMETRY

In this work all of the investigated materials have one thing in common: they contain the Fe ions which in a free state would have electronic configuration of the noble gas Argon (Ar) plus a few electrons in the 3d orbitals which are therefore partially filled. In the crystal we seek a solution of a Schrödinger equation for one electron as linear combinations of those partially filled 3d-orbitals. The symmetry of the appropriate crystal field (which is the symmetry of a site which the Fe-ion occupies) can help us in finding this solution in a way that will be described below.

Let the group of the symmetry elements belonging to a given site be denoted with $\underline{G}$. This is a point group which means that it contains only proper and improper rotations leaving one point of the space invariant (that is the position of the Fe ion). The origin of a Descartes system of coordinates is on the center of the Fe ion. The potential energy $V(\vec{r})$ of an electron in the crystal has the property that it remains invariant under the transformations from $\underline{G}$, which means [Af4]:

$$(\forall \hat{g} \in \underline{G}) V(\hat{g}\vec{r}) = V(\vec{r}) \qquad \text{A.1.1.}$$

Let now $\psi(\vec{r})$ be a solution of the one-electron Schrödinger equation with energy E:

$$-\frac{\hbar^2}{2m}\Delta\psi(\vec{r})+V(\vec{r})\psi(\vec{r})=E\psi(\vec{r}) \qquad \text{A.1.2,}$$

the function $\psi(\hat{g}^{-1}\vec{r})$ is also a solution of the same equation with the same energy E. To see this let us in previous equation insert the change of variables:

$$\vec{r}\overset{def}{=}\hat{g}^{-1}\vec{r}' \qquad \text{A.1.3}$$

where $\hat{g}$ is any element from G. (Since G is a group, $\hat{g}^{-1}$ is also an element of a G). Then it follows:

$$\frac{\partial}{\partial\vec{r}}=\hat{g}\frac{\partial}{\partial\vec{r}'} \qquad \text{A.1.4}$$

and: $\Delta=(\frac{\partial}{\partial\vec{r}},\frac{\partial}{\partial\vec{r}})=(\hat{g}\frac{\partial}{\partial\vec{r}'},\hat{g}\frac{\partial}{\partial\vec{r}'})=(\hat{g}^{+}\hat{g}\frac{\partial}{\partial\vec{r}'},\frac{\partial}{\partial\vec{r}'})=(\frac{\partial}{\partial\vec{r}'},\frac{\partial}{\partial\vec{r}'})=\Delta'$,

where (,) denotes scalar product and we use the fact that $(\forall\hat{g}\in\underline{G})\hat{g}^{+}=\hat{g}^{-1}$. From these considerations and from equation A.1.1 it follows:

$$-\frac{\hbar^2}{2m}\Delta'\psi(\hat{g}^{-1}\vec{r}')+V(\vec{r}')\psi(\hat{g}^{-1}\vec{r}')=E\psi(\hat{g}^{-1}\vec{r}') \qquad \text{A.1.5}$$

which is what had to be proved.

In order to obtain solutions of the Schrödinger equation A.1.2 as a linear combinations of five 3d-orbitals of the Fe ion it is important to recall that “3d-orbitals” means main quantum number n=3 and orbital quantum number l=2 so that we are dealing with 5 eigenfunctions of the problem of hydrogen like ion:

$$\psi_{32m}(r,\theta,\varphi)=R_{32}(r)\mathrm{Y}_2^m(\theta,\varphi);m\in\{-2,-1,0,1,2\} \qquad \text{A.1.6.}$$

Here $R_{32}(r)=\frac{2}{81}\sqrt{\frac{2}{15}}\left(\frac{Z}{a_0}\right)^{\frac{7}{2}}\cdot r^2\cdot e^{-\frac{Zr}{3a_0}}$ is radial wave function of hydrogen-like ion (Z is number of protons in the nucleus, $a_0=\frac{4\pi\varepsilon_0\hbar^2}{m_e e^2}\approx 5\cdot 10^{-11}m$ is Bohr radius) that corresponds to n=3 and l=2 quantum numbers, while $\mathrm{Y}_2^m(\theta,\varphi)$ denotes spherical harmonics. We have also:

$$\mathrm{Y}_2^{-2}(\theta,\varphi)=\frac{1}{4}\sqrt{\frac{15}{2\pi}}\sin^2\theta\cdot e^{-2i\varphi}$$

$$\mathrm{Y}_2^{-1}(\theta,\varphi)=\frac{1}{2}\sqrt{\frac{15}{2\pi}}\sin\theta\cdot\cos\theta\cdot e^{-i\varphi}$$

$$\mathrm{Y}_2^{0}(\theta,\varphi)=\frac{1}{4}\sqrt{\frac{5}{\pi}}(3\cos^2\theta-1) \qquad \text{A.1.7.}$$

$$\mathrm{Y}_2^{1}(\theta,\varphi)=-\frac{1}{2}\sqrt{\frac{15}{2\pi}}\sin\theta\cdot\cos\theta\cdot e^{i\varphi}$$

$$\mathrm{Y}_2^{2}(\theta,\varphi)=\frac{1}{4}\sqrt{\frac{15}{2\pi}}\sin^2\theta\cdot e^{2i\varphi}$$

On the other hand for every $\hat{g}\in\underline{G}$ and for every $m\in\{-2,-1,0,1,2\}$ function $\psi_{32m}(\hat{g}^{-1}\vec{r})$ is a linear combination of functions $\psi_{32-2}(\vec{r}),\psi_{32-1}(\vec{r})$, $\psi_{320}(\vec{r})$, $\psi_{321}(\vec{r})$ and $\psi_{322}(\vec{r})$ (i.e. functions from A.1.6). This can be proven in the following way: $(\forall m\in\{-2,-1,0,1,2\})\hat{\vec{L}}^2\psi_{32m}(\vec{r})=2\cdot 3\cdot\hbar^2\psi_{32m}(\vec{r})$, where $\hat{\vec{L}}=\hat{\vec{r}}\times\hat{\vec{p}}$ is operator of the angular momentum. This equation states that $\psi_{32m}(\vec{r})$ are eigenfunctions of the angular momentum that correspond to l=2. The function $\psi_{32m}(\hat{g}^{-1}\vec{r})$ is also eigenfunction of angular momentum that correspond to the same l. Proof is the same as in the case of derivation of the equation A.1.5. By making change of variables A.1.3 and recalling that

$$\hat{\vec{L}}^2=-\hbar^2r^2\Delta+\hbar^2\frac{\partial}{\partial r}r^2\frac{\partial}{\partial r}=-\hbar^2r'^2\Delta'+\hbar^2\frac{\partial}{\partial r'}r'^2\frac{\partial}{\partial r'}=\hat{\vec{L}}'^2$$

we have $(\forall m\in\{-2,-1,0,1,2\})\hat{\vec{L}}'^2\psi_{32m}(\hat{g}^{-1}\vec{r}')=2\cdot 3\cdot\hbar^2\psi_{32m}(\hat{g}^{-1}\vec{r}')$ which proves the statement (by transformation A.1.3, r^2 transforms to r'^2 (proof is the same as in case of Laplace operator in proof of equation A.1.5) so that r transforms to r' and $\frac{\partial}{\partial r}$ to $\frac{\partial}{\partial r'}$). Since functions $\psi_{32-2}(\vec{r}),\psi_{32-1}(\vec{r})$, $\psi_{320}(\vec{r})$, $\psi_{321}(\vec{r})$ and $\psi_{322}(\vec{r})$ make orthonormal basis in the space of functions that correspond to five times degenerate l=2 level so that $\psi_{32m}(\hat{g}^{-1}\vec{r})$ is linear combination of them, which is what had to be proved.

Previous argumentation allows us to introduce one representation of the group $\underline{G}$ that operates on the space of wave functions spanned over the functions $\psi_{32m}(\vec{r}), m\in\{-2,-1,0,1,2\}$ in the following way:

$$(\forall\hat{g}\in\underline{G})\hat{T}(\hat{g})\psi(\vec{r})\overset{def}{=}\psi(\hat{g}^{-1}\vec{r}) \qquad \text{A.1.8.}$$

This representation is five dimensional and in general reducible. Theorem that led to the equation A.1.5 means that subspace (denoted by V_E) of functions that corresponds to

some energy level E of the system described by equation A.1.2 (referring to a crystal) is invariant with respect to action of the representation T from equation A.1.8 ("invariant" means that every function $\psi(\hat{g}^{-1}\vec{r})$ from A.1.8 remains in V_E if the function $\psi(\vec{r})$ belong to it). On the other hand V_E is irreducible for the representation T ("irreducible" means that there doesn't exist a nontrivial (different from V_E and from the subspace made only of zero vector) subspace of V_E which is invariant with respect to T). The following assumption is crucial for the proof of the last statement: eigenfunctions that belong to different irreducible representations of the group G correspond to different energy levels (for example Landau, in his Quantum Mechanics says that opposite case would be improbable coincidence and then we are speaking of accidental degeneracy [Bd1a/3]). If V_E would be reducible for T than it could be decomposed into irreducible subspaces but then those subspaces would correspond to different energy levels which is in contradiction with the assumption that every member of V_E corresponds to one definite energy level E.

In this way we have proven that every wave function which is solution of the Schrödinger equation A.1.2 belongs to an irreducible representation of the group G which appears in the decomposition of the representation T defined by A.1.8. Degeneracy of the level is equal to the dimension of corresponding irreducible representation.

To summarize, in order to proceed towards solutions of the Schrödinger equation A.1.2 as a linear combinations of orbitals A.1.6 we first find the representation T by means of equation A.1.8, then find into which irreducible representations of the group G it decomposes and then by use of group projectors we find linear combinations of orbitals A.1.6 which belong to a given irreducible representation. In this way we have reduced the number of "candidates" for solution of the equation A.1.2, but the degeneracy of energy levels already comes out of the mentioned calculation. In the next chapters this consideration will be done for each investigated crystal separately.

Since operators of symmetry from the group G leave modulus of the radius vector r unchanged we will be mainly concerned with changes that formula A.1.8 induces on spherical harmonics from formulae A.1.7 (radial wave function $R_{32}(r)$ remains unchanged).

A.1.1 CASE OF $CaFeO_3$

Above the charge ordering transition (at 290K) the valence state of Fe is 4+ and it occupies the site 4b in the space group Pbnm (D_{2h}^{16}; 62). According to the International Tables For Crystallography Vol. A, this site has a symmetry C_i (or $\bar{1}$ in the International notation). This group consists of only 2 elements: identity $\hat{E}$ and inversion $\hat{i}$. Since this group is Abelian all irreducible representations are one dimensional so that table of characters and the table of irreducible representations coincide. Those are:

Table A.1.1.1: Characters (and IR) of the group C_i

C_i	$\hat{E}$	$\hat{i}$
A_g	1	1
A_u	1	-1

Now we have to find a representation from formula A.1.8. In this case every element of the group is its own inverse. Since the identity element doesn't change anything it follows:

$$\hat{T}(\hat{E}) = \begin{pmatrix} 1 & 0 & 0 & 0 & 0 \\ 0 & 1 & 0 & 0 & 0 \\ 0 & 0 & 1 & 0 & 0 \\ 0 & 0 & 0 & 1 & 0 \\ 0 & 0 & 0 & 0 & 1 \end{pmatrix}$$ i.e. it is unit matrix of dimension 5.

In the case of the inversion $\hat{i}$ it is interesting to note that spherical coordinates (r, θ, φ) change to (r, π-θ, φ+π) under the action of $\hat{i}^{-1} = \hat{i}$. For this reason we have:

$$\sin\theta \xrightarrow{\hat{i}} \sin(\pi - \theta) = \sin\theta$$
$$\cos\theta \xrightarrow{\hat{i}} \cos(\pi - \theta) = -\cos\theta$$
$$e^{\pm 2i\varphi} \xrightarrow{\hat{i}} e^{\pm 2i(\varphi+\pi)} = e^{\pm 2i\varphi}$$
$$e^{\pm i\varphi} \xrightarrow{\hat{i}} e^{\pm i(\varphi+\pi)} = -e^{\pm i\pi}$$

If we compare these formulae with definition of spherical harmonics (A.1.7) we can see that they remain unchanged under the inversion, i.e.:

$$\mathrm{Y}_2^m(\pi - \theta, \varphi + \pi) = \mathrm{Y}_2^m(\theta, \varphi); (\forall m \in \{-2, -1, 0, 1, 2\}).$$

For this reason $\hat{T}(\hat{i}) = \hat{T}(\hat{E})$, so that the table of characters (sum of diagonal elements of matrixes of the representation T) of the representation T is:

Table A.1.1.2: Characters of the representation T.

$\underline{C}_i$	$\hat{E}$	$\hat{i}$
χ_T	5	5

We can now decompose representation T into irreducible representations of the group $\underline{C}_i$. For that reason we use the formula:

$$m_j = \frac{1}{|\underline{G}|} \sum_{g \in \underline{G}} \chi_j^*(g) \cdot \chi(g),$$

where m_j is the number of times in which irreducible representation with character χ_j appears in the decomposition of representation with character χ. $|\underline{G}|$ is the number of elements of the group $\underline{G}$ (order of the group $\underline{G}$). From this it follows m=5 for the

irreducible representation A_g and m=0 for the irreducible representation A_u of the group $\underline{C}_i$ or:

$$\Gamma_T = 5A_g$$

We can now interpret this result as follows: five times degenerate (in free Fe ion) 3d level splits in the crystal $CaFeO_3$ into five non-degenerate energy levels (non-degenerate is because A_g irreducible representation is one dimensional). Corresponding wave functions are even ("gerade") with respect to inversion. In this case those statements are maximum what we can say about solution of Schrödinger equation A.1.2 only from symmetry considerations. Exact wave functions can not be obtained by group projectors technique because every linear combination of spherical harmonics A.1.7 is even with respect to inversion so that projector on the sub-space belonging to the $5A_g$ representations is unit matrix (of dimension five).

Below the charge ordering transition $2Fe^{4+} \rightarrow Fe^{3+} + Fe^{5+}$, ion Fe^{3+} occupies the site 2c while ion Fe^{5+} occupies the site 2d of the space group $P2_1/n$ (C_{2h}^5; 14). Site symmetry of both sites is again $\underline{C}_i$ like in the previous case so the above considerations apply in this case, with the same conclusions.

A.1.2 CASE OF $Sr_3Fe_2O_7$

In the $Sr_3Fe_2O_7$ the Fe ion occupies the site 4e in the space group I4/mmm (D_{4h}^{17}; 139). According to Mössbauer measurements it is in a mixed valence state 3+ and 5+ but neutron and X-rays measurement could refine only one site. The site symmetry is $\underline{C}_{4v}$ (or 4mm in the International notation). This group has 8 elements: identity ($\hat{E}$), axis of order 4 ($\hat{C}_4$), second and third powers of this axis ($\hat{C}_4^2$, $\hat{C}_4^3$) and four vertical planes containing axis of order 4 (if z-axis is along the four fold axis of symmetry and x and y axes are perpendicular to it and to each other, and if $\vec{x} \times \vec{y} = \vec{z}$ than these planes are denoted by $\hat{\sigma}_{xz}$ (contains axes x and z), $\hat{\sigma}_{yz}$ (contains axes y and z), $\hat{\sigma}_{d1}$ (contains axis z and diagonal passing through first and third quadrants of xy plane) and $\hat{\sigma}_{d2}$ (contains axis z and diagonal passing through second and fourth quadrants of xy plane)). Character table of $\underline{C}_{4v}$ is given in the following table [Af51]:

Table A.1.2.1: Character table of the group $\underline{C}_{4v}$

$\underline{C}_{4v}$	$\hat{E}$	$\hat{C}_4, \hat{C}_4^3$	$\hat{C}_4^2$	$\hat{\sigma}_{xz}, \hat{\sigma}_{yz}$	$\hat{\sigma}_{d1}, \hat{\sigma}_{d2}$
A_1	1	1	1	1	1
A_2	1	1	1	-1	-1
B_1	1	-1	1	1	-1
B_2	1	-1	1	-1	1
E	2	0	-2	0	0

and the table of irreducible representations is:

Table A.1.2.2: Irreducible representations of the group $\underline{C}_{4v}$.

$\underline{C}_{4v}$	$\hat{E}$	$\hat{C}_4$	$\hat{C}_4^2$	$\hat{C}_4^3$	$\hat{\sigma}_{xz}$	$\hat{\sigma}_{yz}$	$\hat{\sigma}_{d1}$	$\hat{\sigma}_{d2}$
A_1	1	1	1	1	1	1	1	1
A_2	1	1	1	1	-1	-1	-1	-1
B_1	1	-1	1	-1	1	1	-1	-1
B_2	1	-1	1	-1	-1	-1	1	1
E	$\begin{pmatrix} 1 & 0 \\ 0 & 1 \end{pmatrix}$	$\begin{pmatrix} -i & 0 \\ 0 & i \end{pmatrix}$	$\begin{pmatrix} -1 & 0 \\ 0 & -1 \end{pmatrix}$	$\begin{pmatrix} i & 0 \\ 0 & -i \end{pmatrix}$	$\begin{pmatrix} 0 & -1 \\ -1 & 0 \end{pmatrix}$	$\begin{pmatrix} 0 & 1 \\ 1 & 0 \end{pmatrix}$	$\begin{pmatrix} 0 & i \\ -i & 0 \end{pmatrix}$	$\begin{pmatrix} 0 & -i \\ i & 0 \end{pmatrix}$

Every plane of reflection is its own inverse element and the same holds for $\hat{E}$ and $\hat{C}_4^2$ while $\hat{C}_4^{-1} = \hat{C}_4^3$ and $\left(\hat{C}_4^3\right)^{-1} = \hat{C}_4$. Under the action of any of the elements of this group modulus of the radius vector r and angle θ of spherical coordinates remain unchanged. As usual to the identity element corresponds five-dimensional unit matrix. In order to find the representation T for other elements of $\underline{C}_{4v}$ it is interesting to note that spherical coordinates (r, θ, φ) change to (r, θ, φ+(π/2)) under the action of $\hat{C}_4$, to (r, θ, φ+π) under the action of $\hat{C}_4^2$, to (r, θ, φ+3(π/2)) under the action of $\hat{C}_4^3$, to (r, θ, 2π-φ) under the action of $\hat{\sigma}_{xz}$, to (r, θ, π-φ) under the action of $\hat{\sigma}_{yz}$, to (r, θ, (π/2)-φ) under the action of $\hat{\sigma}_{d1}$ and to (r, θ, (3π/2)-φ) under the action of $\hat{\sigma}_{d2}$. For the element $\hat{C}_4$ we have:

$$\psi_{32-2}(\hat{C}_4^{-1}\vec{r}) = \psi_{32-2}(\hat{C}_4^3\vec{r}) = \psi_{32-2}(r,\theta,\varphi+\frac{3\pi}{2}) = -\psi_{32-2}(\vec{r})$$

$$\psi_{32-1}(\hat{C}_4^{-1}\vec{r}) = \psi_{32-1}(\hat{C}_4^3\vec{r}) = \psi_{32-1}(r,\theta,\varphi+\frac{3\pi}{2}) = i\,\psi_{32-1}(\vec{r})$$

$$\psi_{320}(\hat{C}_4^{-1}\vec{r}) = \psi_{320}(\hat{C}_4^3\vec{r}) = \psi_{320}(r,\theta,\varphi+\frac{3\pi}{2}) = \psi_{320}(\vec{r})$$

$$\psi_{321}(\hat{C}_4^{-1}\vec{r}) = \psi_{321}(\hat{C}_4^3\vec{r}) = \psi_{321}(r,\theta,\varphi+\frac{3\pi}{2}) = -i\,\psi_{321}(\vec{r})$$

$$\psi_{322}(\hat{C}_4^{-1}\vec{r}) = \psi_{322}(\hat{C}_4^3\vec{r}) = \psi_{322}(r,\theta,\varphi+\frac{3\pi}{2}) = -\psi_{322}(\vec{r})$$

so that $\hat{T}(\hat{C}_4) = \begin{pmatrix} -1 & 0 & 0 & 0 & 0 \\ 0 & i & 0 & 0 & 0 \\ 0 & 0 & 1 & 0 & 0 \\ 0 & 0 & 0 & -i & 0 \\ 0 & 0 & 0 & 0 & -1 \end{pmatrix}$ in the basis $\{\psi_{32-2}(\vec{r}),\psi_{32-1}(\vec{r}),\psi_{320}(\vec{r}),\psi_{321}(\vec{r}),\psi_{322}(\vec{r})\}$.

For the element $\hat{C}_4^2$ we have $\hat{T}(\hat{C}_4^2) = \left(\hat{T}(\hat{C}_4)\right)^2$ so that $\hat{T}(\hat{C}_4^2) = \begin{pmatrix} 1 & 0 & 0 & 0 & 0 \\ 0 & -1 & 0 & 0 & 0 \\ 0 & 0 & 1 & 0 & 0 \\ 0 & 0 & 0 & -1 & 0 \\ 0 & 0 & 0 & 0 & 1 \end{pmatrix}$.

For the element $\hat{C}_4^3$ we have $\hat{T}(\hat{C}_4^3) = \hat{T}(\hat{C}_4 \cdot \hat{C}_4^2) = \hat{T}(\hat{C}_4) \cdot \hat{T}(\hat{C}_4^2)$ so that

$$\hat{T}(\hat{C}_4^3) = \begin{pmatrix} -1 & 0 & 0 & 0 & 0 \\ 0 & -i & 0 & 0 & 0 \\ 0 & 0 & 1 & 0 & 0 \\ 0 & 0 & 0 & i & 0 \\ 0 & 0 & 0 & 0 & -1 \end{pmatrix}.$$

For the element $\hat{\sigma}_{xz}$ we have

$$\begin{aligned}
\psi_{32-2}(\hat{\sigma}_{xz}^{-1}\vec{r}) &= \psi_{32-2}(\hat{\sigma}_{xz}\vec{r}) = \psi_{32-2}(r,\theta,2\pi-\varphi) = \psi_{322}(\vec{r}) \\
\psi_{32-1}(\hat{\sigma}_{xz}^{-1}\vec{r}) &= \psi_{32-1}(\hat{\sigma}_{xz}\vec{r}) = \psi_{32-1}(r,\theta,2\pi-\varphi) = -\psi_{321}(\vec{r}) \\
\psi_{320}(\hat{\sigma}_{xz}^{-1}\vec{r}) &= \psi_{320}(\hat{\sigma}_{xz}\vec{r}) = \psi_{320}(r,\theta,2\pi-\varphi) = \psi_{320}(\vec{r}) \\
\psi_{321}(\hat{\sigma}_{xz}^{-1}\vec{r}) &= \psi_{321}(\hat{\sigma}_{xz}\vec{r}) = \psi_{321}(r,\theta,2\pi-\varphi) = -\psi_{32-1}(\vec{r}) \\
\psi_{322}(\hat{\sigma}_{xz}^{-1}\vec{r}) &= \psi_{322}(\hat{\sigma}_{xz}\vec{r}) = \psi_{322}(r,\theta,2\pi-\varphi) = \psi_{32-2}(\vec{r})
\end{aligned}$$

so that $\hat{T}(\hat{\sigma}_{xz}) = \begin{pmatrix} 0 & 0 & 0 & 0 & 1 \\ 0 & 0 & 0 & -1 & 0 \\ 0 & 0 & 1 & 0 & 0 \\ 0 & -1 & 0 & 0 & 0 \\ 1 & 0 & 0 & 0 & 0 \end{pmatrix}$.

Since $\hat{\sigma}_{yz} = \hat{\sigma}_{xz} \cdot \hat{C}_4^2$ we have $\hat{T}(\hat{\sigma}_{yz}) = \hat{T}(\hat{\sigma}_{xz}) \cdot \hat{T}(\hat{C}_4^2)$ so that $\hat{T}(\hat{\sigma}_{yz}) = \begin{pmatrix} 0 & 0 & 0 & 0 & 1 \\ 0 & 0 & 0 & 1 & 0 \\ 0 & 0 & 1 & 0 & 0 \\ 0 & 1 & 0 & 0 & 0 \\ 1 & 0 & 0 & 0 & 0 \end{pmatrix}$.

Since $\hat{\sigma}_{d1} = \hat{C}_4 \cdot \hat{\sigma}_{xz}$ we have $\hat{T}(\hat{\sigma}_{d1}) = \hat{T}(\hat{C}_4) \cdot \hat{T}(\sigma_{xz})$ so $\hat{T}(\hat{\sigma}_{d1}) = \begin{pmatrix} 0 & 0 & 0 & 0 & -1 \\ 0 & 0 & 0 & -i & 0 \\ 0 & 0 & 1 & 0 & 0 \\ 0 & i & 0 & 0 & 0 \\ -1 & 0 & 0 & 0 & 0 \end{pmatrix}$.

Finally, since $\hat{\sigma}_{d2} = \hat{\sigma}_{xz} \cdot \hat{C}_4$ we have $\hat{T}(\hat{\sigma}_{d2}) = \hat{T}(\hat{\sigma}_{xz}) \cdot \hat{T}(\hat{C}_4)$ so that the following equation is valid:

$$\hat{T}(\hat{\sigma}_{d2}) = \begin{pmatrix} 0 & 0 & 0 & 0 & -1 \\ 0 & 0 & 0 & i & 0 \\ 0 & 0 & 1 & 0 & 0 \\ 0 & -i & 0 & 0 & 0 \\ -1 & 0 & 0 & 0 & 0 \end{pmatrix}.$$

We have found the representation T. From this follows that the characters of T are:

Table A.1.2.3: Character table of the representation T.

$\underline{C}_{4v}$	$\hat{E}$	$\hat{C}_4, \hat{C}_4^3$	$\hat{C}_4^2$	$\hat{\sigma}_{xz}, \hat{\sigma}_{yz}$	$\hat{\sigma}_{d1}, \hat{\sigma}_{d2}$
χ_T	5	-1	1	1	1

which means that T decomposes into irreducible representations of the group $\underline{C}_{4v}$ in the following manner:

$$\Gamma_T = A_1 + B_1 + B_2 + E \qquad \text{(A.1.2.1).}$$

The conclusion is that 5 times degenerate (in free Fe ion) 3d orbitals split (in the crystal field of $Sr_3Fe_2O_7$) into three non degenerate orbitals denoted by a_1, b_1 and b_2 (and belonging respectively to A_1, B_1 and B_2 irreducible representations of $\underline{C}_{4v}$) and one doubly degenerate orbital denoted by e and belonging to irreducible representation E of the group $\underline{C}_{4v}$. The next question is how to find linear combinations of atomic 3d-orbitals A.1.6 that belong to irreducible representations appearing in decomposition of T (formula A.1.2.1)? For that task we can use a set of operators called group projectors. These operators project arbitrarily vector into a subspace that belongs to the irreducible representation which correspond to a given projector. In our case for the irreducible representation A_1 corresponding group projector is:

$$\hat{P}_{A_1} = \frac{1}{|\underline{G}|}\sum_{\hat{g}\in\underline{G}} \chi^*_{A_1}(\hat{g})\cdot\hat{T}(\hat{g}) = \frac{1}{8}\sum_{\hat{g}\in\underline{C}_{4v}} \hat{T}(\hat{g}) = \begin{pmatrix} 0 & 0 & 0 & 0 & 0 \\ 0 & 0 & 0 & 0 & 0 \\ 0 & 0 & 1 & 0 & 0 \\ 0 & 0 & 0 & 0 & 0 \\ 0 & 0 & 0 & 0 & 0 \end{pmatrix}.$$

Now we have to choose arbitrary function hoping that it is not orthogonal to the function we seek. Let's try with $\begin{pmatrix} 1 \\ 1 \\ 1 \\ 1 \\ 1 \end{pmatrix}$ in the basis $\{\psi_{32-2}(\vec{r}), \psi_{32-1}(\vec{r}), \psi_{320}(\vec{r}), \psi_{321}(\vec{r}), \psi_{322}(\vec{r})\}$. We

have: $\begin{pmatrix} 0 & 0 & 0 & 0 & 0 \\ 0 & 0 & 0 & 0 & 0 \\ 0 & 0 & 1 & 0 & 0 \\ 0 & 0 & 0 & 0 & 0 \\ 0 & 0 & 0 & 0 & 0 \end{pmatrix}\begin{pmatrix} 1 \\ 1 \\ 1 \\ 1 \\ 1 \end{pmatrix} = \begin{pmatrix} 0 \\ 0 \\ 1 \\ 0 \\ 0 \end{pmatrix}$. Vector $\begin{pmatrix} 0 \\ 0 \\ 1 \\ 0 \\ 0 \end{pmatrix}$ corresponds to the function $\psi_{320}(\vec{r})$ so that is function that belongs to the irreducible representation A_1. If we recall the definition of this function (formulae A.1.6 and A.1.7) and recall that in spherical coordinates:

$$x = r\sin\theta \cdot \cos\varphi$$
$$y = r\sin\theta \cdot \sin\varphi$$
$$z = r\cos\theta$$

we can write:

$$\psi_{320}(\vec{r}) = R_{32}(r) \cdot \frac{1}{4} \cdot \sqrt{\frac{5}{\pi}} \cdot \left(3\cos^2\theta - 1\right) = R_{32}(r) \cdot \frac{1 \cdot \sqrt{5}}{4 \cdot \sqrt{\pi}} \cdot \left(\frac{3z^2 - r^2}{r^2}\right) \stackrel{def}{=} d_{3z^2 - r^2}.$$

Conclusion is that one of the solutions of the Schrödinger equation A.1.2 is orbital $d_{3z^2-r^2}$ defined in previous equation and belonging to the irreducible representation A_1. In this case we could find this function only from symmetry considerations.

In the same way we can find the function that belongs to the irreducible representation B_1. Corresponding group projector is:

$$\hat{P}_{B_1} = \frac{1}{8}\sum_{\hat{g}\in \underline{C}_{4v}} \chi^*_{B_1}(\hat{g}) \cdot \hat{T}(\hat{g}) = \frac{1}{2}\begin{pmatrix} 1 & 0 & 0 & 0 & 1 \\ 0 & 0 & 0 & 0 & 0 \\ 0 & 0 & 0 & 0 & 0 \\ 0 & 0 & 0 & 0 & 0 \\ 1 & 0 & 0 & 0 & 1 \end{pmatrix}.$$ When operating on $\begin{pmatrix} 1 \\ 1 \\ 1 \\ 1 \\ 1 \end{pmatrix}$ it gives

$\frac{1}{2}\begin{pmatrix} 1 & 0 & 0 & 0 & 1 \\ 0 & 0 & 0 & 0 & 0 \\ 0 & 0 & 0 & 0 & 0 \\ 0 & 0 & 0 & 0 & 0 \\ 1 & 0 & 0 & 0 & 1 \end{pmatrix}\begin{pmatrix} 1 \\ 1 \\ 1 \\ 1 \\ 1 \end{pmatrix} = \begin{pmatrix} 1 \\ 0 \\ 0 \\ 0 \\ 1 \end{pmatrix}$. Vector $\begin{pmatrix} 1 \\ 0 \\ 0 \\ 0 \\ 1 \end{pmatrix}$ corresponds to the function which is after normalization equal to:

$$\frac{1}{\sqrt{2}}(\psi_{32-2}(\vec{r})+\psi_{322}(\vec{r}))=\frac{1}{\sqrt{2}}R_{32}(r)\cdot(\mathrm{Y}_2^{-2}(\theta,\varphi)+\mathrm{Y}_2^{2}(\theta,\varphi))=$$

$$=\frac{\sqrt{15}}{2\cdot\sqrt{4\pi}}R_{32}(r)(\sin^2\theta\cdot\cos 2\varphi)=$$

$$=\frac{\sqrt{15}}{2\cdot\sqrt{4\pi}}R_{32}(r)\cdot(\sin^2\theta\cdot\cos^2\varphi-\sin^2\theta\cdot\sin^2\varphi)=\frac{\sqrt{15}}{2\cdot\sqrt{4\pi}}R_{32}(r)\cdot\frac{x^2-y^2}{r^2}\overset{def}{=}d_{x^2-y^2}$$

so that conclusion is that function $d_{x^2-y^2}$ is another solution of the equation A.1.2 and it belongs to the irreducible representation B_1 of the group $\underline{C}_{4v}$.

Function that belongs to the irreducible representation B_2 we can find in the similar way. Group projector is:

$$\hat{P}_{B_2}=\frac{1}{8}\sum_{\hat{g}\in\underline{C}_{4v}}\chi^*_{B_2}(\hat{g})\hat{T}(\hat{g})=\frac{1}{2}\begin{pmatrix}1&0&0&0&-1\\0&0&0&0&0\\0&0&0&0&0\\0&0&0&0&0\\-1&0&0&0&1\end{pmatrix}.$$

If we would try again with the same trial vector as in previous two cases (i.e. vector $\begin{pmatrix}1\\1\\1\\1\\1\end{pmatrix}$) we would get zero vector after application of the operator $\hat{P}_{B_2}$, that's why we must choose another trial vector. Let's take for example $\begin{pmatrix}0\\0\\0\\0\\1\end{pmatrix}$, we have:

$\frac{1}{2}\begin{pmatrix}1&0&0&0&-1\\0&0&0&0&0\\0&0&0&0&0\\0&0&0&0&0\\-1&0&0&0&1\end{pmatrix}\begin{pmatrix}0\\0\\0\\0\\1\end{pmatrix}=\frac{1}{2}\begin{pmatrix}-1\\0\\0\\0\\1\end{pmatrix}$. Vector $\frac{1}{2}\begin{pmatrix}-1\\0\\0\\0\\1\end{pmatrix}$ corresponds to the following function (after normalization and multiplication by phase factor -i):

$$\frac{-i}{\sqrt{2}}(\psi_{322}(\vec{r})-\psi_{32-2}(\vec{r}))=\frac{-i}{\sqrt{2}}R_{32}(r)\cdot(\mathrm{Y}_2^2(\theta,\varphi)-\mathrm{Y}_2^{-2}(\theta,\varphi))=$$
$$=\frac{\sqrt{15}}{2\cdot\sqrt{4\pi}}R_{32}(r)\cdot\sin^2\theta\cdot\sin 2\varphi=\sqrt{\frac{15}{4\pi}}R_{32}(r)\cdot\sin^2\theta\cdot\sin\varphi\cdot\cos\varphi=$$
$$=\sqrt{\frac{15}{4\pi}}R_{32}(r)\frac{xy}{r^2}\overset{def}{=}d_{xy}$$

Conclusion is that orbital d_{xy} is another solution of A.1.2 and it belongs to the irreducible representation B_2 of the group $\underline{C}_{4v}$.

Since irreducible representation E is two dimensional we have to find two linearly independent functions that belong to it. Group projectors in this case read:

$$\hat{P}_{E,1}=\frac{2}{8}\sum_{\hat{g}\in\underline{C}_{4v}}d^*_{11,E}(\hat{g})\hat{T}(\hat{g})=\frac{1}{4}\left(\hat{T}(\hat{E})+i\hat{T}(\hat{C}_4)-\hat{T}(\hat{C}_4^2)-i\hat{T}(\hat{C}_4^3)\right)=\begin{pmatrix}0&0&0&0&0\\0&0&0&0&0\\0&0&0&0&0\\0&0&0&1&0\\0&0&0&0&0\end{pmatrix}$$

where $d^*_{11,E}(\hat{g})$ is complex conjugate matrix element one-one of the irreducible representation E which corresponds to element $\hat{g}$ of the group $\underline{C}_{4v}$. If we act with this projector on the trial vector for example $\begin{pmatrix}1\\1\\1\\1\\1\end{pmatrix}$ we get:

$$\begin{pmatrix}0&0&0&0&0\\0&0&0&0&0\\0&0&0&0&0\\0&0&0&1&0\\0&0&0&0&0\end{pmatrix}\begin{pmatrix}1\\1\\1\\1\\1\end{pmatrix}=\begin{pmatrix}0\\0\\0\\1\\0\end{pmatrix}$$ which corresponds to the function $\psi_{321}(\vec{r})$.

Second function that belongs to E we can get with the help of the following projector:

$$\hat{P}_{E,2} = \frac{2}{8}\sum_{\hat{g}\in\underline{C}_{4v}} d^{*}_{22,E}(\hat{g})\hat{T}(\hat{g}) = \frac{1}{4}\left(\hat{T}(\hat{E}) - i\hat{T}(\hat{C}_4) - \hat{T}(\hat{C}_4^2) + i\hat{T}(\hat{C}_4^3)\right) = \begin{pmatrix} 0 & 0 & 0 & 0 & 0 \\ 0 & 1 & 0 & 0 & 0 \\ 0 & 0 & 0 & 0 & 0 \\ 0 & 0 & 0 & 0 & 0 \\ 0 & 0 & 0 & 0 & 0 \end{pmatrix}$$

where $d_{22,E}(\hat{g})$ is matrix element two-two of the irreducible representation E which corresponds to the element $\hat{g}$ of the group $\underline{C}_{4v}$. If we act with this projector into the same trial function we get:

$$\begin{pmatrix} 0 & 0 & 0 & 0 & 0 \\ 0 & 1 & 0 & 0 & 0 \\ 0 & 0 & 0 & 0 & 0 \\ 0 & 0 & 0 & 0 & 0 \\ 0 & 0 & 0 & 0 & 0 \end{pmatrix}\begin{pmatrix} 1 \\ 1 \\ 1 \\ 1 \\ 1 \end{pmatrix} = \begin{pmatrix} 0 \\ 1 \\ 0 \\ 0 \\ 0 \end{pmatrix}$$ which corresponds to the function $\psi_{32-1}(\vec{r})$.

In this way we have found two linearly independent functions that belong to the same irreducible representation E of the group $\underline{C}_{4v}$ and that, consequently belong to the same double degenerate energy level. Instead of functions $\psi_{32-1}(\vec{r})$ and $\psi_{321}(\vec{r})$ we can use their following linear combinations (which belong to the same energy level):

$$\frac{i}{\sqrt{2}}(\psi_{321}(\vec{r}) + \psi_{32-1}(\vec{r})) = \frac{i}{\sqrt{2}} R_{32}(r)\left(\mathrm{Y}_2^{-1}(\theta,\varphi) + \mathrm{Y}_2^{1}(\theta,\varphi)\right) =$$
$$= \sqrt{\frac{15}{4\pi}} R_{32}(r)\cdot\sin\theta\cdot\cos\theta\cdot\sin\varphi = \sqrt{\frac{15}{4\pi}} R_{32}(r)\frac{yz}{r^2} \overset{def}{=} d_{yz}$$

and

$$\frac{1}{\sqrt{2}}\left(\psi_{32-1}(\vec{r}) - \psi_{321}(\vec{r})\right) = \frac{1}{\sqrt{2}} R_{32}(r)\left(\mathrm{Y}_2^{-1}(\theta,\varphi) - \mathrm{Y}_2^{1}(\theta,\varphi)\right) =$$
$$= \sqrt{\frac{15}{4\pi}} R_{32}(r)\cdot\sin\theta\cdot\cos\theta\cdot\cos\varphi = \sqrt{\frac{15}{4\pi}} R_{32}(r)\frac{xz}{r^2} \overset{def}{=} d_{xz}$$

with the conclusion that functions d_{xz} and d_{yz} correspond to the same doubly degenerate level. In this way we have found all solutions of the equation A.1.2 for the Fe ion in the crystal $Sr_3Fe_2O_7$ only from symmetry considerations.

A.1.3 CASE OF $Sr_4Fe_4O_{11}$

In $Sr_4Fe_4O_{11}$ there are two valence states of the Fe ion. Fe^{4+} ion occupies the site 4i and Fe^{3+} ion occupies the site 4f of the space group Cmmm (D_{2h}^{19}; 65). Site symmetry of the site 4i is $\underline{C}_{2v}$ (or 2mm in the International notation). This group has four elements: identity ($\hat{E}$), axis of order two ($\hat{C}_2$) and two vertical planes containing this axis. If the z axis is along the axis of order two and x and y axes are chosen in the same way as in the paragraph A.1.2 those planes are $\hat{\sigma}_{xz}$ (contains the axes x and z) and $\hat{\sigma}_{yz}$ (contains axes y and z). This group is Abelian so that its all irreducible representations are one dimensional. In this case table of characters and of irreducible representations coincide. This is shown in the following table:

Table A.1.3.1: Characters (and IR) of the group $\underline{C}_{2v}$.

$\underline{C}_{2v}$	$\hat{E}$	$\hat{C}_2$	$\hat{\sigma}_{xz}$	$\hat{\sigma}_{yz}$
A_1	1	1	1	1
A_2	1	1	-1	-1
B_1	1	-1	1	-1
B_2	1	-1	-1	1

We can see that the group $\underline{C}_{2v}$ is subgroup of the group $\underline{C}_{4v}$ with whom we were working in the paragraph A.1.2. For that reason we can immediately write the characters of the representation T. From the table A.1.2.3 we can derive the following table ($\hat{C}_4^2 = \hat{C}_2$):

Table A.1.3.2: Characters of the representation T

$\underline{C}_{2v}$	$\hat{E}$	$\hat{C}_2$	$\hat{\sigma}_{xz}$	$\hat{\sigma}_{yz}$
χ_T	5	1	1	1

Representation T decomposes in the irreducible representations of the group $\underline{C}_{2v}$ in the following way:

$$\Gamma_T = 2A_1 + A_2 + B_1 + B_2 .$$

Since all representations in the decomposition of representation T are one dimensional, corresponding energy levels are non degenerate. In this case finding of functions that belong to irreducible representations A_2, B_1 and B_2 lead us directly to the solution of equation A.1.2 while finding functions that belong to A_1 reduces the problem of finding two remaining (linearly independent) solutions of this equation. For the irreducible representation A_2 corresponding group projector is:

$$\hat{P}_{A_2} = \frac{1}{4}\sum_{\hat{g}\in \underline{C}_{2v}} \chi^*_{A_2}(\hat{g})\hat{T}(\hat{g}) = \frac{1}{4}\left(\hat{T}(\hat{E}) + \hat{T}(\hat{C}_2) - \hat{T}(\hat{\sigma}_{xz}) - \hat{T}(\hat{\sigma}_{yz})\right) = \frac{1}{2}\begin{pmatrix} 1 & 0 & 0 & 0 & -1 \\ 0 & 0 & 0 & 0 & 0 \\ 0 & 0 & 0 & 0 & 0 \\ 0 & 0 & 0 & 0 & 0 \\ -1 & 0 & 0 & 0 & 1 \end{pmatrix}.$$

This projector is the same as projector $\hat{P}_{B_2}$ in the paragraph A.1.2 which means that the function that belongs to the irreducible representation A_2 of the group $\underline{C}_{2v}$ is d_{xy} defined in paragraph A.1.2.

Group projector that belongs to the irreducible representation B_1 of the group $\underline{C}_{2v}$ is:

$$\hat{P}_{B_1} = \frac{1}{4}\sum_{\hat{g}\in \underline{C}_{2v}} \chi^*_{B_1}(\hat{g})\hat{T}(\hat{g}) = \frac{1}{4}\left(\hat{T}(\hat{E}) - \hat{T}(\hat{C}_2) + \hat{T}(\hat{\sigma}_{xz}) - \hat{T}(\hat{\sigma}_{yz})\right) = \frac{1}{2}\begin{pmatrix} 0 & 0 & 0 & 0 & 0 \\ 0 & 1 & 0 & -1 & 0 \\ 0 & 0 & 0 & 0 & 0 \\ 0 & -1 & 0 & 1 & 0 \\ 0 & 0 & 0 & 0 & 0 \end{pmatrix}.$$

If we choose $\begin{pmatrix} 0 \\ 1 \\ 0 \\ 0 \\ 0 \end{pmatrix}$ as a trial vector we get: $\frac{1}{2}\begin{pmatrix} 0 & 0 & 0 & 0 & 0 \\ 0 & 1 & 0 & -1 & 0 \\ 0 & 0 & 0 & 0 & 0 \\ 0 & -1 & 0 & 1 & 0 \\ 0 & 0 & 0 & 0 & 0 \end{pmatrix}\begin{pmatrix} 0 \\ 1 \\ 0 \\ 0 \\ 0 \end{pmatrix} = \frac{1}{2}\begin{pmatrix} 0 \\ 1 \\ 0 \\ -1 \\ 0 \end{pmatrix}$. Obtained vector correspond to the function which is after normalization equal to the d_{xz} defined in the last rows of the paragraph A.1.2.

Group projector that belongs to the irreducible representation B_2 of the group $\underline{C}_{2v}$ is:

$$\hat{P}_{B_2} = \frac{1}{4}\sum_{\hat{g}\in \underline{C}_{2v}} \chi^*_{B_2}(\hat{g})\hat{T}(\hat{g}) = \frac{1}{4}\left(\hat{T}(\hat{E}) - \hat{T}(\hat{C}_2) - \hat{T}(\hat{\sigma}_{xz}) + \hat{T}(\hat{\sigma}_{yz})\right) = \frac{1}{2}\begin{pmatrix} 0 & 0 & 0 & 0 & 0 \\ 0 & 1 & 0 & 1 & 0 \\ 0 & 0 & 0 & 0 & 0 \\ 0 & 1 & 0 & 1 & 0 \\ 0 & 0 & 0 & 0 & 0 \end{pmatrix}.$$

For the same trial vector we get: $\frac{1}{2}\begin{pmatrix} 0 & 0 & 0 & 0 & 0 \\ 0 & 1 & 0 & 1 & 0 \\ 0 & 0 & 0 & 0 & 0 \\ 0 & 1 & 0 & 1 & 0 \\ 0 & 0 & 0 & 0 & 0 \end{pmatrix}\begin{pmatrix} 0 \\ 1 \\ 0 \\ 0 \\ 0 \end{pmatrix} = \frac{1}{2}\begin{pmatrix} 0 \\ 1 \\ 0 \\ 1 \\ 0 \end{pmatrix}$. Vector $\frac{1}{2}\begin{pmatrix} 0 \\ 1 \\ 0 \\ 1 \\ 0 \end{pmatrix}$ corresponds after normalization to the function d_{yz} defined in the last lines of the paragraph A.1.2.

Conclusion is that solutions of the equation A.1.2 for the case of Fe^{4+} ion in $Sr_4Fe_4O_{11}$ are functions d_{xy} (belonging to the irreducible representation A_2 of the group $\underline{C}_{2v}$), d_{xz} (belonging to the irreducible representation B_1 of the group $\underline{C}_{2v}$) and d_{yz} (belonging to the irreducible representation B_2 of the group $\underline{C}_{2v}$). All corresponding levels are non degenerate. Concerning remaining two solutions we can not say more about them except that they belong to the totally symmetric irreducible representation A_1 of the group $\underline{C}_{2v}$. It can be shown that functions $d_{3z^2-r^2}$ and $d_{x^2-y^2}$ obtained in paragraph A.1.2 belong to this irreducible representation and since they are orthogonal they make the basis in which we can search remaining two solutions of the equation A.1.2.

Site 4f that contains Fe^{3+} ion has site symmetry $\underline{C}_{2h}$ (or 2/m in the International notation). This group contains following four elements: identity ($\hat{E}$), axis of the order two ($\hat{C}_2$), inversion ($\hat{i}$) and a plane of reflection that is perpendicular to the axis of order two ($\hat{\sigma}_h$, h stays for "horizontal". If z axis is along the axis of order 2, and x and y axes are oriented as described in the paragraph A.1.2, than this plane contains x and y axes). Group is Abelian so all its irreducible representations are one dimensional. They are:

Table A.1.3.3: Characters (and IR) of the group $\underline{C}_{2h}$.

$\underline{C}_{2h}$	$\hat{E}$	$\hat{C}_2$	$\hat{i}$	$\hat{\sigma}_h$
A_g	1	1	1	1
B_g	1	-1	1	-1
A_u	1	1	-1	-1
B_u	1	-1	-1	1

Representation T for identity, axis of order 2 and inversion we have already find in previous paragraphs. For the horizontal plane of reflection we have to have in mind that spherical coordinates (r, θ, φ) change to (r, π-θ, φ) under it and that this operation is its own inverse. For these reasons we have:

$$\psi_{32-2}(\hat{\sigma}_h^{-1}\vec{r}) = \psi_{32-2}(\hat{\sigma}_h\vec{r}) = \psi_{32-2}(r,\pi-\theta,\varphi) = \psi_{32-2}(\vec{r})$$
$$\psi_{32-1}(\hat{\sigma}_h^{-1}\vec{r}) = \psi_{32-1}(\hat{\sigma}_h\vec{r}) = \psi_{32-1}(r,\pi-\theta,\varphi) = -\psi_{32-1}(\vec{r})$$
$$\psi_{320}(\hat{\sigma}_h^{-1}\vec{r}) = \psi_{320}(\hat{\sigma}_h\vec{r}) = \psi_{320}(r,\pi-\theta,\varphi) = \psi_{320}(\vec{r})$$
$$\psi_{321}(\hat{\sigma}_h^{-1}\vec{r}) = \psi_{321}(\hat{\sigma}_h\vec{r}) = \psi_{321}(r,\pi-\theta,\varphi) = -\psi_{321}(\vec{r})$$
$$\psi_{322}(\hat{\sigma}_h^{-1}\vec{r}) = \psi_{322}(\hat{\sigma}_h\vec{r}) = \psi_{322}(r,\pi-\theta,\varphi) = \psi_{322}(\vec{r})$$

so that

$$\hat{T}(\hat{\sigma}_h) = \begin{pmatrix} 1 & 0 & 0 & 0 & 0 \\ 0 & -1 & 0 & 0 & 0 \\ 0 & 0 & 1 & 0 & 0 \\ 0 & 0 & 0 & -1 & 0 \\ 0 & 0 & 0 & 0 & 1 \end{pmatrix}.$$

From this and from tables A.1.3.2 and A.1.1.2 we have the following table of characters for the representation T:

Table A.1.3.4: Characters of the representation T,

$\underline{C}_{2h}$	$\hat{E}$	$\hat{C}_2$	$\hat{i}$	$\hat{\sigma}_h$
χ_T	5	1	5	1

which means that T decomposes into the irreducible representations of $\underline{C}_{2h}$ in the following way:

$$\Gamma_T = 3A_g + 2B_g .$$

This result means that our five times degenerate 3d level splits in the crystal field of $Sr_4Fe_4O_{11}$ (at the site 4f) at five non degenerate levels three of which belong to the totally symmetric irreducible representation A_g and two of them to the representation B_g of the group $\underline{C}_{2h}$. It is interesting to note that orbitals $d_{3z^2-r^2}$, $d_{x^2-y^2}$ and d_{xy} are three mutually orthogonal functions that belong to the irreducible representation A_g, while d_{xz} and d_{yz} are two mutually orthogonal functions that belong to the irreducible representation B_g of the group $\underline{C}_{2h}$. However, that doesn't mean that they are the solutions of the equation A.1.2 but by use of them we can reduce problem of finding eigenvalues of five dimensional matrix into the problem of finding eigenvalues of three dimensional and two dimensional matrices. This calculation is not the topic of this work.

A.1.4 CASE OF $Sr_8Fe_8O_{23}$

In the $Sr_8Fe_8O_{23}$ there are three different crystallographic sites of the space group I4/mmm (D_{4h}^{17}; 139) where Fe ions stay. First of them is 4e which is occupied by Fe^{4+} ion and has the site symmetry $\underline{C}_{4v}$. This case we have already had in paragraph A.1.2 so that conclusions from it can be applied here. Second site is 8f which is occupied by Fe ion with average valence 3.5+. Corresponding site symmetry is $\underline{C}_{2h}$ and this case we had in the paragraph A.1.3. The last site is 4d, occupied by Fe^{4+} and has the site symmetry $\underline{D}_{2d}$ ($\bar{4}2m$ or $\bar{4}m2$ in the International notation). This group has following eight elements: identity ($\hat{E}$), improper rotation of order 4 ("improper rotation" means rotation around the axis followed by the reflection through a plane that is perpendicular to the axis

of rotation) ($\hat{S}_4$), second and third powers of this operation ($\hat{S}_4^2 = \hat{C}_2, \hat{S}_4^3$) two axis of order 2 (if z axis is along the improper axis of order 4 and x and y are perpendicular to it and to each other and if x, y and z are making right handed system than those axes are denoted by $\hat{C}_{2x}$ (contains the axis x) and $\hat{C}_{2y}$ (contains the axis y)) and two diagonal planes of reflection defined as in the case of the group $\underline{C}_{4v}$ in paragraph A.1.2 and denoted with the same symbols, i.e. $\hat{\sigma}_{d1}$ and $\hat{\sigma}_{d2}$. Character table of this group is:

Table A.1.4.1: Characters of the point group $\underline{D}_{2d}$

$\underline{D}_{2d}$	$\hat{E}$	$\hat{S}_4, \hat{S}_4^3$	$\hat{S}_4^2$	$\hat{C}_{2x}, \hat{C}_{2y}$	$\hat{\sigma}_{d1}, \hat{\sigma}_{d2}$
A_1	1	1	1	1	1
A_2	1	1	1	-1	-1
B_1	1	-1	1	1	-1
B_2	1	-1	1	-1	1
E	2	0	-2	0	0

and the table of irreducible representations is:

Table A.1.4.2: Irreducible representations of the point group $\underline{D}_{2d}$.

$\underline{D}_{2d}$	$\hat{E}$	$\hat{S}_4$	$\hat{S}_4^2$	$\hat{S}_4^3$	$\hat{C}_{2x}$	$\hat{C}_{2y}$	$\hat{\sigma}_{d1}$	$\hat{\sigma}_{d2}$
A_1	1	1	1	1	1	1	1	1
A_2	1	1	1	1	-1	-1	-1	-1
B_1	1	-1	1	-1	1	1	-1	-1
B_2	1	-1	1	-1	-1	-1	1	1
E	$\begin{pmatrix} 1 & 0 \\ 0 & 1 \end{pmatrix}$	$\begin{pmatrix} -i & 0 \\ 0 & i \end{pmatrix}$	$\begin{pmatrix} -1 & 0 \\ 0 & -1 \end{pmatrix}$	$\begin{pmatrix} i & 0 \\ 0 & -i \end{pmatrix}$	$\begin{pmatrix} 0 & 1 \\ 1 & 0 \end{pmatrix}$	$\begin{pmatrix} 0 & -1 \\ -1 & 0 \end{pmatrix}$	$\begin{pmatrix} 0 & i \\ -i & 0 \end{pmatrix}$	$\begin{pmatrix} 0 & -i \\ i & 0 \end{pmatrix}$

Since calculation that leads to finding representation T has already been shown in previous paragraphs this time it will be skipped. Final result is that the characters of the representation T are:

Table A.1.4.3: Characters of the representation T

$\underline{D}_{2d}$	$\hat{E}$	$\hat{S}_4, \hat{S}_4^3$	$\hat{S}_4^2$	$\hat{C}_{2x}, \hat{C}_{2y}$	$\hat{\sigma}_{d1}, \hat{\sigma}_{d2}$
χ_T	5	-1	1	1	1

which means that T decomposes into the following irreducible representations of the point group $\underline{D}_{2d}$:

$$\Gamma_T = A_1 + B_1 + B_2 + E \ .$$

The interpretation of this result is the same as in the case of the group $\underline{C}_{4v}$ (paragraph A.1.2). It can be shown that the orbital $d_{3z^2-r^2}$ belongs to the irreducible representation A_1

of the group $\underline{D}_{2d}$, orbital $d_{x^2-y^2}$ belongs to B_1, orbital d_{xy} belongs to B_2 while d_{xz} and d_{yz} belong to the irreducible representation E of the group $\underline{D}_{2d}$. In this way we have obtained all the solutions of the equation A.1.2 only from symmetry considerations.

A.1.5 CASE OF $SrFeO_3$

In this compound Fe^{4+} ion occupies site 1a of the space group Pm3m (O_h^1; 221). Corresponding site symmetry is $\underline{O}_h$ (m3m in International notation). This group has 48 elements and since it is so complex the elements will not be described here (most of them were described earlier) neither the table of irreducible representations will be given. Table of characters is:

Table A.1.5.1: Characters of the point group $\underline{O}_h$.

$\underline{O}_h$	E	$8C_3$	$6C_2$	$6C_4$	$3C_2=C_4^2$	i	$6S_4$	$8S_6$	$3\sigma_h$	$6\sigma_d$
A_{1g}	1	1	1	1	1	1	1	1	1	1
A_{2g}	1	1	-1	-1	1	1	-1	1	1	-1
E_g	2	-1	0	0	2	2	0	-1	2	0
T_{1g}	3	0	-1	1	-1	3	1	0	-1	-1
T_{2g}	3	0	1	-1	-1	3	-1	0	-1	1
A_{1u}	1	1	1	1	1	-1	-1	-1	-1	-1
A_{2u}	1	1	-1	-1	1	-1	1	-1	-1	1
E_u	2	-1	0	0	2	-2	0	1	-2	0
T_{1u}	3	0	-1	1	-1	-3	-1	0	1	1
T_{2u}	3	0	1	-1	-1	-3	1	0	1	-1

Details of the calculation which leads to the representation T will be skipped (for most of elements T has been already obtained in previous paragraphs). It can be shown that the characters of the representation T are:

Table A.1.5.2: Characters of the representation T

$\underline{O}_h$	E	$8C_3$	$6C_2$	$6C_4$	$3C_2=C_4^2$	i	$6S_4$	$8S_6$	$3\sigma_h$	$6\sigma_d$
χ_T	5	-1	1	-1	1	5	-1	-1	1	1

which means that it decomposes into the following irreducible representations of $\underline{O}_h$:

$$\Gamma_T = E_g + T_{2g}.$$

Conclusion is that 5 times degenerate 3d orbitals split into one double degenerate and one triply degenerate level under the influence of the crystal field of $SrFeO_3$. It can be shown that orbitals $d_{3z^2-r^2}$ and $d_{x^2-y^2}$ belong to the E_g level, while orbitals d_{xy}, d_{xz} and d_{yz} belong to the T_{2g} level. In this case we have solved equation A.1.2 only from symmetry considerations.

A.2 INFLUENCE THAT CRYSTAL SYMMETRY HAS ON MAGNETIC SUSCEPTIBILITY AND RESISTIVITY TENSORS

In this chapter it is described which conclusions one can draw from the crystal symmetry related to the resistivity and magnetic susceptibility tensors of a crystal. Corresponding calculation will be done for crystal $Sr_3Fe_2O_7$ since in this material measurements of those properties were done along crystal axes. The theory which is described here can be found for example in [Rb6].

Let's start with consideration for a resistivity tensor. It is defined by:

$$\vec{E} = \hat{\rho} \cdot \vec{j} \,,$$

where $\vec{E}$ is electric field and $\vec{j}$ is the current density (both are polar vectors). Let's now choose vectors $\{\vec{e}_1, \vec{e}_2, \vec{e}_3\}$ as orthonormal basis. If $\vec{j} = j_1\vec{e}_1 + j_2\vec{e}_2 + j_3\vec{e}_3$ we say that matrix $\begin{pmatrix} j_1 \\ j_2 \\ j_3 \end{pmatrix}$ represents vector $\vec{j}$ in the basis $\{\vec{e}_1, \vec{e}_2, \vec{e}_3\}$. In the similar way $\begin{pmatrix} E_1 \\ E_2 \\ E_3 \end{pmatrix}$ represents vector $\vec{E}$ in the same basis. If now the following equations are valid:

$$\begin{aligned}
\hat{\rho} \cdot \vec{e}_1 &= \rho_{11}\vec{e}_1 + \rho_{21}\vec{e}_2 + \rho_{31}\vec{e}_3 \\
\hat{\rho} \cdot \vec{e}_2 &= \rho_{12}\vec{e}_1 + \rho_{22}\vec{e}_2 + \rho_{32}\vec{e}_3 \\
\hat{\rho} \cdot \vec{e}_3 &= \rho_{13}\vec{e}_1 + \rho_{23}\vec{e}_2 + \rho_{33}\vec{e}_3
\end{aligned}$$

then we have:

$$\begin{aligned}
\vec{E} = \hat{\rho} \cdot \vec{j} &= (\rho_{11} j_1 + \rho_{12} j_2 + \rho_{13} j_3)\vec{e}_1 + (\rho_{21} j_1 + \rho_{22} j_2 + \rho_{23} j_3)\vec{e}_2 + \\
&+ (\rho_{31} j_1 + \rho_{32} j_2 + \rho_{33} j_3)\vec{e}_3
\end{aligned}$$

or in matrix notation:

$$\begin{pmatrix} E_1 \\ E_2 \\ E_3 \end{pmatrix} = \begin{pmatrix} \rho_{11} j_1 + \rho_{12} j_2 + \rho_{13} j_3 \\ \rho_{21} j_1 + \rho_{22} j_2 + \rho_{23} j_3 \\ \rho_{31} j_1 + \rho_{32} j_2 + \rho_{33} j_3 \end{pmatrix} = \begin{pmatrix} \rho_{11} & \rho_{12} & \rho_{13} \\ \rho_{21} & \rho_{22} & \rho_{23} \\ \rho_{31} & \rho_{32} & \rho_{33} \end{pmatrix} \begin{pmatrix} j_1 \\ j_2 \\ j_3 \end{pmatrix},$$

which means that the resistivity tensor $\hat{\rho}$ is in basis $\{\vec{e}_1, \vec{e}_2, \vec{e}_3\}$ represented by the matrix $\begin{pmatrix} \rho_{11} & \rho_{12} & \rho_{13} \\ \rho_{21} & \rho_{22} & \rho_{23} \\ \rho_{31} & \rho_{32} & \rho_{33} \end{pmatrix}$. Question arises what will happen if we decide to change basis vectors? Let's define an operator $\hat{R}$ which change orthonormal basis $\{\vec{e}_1, \vec{e}_2, \vec{e}_3\}$ into a

new orthonormal basis $\{\vec{e}_1^{'}, \vec{e}_2^{'}, \vec{e}_3^{'}\}$ (this means that $\hat{R}$ is orthogonal i.e. $\hat{R}^T = \hat{R}^{-1}$) in a following way:

$$\begin{aligned}
\vec{e}_1^{'} &= \hat{\mathrm{R}}\vec{\mathrm{e}}_1 = r_{11}\vec{e}_1 + r_{21}\vec{e}_2 + r_{31}\vec{e}_3 \\
\vec{e}_2^{'} &= \hat{\mathrm{R}}\vec{\mathrm{e}}_2 = r_{12}\vec{e}_1 + r_{22}\vec{e}_2 + r_{32}\vec{e}_3 \\
\vec{e}_3^{'} &= \hat{\mathrm{R}}\vec{\mathrm{e}}_3 = r_{13}\vec{e}_1 + r_{23}\vec{e}_2 + r_{33}\vec{e}_3
\end{aligned} .$$

We have:

$$\begin{aligned}
\vec{j} &= j_1^{'}\vec{e}_1^{'} + j_2^{'}\vec{e}_2^{'} + j_3^{'}\vec{e}_3^{'} = (r_{11}j_1^{'} + r_{12}j_2^{'} + r_{13}j_3^{'})\vec{e}_1 + (r_{21}j_1^{'} + r_{22}j_2^{'} + r_{23}j_3^{'})\vec{e}_2 + \\
&+ (r_{31}j_1^{'} + r_{32}j_2^{'} + r_{33}j_3^{'})\vec{e}_3 = j_1\vec{e}_1 + j_2\vec{e}_2 + j_3\vec{e}_3
\end{aligned} ,$$

or in matrix notation:

$$\begin{pmatrix} j_1 \\ j_2 \\ j_3 \end{pmatrix} = \begin{pmatrix} r_{11}j_1^{'} + r_{12}j_2^{'} + r_{13}j_3^{'} \\ r_{21}j_1^{'} + r_{22}j_2^{'} + r_{23}j_3^{'} \\ r_{31}j_1^{'} + r_{32}j_2^{'} + r_{33}j_3^{'} \end{pmatrix} = \begin{pmatrix} r_{11} & r_{12} & r_{13} \\ r_{21} & r_{22} & r_{23} \\ r_{31} & r_{32} & r_{33} \end{pmatrix} \begin{pmatrix} j_1^{'} \\ j_2^{'} \\ j_3^{'} \end{pmatrix} .$$

If we now denote with $\vec{j}$ matrix that denotes current density in the basis $\{\vec{e}_1, \vec{e}_2, \vec{e}_3\}$, $\vec{j}^{'}$ matrix that denotes current density in the basis $\{\vec{e}_1^{'}, \vec{e}_2^{'}, \vec{e}_3^{'}\}$ and $\hat{R}$ matrix that denotes operator $\hat{R}$ in the basis $\{\vec{e}_1, \vec{e}_2, \vec{e}_3\}$, we have:

$$\vec{j} = \hat{R} \cdot \vec{j}^{'}$$

and in analogous way we have

$$\vec{E} = \hat{R}\vec{E}^{'} .$$

If we insert last two equations into the definition of resistivity tensor we get:

$$\hat{R}\vec{E}^{'} = \hat{\rho} \cdot \hat{R} \cdot \vec{j}^{'} \Leftrightarrow \vec{E}^{'} = \hat{R}^T \hat{\rho} \cdot \hat{R} \cdot \vec{j}^{'}$$ (here we used orthogonality of $\hat{R}$).

From this equation we have

$$\hat{\rho}^{'} = \hat{R}^T \hat{\rho} \cdot \hat{R}$$

where $\hat{\rho}^{'}$ ($\hat{\rho}$) is the matrix that represents the resistivity tensor in the basis $\{\vec{e}_1^{'}, \vec{e}_2^{'}, \vec{e}_3^{'}\}$ ($\{\vec{e}_1, \vec{e}_2, \vec{e}_3\}$).

At this point the symmetry of a crystal comes into a play through so called Neumann's principle. It states that any physical property of a crystal has at least the symmetry of a point group of a crystal (this "at least" means that there might be additional restrictions on the tensor properties of a crystal. In case of the resistivity tensor, for example, Onsager's theorem states that outside of the magnetic field it is symmetric). In the case of $Sr_3Fe_2O_7$ point group of the crystal is $\underline{D}_{4h}$. If $\hat{R}$ is from this group than we have:

$$\hat{\rho}' = \hat{\rho} \text{ or equivalently } \hat{R}\hat{\rho} = \hat{\rho}\hat{R} \qquad \text{A.2.1.}$$

Set of operators $\hat{R}$ from $\underline{D}_{4h}$ forms one representation of this group which acts in the real 3-dimensional vector space. This representation is in general reducible and is called polar vector representation. It's characters are $Tr(\hat{R}) = 1 + 2\cos\varphi$ for proper rotation and $-1 + 2\cos\varphi$ for improper rotation (i.e. rotation around the axis followed by reflection through the plane which is perpendicular to that axis) where φ is angle of rotation. In order to reduce this representation in the case of $Sr_3Fe_2O_7$ we need table of characters of the point group $\underline{D}_{4h}$ (irreducible representations of this group are not necessary for our considerations). It is:

Table A.2.1: Characters of the point group $\underline{D}_{4h}$

$\underline{D}_{4h}$	E	$2C_4$	C_2	$2C_2'$	$2C_2''$	i	$2S_4$	σ_h	$2\sigma_v$	$2\sigma_d$
A_{1g}	1	1	1	1	1	1	1	1	1	1
A_{2g}	1	1	1	-1	-1	1	1	1	-1	-1
B_{1g}	1	-1	1	1	-1	1	-1	1	1	-1
B_{2g}	1	-1	1	-1	1	1	-1	1	-1	1
E_g	2	0	-2	0	0	2	0	-2	0	0
A_{1u}	1	1	1	1	1	-1	-1	-1	-1	-1
A_{2u}	1	1	1	-1	-1	-1	-1	-1	1	1
B_{1u}	1	-1	1	1	-1	-1	1	-1	-1	1
B_{2u}	1	-1	1	-1	1	-1	1	-1	1	-1
E_u	2	0	-2	0	0	-2	0	2	0	0

while the characters of the polar vector representation are:

Table A.2.2: Characters of the polar vector representation

$\underline{D}_{4h}$	E	$2C_4$	C_2	$2C_2'$	$2C_2''$	i	$2S_4$	σ_h	$2\sigma_v$	$2\sigma_d$
χ_{pv}	3	1	-1	-1	-1	-3	-1	1	1	1

which means that the polar vector representation reduces in the following way:

$$\Gamma_{PV} = A_{2u} + E_u .$$

It can be shown that vector (let's denote it with $\vec{e}_3$) which is aligned parallel to the axis of order 4 belongs to the irreducible representation A_{2u} while two vectors which are perpendicular to it and to each other (let's denote them with $\vec{e}_1$ and $\vec{e}_2$) belong to the irreducible representation E_u of the point group $\underline{D}_{4h}$. In this basis operators $\hat{R}$ have the following block diagonal form:

$$\hat{R} = \begin{pmatrix} \hat{E}_u(\hat{R}) & & 0 \\ & & 0 \\ 0 & 0 & a_{2u}(\hat{R}) \end{pmatrix}, \text{ for every } \hat{R} \text{ from } \underline{D}_{4h} \qquad \text{A.2.2.}$$

Here $\hat{E}_u(\hat{R})$ is quadratic two dimensional matrix of the irreducible representation E_u (which is two-dimensional) that corresponds to the element $\hat{R}$ of the point group $\underline{D}_{4h}$ and $a_{2u}(\hat{R})$ is a number which in irreducible representation A_{2u} (which is one-dimensional) corresponds to the same element. For example $a_{2u}(\hat{\sigma}_h) = -1$ while $\hat{E}_u(\hat{\sigma}_h) = \begin{pmatrix} 1 & 0 \\ 0 & 1 \end{pmatrix}$. In the spirit of this shape of operators $\hat{R}$ we can write matrix $\hat{\rho}$ in the basis $\{\vec{e}_1, \vec{e}_2, \vec{e}_3\}$ in the following way:

$$\hat{\rho} = \begin{pmatrix} & \hat{A} & \rho_{13} \\ & & \rho_{23} \\ \rho_{31} & \rho_{32} & \rho_{33} \end{pmatrix} \text{ where } \hat{A} \overset{def}{=} \begin{pmatrix} \rho_{11} & \rho_{12} \\ \rho_{21} & \rho_{22} \end{pmatrix} \text{ is quadratic 2-dimensional matrix.}$$

If we now insert last equation and equation A.2.2 into the equation A.2.1 we get following three matrix equations:

$$\left(\forall \hat{R} \in \underline{D}_{4h}\right) \hat{A}\hat{E}_u(\hat{R}) = \hat{E}_u(\hat{R})\hat{A} \qquad \text{A.2.3}$$

$$\left(\forall \hat{R} \in \underline{D}_{4h}\right) \hat{E}_u(\hat{R}) \begin{pmatrix} \rho_{13} \\ \rho_{23} \end{pmatrix} = \begin{pmatrix} \rho_{13} \\ \rho_{23} \end{pmatrix} a_{2u}(\hat{R}) \qquad \text{A.2.4}$$

$$\left(\forall \hat{R} \in \underline{D}_{4h}\right) a_{2u}(\hat{R}) \begin{pmatrix} \rho_{31} & \rho_{32} \end{pmatrix} = \begin{pmatrix} \rho_{31} & \rho_{32} \end{pmatrix} \hat{E}_u(\hat{R}) \qquad \text{A.2.5.}$$

Now it is a good moment to recall two Schur's lemmas. First of them states: If a linear operator $\hat{A}$ commutes with all operators $\hat{\tau}(\hat{g})(\hat{g} \in \underline{G})$ of irreducible representation of a group $\underline{G}$ (the operator and the irreducible representation act in the same vector space with dimension of the vector space equal to the dimension of irreducible representation) then this operator is a multiple of a unit operator, i.e.:

$(\forall \hat{g} \in \underline{G})\hat{\tau}(\hat{g})\hat{A} = \hat{A}\hat{\tau}(\hat{g}) \Rightarrow \hat{A} = a\hat{E}$, where a is a number and $\hat{E}$ is unit operator.

[Proof of this lemma is [Af4]: Let's consider one eigenvector x of the operator $\hat{A}$ that corresponds to the eigenvalue a:

$$\hat{A}x = ax$$

Subspace (let's denote it with L_a) that contains all eigenvectors that correspond to the same eigenvalue a, is invariant with respect to the representation $\hat{\tau}$ as can be shown by following equations:

$$(\forall \hat{g} \in \underline{G})\hat{A}\hat{\tau}(\hat{g})x = \hat{\tau}(\hat{g})\hat{A}x = \hat{\tau}(\hat{g})ax = a\hat{\tau}(\hat{g})x$$

which proves that: $(\forall \hat{g} \in \underline{G})(\forall x \in L_a)\hat{\tau}(\hat{g})x \in L_a$. Now since the representation $\hat{\tau}$ is irreducible and since L_a is not an empty space (i.e. containing only zero vector) we have L_a=L where L is the whole space in which irreducible representation $\hat{\tau}$ and the operator $\hat{A}$ act. From this follows: $(\forall x \in L)\hat{A}x = ax$ i.e. $\hat{A} = a\hat{E}$, which proves the lemma].

Second Schur's lemma states: Let V_{n1} be n1 dimensional vector space in which irreducible representation $\hat{D}_1(\hat{g})(\hat{g} \in \underline{G})$ of a group $\underline{G}$ acts. Dimension of this irreducible representation is equal to n1 so that V_{n1} is irreducible for it. Let V_{n2} be n2 dimensional vector space in which irreducible representation $\hat{D}_2(\hat{g})(\hat{g} \in \underline{G})$ of the same group $\underline{G}$ acts. Dimension of this irreducible representation is equal to n2 so that V_{n2} is irreducible for it. Let now $\hat{B}$ be linear operator that maps V_{n1} to V_{n2} (in the bases of those two vector spaces $\hat{B}$ is represented by matrix with n2 rows and n1 colons). If the following is valid:

$$(\forall \hat{g} \in \underline{G})\hat{B}\hat{D}_1(\hat{g}) = \hat{D}_2(\hat{g})\hat{B} \qquad \text{A.2.6}$$

then: 1.) $\hat{B} = 0$ if $\hat{D}_1$ and $\hat{D}_2$ are non equivalent irreducible representations of $\underline{G}$

or 2.) $\hat{B}$ has inverse operator, n1=n2 and those two irreducible representations are equivalent.

[Proof of this lemma is: let $W_2 \overset{def}{=} \{y | y \in V_{n2}, y = \hat{B}x, x \in V_{n1}\} = RANGE(\hat{B})$ then $(\forall y \in W_2)(\forall \hat{g} \in \underline{G})\hat{D}_2(\hat{g})y = \hat{D}_2(\hat{g})\hat{B}x = \hat{B}\hat{D}_1(\hat{g})x = \hat{B}x' \in W_2$ so that W_2 is invariant for the irreducible representation $\hat{D}_2$ but since $\hat{D}_2$ is irreducible in V_{n2} then either $W_2 = V_{n2}$ or $W_2 = \{0\}$(i.e. empty space; space which contains only null vector). The last case means $\hat{B} = 0$ and the first case means that $\hat{B}$ is mapping "onto". Let now $W_1 \overset{def}{=} \{x | x \in V_{n1}, \hat{B}x = 0\} = NULL(\hat{B})$,

then $(\forall x \in W_1)(\forall \hat{g} \in \underline{G})\hat{B}\hat{D}_1(\hat{g})x = \hat{D}_2(\hat{g})\hat{B}x = \hat{D}_2(\hat{g})0 = 0$ so that W_1 is invariant for the irreducible representation $\hat{D}_1$. Since $\hat{D}_1$ is irreducible in V_{n1} then either $W_1 = V_{n1}$ or $W_1 = \{0\}$. The first case means $\hat{B} = 0$ while the last case means that $\hat{B}$ is mapping "1-1".

Now we have two cases: either $\hat{B}=0$ or $\hat{B}$ is mapping "onto" and "1-1" which means that it is isomorphism so that V_{n1} is isomorphic with V_{n2} from which follows that n1=n2. From A.2.6 in this case follows: $(\forall \hat{g} \in \underline{G})\hat{D}_1(\hat{g}) = \hat{B}^{-1}\hat{D}_2(\hat{g})\hat{B}$ which means that irreducible representations $\hat{D}_1$ and $\hat{D}_2$ are equivalent (since $\hat{B}$ is isomorphism $\hat{B}^{-1}$ exist). In this way the lemma is proved].

After this small digression we can go back to the equations A.2.3-A.2.5. We can apply first Schur's lemma to the equation A.2.3 to get:

$$\hat{A} = \begin{pmatrix} a & 0 \\ 0 & a \end{pmatrix}.$$

In the case of equations A.2.4 and A.2.5 we can apply second Schur's lemma by having in mind that irreducible representations A_{2u} and E_u of the group $\underline{D}_{4h}$ are nonequivalent so that:

$$\rho_{13} = \rho_{23} = \rho_{31} = \rho_{32} = 0.$$

Final conclusion is that the resistivity tensor of the $Sr_3Fe_2O_7$ single crystal in the basis in which z-axis is along the axis of the order 4 and remaining two axes are perpendicular to it and to each other has the following form:

$$\hat{\rho} = \begin{pmatrix} a & 0 & 0 \\ 0 & a & 0 \\ 0 & 0 & b \end{pmatrix} \text{ where a and b are real numbers.} \qquad \text{A.2.7}$$

We can see that the symmetry of the crystal helped us in reducing number of unknown parameters from 9 to 2 and we have got that it is symmetric even without applying Onsager's theorem (considerations that led to equation A.2.7 are valid only in absence of magnetic field since otherwise magnetic field spoils the symmetry of the system).

In the case of magnetic susceptibility tensor we have definition:

$$\vec{M} = \hat{\chi}_m \vec{H}$$

where $\vec{M}$ is magnetization and $\vec{H}$ is magnetic field (both are axial vectors which means that they have transformation properties of for example angular momentum (in classical physics) under orthogonal transformations). In order to find the form of the magnetic susceptibility $\hat{\chi}_m$ we need the transformation properties of the magnetization and the magnetic field. For this reason we have to find the transformation properties of angular momentum in classical physics. If $\vec{x}$ is radius vector and $\vec{p}$ is momentum and if $\hat{R}$ is orthogonal matrix then from $\vec{x} = \hat{R}\vec{x}'$ follows $\vec{p} = \hat{R}\vec{p}'$. Since

$$\vec{L} = \vec{x} \times \vec{p} = (x_2 p_3 - x_3 p_2)\vec{e}_1 + (x_3 p_1 - x_1 p_3)\vec{e}_2 + (x_1 p_2 - x_2 p_1)\vec{e}_3$$

it follows:

$$x_2 p_3 - x_3 p_2 = (r_{22}r_{33} - r_{32}r_{23})(x_2' p_3' - x_3' p_2') + (r_{23}r_{31} - r_{33}r_{21})(x_3' p_1' - x_1' p_3') +$$
$$+ (r_{21}r_{32} - r_{31}r_{22})(x_1' p_2' - x_2' p_1')$$
$$x_3 p_1 - x_1 p_3 = (r_{32}r_{13} - r_{12}r_{33})(x_2' p_3' - x_3' p_2') + (r_{11}r_{33} - r_{31}r_{13})(x_3' p_1' - x_1' p_3') +$$
$$+ (r_{31}r_{12} - r_{11}r_{32})(x_1' p_2' - x_2' p_1')$$
$$x_1 p_2 - x_2 p_1 = (r_{12}r_{23} - r_{22}r_{13})(x_2' p_3' - x_3' p_2') + (r_{13}r_{21} - r_{23}r_{11})(x_3' p_1' - x_1' p_3') +$$
$$+ (r_{11}r_{22} - r_{21}r_{12})(x_1' p_2' - x_2' p_1')$$

For every nonsingular three dimensional quadratic matrix $\hat{R}$ the following equation is valid:

$$\hat{R}^{-1} = \frac{1}{\det \hat{R}} \begin{pmatrix} r_{22}r_{33} - r_{23}r_{32} & r_{13}r_{32} - r_{12}r_{33} & r_{12}r_{23} - r_{13}r_{22} \\ r_{23}r_{31} - r_{21}r_{33} & r_{11}r_{33} - r_{31}r_{13} & r_{13}r_{21} - r_{11}r_{23} \\ r_{21}r_{32} - r_{22}r_{31} & r_{12}r_{31} - r_{11}r_{32} & r_{11}r_{22} - r_{12}r_{21} \end{pmatrix}$$

now since $\hat{R}$ is orthogonal we have $\hat{R}^{-1} = \hat{R}^T$. From all these considerations the following interesting formula follows:

$$(\hat{R}\vec{x}') \times (\hat{R}\vec{p}') = (\det \hat{R})\hat{R}(\vec{x}' \times \vec{p}') = (\det \hat{R})\hat{R}\vec{L}'.$$

Since $\det \hat{R} = 1$ for proper rotations and $\det \hat{R} = -1$ for improper rotations we have the following characters of the axial vector representation: $Tr[(\det \hat{R})\hat{R}] = 1 + 2\cos\varphi$ for proper rotations and $Tr[(\det \hat{R})\hat{R}] = 1 - 2\cos\varphi$ for improper rotations. Applied to the case of $\underline{D}_{4h}$ we have:

Table A.2.3: Characters of the axial vector representation

$\underline{D}_{4h}$	E	$2C_4$	C_2	$2C_2'$	$2C_2''$	i	$2S_4$	σ_h	$2\sigma_v$	$2\sigma_d$
χ_{AV}	3	1	-1	-1	-1	3	1	-1	-1	-1

which means that axial vector representation decomposes in the group $\underline{D}_{4h}$ in the following way:

$$\Gamma_{AV} = A_{2g} + E_g$$

the first representation in the decomposition being one-dimensional and the second two dimensional. Now we can apply the same reasoning as in the case of the resistivity tensor from which we get:

$$\hat{\chi}_m = \begin{pmatrix} e & 0 & 0 \\ 0 & e & 0 \\ 0 & 0 & f \end{pmatrix}$$ where e and f are real numbers.

Basis vectors are chosen in the same way as in the case of formula A.2.7.

A.3 CLASSIFICATION OF PHONON MODES OF A CRYSTAL AT THE GAMMA POINT

Classification of phonon modes of a crystal at the gamma point (i.e. center of Brillouin zone or zero wave vector point) according to the crystal symmetry is done by decomposition of so called mechanical representation into irreducible representations of point group of a crystal. Mechanical representation is 3r dimensional representation (r-number of atoms in the primitive unit cell) which acts in a vector space spanned by displacement vectors of atoms in a primitive unit cell. It can be shown (the proof is not so simple) that characters of the mechanical representation are given by:

$$\chi_{meh}(\hat{R}) = n_{\hat{R}} \cdot \chi_{PV}(\hat{R})$$

where $n_{\hat{R}}$ is the number of atoms that are transformed into equivalent positions (positions that differs from the original only by lattice vector) by acting of the operator $\hat{R}$ and $\chi_{PV}(\hat{R})$ is the character of polar vector representation that corresponds to the operator $\hat{R}$. Alternative way of decomposing mechanical representation is to take into account the symmetries of sites which atoms of a given crystal occupy (so called Wyckoff positions). A site symmetry is always a subgroup of a point group of a crystal. Polar vector representation decomposes in site symmetry group into irreducible representations of the site symmetry group. Now these irreducible representations induce representations of a point group of a crystal which are in general reducible. Decomposition of all those representations give the decomposition of mechanical representation. Proof and explanations of these sentences can be found for example in [Rb8], [AF49] and [AF48].

A.3.1 CASE OF $SrFeO_3$

In order to apply first method of decomposing mechanical representation we need a primitive cell of $SrFeO_3$. It is shown in the figure A.3.1.1. This structure has a point group $\underline{O}_h$. By method which is described below we can obtain the following table:

Table A.3.1.1: Calculation of characters of mechanical representation.

$\underline{O}_h$	E	$8C_3$	$6C_2$	$6C_4$	$3C_2=C_4^2$	i	$6S_4$	$8S_6$	$3\sigma_h$	$6\sigma_d$
$n_{\hat{R}}$	5	2	3	3	5	5	3	2	5	3
χ_{pv}	3	0	-1	1	-1	-3	-1	0	1	1
χ_{meh}	15	0	-3	3	-5	-15	-3	0	5	3

How did we get this table? Let's have a look at the figure A.3.1.1. Let's assume that the atoms numbered 1, 2, 3, 4 and 5 belong to the drown crystal cell and all others belong to the adjacent crystal cells. If we apply identity operator all those five atoms remain at their

original position so that for this operation n=5. Concerning class $8C_3$ let's choose axis of the order 3 such that it passes through atoms16, 5 and 19. By operation of such chosen C_3

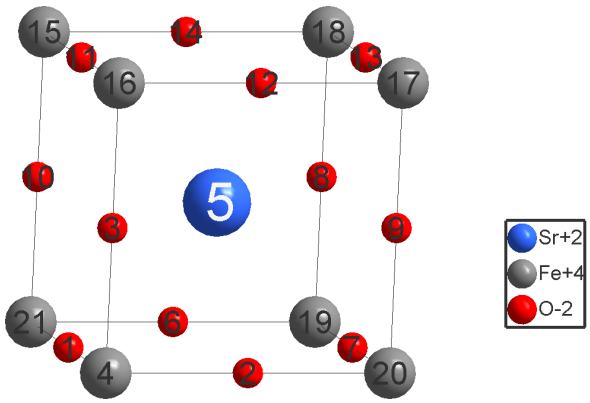

Figure A.3.1.1 (color): Crystal structure of $SrFeO_3$ (numbers on atoms are added in order to make the explanation of calculation easier).

atom 3 moves to the position of atom 12 and this position is equivalent to the position of atom 2, atom 4 moves to atom 17 which is equivalent to atom 4, atom 1 moves to atom 9 which is equivalent to atom 3, atom 2 moves to atom 13 which is equivalent to atom 1 and atom 5 remains on its own place. From all this follows since only atoms 4 and 5 move to equivalent position that for the class $8C_3$ n=2. Concerning the class $6C_2$ let's choose as a representative the axis of order 2 which goes through atoms 3, 5 and 8. By this operation atom 1 goes to position 12 which is equivalent to 2, atom 2 goes to 11 which is equivalent to 1, atom 3 remains in it's original place, atom 4 goes to atom 16 which is equivalent to 4 and atom 5 remains in it's original place. From this follows n=3 for the class $6C_2$. Let's as a final example take the inversion i. It is located at the center of the atom 5. By inversion atom 1 goes to atom 13 which is equivalent to 1, atom 2 goes to atom 14 which is equivalent to 2, atom 3 goes to atom 8 which is equivalent to 3, atom 4 goes to atom 18 which is equivalent to 4 and atom 5 remains in it's place. From all this follows n=5 for the inversion. In a similar way we can obtain n's for remaining operations. The final result is presented in the table A.3.1.1. From it it follows that mechanical representation of $SrFeO_3$ at the gamma point decomposes in the following way:

$$\Gamma_{meh} = \overbrace{3T_{1u}}^{IR-active} + T_{2u} + \overbrace{T_{1u}}^{acoustic} \qquad \text{(A.3.1.1).}$$

Last decomposition means that cubic perovskite structure (to which $SrFeO_3$ belongs) doesn't have Raman active phonons in a first order Raman scattering.

Alternative way of obtaining formula A.3.1.1 is by means of induced representations. For this reason we have to see which irreducible representations of point group of our crystal (in this case it is $\underline{O}_h$) when it is subduced to the point group of a site

in its reduction contains the irreducible representations of point group of a site which appear in the decomposition of polar vector representation. For this reason it is important to note that oxygen atoms occupy site 3d which has the site symmetry $\underline{D}_{4h}$. By subducing each irreducible representation of $\underline{O}_h$ into it's subgroup $\underline{D}_{4h}$ and decomposing it into the irreducible representations of $\underline{D}_{4h}$ we get the following equalities:

$$
\begin{aligned}
&A_{1g}(\underline{O}_h)\downarrow \underline{D}_{4h} = A_{1g}(\underline{D}_{4h})\\
&A_{2g}(\underline{O}_h)\downarrow \underline{D}_{4h} = B_{1g}(\underline{D}_{4h})\\
&E_{g}(\underline{O}_h)\downarrow \underline{D}_{4h} = A_{1g}(\underline{D}_{4h}) + B_{1g}(\underline{D}_{4h})\\
&T_{1g}(\underline{O}_h)\downarrow \underline{D}_{4h} = A_{2g}(\underline{D}_{4h}) + E_{g}(\underline{D}_{4h})\\
&T_{2g}(\underline{O}_h)\downarrow \underline{D}_{4h} = B_{2g}(\underline{D}_{4h}) + E_{g}(\underline{D}_{4h}) \qquad \text{(A.3.1.2).}\\
&A_{1u}(\underline{O}_h)\downarrow \underline{D}_{4h} = A_{1u}(\underline{D}_{4h})\\
&A_{2u}(\underline{O}_h)\downarrow \underline{D}_{4h} = B_{1u}(\underline{D}_{4h})\\
&E_{u}(\underline{O}_h)\downarrow \underline{D}_{4h} = A_{1u}(\underline{D}_{4h}) + B_{1u}(\underline{D}_{4h})\\
&T_{1u}(\underline{O}_h)\downarrow \underline{D}_{4h} = A_{2u}(\underline{D}_{4h}) + E_{u}(\underline{D}_{4h})\\
&T_{2u}(\underline{O}_h)\downarrow \underline{D}_{4h} = B_{2u}(\underline{D}_{4h}) + E_{u}(\underline{D}_{4h})
\end{aligned}
$$

Since in $\underline{D}_{4h}$ polar vector representation decomposes as: $\Gamma_{PV} = A_{2u} + E_u$ we have to find induced representations on the group $\underline{O}_h$ from irreducible representations A_{2u} and E_u of the group $\underline{D}_{4h}$. From Frobenius reciprocity theorem and from equations A.3.1.2 it follows:

$$
\begin{aligned}
&A_{2u}(\underline{D}_{4h})\uparrow \underline{O}_h = T_{1u}(\underline{O}_h)\\
&E_{u}(\underline{D}_{4h})\uparrow \underline{O}_h = T_{1u}(\underline{O}_h) + T_{2u}(\underline{O}_h) \qquad \text{(A.3.1.3).}
\end{aligned}
$$

In this way it is calculated that the contribution of oxygen atoms to the mechanical representation is $2T_{1u} + T_{2u}$. Sr atom occupies the site 1b which has the site symmetry equal to the point group of the crystal i.e. $\underline{O}_h$. In this group polar vector representation decomposes in the following way: $\Gamma_{PV} = T_{1u}$. Since in this case point group of the crystal and site symmetry coincide we have the following formula:

$$T_{1u}(\underline{O}_h)\uparrow \underline{O}_h = T_{1u}(\underline{O}_h)$$

so that the contribution of Sr atom to the mechanical representation is T_{1u}. Fe atom occupies the site 1a. Since this site has also the symmetry $\underline{O}_h$ the contribution of Fe atoms to the mechanical representation is also T_{1u}. If we sum up all these contributions we get:

$$\Gamma_{meh} = 4T_{1u} + T_{2u}$$

which is the same as decomposition obtained by first method (formula A.3.1.1).

A.3.2 CASE OF $CaFeO_3$

Below charge ordering transition (at 290K) $CaFeO_3$ adopts a monoclinic structure with point group C_{2h}. It has four formula units in primitive unit cell which gives in total 20 atoms. For this reason the crystal structure will not be presented here and final result for characters of mechanical representation obtained by first method with a help of program Atoms is:

Table A.3.2.1: Calculation of characters of mechanical representation.

$\underline{C}_{2h}$	$\hat{E}$	$\hat{C}_2$	$\hat{i}$	$\hat{\sigma}_h$
$n_{\hat{R}}$	20	0	4	0
χ_{pv}	3	-1	-3	1
χ_{meh}	60	0	-12	0

From this it follows that mechanical representation at gamma point for the crystal $CaFeO_3$ below charge ordering transition decomposes in the following way:

$$\Gamma_{meh} = \overbrace{12A_g + 12B_g}^{Raman-active} + \overbrace{17A_u + 16B_u}^{IR-active} + \overbrace{A_u + 2B_u}^{acoustic} \qquad \text{(A.3.2.1).}$$

In order to obtain decomposition A.3.2.1 by second method we can start with Ca atoms that occupy site 4e with site symmetry $\underline{C}_1$. This group has only one element: identity and consequently only one irreducible representation denoted with A. Polar vector representation in this group decomposes in the following way: $\Gamma_{PV} = 3A$. Now let's see what subduction of irreducible representations of $\underline{C}_{2h}$ onto its subgroup $\underline{C}_1$ will give. We have:

$$A_g(\underline{C}_{2h}) \downarrow \underline{C}_1 = A(\underline{C}_1)$$
$$B_g(\underline{C}_{2h}) \downarrow \underline{C}_1 = A(\underline{C}_1)$$
$$A_u(\underline{C}_{2h}) \downarrow \underline{C}_1 = A(\underline{C}_1)$$
$$B_u(\underline{C}_{2h}) \downarrow \underline{C}_1 = A(\underline{C}_1)$$

which means (Frobenius theorem) that:

$$A(\underline{C}_1) \uparrow \underline{C}_{2h} = A_g(\underline{C}_{2h}) + B_g(\underline{C}_{2h}) + A_u(\underline{C}_{2h}) + B_u(\underline{C}_{2h}).$$

Conclusion is that Ca atoms contribute with $3A_g + 3B_g + 3A_u + 3B_u$ to the mechanical representation. Fe^{5+} ion occupies the site 2d with site symmetry $\underline{C}_i$. In this group polar vector representation decomposes as: $\Gamma_{PV} = 3A_u$. Subduction of irreducible representations of $\underline{C}_{2h}$ onto $\underline{C}_i$ gives:

$$A_g(\underline{C}_{2h}) \downarrow \underline{C}_i = A_g(\underline{C}_i)$$

$$B_g(\underline{C}_{2h}) \downarrow \underline{C}_i = A_g(\underline{C}_i)$$
$$A_u(\underline{C}_{2h}) \downarrow \underline{C}_i = A_u(\underline{C}_i)$$
$$B_u(\underline{C}_{2h}) \downarrow \underline{C}_i = A_u(\underline{C}_i)$$

from what it follows:

$$A_u(\underline{C}_i) \uparrow \underline{C}_{2h} = A_u(\underline{C}_{2h}) + B_u(\underline{C}_{2h}) .$$

Last equation means that Fe^{5+} ions contribute with $3A_u + 3B_u$ to the mechanical representation. Fe^{3+} ion is located on the site 2c. This site has also site symmetry $\underline{C}_i$ so that the contribution of these ions is the same as of Fe^{5+} ions. Oxygen ions occupy three distinct sites all of them being 4e. This means that their contribution is three times the contribution of Ca atoms i.e. $9A_g + 9B_g + 9A_u + 9B_u$. When we sum up all contributions we get the following decomposition of mechanical representation:

$$\Gamma_{meh} = 12A_g + 12B_g + 18A_u + 18B_u$$

which is the same as decomposition obtained by first way (formula A.3.2.1).

$CaFeO_3$ above charge ordering transition has the point group $\underline{D}_{2h}$ with the following character table (group is Abelian):

Table A.3.2.2: Characters and IR of the point group $\underline{D}_{2h}$.

$\underline{D}_{2h}$	$\hat{E}$	$\hat{C}_2(z)$	$\hat{C}_2(y)$	$\hat{C}_2(x)$	$\hat{i}$	$\hat{\sigma}(xy)$	$\hat{\sigma}(xz)$	$\hat{\sigma}(yz)$
A_g	1	1	1	1	1	1	1	1
B_{1g}	1	1	-1	-1	1	1	-1	-1
B_{2g}	1	-1	1	-1	1	-1	1	-1
B_{3g}	1	-1	-1	1	1	-1	-1	1
A_u	1	1	1	1	-1	-1	-1	-1
B_{1u}	1	1	-1	-1	-1	-1	1	1
B_{2u}	1	-1	1	-1	-1	1	-1	1
B_{3u}	1	-1	-1	1	-1	1	1	-1

Crystal structure is complicated since it contains four formula units per primitive cell. By use of program Atoms with which it was possible to view the crystal structure from different sides the following table was derived:

Table A.3.2.3: Calculation of characters of mechanical representation.

$\underline{D}_{2h}$	$\hat{E}$	$\hat{C}_2(z)$	$\hat{C}_2(y)$	$\hat{C}_2(x)$	$\hat{i}$	$\hat{\sigma}(xy)$	$\hat{\sigma}(xz)$	$\hat{\sigma}(yz)$
$n_{\hat{R}}$	20	0	0	0	4	8	0	0
χ_{pv}	3	-1	-1	-1	-3	1	1	1
χ_{mex}	60	0	0	0	-12	8	0	0

From this it follows that mechanical representation at gamma point for the crystal $CaFeO_3$ above charge ordering transition decomposes in the following way:

$$\Gamma_{meh} = \overbrace{7A_g + 7B_{1g} + 5B_{2g} + 5B_{3g}}^{Raman-active} + 8A_u + \overbrace{7B_{1u} + 9B_{2u} + 9B_{3u}}^{IR-active} + \overbrace{B_{1u} + B_{2u} + B_{3u}}^{acoustic} \quad \text{(A.3.2.2).}$$

Let's now derive formula A.3.2.2 by alternative way. Atoms Ca occupy site 4c with site symmetry $\underline{C}_S$. This group has only two elements: identity and one plane of reflection. Careful analysis of the crystal structure shows that this plane is $\hat{\sigma}(xy)$ (tables A.3.2.2 and A.3.2.3). Irreducible representations and character table are:

Table A.3.2.4: Characters and IR of point group $\underline{C}_S$.

$\underline{C}_S$	$\hat{E}$	$\hat{\sigma}(xy)$
A'	1	1
A''	1	-1

Polar vector representation decomposes as: $\Gamma_{PV} = 2A' + A''$. It can be seen from table A.3.2.2 that only those irreducible representation of $\underline{D}_{2h}$ when subduced to $\underline{C}_S$ give A' (i.e.A'') if they have character 1 (i.e. -1) for $\hat{\sigma}(xy)$. From this it follows:

$$A'(\underline{C}_S) \uparrow \underline{D}_{2h} = A_g(\underline{D}_{2h}) + B_{1g}(\underline{D}_{2h}) + B_{2u}(\underline{D}_{2h}) + B_{3u}(\underline{D}_{2h})$$
$$A''(\underline{C}_S) \uparrow \underline{D}_{2h} = B_{2g}(\underline{D}_{2h}) + B_{3g}(\underline{D}_{2h}) + A_u(\underline{D}_{2h}) + B_{1u}(\underline{D}_{2h})$$

which means that Ca atoms contribute to the mechanical representation with $2A_g + 2B_{1g} + B_{2g} + B_{3g} + A_u + B_{1u} + 2B_{2u} + 2B_{3u}$. Fe atoms occupy site 4b with site symmetry $\underline{C}_i$ in which polar vector representation decomposes as $\Gamma_{PV} = 3A_u$. Only those irreducible representations of $\underline{D}_{2h}$ when subduced to $\underline{C}_i$ give A_u whose character is -1 for inversion. Those are all irreducible representations of $\underline{D}_{2h}$ with subscript "u" so that:

$$A_u(\underline{C}_i) \uparrow \underline{D}_{2h} = A_u(\underline{D}_{2h}) + B_{1u}(\underline{D}_{2h}) + B_{2u}(\underline{D}_{2h}) + B_{3u}(\underline{D}_{2h}).$$

The conclusion is that $3A_u + 3B_{1u} + 3B_{2u} + 3B_{3u}$ is contribution of Fe atoms to the mechanical representation. Oxygen ions occupy sites 8d and 4c. 8d has site symmetry $\underline{C}_1$.

Since this group has only one element and consequently only one irreducible representation it follows that all irreducible representations of $\underline{D}_{2h}$ contain it in the decomposition. This means that contribution of site 8d to the mechanical representation is $3A_g + 3B_{1g} + 3B_{2g} + 3B_{3g} + 3A_u + 3B_{1u} + 3B_{2u} + 3B_{3u}$. Oxygens on site 4c give the same contribution as Ca ions. When we sum up all these contributions we get:

$$\Gamma_{meh} = 7A_g + 7B_{1g} + 5B_{2g} + 5B_{3g} + 8A_u + 8B_{1u} + 10B_{2u} + 10B_{3u}$$

which is the same as decomposition obtained by first method (formula A.3.2.2).

A.3.3 CASE OF $Sr_3Fe_2O_7$

As can be seen in previous three examples decomposition of the mechanical representation at gamma point is not a simple task. Fortunately there is a program on internet [Bilbao Crystallographic Server] which does this task automatically. By use of this program decomposition of mechanical representation on remaining compounds is done. Program uses the method of induced representation (second method in our notation). For the crystal $Sr_3Fe_2O_7$ which belongs to the point group $\underline{D}_{4h}$ we have:

Table A.3.3.1: Contribution to the mechanical representation from corresponding sites.

Sr	2b	$A_{2u}+E_u$
Sr	4e	$A_{1g}+A_{2u}+E_u+E_g$
Fe	4e	$A_{1g}+A_{2u}+E_u+E_g$
O	8g	$A_{1g}+A_{2u}+B_{1g}+B_{2u}+2E_u+2E_g$
O	4e	$A_{1g}+A_{2u}+E_u+E_g$
O	2a	$A_{2u}+E_u$

By summing all those contributions we get the following decomposition of mechanical representation at gamma point for the crystal $Sr_3Fe_2O_7$:

$$\Gamma_{meh} = \overbrace{4A_{1g} + B_{1g} + 5E_g}^{Raman-active} + B_{2u} + \overbrace{5A_{2u} + 6E_u}^{IR-active} + \overbrace{A_{2u} + E_u}^{acoustic} .$$

A.3.4 CASE OF $Sr_8Fe_8O_{23}$

This crystal belongs also to the point group $\underline{D}_{4h}$. Moreover it belongs to the same space group as $Sr_3Fe_2O_7$ (I4/mmm or D_{4h}^{17} or 139). Of course, that doesn't mean that the mechanical representation decomposes in the same way as in the case of $Sr_3Fe_2O_7$. The reason is that in this case different Wyckoff positions are occupied. Contributions from corresponding sites are given in the table A.3.4.1. After summing up all those contributions we get the following decomposition of mechanical representation at gamma point for $Sr_8Fe_8O_{23}$:

$$\Gamma_{meh} = \overbrace{7A_{1g} + 7B_{1g} + 6B_{2g} + 11E_g}^{Raman-active} + \overbrace{12A_{2u} + 19E_u}^{IR-active} + \overbrace{A_{2u} + E_u}^{acoustic} + 3A_{1u} + 6A_{2g} + 7B_{1u} + 6B_{2u}\,.$$

Table A.3.4.1: Contributions of corresponding sites to the mechanical representation.

Sr	8i	$A_{1g}+A_{2g}+A_{2u}+B_{1g}+B_{2g}+B_{2u}+2E_u+E_g$
Sr	8j	$A_{1g}+A_{2g}+A_{2u}+B_{1g}+B_{2g}+B_{2u}+2E_u+E_g$
Fe	4e	$A_{1g}+A_{2u}+E_u+E_g$
Fe	8f	$A_{1u}+2A_{2u}+2B_{1u}+B_{2u}+3E_u$
Fe	4d	$A_{2u}+B_{1g}+E_u+E_g$
O	2b	$A_{2u}+E_u$
O	16m	$2A_{1g}+A_{1u}+A_{2g}+2A_{2u}+B_{1g}+2B_{1u}+2B_{2g}+B_{2u}+3E_u+3E_g$
O	8h	$A_{1g}+A_{2g}+A_{2u}+B_{1g}+B_{1u}+B_{2g}+2E_u+E_g$
O	16k	$A_{1g}+A_{1u}+2A_{2g}+2A_{2u}+2B_{1g}+2B_{1u}+B_{2g}+B_{2u}+3E_u+3E_g$
O	4c	$A_{2u}+B_{2u}+2E_u$

A.3.5 CASE OF $Sr_4Fe_4O_{11}$

$Sr_4Fe_4O_{11}$ belongs to the point group $\underline{D}_{2h}$. Contributions of corresponding sites to the mechanical representation are given in the following table:

Table A.3.5.1: Contributions of corresponding sites to the mechanical representation.

Sr	2c	$B_{1u}+B_{2u}+B_{3u}$
Sr	2d	$B_{1u}+B_{2u}+B_{3u}$
Sr	4g	$A_g+B_{1g}+B_{1u}+B_{2g}+B_{2u}+B_{3u}$
Fe	4i	$A_g+B_{1g}+B_{1u}+B_{2u}+B_{3g}+B_{3u}$
Fe	4f	$A_u+B_{1u}+2B_{2u}+2B_{3u}$
O	2b	$B_{1u}+B_{2u}+B_{3u}$
O	4h	$A_g+B_{1g}+B_{1u}+B_{2g}+B_{2u}+B_{3u}$
O	16r	$3A_g+3A_u+3B_{1g}+3B_{1u}+3B_{2g}+3B_{2u}+3B_{3g}+3B_{3u}$

After summing up all contributions we get the following decomposition of mechanical representation at gamma point for $Sr_4Fe_4O_{11}$:

$$\Gamma_{meh} = \overbrace{6A_g + 6B_{1g} + 5B_{2g} + 4B_{3g}}^{Raman-active} + \overbrace{9B_{1u} + 10B_{2u} + 10B_{3u}}^{IR-active} + \overbrace{B_{1u} + B_{2u} + B_{3u}}^{acoustic} + 4A_u\,.$$

A.4 PREDICTION OF INFRA-RED AND RAMAN ACTIVITIES AND FORM OF THE RAMAN TENSOR

This chapter is mainly recapitulation of results obtained for example in [PouMat]. Results will be just stated, without a proof. First question that arises is what is phonon symmetry convenient for the observation in infra red spectroscopy. By using formula for infra red

absorption and looking symmetry properties of it, it is possible to deduce the following rule:
for a first order scattering at gamma point infra red active are only those irreducible representations of a point group of a crystal which appear in the decomposition of polar vector representation.

Concerning Raman scattering the following rule is valid:
If an irreducible representation of a point group of a crystal with character $\chi^i(\hat{R})$ satisfies the following criterion:

$$\frac{1}{g}\sum_{\hat{R}\in\underline{G}} 2\cos\theta_{\hat{R}} \cdot \chi_{PV}(\hat{R}) \cdot \chi^i(\hat{R}) \neq 0$$

then phonon of a same symmetry is active in a first order Raman scattering ($\hat{R}$ is proper or improper rotation from a point group (with order g) of a crystal $\underline{G}$ and $\theta_{\hat{R}}$ is the angle of rotation that corresponds to $\hat{R}$).
This formula is obtained from the definition of Raman tensor and consideration of its transformation properties. Those two conditions are used in the section A.3 for designation of Raman and infra red active modes that appear in the decomposition of mechanical representation.

Concerning the form of a Raman tensor the symmetry of a crystal helps us in deducing that some of its components are zero while others are mutually equal. In above cited reference this form is deduced for all 32 crystallographic point groups and for all possible irreducible representations which are Raman active. We copy here the results only for the case of $Sr_3Fe_2O_7$ since we will need it in the discussion of Raman data. The result is (basis vectors are oriented along crystal axes):

$$A_{1g}:\hat{R}=\begin{pmatrix} a & 0 & 0 \\ 0 & a & 0 \\ 0 & 0 & b \end{pmatrix},\ B_{1g}:\hat{R}=\begin{pmatrix} c & 0 & 0 \\ 0 & -c & 0 \\ 0 & 0 & 0 \end{pmatrix},\ E_g:\hat{R}=\begin{pmatrix} 0 & 0 & 0 \\ 0 & 0 & e \\ 0 & e & 0 \end{pmatrix} and \hat{R}=\begin{pmatrix} 0 & 0 & e \\ 0 & 0 & 0 \\ e & 0 & 0 \end{pmatrix}.$$

Here $\hat{R}$ denotes Raman tensor. The intensity of scattered radiation in Raman process is proportional to:

$$I \propto \left|\vec{e}_S \cdot \hat{R} \cdot \vec{e}_i\right|^2$$

where $\vec{e}_i$ is polarization of incident photon and $\vec{e}_S$ polarization of scattered photon. This formula is useful in determination of symmetry of observed phonons.

APPENDIX B. DERIVATION OF THE FORMULA 4.6

In order to estimate resistivity from the measured voltage-current ratio ("resistance") we will instead of figure 4.14 consider the following figure:

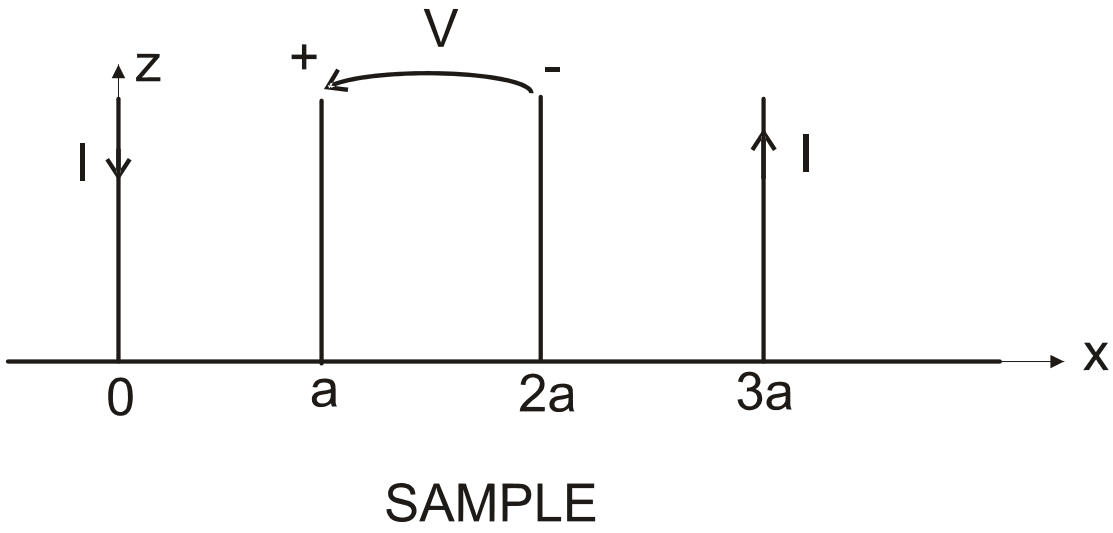

Figure B.1: Approximation of real case (figure 4.14) for calculation of resistivity from the voltage-current ratio ("resistance").

In this figure the following assumptions were used:

-sample is homogenous and isotropic
-sample is infinite in ±x directions
-sample is infinite in –z direction (i.e. below horizontal line in the figure B.1)
-sample is contained between y=-L/2 and y=L/2 planes (y axis is perpendicular to the x and z axes in point 0, i.e. it is perpendicular to the drawing)

in other words, sample is of such shape that it fills the space which is contained between z=0 plane, y=-L/2 plane and y=L/2 plane. Vertical lines represent electrodes and connecting wires. Each line is of rectangular shape such that the width of each line (i.e. dimension perpendicular to the plane of drawing) is equal to L (value shown in the figure

4.14). Through the first left wire the total current I is sent towards the sample. Through first right wire the total current I is taken from the sample. The voltage V is measured between inner two wires. Our task is to find connection between V/I ratio and the resistivity of the sample. This can be done in the following way. The current density in the sample due to the current which flows through the first left wire has the cylindrical symmetry around the line of intersection of the first left wire and the sample surface and is therefore equal to:

$$\vec{j}_1 = \frac{I}{\pi L r_1} \vec{e}_{r1},$$

where r_1 is the distance between the point in the sample where this current density is calculated and the axis of intersection of the first left wire and the sample surface. $\vec{e}_{r1}$ is the unit vector for radial coordinate of cylindrical coordinate system which has origin at the intersection of the first left wire and the sample surface. Similarly the current density in the sample due to the current that flows through the first wire from the right has cylindrical symmetry with the intersection of this wire and the sample surface as the axis of symmetry and this current is equal to:

$$\vec{j}_2 = -\frac{I}{\pi L r_2} \vec{e}_{r2},$$

where r_2 is the distance between the point in the sample where this current density is calculated and the axis of intersection of the first right wire and the sample surface. $\vec{e}_{r2}$ is the unit vector for radial coordinate of cylindrical coordinate system which has origin at the intersection of the first right wire and the sample surface. If we apply the principle of superposition we get for the total current density in the sample:

$$\vec{j} = \vec{j}_1 + \vec{j}_2 .$$

Since sample is homogenous and isotropic we get for the electric field in the sample the following relation:

$$\vec{E} = \rho \cdot \vec{j},$$

with the resistivity ρ independent of the position in the sample. From this we can calculate voltage V in the following way:

$$V = \int_a^{2a} \vec{E} \circ d\vec{r}$$

where the value of the line integral doesn't depend on the path we have chosen to go from a to 2a (this is because the field is static). Because of this independence we can

choose the path to go along the sample surface (i.e along the axis x). For this reasons we get:

$$V = \frac{\rho I}{\pi L}\int_a^{2a}\left(\frac{1}{x}+\frac{1}{3a-x}\right)dx = \frac{\rho I}{\pi L}\left(\ln x\Big|_a^{2a} + \ln(3a-x)\Big|_{2a}^{a}\right) = \frac{\rho I \ln 4}{\pi L},$$

from which it follows:

$$\rho = \frac{V}{I}\cdot\frac{L\pi}{\ln 4}.$$

We have got the formula we seek.

REFERENCES

References are given for each chapter separately and are sorted within each chapter in alphabetical order with respect to the code.

REFERENCES CHAPTER 1

[AndHas] P.W. Anderson and H. Hasegawa: “Considerations on Double Exchange”, Physical Review **100**, 675 (1955).

[BaBrFe] M.N. Baibich, J.M. Broto, A. Fert, F. Nguyen Van Dau, F. Petroff, P. Eitenne, G. Creuzet, A. Friederich and J. Chazelas: “Giant Magnetoresistance of (001)Fe/(001)Cr Magnetic Superlattices”, Physical Review Letters **61**, 2472 (1988).

[BiGrSa] G. Binasch, P. Grünberg, F. Saurenbach and W. Zinn: „Enhanced magnetoresistance in layered magnetic structures with antiferromagnetic inetlayer exchange“, Physical Review B **39**, 4828 (1989).

[BoeVer] J.H. de Boer and E.J.W. Verwey: “Semi-conductors with partially and with completely filled 3d-lattice bands”, Proceedings of the Physical Society of London **49**, 59 (1937).

[deGennes] P.G. de Gennes: “Effects of Double Exchange in Magnetic Crystals”, Physical Review **118**, 141 (1960).

[HeWeHo] R. von Helmolt, J. Wecker, B. Holzapfel, L. Schultz and K. Samwer: „Giant Negative Magnetoresistance in Perovskitelike $La_{2/3}Ba_{1/3}MnO_x$ Ferromagnetic Films”, Physical Review Letters **71**, 2331 (1993).

[Hubb] J. Hubbard: “Electron Correlations in Narrow Energy Bands”, Proceedings of the Royal Society of London. Series A, Mathematical and Physical Sciences **276**, 238 (1963).

[JonSan] G.H Jonker and J.H. van Santen: “Ferromagnetic compounds of manganese with perovskite structure”, Physica **16**, 337 (1950).

[MiLiSh] A.J. Millis, P.B. Littlewood and B.I. Shraiman: “Double Exchange Alone Does Not Explain the Resistivity of $La_{1-x}Sr_xMnO_3$”, Physical Review Letters **74**, 5144 (1995).

[Mott] N.F. Mott: “Discussion of the paper by de Boer and Verwey”, Proceedings of the Physical Society of London **49**, 72 (1937).

[ToAsMo] Yasuhide Tomioka, Atsushi Asamitsu, Yutaka Morimoto and Yoshinori Tokura: “Anomalous Magnetotransport Properties of $Pr_{1-x}Ca_xMnO_3$”, Journal of the Physical Society of Japan **64**, 3626 (1995).

[Zener] Clarence Zener: “Interaction between the d-Shells in the Transition Metals. II. Ferromagnetic Compounds of Manganese with Perovskite Structure”, Physical Review **82**, 403 (1951).

REFERENCES CHAPTER 2

[AdLeDa] P. Adler, A. Lebon, V. Damljanović, C. Ulrich, C. Bernhard, A. V. Boris, A. Maljuk, C. T. Lin and B. Keimer: ”Magnetoresistance effects in $SrFeO_{3-\delta}$: Dependence on phase composition and relation to magnetic and charge order”, Physical Review B **73**, 094451 (2006).

[Adler] P. Adler: „Comment on „Spin- and charge-ordering in oxygen-vacancy-ordered mixed-valence $Sr_4Fe_4O_{11}$””, Physical Review B **77**, 136401 (2008).

[BoFuMi] A. E. Bocquet, A. Fujimori, T. Mizokawa, T. Saitoh, H. Namatame, S. Suga, N. Kimizuka, Y. Takeda and M. Takano: “Electronic structure of $SrFe^{4+}O_3$ and related Fe perovskite oxides”, Physical Review B **45**, 1561 (1992).

[FoPoGr] L. Fournès, Y. Potin, J. C. Grenier, G. Demazeau and M. Pouchard: “High temperature Mössbauer spectroscopy of some $SrFeO_{3-y}$ phases”, Solid State Communications **62**, 239 (1987).

[Gall] P. K. Gallagher, J.B. MacChesney and D. N. E. Buchanan: “Mössbauer Effect in the System $SrFeO_{2.5-3.0}$”, The Journal of Chemical Physics **41**, 2429 (1964).

[GalRoh] Julian D. Gale and Andrew L. Rohl: “The General Utility Lattice Program (GULP)”, Molecular Simulation **29**, 291 (2003).

[Gibb1] Terence C. Gibb: “Magnetic Exchange Interactions in Perovskite Solid Solutions Part 5. The Unusual Defect Structure of $SrFeO_{3-y}$”, Journal of the Chemical Society -- Dalton Transactions (7), 1455 (1985).

[Gibb2] Terence C. Gibb: “Reinterpretation of the Magnetic Structures of the Perovskites $SrFeO_{2.710}$ and $Sr_2LaFe_3O_{8.417}$”, Journal of Materials Chemistry **4**, 1445 (1994).

[Ha10] “Einführung in die Atomphysik”, Wolfgang Finkelnburg, Springer Berlin Heidelberg, 1976.

[HaAtKa] Camilla Haavik, Tooru Atake, Hitoshi Kawai and Svein Stølen: “On the entropic contribution to the redox energetics of $SrFeO_{3-\delta}$”, Physical Chemistry Chemical Physics **3**, 3863 (2001).

[HaBaNo] Camilla Haavik, Egil Bakken, Truls Norby, Svein Stølen, Tooru Atake and Takeo Tojo: “Heat capacity of $SrFeO_{3-\delta}$; δ=0.50, 0.25 and 0.15 – configurational entropy of structural entities in grossly non-stoichiometric oxides”, Dalton Transactions (3), 361 (2003).

[Hodg] J. P. Hodges, S. Short, J. D. Jorgensen, X. Xiong, B. Dabrovski, S. M. Mini and C. W. Kimball: “Evolution of Oxygen-Vacancy Ordered Crystal Structures in the Perovskite Series $Sr_nFe_nO_{3n-1}$ (n=2, 4, 8 and ∞), and the Relationship to Electronic and Magnetic Properties”, Journal of Solid State Chemistry **151**, 190 (2000).

[JBMac] J. B. MacChesney, R. C. Sherwood and J. F. Potter: “Electric and Magnetic Properties of the Strontium Ferrates”, The Journal of Chemical Physics **43**, 1907 (1965).

[JJ3] “Elements of theoretical magnetism”, Svatopluk Krupička (editor), Iliffe Books London, 1968.

[Jm9] “Color centers in solids”, James H. Schulman and W. Dale Compton, Pergamon Press Oxford, 1962.

[KaNaKu] Takateru Kawakami, Saburo Nasu, Kaori Kuzushita, Tetsuya Sasaki, Shotaro Morimoto, Takahiro Yamada, Shoichi Endo, Shuji Kawasaki and Mikio Takano: “High-Pressure Mössbauer and X-Ray Powder Diffraction Studies of $SrFeO_3$”, Journal of the Physical Society of Japan **72**, 33 (2003).

[Kosl1] Thorsten Koslowski: “Unusual defects and the electronic structure of the nonstoichiometric perovskite $SrFeO_{3-\delta}$: a numerical approach”, Physical Chemistry Chemical Physics **1**, 3017 (1999).

[LeAdBe] A. Lebon, P. Adler, C. Bernhard, A. V. Boris, A. V. Pimenov, A. Maljuk, C.T. Lin, C. Ulrich and B. Keimer: „Magnetism, Charge Order and Giant Magnetoresistance in $SrFeO_{3-\delta}$ Single Crystals”, Physical Review Letters **92**, 037202 (2004).

[MaLeDa] A. Maljuk, A. Lebon, V. Damljanović, C. Ulrich, C. T. Lin, P. Adler and B. Keimer: „Growth and oxygen treatment of $SrFeO_{3-y}$ single crystals”, Journal of Crystal Growth **291**, 412 (2006).

[MaMoDe] S. F. Matar, P. Mohn and G. Demazeau: “The magnetic structure of $SrFeO_3$ calculated within LDA”, Journal of Magnetism and Magnetic Materials **140-144**, 169 (1995).

[MaStUl] A. Maljuk, J. Strempfer, C. Ulrich, A. Lebon and C. T. Lin: „Growth and characterization of high-quality $SrFeO_x$ single crystals”, Journal of Crystal Growth **257**, 427 (2003).

[MiOkYa] Junichiro Mizusaki, Masanobu Okayasu, Shigeru Yamauchi and Kazuo Fueki: “Nonstoichiometry and Phase Relationship of the $SrFeO_{2.5}$-$SrFeO_3$ System at High Temperature”, Journal of Solid State Chemistry **99**, 166 (1992).

[NakIid] Shin Nakamura and Shuichi Iida: “New Data on Electrical Properties and Antiferromagnetism of Highly Oxidized Perovskite $SrFeO_x$ ($2.5<x<3.0$)”, Japanese Journal of Applied Physics Part 2 – Letters **34** (3A), L291 (1995).

[OdaYaTa] Hitoshi Oda, Yasuo Yamaguchi, Humihiko Takei and Hiroshi Watanabe: “Single Crystal Neutron Diffraction Study of $SrFeO_{3-x}$ (x=0.1)”, Journal of the Physical Society of Japan **42**, 101 (1977).

[PCb21] “Solid state chemistry”, Lesley E. Smart and Elaine A. Moore, CRC Taylor & Francis Boca Raton, 2005.

[Qa4] “Modern aspects of solid state chemistry”, Chintamani N. R. Rao (editor), Plenum Press New York, 1970.

[SchCam] M. Schmidt and S. J. Campbell: „In situ neutron diffraction study (300-1273K) of non-stoichiometric strontium ferrite $SrFeO_x$”, Journal of Physics and Chemistry of Solids **63**, 2085 (2002).

[ScHoCa] M. Schmidt, M. Hofmann and S. J. Campbell: „Magnetic structure of strontium ferrite $Sr_4Fe_4O_{11}$”, Journal of Physics: Condensed Matter **15**, 8691 (2003).

[ScJiSc] Stefanie Schott, Zhihong Jia, Andreas K. Schaper, Venkataraman Thangadurai, Werner Weppner and Peter Schmid-Beurmann: “Superlattice ordering in $SrFeO_{3-\delta}$: Electron microscopy and diffraction study”, Physica Status Solidi (a) **202**, 2330 (2005).

[TaKaTaYa] Y. Takeda, K. Kanno, T. Takada, O. Yamamoto, M. Takano, N. Nakayama and Y. Bando: “Phase Relation in the Oxygen Nonstoichiometric System, $SrFeO_x$ ($2.5 \leq x \leq 3.0$)”, Journal of Solid State Chemistry **63**, 237 (1986).

[TaOkNa] M. Takano, T. Okita, N. Nakayama, Y. Bando, Y. Takeda, O. Yamamoto and J. B. Goodenough: “Dependence of the Structure and Electronic State of $SrFeO_x$ ($2.5 \leq x \leq 3$) on Composition and Temperature”, Journal of Solid State Chemistry **73**, 140 (1988).

[TaYaWa] Takayoshi Takeda, Yasuo Yamaguchi and Hiroshi Watanabe: “Magnetic Structure of $SrFeO_3$”, Journal of the Physical Society of Japan **33**, 967 (1972).

[ToGrFe] B. C. Tofield, C. Greaves and B.E.F. Fender: “The $SrFeO_{2.5}$ – $SrFeO_{3.0}$ system. Evidence of a new phase $Sr_4Fe_4O_{11}$ ($SrFeO_{2.75}$)”, Materials Research Bulletin **10**, 737 (1975).

[ViRaFj] R. Vidya, P. Ravindran, H. Fjellvåg and A. Kjekshus: “Spin- and charge-ordering in oxygen-vacancy-ordered mixed-valence $Sr_4Fe_4O_{11}$”, Physical Review B **74**, 054422 (2006).

[WaFoDe] A. Wattiaux, L. Fournès, A. Demourgues, N. Bernaben, J. C. Grenier and M. Pouchard: “A Novel Preparation Method of the $SrFeO_3$ Cubic Perovskite by Electrochemical Means”, Solid State Communications **77**, 489 (1991).

[Wata] Hiroshi Watanabe: “Magnetic Properties of Perovskites Containing Strontium I. Strontium-Rich Ferrites and Cobaltites”, Journal of the Physical Society of Japan **12**, 515 (1957).

[WisBec] S. Wiβmann and K. D. Becker: “Localization of electrons in nonstoichiometric $SrFeO_{3-\Delta}$”, Solid State Ionics **85**, 279 (1996).

[YuKoIv] É. I. Yuryeva, V. L. Kozhevnikov and A. L. Ivanovskii: “Charge States and Hyperfine Interaction Parameters in Perovskite $SrFeO_3$”, Journal of Structural Chemistry **47**, 553 (2006).

[ZhaoZhou] Y. M. Zhao and P. F. Zhou: “Metal-insulator transition in helical $SrFeO_{3-\delta}$ antiferromagnet”, Journal of Magnetism and Magnetic Materials **281**, 214 (2004).

[ZhMaNg] Y. M. Zhao, R. Mahendiran, N. Nguyen, B. Raveau and R. H. Yao: “$SrFeO_{2.95}$: A helical antiferromagnet with large magnetoresistance”, Physical Review B **64**, 024414 (2001).

[ZhYaZh] Y. M. Zhao, X. J. Yang, Y. F. Zheng, D. L. Li and S. Y. Chen: “Large magnetoresistance in $SrFeO_{2.95}$”, Solid State Communications **115**, 365 (2000).

[ZhZhYa] Y.M. Zhao, P. F. Zhou, X. J. Yang, G. M. Qiu and L. Ping: “Magnetotransport properties of $SrFeO_{2.95}$ perovskite”, Solid State Communications **120**, 283 (2001).

REFERENCES CHAPTER 3

[AbAsMo] M. Abbate, H. Ascolani, L. Mogni, F. Prado, A. Caneiro: “Electronic structure of the negative charge-transfer material Sr_3FeMO_7 (M = Fe, Co, Ni)”, Physica B **354**, 7 (2004).

[AbAsPr] M. Abbate, H. Ascolani, F. Prado, A. Caneiro: “Electronic structure and band gap of the negative charge-transfer material $Sr_3Fe_2O_7$”, Solid State Communications **129**, 113 (2004).

[AbMoPr] M. Abbate, L. Mogni, F. Prado, A. Caneiro: “Electronic structure of the two--dimensional negative charge-transfer material Sr_3FeMO_7 (M = Fe, Co)”, Physical Review B **71**, 195113 (2005).

[AbZaOk] M. Abbate, G. Zampieri, J. Okamoto, A. Fujimori, S. Kawasaki, M. Takano: “X-ray absorption of the negative charge-transfer material $SrFe_{1-x}Co_xO_3$”, Physical Review B **65**, 165120 (2002).

[Adler] P. Adler: ”Electronic State, Magnetism, and Electrical Transport Behavior of $Sr_{3-x}A_xFe_2O_7$ ($x \leq 0.4$, A=Ba, La)”, Journal of Solid State Chemistry **130**, 129 (1997).

[AdScSy] P. Adler, U. Schwarz, K. Syassen, G. Kh. Rozenberg, G. Yu. Machavariani, A. P. Milner, M. P. Pasternak and M. Hanfland: ”Collapse of the charge disproportionation and covalency-driven insulator-metal transition in $Sr_3Fe_2O_7$ under pressure”, Physical Review B **60**, 4609 (1999).

[Boris] A.V. Boris (unpublished data).

[Crys] CRYSTAL06 User’s Manual (2007), page 181.

[DaWeCu1] S.E. Dann, M.T. Weller and D.B. Currie: “Structure and Oxygen Stoichiometry in $Sr_3Fe_2O_{7-y}$, $0 \leq y \leq 1.0$”, Journal of Solid State Chemistry **97**, 179 (1992).

[DaWeCu2] Sandra E. Dann, Mark T. Weller, David B. Currie, Michael F. Thomas and Ahmed D. Al-Rawwas: „Structure and Magnetic Properties of Sr_2FeO_4 and $Sr_3Fe_2O_7$ studied by Powder Neutron Diffraction and Mössbauer Spectroscopy”, Journal of Materials Chemistry **3**, 1231 (1993).

[GaMacBu] P.K. Gallagher, J.B. MacChesney, and D.N.E. Buchanan: “Mössbauer effect in the System $Sr_3Fe_2O_{6-7}$”, The Journal of Chemical Physics **45**, 2466 (1966).

[GhoAdl] Samrat Ghosh and Peter Adler: “Evolution of electronic state, magnetism, and magnetotransport properties in $Sr_3Fe_{2-x}Co_xO_{7-y}$ ($x \leq 1$)”, Journal of Materials Chemistry **12**, 511 (2002).

[GlMiSu] M. Gloris, R. Michel, F. Sudbrock, U. Herpers, P. Malmborg, B. Holmqvist: “Proton-induced production of residual radionuclides in lead at intermediate energies” Nuclear Instruments and Methods in Physics Research A **463**, 593 (2001).

[Glor] “Proton-induzierte Restkernproduktion in schweren Elementen bei mittleren Energien“, Dissertation von Martin Gloris, Universität Hannover 1998.

[Jl47/1] “Light Scattering in Solids I”, M. Cardona (editor), second edition, Springer--Verlag 1983.

[Jl47/3] “Light Scattering in Solids III”, M. Cardona (editor), Springer-Verlag 1982.

[Jl47/4] “Light Scattering in Solids IV”, M. Cardona (editor), Springer-Verlag 1984.

[Jn15] “Introduction to the Theory of Thermal Neutron Scattering”, G. L. Squires, Dover Publications INC., Mineola, New York 1996.

[KuMoNa1] Kaori Kuzushita, Shotaro Morimoto, Saburo Nasu and Shin Nakamura: “Charge Disproprtionation and Antiferromagnetic Order of $Sr_3Fe_2O_7$”, Journal of the Physical Society of Japan **69**, 2767 (2000).

[KuMoNa2] Kaori Kuzishita, Shotaro Morimoto, Saburo Nasu: “Charge disproportionation and magnetic properties in perovskite iron oxides”, Physica B-Condensed Matter **329**, 736 (2003).

[LonWon] M. A. Lone, P. Y. Wong: “Neutron yields from proton-induced spallation reactions in thick targets of lead”, Nuclear Instruments and Methods in Physics Research A **362**, 499 (1995).

[LuMiSl1] Elio Lucchini, Dino Minichelli and Giorgo Sloccari: “The crystal structure of α-$Sr_3Fe_2O_{7-x}$”, Acta Crystallographica Section B-Structural Science **B29**, 2356 (1973).

[LuMiSl2] Elio Lucchini, Dino Minicheli, Giorgio Sloccari: “Polymorphism in $Sr_3Fe_2O_{7-x}$”, Journal of Materials Science **9**, 212 (1974).

[MaMiFu] J. Matsuno, T. Mizokawa, A. Fujimori, Y. Takeda, S. Kawasaki, M. Takano: “Different routes to charge disproportionation in perovskite-type Fe oxides”, Physical Review B **66**, 193103 (2002).

[MaStUl] A. Maljuk, J. Strempfer, C. Ulrich, M. Sofin, L. Capogna, C.T. Lin, B. Keimer „Growth of $Sr_3Fe_2O_{7-x}$ single crystals by the floating zone method“, Journal of Crystal growth **273**, 207 (2004).

[MoFoPr] L. Mogni, J. Fouletier, F. Prado, A. Caneiro: “High-temperature thermodynamic and transport properties of the $Sr_3Fe_2O_{6+\delta}$ mixed conductor”, Journal of Solid State Chemistry **178**, 2715 (2005).

[MoKaKo1] K. Mori, T. Kamiyama, H. Kobayashi, S. Torii, F. Izumi, H. Asano: “Crystal structure of $Sr_3Fe_2O_{7-\delta}$”, Journal of Physics and Chemistry of Solids **60**, 1443 (1999).

[MoKaKo2] K. Mori, T. Kamiyama, H. Kobayashi, T. Arima, K. Ohoyama, S. Ikeda: "The oxygen dependence of the magnetic structure for $Sr_3Fe_2O_{7-\delta}$", Applied Physics A -Materials Science and Processing **74**, S914 (2002).

[Mont] H.C. Montgomery: "Method for Measuring Electrical Resistivity of Anisotropic Materials", Journal of Applied Physics **42**, 2971 (1971).

[MoPrAs] Liliana Mogni, Fernanado Prado, Hugo Ascolani, Miguel Abbate, Mario S. Moreno, Arumugam Manthiram, Alberto Caneiro: "Synthesis, crystal chemistry and physical properties of the Ruddlesden-Popper phases $Sr_3Fe_{2-x}Ni_xO_{7-\delta}$ ($0 \leq x \leq 1.0$)", Journal of Solid State Chemistry **178**, 1559 (2005).

[Mos1] Maxim Mostovoy: "Helicoidal magnetic ordering in double exchange systems", Journal of Physics: Condensed Matter **17**, S753 (2005).

[Mos2] Maxim Mostovoy: "Helicoidal Ordering in Iron Perovskites", Physical Review Letters **94**, 137205 (2005).

[Naga] Takeo Nagamiya: "Helical Spin Ordering – 1 Theory of Helical Spin Configurations", Solid State Physics **20**, 305 (1967).

[Pauw1] L.J. van der Pauw: "A Method of Measuring Specific Resistivity and Hall Effect of Discs of Arbitrary Shape", Philips Research Reports **13**, 1 (1958).

[Pauw2] L.J. van der Pauw: "Determination of Resistivity Tensor and Hall Tensor of Anisotropic Conductors", Philips Research Reports **16**, 187 (1961).

[PraMan] F. Prado and A. Manthiram: "Synthesis, Crystal Chemistry, and Electrical and Magnetic Properties of $Sr_3Fe_{2-x}Co_xO_{7-\delta}$ ($0 \leq x \leq 0.8$)", Journal of Solid State Chemistry **158**, 307 (2001).

[PrMoCu] F. Prado, L. Mogni, G.J. Cuello, A. Caneiro: "Neutron powder diffraction study at high temperature of the Ruddlesden-Popper phase $Sr_3Fe_2O_{6+\delta}$", Solid State Ionics **178**, 77 (2007).

[RoMaPa] G.Kh. Rozenberg, G.Yu. Machavariani, M.P. Pasternak, A.P. Milner, G.R. Hearne, R.D. Taylor, and P. Adler: "Pressure-Induced Metallization of the Perovskite $Sr_3Fe_2O_7$", Physica Status Solidi B – Basic Research **211**, 351 (1999).

[RudPop] S.N. Ruddlesden and P. Popper: "The compound $Sr_3Ti_2O_7$ and its structure", Acta Crystallographica **11**, 54 (1958).

[ZaKoKo1] V.M. Zainullina, M.A. Korotin, and V.L. Kozhevnikov: "Electronic structure and properties of strontium ferrite $Sr_3Fe_2O_6$", The European Physical Journal B **49**, 425 (2006).

[ZaKoKo2] V.M Zainullina, M.A. Korotin, and V.L. Kozhevnikov: “Electronic and Magnetic Structures and Conductivity of Strontium Ferrite: An Ab Initio LSDA + U Approach”, Russian Journal of Electrochemistry **43**, 570 (2007).

REFERENCES CHAPTER 4

[AdaHar] S. B. Adams, T. R. Hart: “Raman Scattering from Phonons in α-Fe_2O_3”, Bulletin of the American Physical Society **18**, 658 (1973).

[BeErHu] P. Berastegui, S. –G. Eriksson, S. Hull: „A neutron diffraction study of the temperature dependence of $Ca_2Fe_2O_5$”, Materials Research Bulletin **34**, 303 (1999).

[BeKuUb] Gesa Behrens, Liisa T. Kuhn, Rick Ubic, Arthur H. Heuer: „Raman Spectra of Vateritic Calcium Carbonate“, Spectroscopy Letters **28**, 983 (1995).

[DaDeFa] S. Darracq, G. Demazeau, P. Fabritchnyi, L. Fournes, I. A. Presniakov, K. V. Pokholok, V. P. Gorkov: “Etude par spectrometrie Mössbauer de la perovskite CaFe(IV)O_3 a l’aide d’une sonde diamagnetique ^{119}Sn “, Solid State Communications **91**, 681 (1994).

[GaTaRo] L. V. Gasparov, D. B. Tanner, D. B. Romero, H. Berger, G. Margaritondo, L. Forró: “Infrared and Raman studies of the Verwey transition in magnetite”, Physical Review B **62**, 7939 (2000).

[GhKaSe] Shankar Ghosh, N. Kamaraju, M. Seto, A. Fujimori, Y. Takeda, S. Ishiwata, S. Kawasaki, M. Azuma, M. Takano, A. K. Sood: „Raman scattering in $CaFeO_3$ and $La_{0.33}Sr_{0.67}FeO_3$ across the charge-disproportionation phase transition”, Physical Review B **71**, 245110 (2005).

[GuSoMe] Rajeev Gupta, A. K. Sood, P. Metcalf, J. M. Honig: “Raman study of stoichiometric and Zn-doped Fe_3O_4”, Physical Review B **65**, 104430 (2002).

[HarAda] T. R. Hart, S. B. Adams: “Raman Scattering from Magnons in α-Fe_2O_3”, Bulletin of the American Physical Society **18**, 658 (1973).

[IshSak] M. Ishigame, T. Sakurai: “Temperature Dependence of the Raman Spectra of ZrO_2”, Journal of the American Ceramic Society **60**, 367 (1977).

[Ja52] “Solid State Physics”, Neil W. Ashcroft and N. David Mermin, Thomson Learning INC. 1976.

[Jahn] H. A. Jahn: “Stability of Polyatomic Molecules in Degenerate Electronic States. II-Spin Degeneracy”, Proceedings of the Royal Society of London. Series A, Mathematical and Physical Sciences **164**, 117 (1938).

[JahTel] H. A. Jahn, E. Teller: „Stability of Polyatomic Molecules in Degenerate Electronic States. I-Orbital Degeneracy", Proceedings of the Royal Society of London. Series A, Mathematical and Physical Sciences **161**, 220 (1937).

[Jc177] "Physics of Transition Metal Oxides", S. Maekawa, T. Tohyama, S. E. Barnes, S. Ishihara, W. Koshibae, G. Khaliullin, Springer-Verlag Berlin Heidelberg, 2004.

[KaMiMi] F. Kanamaru, H. Miyamoto, Y. Mimura, M. Koizumi, M. Shimada, S. Kume, S. Shin: "Synthesis of a New Perovskite $CaFeO_3$", Materials Research Bulletin **5**, 257 (1970).

[KaTaKa] Shuji Kawasaki, Mikio Takano, Ryoji Kanno, Takashi Takeda, Atsushi Fujimori: "Phase Transitions in Fe^{4+} ($3d^4$)-Perovskite Oxides Dominated by Oxygen-Hole Character", Journal of the Physical Society of Japan **67**, 1529 (1998).

[Ke] S. C. Ke: "Raman spectrum of H^{2-} ions in calcium oxide crystals", Physical Review B **62**, 4194 (2000).

[KeMaTo] S. C. Ke, J. C. Martin, H. T. Tohver: "Symmetry assignment of Raman scattering by F^+ and F centers in calcium oxide", Journal of Physics: Condensed Matter **7**, 7063 (1995).

[MaBaMe] M. J. Massey, U. Baier, R. Merlin, W. H. Weber: "Effects of pressure and isotopic substitution on the Raman spectrum of α-Fe_2O_3: Identification of two-magnon scattering", Physical Review B **41**, 7822 (1990).

[MaMeHu] T. P. Martin, R. Merlin, D. R. Huffman, M. Cardona: „Resonant Two Magnon Raman Scattering in α-Fe_2O_3", Solid State Communications **22**, 565 (1977).

[MaStLi] A. Maljuk, J. Strempfer, C. T. Lin: „Floating zone growth and characterization of $Ca_2Fe_2O_5$ single crystals", Journal of Crystal Growth **258**, 435 (2003).

[McElf] "Fundamentals of Magnetism and Magnetic Measurements Featuring Quantum Design's Magnetic Property Measurement System", Mike McElfresh, Quantum Design 1994.

[NicEll] Malcolm Nicol, William D. Ellenson: "Raman Spectrum of $CaCO_3$III at 77K", The Journal of Chemical Physics **56**, 677 (1972).

[SheLaz1] Olga N. Shebanova, Peter Lazor: "Raman spectroscopic study of magnetite ($FeFe_2O_4$): a new assignment for the vibrational spectrum", Journal of Solid State Chemistry **174**, 424 (2003).

[SheLaz2] Olga N. Shebanova, Peter Lazor: "Raman study of magnetite (Fe_3O_4): laser--induced thermal effects and oxidation", Journal of Raman Spectroscopy **34**, 845 (2003).

[TaFuKo] Y. Tanabe, Y. Fujimaki, K. Kojima, S. Uchida, S. Onari, T. Matsuo, S. Azuma, E. Hanamura: "Direct optical excitation of two and three magnons in α-Fe_2O_3", Low Temperature Physics **31**, 780 (2005).

[TaKaKa] Takashi Takeda, Ryoji Kanno, Yoji Kawamoto, Mikio Takano, Syuji Kawasaki, Takashi Kamiyama, Fujio Izumi: "Metal-semiconductor transition, charge disproportionation, and low-temperature structure of $Ca_{1-x}Sr_xFeO_3$ synthesized under high-oxygen pressure", Solid State Sciences **2**, 673 (2000).

[TaNaTa] M. Takano, N. Nakanishi, Y. Takeda, S. Naka, T. Takada: "Charge Disproportionation in $CaFeO_3$ Studied With the Möβbauer Effect", Materials Research Bulletin **12**, 923 (1977).

[ToPoPo] N. Toupry, H. Poulet, M. Le Postollec, R. M. Pick, M. Yvinec: "A Raman Spectroscopic Study of the Structural Phase Transition and Reorientational Motions of the ClO_4^- Ions in $KClO_4$", Journal of Raman Spectroscopy **14**, 166 (1983).

[WhKoVi] M. –H. Whangbo, H. –J. Koo, A. Villesuzanne, M. Puochard: „Effect of Metal-Oxygen Covalent Bonding on the Competition between Jahn-Teller Distortion and Charge Disproportionation in the Perovskites of High-Spin d^4 Metal Ions $LaMnO_3$ and $CaFeO_3$", Inorganic Chemistry **41**, 1920 (2002).

[WoCoMo] P. M. Woodward, D. E. Cox, E. Moshopoulou , A. W. Sleight, S. Morimoto: "Structural studies of charge disproportionation and magnetic order in $CaFeO_3$", Physical Review B **62**, 844 (2000).

REFERENCES APPENDIX A

[Af4] "The application of group theory in physics", Grigorij Ja. Ljubarskii, Oxford Pergamon Press, 1960.

[Af48] "Group theory and its applications in physics", Teturo Inui, Yukito Tanabe, Yositaka Onodera, Berlin, Heidelberg, Springer Verlag, 1990.

[Af49] "Symmetries in physics", Wolfgang Ludwig, Claus Falter, Berlin, Heidelberg, Springer Verlag, 1988.

[Af51] All tables of irreducible representations and their characters in this chapter are taken from the following book: "Point-group theory tables", Simon L. Altmann and Peter Herzig, Oxford Clarendon Press, 1994.

[Bd1a/3] "Quantum mechanics", Lev Davidovič Landau, Evgenij Michailovič Lifšic, Oxford Pergamon Press, 1965.

[PouMat] “Vibration spectra and symmetry of crystals”, Henri Poulet, Jean-Paul Mathieu, New York, Gordon and Breach, 1976.

[Rb6] “Crystal properties via group theory”, Arthur S. Nowick, Cambridge University Press, 1995.

[Rb8] “Site symmetry in crystals”, Robert A. Evarestov, Vjačeslav P. Smirnov, Berlin, Heidelberg, Springer Verlag, 1997.

ACKNOWLEDGMENTS

I am thankful to the following persons whose help was important for my PhD thesis:

* Professor Dr. Bernhard Keimer for accepting me as a PhD student in his group, for supervising my work during the whole time and for reading and correcting this thesis. All topics and tasks fulfilled here are his ideas (except the study of how can we apply existing results of group theory in connection with our experiments on the systems investigated, which was my personal interest).

* Professor Dr. Peter Michler for kindly accepting the task of being Mitberichter for this thesis, which implies reading it and reviewing it.

* Dr. C. Ulrich for daily discussion of experimental data I have obtained, help in the Raman lab, help with the program GULP and especially for neutron scattering experiments (presented in section 3.2) where I took part mostly as an observer/helper. He also prepared figures 3.11 and 3.12.

* Dr. Peter Adler for performing Möβbauer experiments on the sample B2 and preparing figure 2.13. Also for useful discussions related to Möβbauer spectroscopy.

* Dr. Andrei Maljuk for growing single crystals investigated in this thesis.

* Dr. Paul Balog for performing high pressure annealing of $CaFeO_3$ and $SrFeO_3$ samples.

* Dr. Robert E. Dinnebier for help with powder X-ray diffraction experiments on samples #1 and #2.

* Dr. A. V. Boris for showing me his infra-red data on $Sr_3Fe_2O_{7-\delta}$ which I used latter to estimate its resistivity from voltage-current ratio (figure 5.4).

* Barbara Baum and Helmut Wendel for cutting and polishing samples.

* S. Schmid, B. Stuhlhofer and F. Schartner for sputtering the electrodes and making contacts and wires on the samples used to measure resistivity and magnetoresistance.

* Heinrich Klann for his generous help in using PPMS setup.

* Dr. N. Kovaleva and M. Guennou for useful hints in using program GULP.

* M. Bakr for his help in the Raman lab in the last two experiments.

* Anton Suchaneck, Britta Bohnenbuck and Dr. Markus Raichle for translating English Abstract into German Zusamennfassung.

In addition I wish to thank the following persons who didn't directly contribute to my thesis but have helped me in administrative tasks, supporting literature, provided participation in events which one normally sees only once in life or made my life in Stuttgart more enjoyable. I wish to thank:

* Claudia Hagemann for her help in administration during my stay in Stuttgart.

* Brigit King for help in formalities related to German visas.

* EDV team for maintenance of computers which I used.

* MPI Library team for getting hardly available books or journal articles, also for the access to the on-line journals. It was a pleasant surprise to see that some old papers (for example those of classics of quantum mechanics) are available. This thing I will miss very much once I leave MPI.

* Professor Dr. Klaus von Klitzing, Nobel laureate, for giving me the opportunity together with some other PhD students from our both institutes and the University of Stuttgart to attend the meeting of PhD students with Nobel laureates in Physics held in Lindau (Germany) from 27th June 2004. to 2nd July 2004. Although my three favorites cancelled in the last moment, this was still valuable and unforgettable experience.

* My former and present office mates: Ioannis Zegkinoglou, Vladimir Hinkov, Markus Raichle, Daniel Haug and Ji Tae Park for making a friendly atmosphere in our office and stimulating discussions.

* The people who were from October 2003. till the end of 2008. members of Professor Keimer's group (sorry for not naming them all) for good working environment.

* All those wonderful people from all around the world which I have met during my PhD time in Stuttgart for the nice moments we spent together, special thanks to (the titles like "Dr." are omitted): Jorge Serrano Gutiérrez, Carlos de Jesus Manzano Garcia, Kannan Balasubramanian, Thembela Hillie, Milan and Marina Struhar, Alena Palanievich, Esther Barrena Villas, David Quirion, Lucia Capogna, Rubén Esteban, Franck Dahlem, Jean-René Duclère, Alicia Nieto, Dimas García de Oteyza Feldermann, Ajo Mula, Vladimir Hinkov, Magalí Lingenfelder, Alicia Maroto, Hiroki Okudera, Julius Reiβ, Diego Repetto, Miloš Vračar, Eva Zurek, Mael Guennou, Marcos Rigol Madrazo, Omar Stern,

Ana Maria Yelmo Garcia, Ioannis Zegkinoglou, Petar Yordanov, Barbara Panella, Afif and Ayse Siddiki, Željka Elek, Yuri Mastrikov (additional thanks for trying to improve my Russian language), Oleg Yagovtsev, Franziska Leistern and C.W. (for being good WG-mates), Judith and Volker (for trying to teach me some Salsa steps) and: Jorgen Kringen Johnsen, Elena Martinez, Gabriela Guevara, Jakub Cichoszewski, Margit Pattantyús-Ábrahám, Alessandro Ferrari and Ariel Edu Narvaez Salazar (für deutschsprachige Dienstagabends).

* My parents and relatives in Belgrade for the support from long distance.

PUBLICATION LIST

* Vladimir Damljanović: ”An Example of Double-Error Correcting Code”, Proceedings of conference TELFOR ’98, Belgrade, 609-611

* Radoš B. Gajić, Novica Paunović, Vladimir Damljanović, Aleksandar Golubović, Dragana Vuković: “Sensitive Magnetometers Based On The Harmonic Generation Effect in High Temperature Superconductors”, Proceedings of 44th conference ETRAN, Belgarde 2000, 305-307

* Jelena Radovanović, Vladimir Damljanović, Radoš Gajić: “Fitting Procedure Of Reflectance Spectra Based On Simulated Annealing Methods”, 40th consulting of Serbian Chemical Society, Novi Sad 2001, 184

* A. T. Matveev, G. Cristiani, E. Sader, V. Damljanović, H. –U. Habermeier: “Growth of $RuSr_2GdCu_2O_8$ films by post-annealing of pulsed laser deposited precursors”, Physica C **417**, 50-57 (2004).

* V. Damljanović, C. Ulrich, C. Bernhard, B. Keimer, P. Mandal, A. Krimmel, A. Loidl: „Raman scattering study of $Ru(Sr,La)_2GdCu_2O_8$“, Physical Review B **73**, 172502 (2006).

* P. Adler, A. Lebon, V. Damljanović, C. Ulrich, C. Bernhard, A. V. Boris, A. Maljuk, C. T. Lin, B. Keimer: „Magnetoresistance effects in $SrFeO_{3-\delta}$: Dependence on phase composition and relation to magnetic and charge order”, Physical Review B **73**, 094451 (2006).

* A. Maljuk, A. Lebon, V. Damljanović, C. Ulrich, C. T. Lin, P. Adler, B. Keimer: „Growth and oxygen treatment of $SrFeO_{3-y}$ single crystals”, Journal of Crystal Growth **291**, 412-415 (2006).